KfK 3202 / 1
UWFDM-450
Dezember 1981

HIBALL — A Conceptual Heavy Ion Beam Driven Fusion Reactor Study

Volume 1

Institut für Neutronenphysik und Reaktortechnik

Kernforschungszentrum Karlsruhe

KERNFORSCHUNGSZENTRUM KARLSRUHE

Institut für Neutronenphysik und Reaktortechnik

KfK 3202

UWFDM-450

HIBALL - A Conceptual Heavy Ion Beam Driven Fusion Reactor Study

Volume 1

B. Badger[a]
F. Arendt[b]
K. Becker[c]
K. Beckert[d]
R. Bock[d]
D. Böhne[d]
I. Bozsik[e]
J. Brezina[c]
M. Dalle Donne[f]
L. El-Guebaly[a]
R. Engelstad[a]
W. Eyrich[f]
R. Fröhlich[f]
N. Ghoniem[g]
B. Goel[f]
A. Hassanein[a]
D. Henderson[f]
W. Höbel[f]
I. Hofmann[e]
E. Hoyer[h]
R. Keller[d]
G. Kessler[f]
A. Klein[a]
R. Kreutz[i]
G. Kulcinski[a]
E. Larsen[a]
K. Lee[a]
K. Long[f]
E. Lovell[a]
N. Metzler[j]
J. Meyer-ter-Vehn[j]
U. von Möllendorff[f]
N. Moritz[f]
G. Moses[a]
R. Müller[d]
K. O'Brien[a]
R. Peterson[a]
K. Plute[a]
L. Pong[a]
R. Sanders[a]
J. Sapp[k]
M. Sawan[a]
K. Schretzmann[f]
T. Spindler[a]
I. Sviatoslavsky[a]
K. Symon[a]
D. Sze[a]
N. Tahir[f]
W. Vogelsang[a]
A. White[a]
S. Witkowski[j]
H. Wollnik[c]

[a]University of Wisconsin, Madison
[b]KfK, Institut für Technische Physik
[c]Universität Gießen, II. Physikalisches Institut
[d]Gesellschaft für Schwerionenforschung, Darmstadt
[e]Max-Planck-Institut für Plasmaphysik, Garching
[f]KfK, Institut für Neutronenphysik und Reaktortechnik
[g]University of California, Los Angeles
[h]Lawrence Berkeley Laboratory, Berkeley
[i]Interatom, Bergisch Gladbach
[j]Max-Planck-Institut für Quantenoptik, Garching
[k]McDonnell-Douglas

Kernforschungszentrum Karlsruhe GmbH, Karlsruhe

Kernforschungszentrum Karlsruhe GmbH
und University of Wisconsin-Madison
ISSN 0303-4003

Abstract

HIBALL - A Conceptual Heavy Ion Beam Driven Fusion Reactor Study

A preliminary concept for a heavy-ion beam driven inertial confinement fusion power plant is presented. The high repetition rate of the RF accelerator driver is utilized to serve four reactor chambers alternatingly. In the chambers a novel first-wall protection scheme is used. At a target gain of 83 the total net electrical output is 3.8 GW. The recirculating power fraction is below 15%.

The main goal of the comprehensive HIBALL study (which is continuing) is to demonstrate the compatibility of the design of the driver, the target and the reactor chambers. Though preliminary, the present design is essentially self-consistent. Tentative cost estimates are given. The costs compare well with those found in similar studies on other types of fusion reactors.

Zusammenfassung

HIBALL - Eine Konzeptstudie für einen durch Schwerionenstrahlen getriebenen Fusionsreaktor

Es wird ein vorläufiges Konzept für ein Trägheitsfusionskraftwerk mit Schwerionenstrahltreiber vorgestellt. Die hohe Pulsfolgefrequenz des Treibers vom HF-Beschleuniger-Typ wird ausgenutzt, um vier Reaktorkammern abwechselnd zu bedienen. In den Kammern wird eine neuartige Technik zum Schutz der ersten Wand eingesetzt. Bei einem Target-Energiegewinn von 83 beträgt die elektrische Netto-Gesamtleistung 3.8 GW. Der rezirkulierende Leistungsanteil liegt unter 15%.

Hauptziel der umfassenden HIBALL-Studie (die fortgesetzt wird) ist es, die Verträglichkeit der Entwürfe für Treiber, Target und Reaktorkammern nachzuweisen. Obwohl vorläufig, ist der vorliegende Entwurf im wesentlichen konsistent. Es werden vorläufige Kostenschätzungen angegeben. Die Kosten sind gut vergleichbar mit denen, die in ähnlichen Studien für andere Typen von Fusionsreaktoren gefunden wurden.

PREFACE

HIBALL (Heavy Ion Beams and Lithium Lead) is a conceptual reactor design study for inertial confinement fusion (ICF) with beams of heavy ions. The HIBALL study was started in January 1980 and is being jointly performed by research groups of the

University of Wisconsin, Fusion Engineering Program (UW)

Kernforschungszentrum Karlsruhe (KfK)

Gesellschaft für Schwerionenforschung, Darmstadt (GSI)

Max-Planck-Institut für Quantenoptik, Garching (MPQ)

Institut für Plasmaphysik, Garching (IPP), and

II. Physikalisches Institut, Universität Giessen.

The objectives of this study are the investigation of the system characteristics of a fusion reactor based on a heavy ion accelerator as the driver facility and the identification of problems to be investigated in the future.

The HIBALL study is part of a basic research program established by the German Federal Ministry of Research and Technology (BMFT). This program is aimed at the investigation of key problems in the fields of accelerator research, atomic physics, target physics and reactor design. Another main purpose is to examine the present conviction, generally accepted in the accelerator community, that no fundamental physics problems inhibit the use of heavy ions as a driver for ICF.

The present report, published jointly by KfK and UW, is of a preliminary nature and represents the status as of June 1981. In the text, this stage of the design will sometimes be referred to as HIBALL-I. A final report with an advanced, more complete and more consistent design (HIBALL-II) is scheduled for the end of 1982.

Acknowledgments

We wish to acknowledge R. Bangerter, A. Bell, J. Beyer, R. Burke, R. Evans, C. Hendricks, N. Hoffman, Y. Kim, G. Magelssen, D.J. Nicholas, U. Trinks and Z. Zinamon for valuable technical discussions.

The German contributions to this study have been funded by the BMFT heavy-ion fusion research program. The UW efforts were performed under a contract jointly funded by KfK (70%) and the BMFT program (30%). We express our appreciation to W. Klose for his support and to R. Rennebohm for making financial arrangements.

Finally, we gratefully acknowledge the help of the secretarial and support staff at UW -- Elizabeth Brown, Gail Herrington, Linda Kraft, and Dennis Bruggink - for their most professional efforts in typing and assembling this report.

Note

This report was printed in two editions, one at the University of Wisconsin and subsequently the present one at KfK. For the present edition, some mistakes have been corrected and the figures II.1-5 to 8 added.

TABLE OF CONTENTS

VOLUME 1

References are found after each subchapter (e.g., III.1) or chapter (e.g., I).

I Introduction

I.1 General Perspectives

Inertial Confinement Fusion (ICF) is considered as an alternative to Magnetic Confinement Fusion, with the goal, in both cases, of exploiting the energy released from thermonuclear fusion reactions to produce electric energy. In the case of ICF, this is accomplished by imploding targets containing DT fuel to very high densities (1000 x liquid density) with the use of intense beams of photons or charged particles. The ICF program started later (~ 1961) and with substantially less financial support than magnetic fusion. Because of this fact, as well as the emphasis on military rather than civilian applications in the United States, the ICF approach to electric power generation is not as well developed at this time as the magnetic fusion approach. However, inertial confinement fusion has many attractive features, including: the separation of the driver from the reactor cavity with its high level of radioactivity, and a relatively simple geometry (compared with tokamak reactors) and therefore greater design flexibility along with better maintenance accessibility of the reactor. On the other hand, new problems related to the pulsed release of energy (~ 10^{-8} sec) require innovative protection schemes for the first wall and the final components that focus the driver beams onto the target.

The specific design and overall economics of an ICF reactor are mainly determined by the choice of driver and the target characteristics. Heavy ion beams, from accelerator systems similar to those widely used in high energy physics, have been considered since 1975-76 as an attractive driver choice for reactors. This is because they can deliver large amounts of energy per pulse at a high repetition frequency. Different criteria might favor other drivers if an experimental proof-of-principle device for a single shot facility is

visualized. A major target physics requirement common to all drivers - whether lasers, light ions or heavy ions - is that several hundreds of terawatts of power should be delivered onto a target of a few mm radius to achieve compression and ignition with high gain. Heavy ions are the only candidate which permit essentially classical beam transport to the target and classical deposition of energy in the target ablator shell. This is due to the fact that, based on the same classical penetration depth, the energy of very heavy ions ($A > 200$) can be of the order of 10 GeV, whereas the equivalent energy of very light ions is below 10 MeV. As a consequence, the same demand for beam power has to be met with megaamperes of light ions (along with possible collective effects in both the cavity transport and the target deposition region) whereas heavy ion beam currents can remain in the kiloampere range. It is generally accepted now[1] that these requirements can be met - at least in principle - with existing accelerator technology. This technology has other significant advantages.

- A high efficiency of 20-25% is credited to high energy accelerators. This allows for "conservative" target design with allowable target gain of less than 100.
- A high repetition rate of 20 Hz is realizable for the RF accelerator based scenario. Such an accelerator can support several reactor cavities, the number of which is determined by the time needed to reestablish beam propagation conditions.
- High working reliability (70-80%) can be extrapolated from existing accelerators.
- The option of ballistic beam focusing on target - as though in vacuum - using superconducting quadrupole magnets is available. This provides an independence from plasma channel transport schemes which cannot yet be

assessed for a reactor with the present level of theoretical and experimental understanding.

On the other hand, it has become clear since the first Heavy Ion Fusion Study at Berkeley[2] in 1976 that the size and cost of a heavy ion driver can be considerable and such factors certainly have a major influence on the anticipated cost of electricity. This gives strong justification to a complete conceptual reactor design study at the present time.

I.2 Basis and Objectives of HIBALL

The specific goal of the HIBALL study is to demonstrate the compatibility of physics and engineering design in the areas of the driver (including final beam transport), target, and reactor chamber through a self-consistent conceptual reactor design. In addition, it is required that HIBALL be a DT fusion power plant that produces electricity on an economically and environmentally acceptable basis as compared to other fusion conceptual reactor designs. Before HIBALL can be built, successful operation of at least three heavy-ion driven fusion facilities will probably have to be achieved:

1) a "scientific breakeven" device ($\frac{\text{energy out}}{\text{energy in}} = 1$),
2) an Engineering Test Facility, and
3) a Demonstration Fusion Power Plant (net electricity and tritium production).

This means that HIBALL, as a reactor concept, will have the benefit from at least two or three decades of research in imploding targets.

I.2.1 Driver Scenario

The task of the driver in HIBALL is to produce high beam intensity within a six-dimensional phase space volume that is small enough to be focused onto a 3 mm radius target at the reactor stand-off distance of 8.5 m with a pulse duration of 20 nsec. This has been evaluated within the following scenario:

- A RF linear accelerator is used to achieve the final energy of 10 GeV for Bi^{+2} at a current level of 160 mA. This choice benefits from the high level of confidence in design reliability and cost estimates for RF accelerator technology.
- A large radius transfer ring and several more compact condenser and storage rings are used to raise the current by almost three orders of magnitude through a sequence of stacking and bunching procedures.

- Induction linear accelerators in the final beam lines supply a ramped voltage of several hundred M V to achieve a final ten-fold compression on the long path (2/3 of a kilometer) of the ions to the target chamber. This raises the particle current per beamlet from 120 A to 1200 A, hence 20 beamlets per cavity will produce a power of 240 terawatts on target.

The overall scenario for HIBALL resembles the BNL RF accelerator scenario suggested several years ago. The design has benefitted also from the results of heavy ion fusion (HIF) studies performed in the past years at major U.S. high energy laboratories (ANL, BNL and LBL) and at the Rutherford Laboratory in England[1-4].

Recent experimental progress at GSI in Germany, in the development of ion sources with the required performance (50 mA of extracted ions with $A/q \approx 100$ and a normalized emittance of $\lesssim 2 \cdot 10^{-7}$ m-rad), has been incorporated in the design. Progress has also been achieved at GSI in the design of the low-velocity accelerating structures. This includes the RFQ structure (developed jointly with the University of Frankfurt) and a Wideröe-based funneling scheme to feed the current of a total of eight ion sources into the main Alvarez accelerator.

Less design effort has been dedicated to the storage rings, where a number of topics will have to be the subject of future theoretical and experimental studies. The main distinction of these storage rings from machines designed and built so far stems from the high intensity and consequently, the dominant space charge effects. The following novel issues also appear important:

- stacking under conditions of large space charge,
- beam loss at septa,
- longitudinal microwave instabilities with a space charge dominated coupling impedance, and
- resonance crossing during bunching.

A detailed study will also be needed to assess the performance and cost of final compression induction modules. Significant design work in this area has been done by the HIF group at Lawrence Berkeley Laboratory, and the modules suggested here are based on their design results.

In the framework of the HIBALL study, progress has been made also in the area of final transport and focusing. Control of emittance growth and space charge effects has been achieved and the consistency of the vacuum propagation mode with cavity conditions ($\sim 10^{-5}$ Torr of Pb reestablished after each shot) has been demonstrated.

I.2.2 Target Design

The target is the central element of the reactor system on which the heavy ion beams are focused and where the fusion energy is released. High gain targets (fusion energy/input beam energy = 50-100) are required for a Heavy Ion Beam ICF power reactor. The feasibility of such targets is inferred from theoretical analysis, but we are still far from actual experimental tests of such targets. For the time being, one has to rely on parameter models and numerical simulation.

The responsibility for HIBALL target design was designated to be at MPQ and KfK. Since the target activities at MPQ and KfK had started just recently and no detailed design was available at the beginning of the HIBALL study, a set of parameters was fixed at an early stage under the guidance of the UW group, relying on unclassified target design literature from the Lawrence Livermore National Laboratory. This set has served as a "frozen" basis for the driver design and the reactor cavity analysis. The objective for the target design work then was to check the general consistency of these parameters.

The chosen working point for the HIBALL target (input beam energy, 4.8 MJ, released fusion energy, 400 MJ, and gain, 83) was well justified by a simple parameter study with reasonable assumptions concerning hydrodynamic efficiency, convergence ratio, cold fuel isentrope, ignition pressure and burn rate. The work now in progress at KfK and MPQ will connect these parameters with the ion energy of the beam and maximum beam power as well as target geometry to allow for a general optimization. The physics of heavy ion stopping in hot dense plasma has been investigated, and actual ranges and deposition profiles have been calculated for a specific target configuration. As a first attempt, a cryogenic single shell design has been chosen, closely following a Livermore design for light-ion beam fusion. The objective was to study one-dimensional implosions of this target to obtain a general insight and to identify critical issues rather than to present an optimal design which, at the moment, is beyond the capabilities of the groups involved. The spectra of X-rays and ions emerging from the burning target as well as the target neutronics have been calculated by both of the groups at the UW and KfK and their effect on the cavity design has been analyzed.

I.3 Assumptions on Level of Technology and on Utilization of HIBALL

The level of technology that has been assumed for HIBALL is what we think will be typical of the year 2000-2020 period. This means that information developed over the next 20 years on accelerator design, superconducting magnets, liquid metal handling, radiation damage, and remote maintenance will be available. The target physics is assumed to have been established on a proof-of-principle device, the delivery of the target and repetitive operation of the system will have been demonstrated in an Engineering Test Facility, and the power handling, as well as indications of economic performance will have been established in a Demonstration Power Reactor. Since the HIBALL class of reactors is designed to operate perhaps in the 2020-2030 period, the size of the electrical grids will be larger than at the present time, thus allowing larger units to be integrated into the utility without fear of overdependence on a single reactor. (The largest Light Water Reactor units have at present a power output of 1300 MWe. There are several sites already now in Europe and the USA where 4-5 units with about 5 GWe total output will be operated at one site.)

Finally, we have chosen to examine the production of electricity first because we think that is where HIF reactor systems will have the most immediate impact. Other modes of operation, e.g., production of fissile fuel, synthetic fuels, or steam could also have been considered. At the present time, the relative economics of the various options are not readily apparent so there is no way to define the optimum form in which to derive energy from HIBALL. The large capital costs of a high energy accelerator driven reactor and the finite limits to waste heat disposal or electrical grid size, may require a combination of integrative (e.g., fissile or synthetic fuel

production) and real time (e.g., electricity or process steam) systems for optimum performance.

References for Chapter I

1. Proceedings of the Heavy Ion Fusion Workshop, Argonne, September 1978, ANL 79-41.

2. ERDA Summer of Heavy Ions for Inertial Fusion Final Report, December 1976, LBL-5543.

3. Proceedings of the Heavy Ion Fusion Workshop, Brookhaven, October 1977, BNL-50769.

4. Proceedings of the Heavy Ion Fusion Workshop, Berkeley, September 1980, LBL-10301.

II Overview and Recommendations

II.1 Overview of HIBALL

The main operating parameters of the HIBALL (Heavy Ion Beams and Lithium-Lead) reactor are given in Table II.1-1. A detailed list of operating parameters is included in Appendix A. We have chosen a DT fusion power of 8000 MW from a preliminary economic consideration of the number of reactor chambers to be served by a common heavy-ion driver. This power level results in a net electrical output of 3768 MW.

HIBALL utilizes 4 reactor chambers, each fired at a repetition rate of 5 Hz. The overall plant layout is shown in Fig. II.1-1. The beam ions are Bi^{+2} at 10 GeV and the total energy of each pulse is 4.8 MJ. This energy is delivered in a reactor chamber to the target by 20 beams with a maximum electrical current of 2.5 kA/beam. The 20 beams are propagated through the gas vapor atmosphere of a reaction chamber (Fig. II.1-2) which contains no more than 10^{11} atoms of Pb vapor per cm^3 before each shot. The targets are made from Pb and PbLi surrounding a cryogenic layer of deuterium and tritium (Fig. II.1-3). The 4.8 MJ pulse of Bi^{+2} ions is assumed to give a target gain of 83 and a total DT yield of about 400 MJ. With a driver efficiency of 26.7%, the fusion gain (driver efficiency x target gain) is 22. This results in a recirculating power fraction of 12.3% if we assume that all of the beam hits the target and we include the power requirements of the coolant circulation pumps, vacuum system, etc.

The first metallic wall, made of HT-9 ferritic steel, is 7 meters from the target (see Fig. II.1-2). It is protected from the target X-rays, ions, and neutrons by an array of porous SiC tubes through which $Pb_{83}Li_{17}$ is flowing. These tubes, called INPORT units, for the Inhibited Flow-Porous Tube Concept, occupy a region 2 meters in front of the first wall and are arranged

Table II.1-1 HIBALL Parameters

DT power level	8000 MW
Gross thermal power	10233 MW
Gross electrical output	4298 MWe
Net electrical output	3768 MWe
Accelerator type	RF-Linac
Driver efficiency	26.7%
Ion	Bi^{+2}
Ion energy	10 GeV
Beam pulse energy	4.8 MJ
Beam power	240 TW
Total pulse rate	20 Hz
Base chamber pressure, torr at RT	10^{-5} (Pb vapor)
No. of ion beams per chamber	20
Electrical current per ion beam	2.5 kA
Target	Pb-PbLi-DT
Target yield	396 MJ
Target gain	83
Target shot rate per cavity	5 Hz
Fusion gain (ηG)	22
No. of cavities	4
Breeder and coolant	$Pb_{83}Li_{17}$
Tritium breeding ratio	1.25
Tritium inventory (active)	1 kg
Structural material	HT-9
Maximum coolant temperature	500°C
F. W. protection scheme	INPORT units ($SiC/Pb_{83}Li_{17}$)
Maximum dpa rate in HT-9 first wall	2.7/FPY
Lifetime of first wall	20 FPY
Lifetime of INPORT units	2 FPY

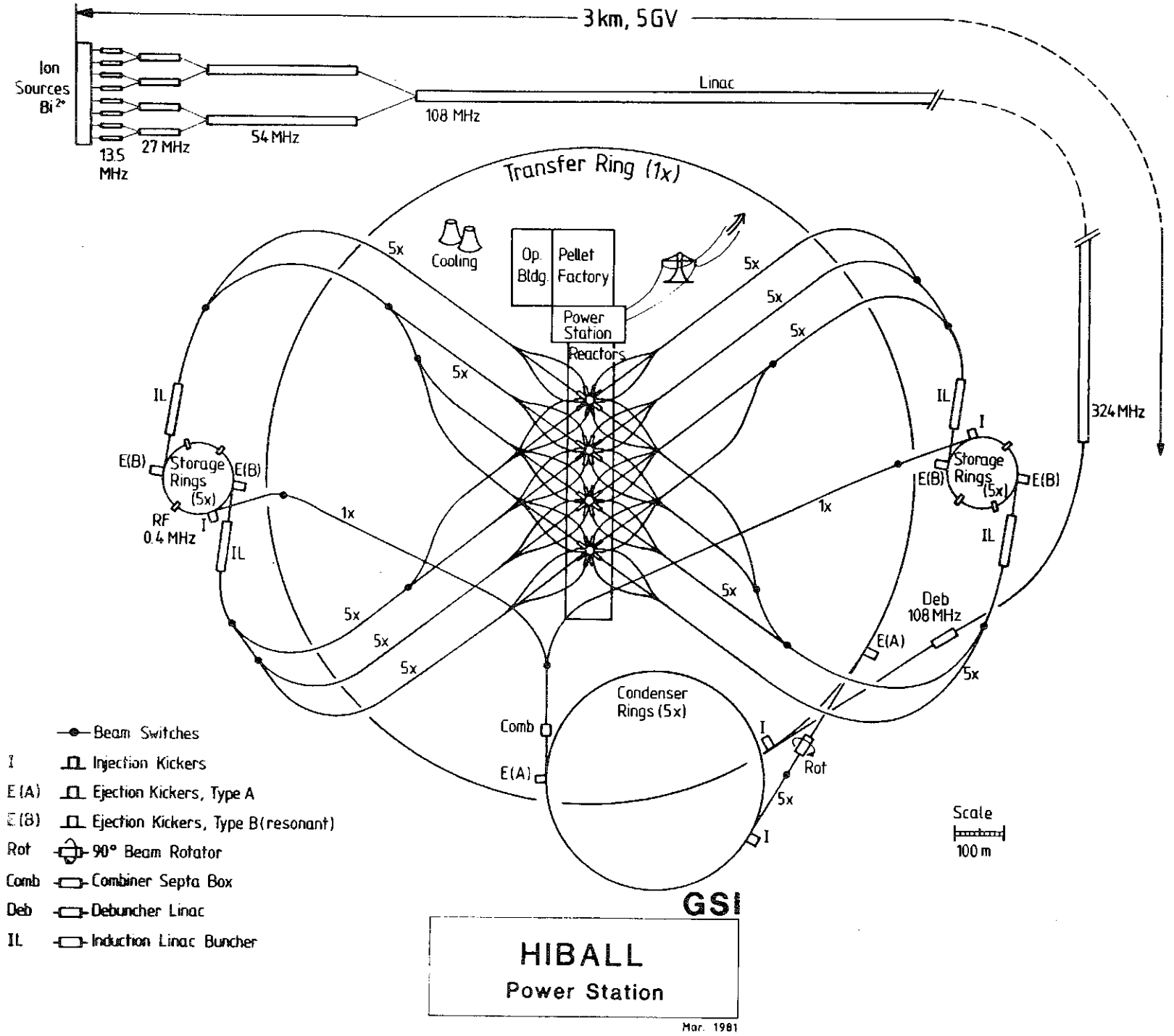
3 km, 5 GV
Ion Sources Bi 2+
13.5 MHz
27 MHz
54 MHz
Linac
108 MHz
324 MHz
Transfer Ring (1x)
Cooling
Op. Bldg.
Pellet Factory
Power Station
Reactors
5x
1x
IL
I
E(B)
Storage Rings (5x)
RF 0.4 MHz
Deb 108 MHz
E(A)
Condenser Rings (5x)
Comb
Rot
Beam Switches
Injection Kickers
Ejection Kickers, Type A
Ejection Kickers, Type B (resonant)
90° Beam Rotator
Combiner Septa Box
Debuncher Linac
Induction Linac Buncher
Scale
100 m
GSI
HIBALL
Power Station
Mar. 1981

Fig. II.1-1

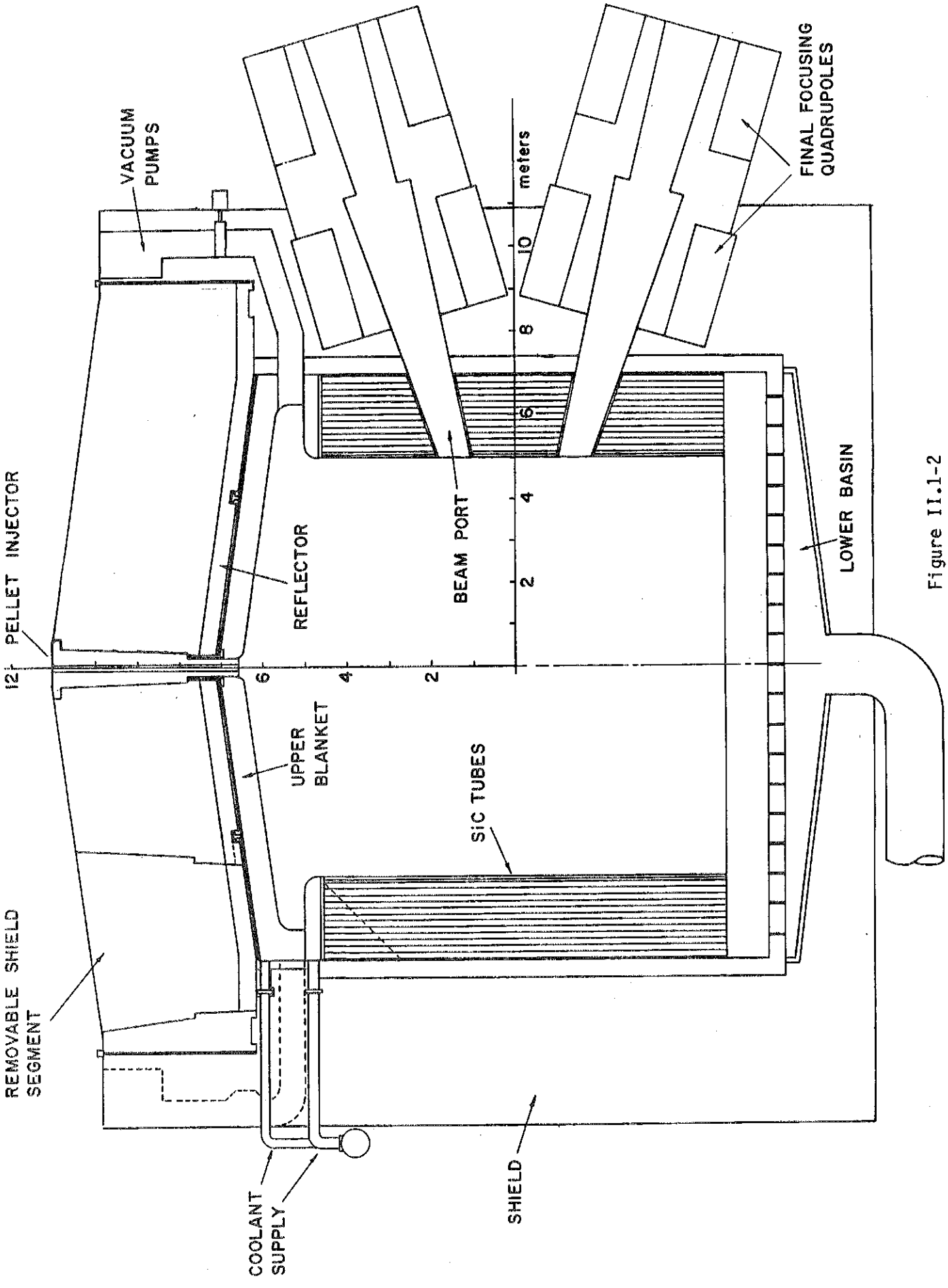
VACUUM PUMPS
FINAL FOCUSING QUADRUPOLES
meters
10
8
6
4
2
PELLET INJECTOR
REFLECTOR
BEAM PORT
LOWER BASIN
UPPER BLANKET
SiC TUBES
REMOVABLE SHIELD SEGMENT
COOLANT SUPPLY
SHIELD

Figure II.1-2

Figure II.1-3

Perspective view of the HIBALL pellet.

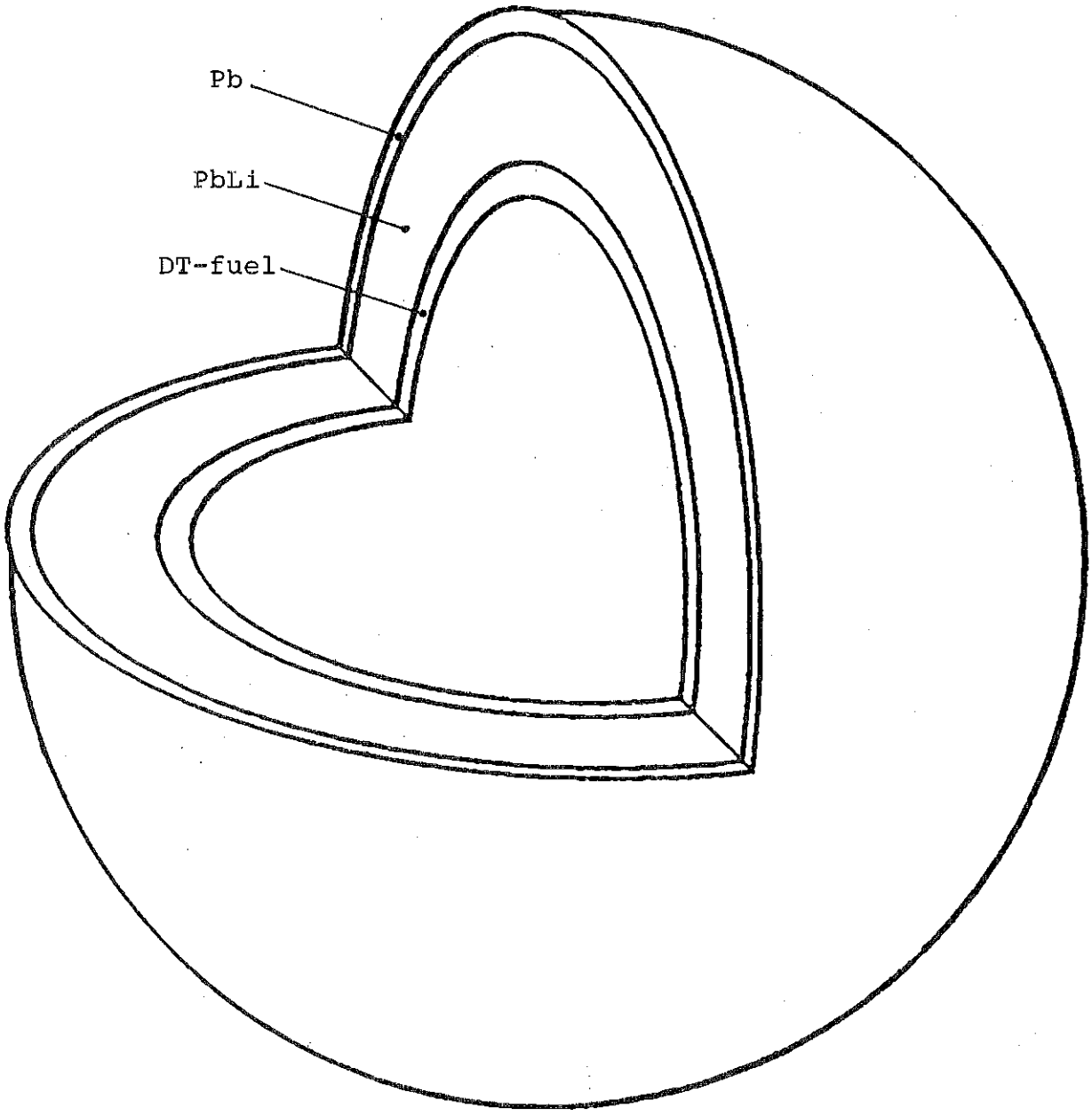

Figure II.1-4

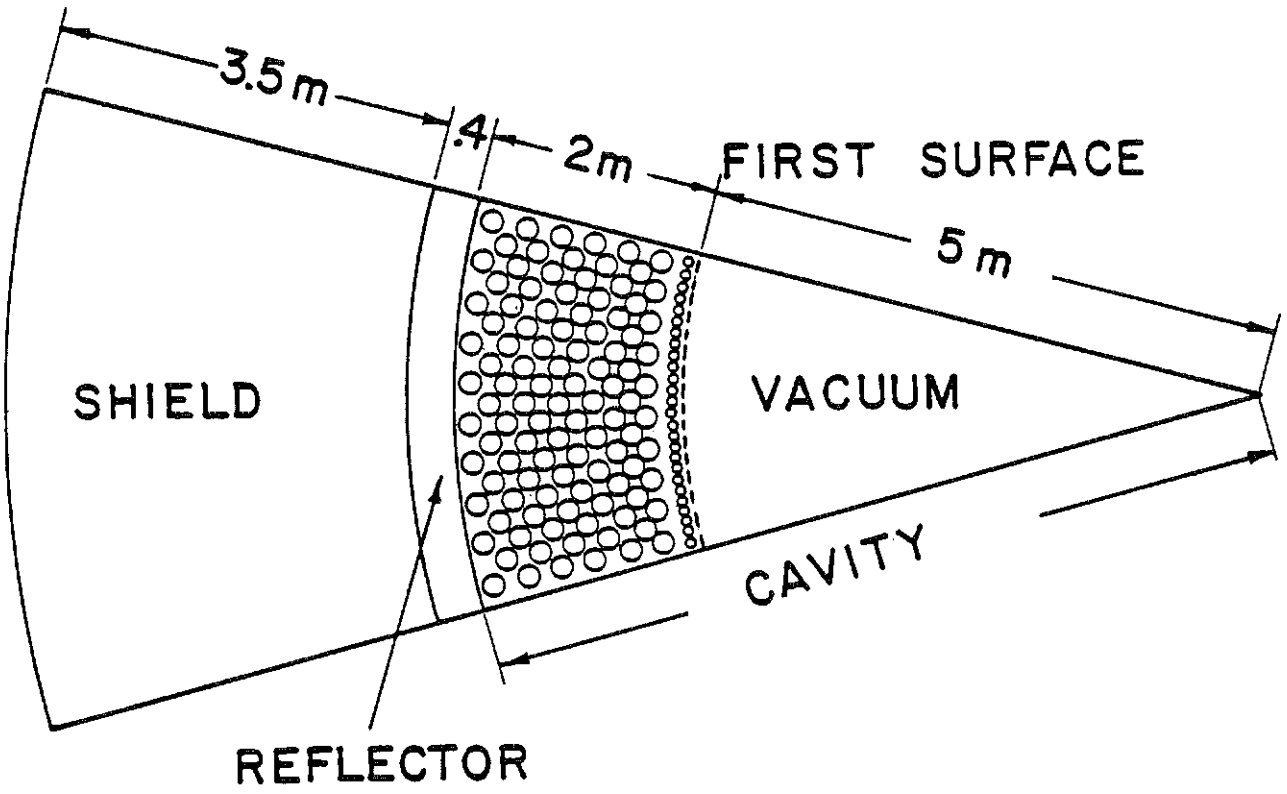

with a 33% volume fraction (Fig. II.1-4). The SiC INPORT tubes are protected from the short range X-rays and ion debris by a thin coating of $Pb_{83}Li_{17}$ flowing through the porous tube wall. This coating is partially vaporized on each shot and recondenses on the tubes in the 200 ms between shots. The maximum coolant temperature is 500°C insuring that the Pb pressure in the cavity is less than 10^{-5} torr (normalized to 0°C). The tritium breeding ratio is 1.25 and the low solubility of tritium in $Pb_{83}Li_{17}$ results in less than 100 grams of inventory in the blanket and fuel processing system. The low solubility also allows all tritium extraction to be done in the cavity itself. Hence, the bred tritium is removed through the vacuum system along with the unburned tritium from the target.

The effective 66 cm thickness of the INPORT blanket, composed of 98% $Pb_{83}Li_{17}$ and 2% SiC, reduces the radiation damage in the first structural wall to 2.7 dpa per full power year (FPY) meaning that damage equivalent to 5 MW-y/m^2 will be accumulated over 30 calendar years. Since the fusion materials community hopes to develop steels which will last more than 10 MW-y/m^2 under those conditions, we fully expect the steel chamber to last the life of the plant.

The preliminary economic analysis of HIBALL reveals that the capital cost (in 1981 dollars) is $1795 per KWe and the busbar cost of electricity is 41 mills per kWh. Such numbers are very competitive with previous tokamaks and tandem mirror reactor studies and therefore give us a good reason to pursue the HIBALL concept to an even greater level of detail.

Visualizations of the plant layout and some important details are shown in Figs. II.1-5 to 8.

1
2
3
4
5
6
7
8
9
10
HIBALL FUSION REACTOR PLANT (3.8 GW$_{el}$)
kfk
GSI
UWM

Fig. II.1-5 HIBALL Fusion Reactor Plant (3.8 GW_{el})

1 Ion Sources and RFQ Linacs
2 Funneling Section
3 Alvarez Linac
4 Transfer Ring
5 5 Condenser Rings
6 2x5 Storage Rings
7 4x5 Induction Linac Compressors
8 Reactor Chamber
9 Target Factory
10 Control Building

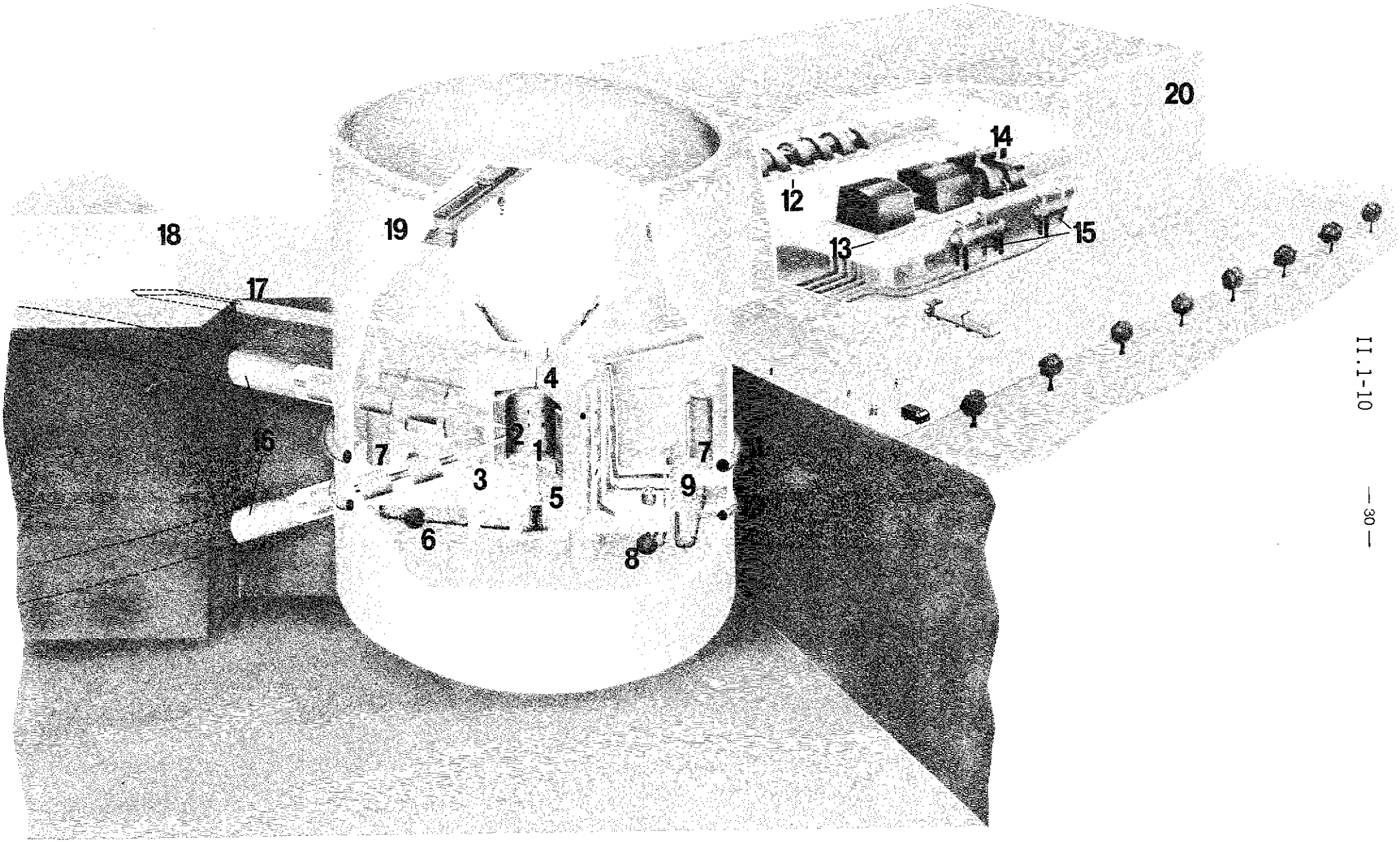

HIBALL REACTOR BUILDING (940 MW_{el})

Fig. II.1-6 HIBALL Reactor Building (940 MW_{el})

1 Reactor Chamber
2 INPORT Blanket
3 Final Focusing Quadrupole Magnets
4 Rotatable Top Shield
5 Coolant Exit
6 Primary Pump
7 Heat Exchanger
8 Secondary Coolant Pump
9 Steam Generator
10 Water Intake
11 Steam Exit
12 High Pressure Turbine
13 Low Pressure Turbine
14 Electricity Generators
15 Condenser and Water Preheater
16 Beam Lines
17 Target Transport Line
18 Target Factory
19 Reactor Containment
20 Machine Building

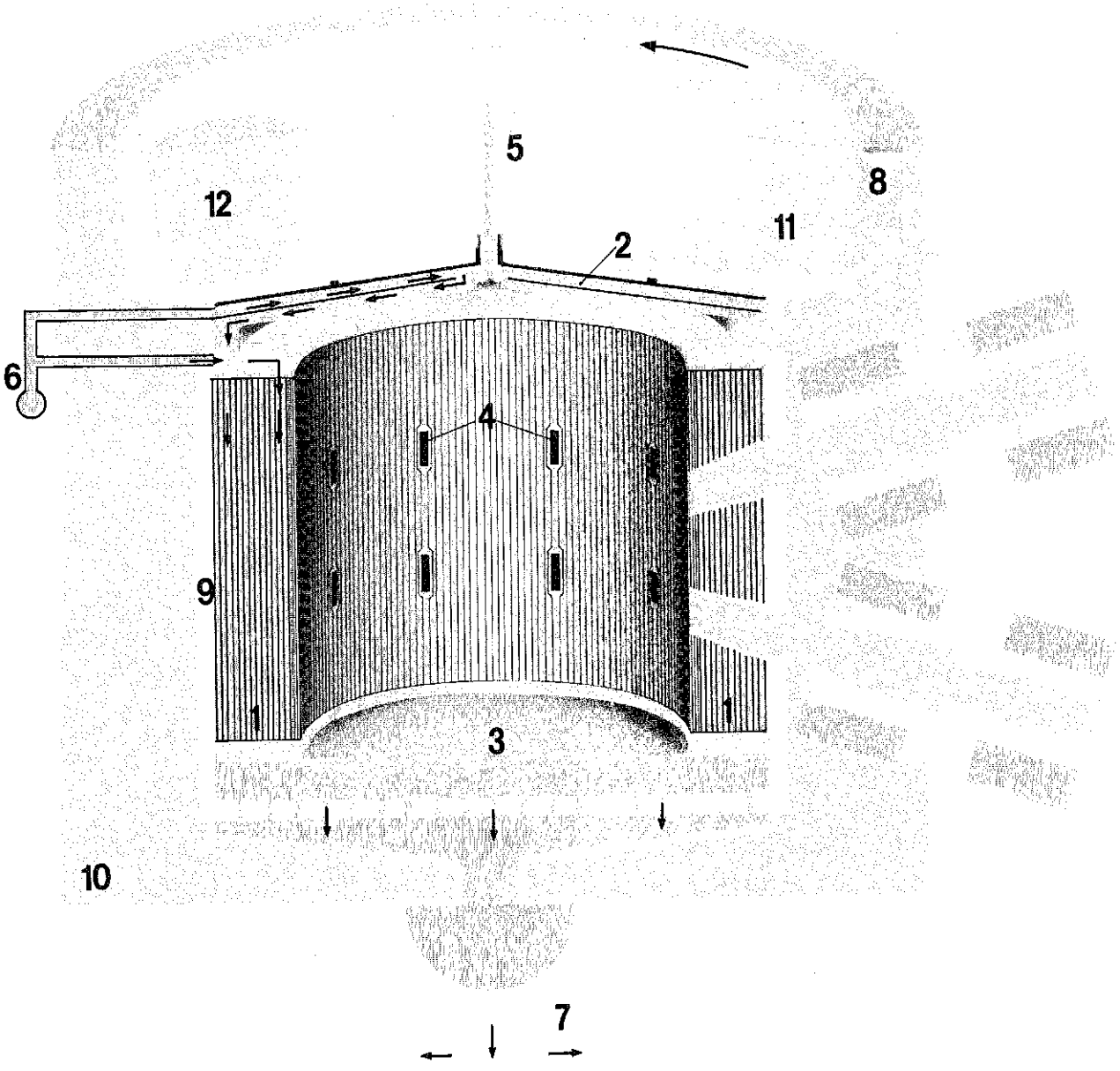

HIBALL REACTOR CHAMBER

Fig. II.1-7 HIBALL Reactor Chamber

1 Lateral INPORT Blanket
2 Top INPORT Blanket
3 Bottom Pool
4 Beam Ports
5 Pellet Injector
6 Coolant Intake
7 Coolant Exit
8 Vacuum Pumps
9 Steel Reflector
10 Concrete Shield
11 Rotatable Top Concrete Shield
12 Removable Plug

STRAIGHT PART OF FINAL FOCUSSING QUADRUPOLE MAGNET

Fig. II.1-8 Straight Part of Final Focusing Quadrupole Magnet

1 Superconducting Coils
2 Neutron and γ-Ray Shield
(Steel, Lead, Water and Boron)
3 Ion Beam

The curved arrows indicate the direction of current in the coils.

II.2 Areas of Further Improvement

As mentioned previously, the first phase of the HIBALL design study has already pointed out several areas where more work needs to be done. The present self-consistent point design, with 10 GeV Bi^{2+} ions, should be extended to accelerator scenarios where the heavy ions have either lower (5 GeV) or higher energy (20 GeV). This will directly affect the accelerator design, the number of beam lines, the pulse energy on target as well as the target size and design. Only a parametric analysis including cost considerations can lead to an optimum set of design characteristics. The present pulse repetition rate of the HIBALL-I driver should be raised from 20 Hz to 30 Hz in order to support more reactor chambers and thereby decrease the capital costs. The induction linac section envisaged for the final fast bunch compression must be considered in more detail. The present focal spot of the Bi^{2+} beams at the center of the cavity is not consistent with the target diameter, so that an unacceptably large fraction of the ions miss the target. Additional studies are required to increase the target size but at the same time the beam focussing must be improved to yield a smaller spot. Also, from the target physics point of view, it is highly desirable to use a shaped pulse. The realization of this by superimposing pulses from different beam lines has to be investigated in detail. More refined calculations are also necessary to determine the debris and the photon spectra from the burning target. All parameters used in the current parameter list are scaled up from a 1 mg target design. Once a credible 400 MJ target is designed, it should be used to generate the target output characteristics.

In the area of reactor chamber design the last mentioned discrepancies directly affect the vaporization and condensation processes of the PbLi film at the surface of the SiC woven INPORT blanket tubes. More detailed beam

transmission calculations in Pb vapor are still needed. The solubility of tritium in PbLi must be experimentally substantiated, the tritium inventory in the target facilities should be decreased, and the tritium permeation through the barriers of the primary heat exchangers must be analyzed in more detail. Material problems like the compatibility of SiC with PbLi, the strength and fatigue lifetime of the woven tubes must be further considered. In addition, further analysis of the PbLi heat transport system, the secondary coolant systems, and the vacuum system for the reactor chamber is necessary. A more detailed assessment of costs and the design of reactor buildings with beam lines will be needed.

Finally, some areas could not be addressed at all in the first phase of the work. Among these are the assembly process of the targets and the target manufacturing costs, the reliability of the driver system and its impact on plant performance, as well as safety and environmental questions. All or most of these improvements and extensions of the present study are scheduled for HIBALL-II.

In addition to the above items, we also should investigate applications other than electricity generation for HIBALL. For example, we might investigate the use of HIBALL to produce:

1.) fissile fuel

2.) synthetic fuel

3.) process steam

Another area of interest could be the use of HIBALL to support "captive" industries, such as Al producers, which could accommodate interruptable power easier than the general public. The trade-off in economics and flexibility between using different chambers to provide energy in different forms should also be examined. For example, one scenario might be as follows:

Chamber 1 - Support captive Al plant with 800 MWe.

Chamber 2 - Provide ~ 10 tonnes ^{239}Pu per full power year.

Chamber 3 - Generate ~ 200,000 tonnes of H_2 per FPY.

Chamber 4 - Provide ~ 4 x 10^6 tonnes of steam at 500°C per FPY.

It is possible that the tritium breeding ratio (TBR) could be maximized or minimized in each chamber to optimize production of the end product. One could reduce the TBR in the hybrid chamber while maximizing it in the process steam chamber through the use of enriched Li for instance.

We have not determined how small the HIBALL reactor could be and still be "competitive". Such an analysis could be done in the future with the HIBALL configuration.

Finally we have investigated the RF linac driver in HIBALL but it would be interesting to see what effect an induction linac may have on the overall cost of the system. The rest of the plant could be held constant for this study.

It is clear that much work has been done, but there is much more work to do. The large size of the heavy ion beam system should be turned to an advantage through flexibility and integration into "energy park" scenarios. We have only scratched the surface of the possibilities for heavy ion fusion reactors.

III Target Design

Fusion reactor conceptual designs depend in a fundamental way on the plasma physics models and assumptions used to estimate the fusion performance. In the case of inertial confinement fusion, the plasma physics is replaced by so-called target physics which includes: driver beam-target interaction, plasma hydrodynamics, high pressure equations of state, thermonuclear burn phenomena, fluid instabilities, design creativity, etc. In this chapter we describe the parameters chosen for the HIBALL design and supporting analysis that serves as a basis for our choices. Three different groups at MPQ, KfK, and UW have contributed to these studies and the results of each group's activities are reported in different subsections of this chapter, following the discussion of the HIBALL target parameters.

This organization of Chapter III is necessitated by the chronological difficulties that we met in determining target parameters for HIBALL. A set of target parameters was required early in the study to serve as the basis for much of the reactor analysis (source neutron spectrum, X-ray and ion spectra and yields, target materials, DT fractional burnup, etc.). However, during the HIBALL study the target analysis groups at MPQ and KfK were in a developmental stage where their main emphasis was on computer code development and physical understanding of the target phenomena. Actual target design activities were premature. To solve this problem the UW group made a "best-guess" at reasonable target parameters and these were used for the HIBALL reactor analysis. Subsequent analysis by the MPQ and KfK groups showed that this crude estimate was not totally correct in detail. However, there is nothing fundamentally in error.

The independent target design contributions of the MPQ and KfK groups are reported in sections III.2 and III.3, respectively. These represent

preliminary attempts at target designs that meet the HIBALL requirements. Because this is an iterative process (and we have not yet iterated once) there are inconsistencies between the target designs reported here and the fixed set of target parameters used in HIBALL. At this early stage of target design activity, these inconsistencies are unavoidable. In the future we hope to perform the iteration between target design and driver and cavity requirements to provide a fully consistent picture of HIBALL.

III.1 Set of Target Parameters for HIBALL

The main target parameters used for the HIBALL study are given in Table III.1-1. The yield from the DT fuel is 400 MJ but the net target yield is only 396 MJ when endoergic neutron reactions are taken into account. This subtlety will be discussed later. The absorbed ion energy of 4.8 MJ therefore gives a gain of 83. This value of target gain is within the "conservative" band of the Livermore gain curves shown in Fig. III.1-1. Analysis in section III.2 shows that this gain is also consistent with the work of Bodner.[1] Details of the target design are an adaptation of a light ion beam target design reported by Bangerter[2,3] and Meeker. Some explanation of these adaptations is necessary.

No heavy ion beam target designs for reactor applications have been reported in the journal literature. Furthermore, we were not prepared to undertake a detailed target design activity during this initial HIBALL study. Consequently, we elected to use the closest available substitute target design that was available in the open literature. This was the so-called "Bangerter" design shown in Fig. III.1-2. This is a single shell design consisting of three material layers: DT fuel levitated at an aspect ratio of 10, a low density high-Z impregnated plastic (TaCOH) to serve as an ablator-pusher, and a high-Z lead layer to act as an inertial tamper. This target requires 1.3 MJ of 6.5 MeV protons in a pulse shape shown in Fig. III.1-3. The very pronounced Bragg peak in the ion range energy curve, Fig. III.1-4, is used to great advantage in this design. The protons preferentially deposit their energy in the TaCOH ablator-pusher rather than in the lead tamper. This leads to a very efficient implosion. The gain of this target is 88 giving a yield of 113 MJ.

Table III.1-1 Target Parameters for HIBALL

DT yield	400 MJ
Target yield	396 MJ
Target energy multiplication	0.99
Ion beam energy	4.8 MJ
Ion beam power	240 TW
Ion energy	10 GeV
Ion type	Bi^{+2}
Target gain	83
Target diameter	0.6 cm
Configuration (# of shells, # of layers)	1 shell, 3 layers
Composition	
D	1.6 mg
T	2.4 mg
Pb_5Li_{95}	67.1 mg
Pb	288. mg
Total target mass	359. mg
Fuel R at ignition	2 g/cm^2
Pusher R at ignition	1 g/cm^2
Fractional DT burnup	29%
Neutron yield	284.8 MJ
Average neutron energy	11.98 MeV
Neutron multiplication	1.046
Gamma yield	0.6 MJ
Average gamma energy	1.53 MeV
X-ray yield	89.5 MJ
X-ray spectrum (equivalent blackbody)	1 keV
Debris yield	21.0 MJ
Debris spectrum	0.85 keV/amu
Radioactivity production	1.2×10^6 Curies at t = 0

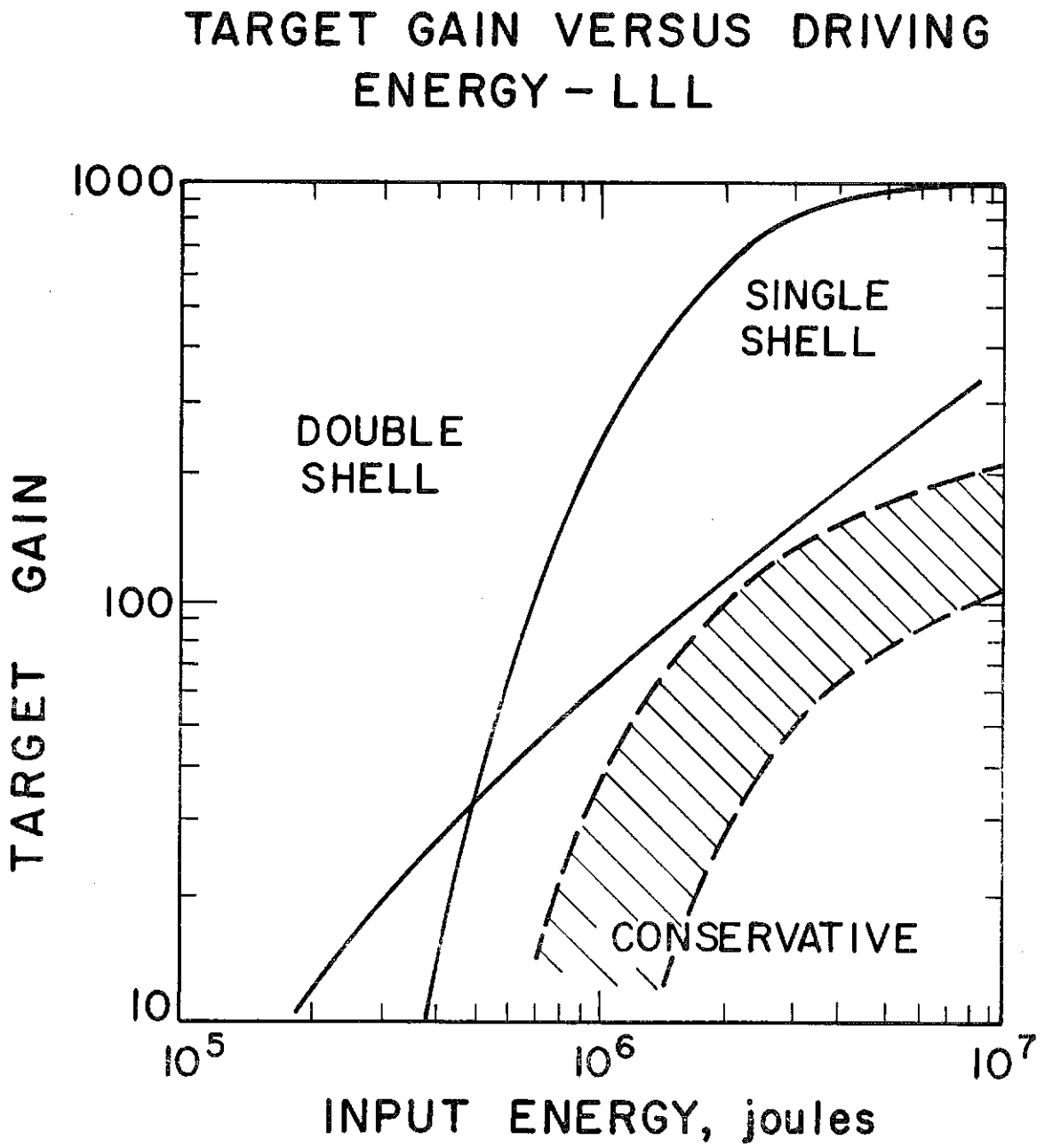
TARGET GAIN VERSUS DRIVING ENERGY - LLL
1000
100
10
TARGET GAIN
SINGLE SHELL
DOUBLE SHELL
CONSERVATIVE
10^5
10^6
10^7
INPUT ENERGY, joules

Fig. III.1-1

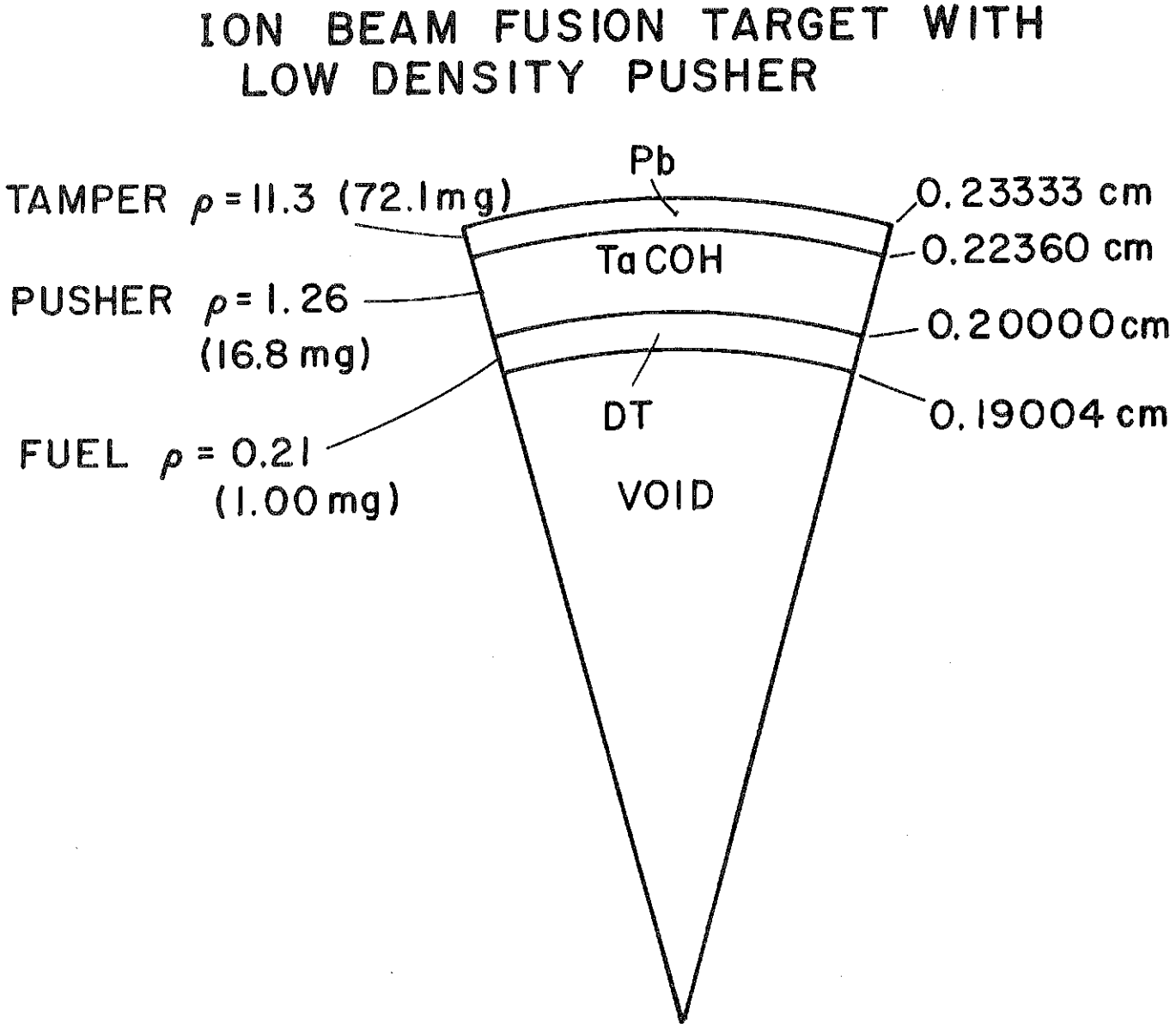
ION BEAM FUSION TARGET WITH
LOW DENSITY PUSHER
TAMPER ρ = 11.3 (72.1 mg)
PUSHER ρ = 1.26
(16.8 mg)
FUEL ρ = 0.21
(1.00 mg)
Pb
Ta COH
DT
VOID
0.23333 cm
0.22360 cm
0.20000 cm
0.19004 cm

Fig. III.1-2

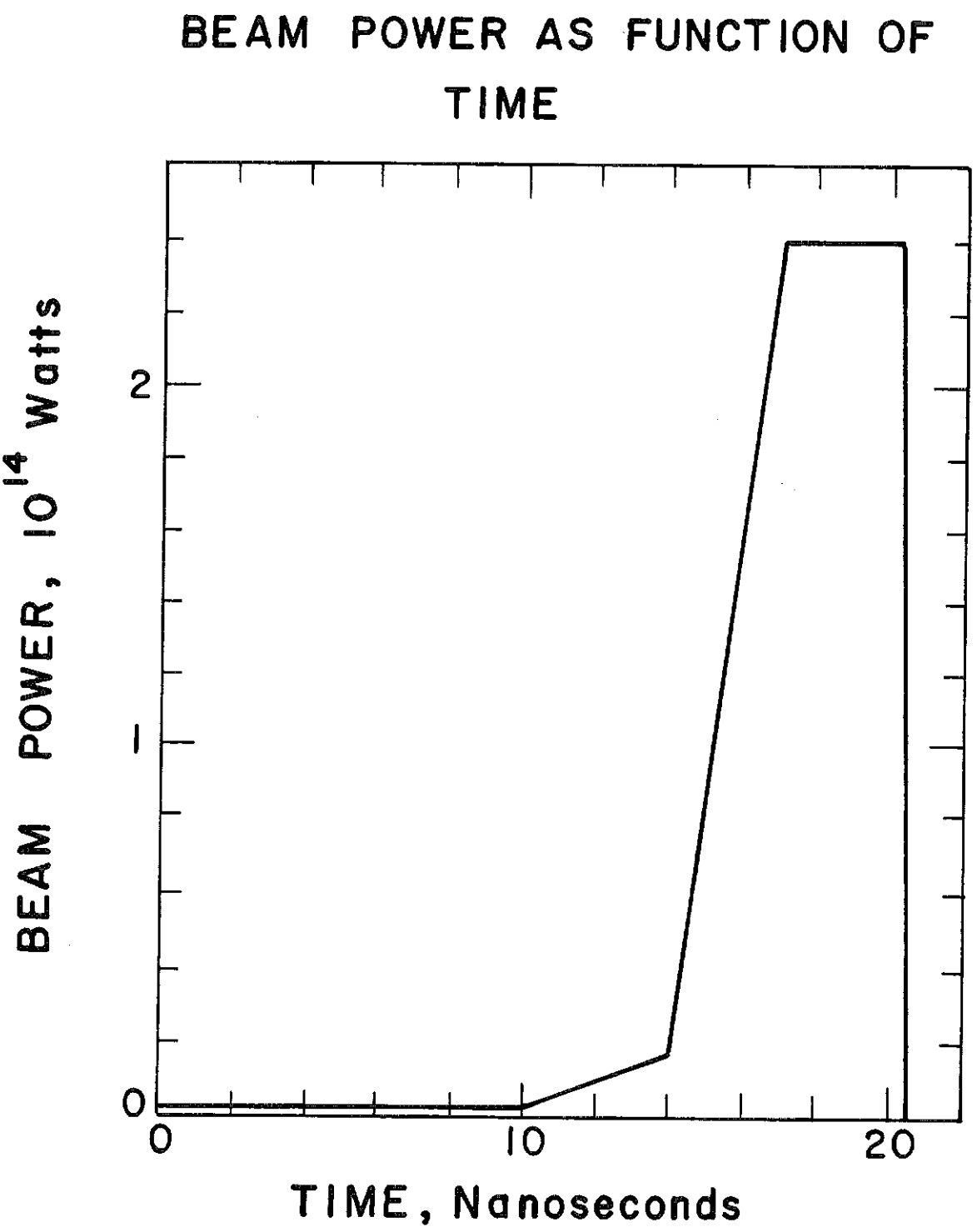
BEAM POWER AS FUNCTION OF TIME
BEAM POWER, 10^{14} Watts
2
1
0
0
10
20
TIME, Nanoseconds

Fig. III.1-3

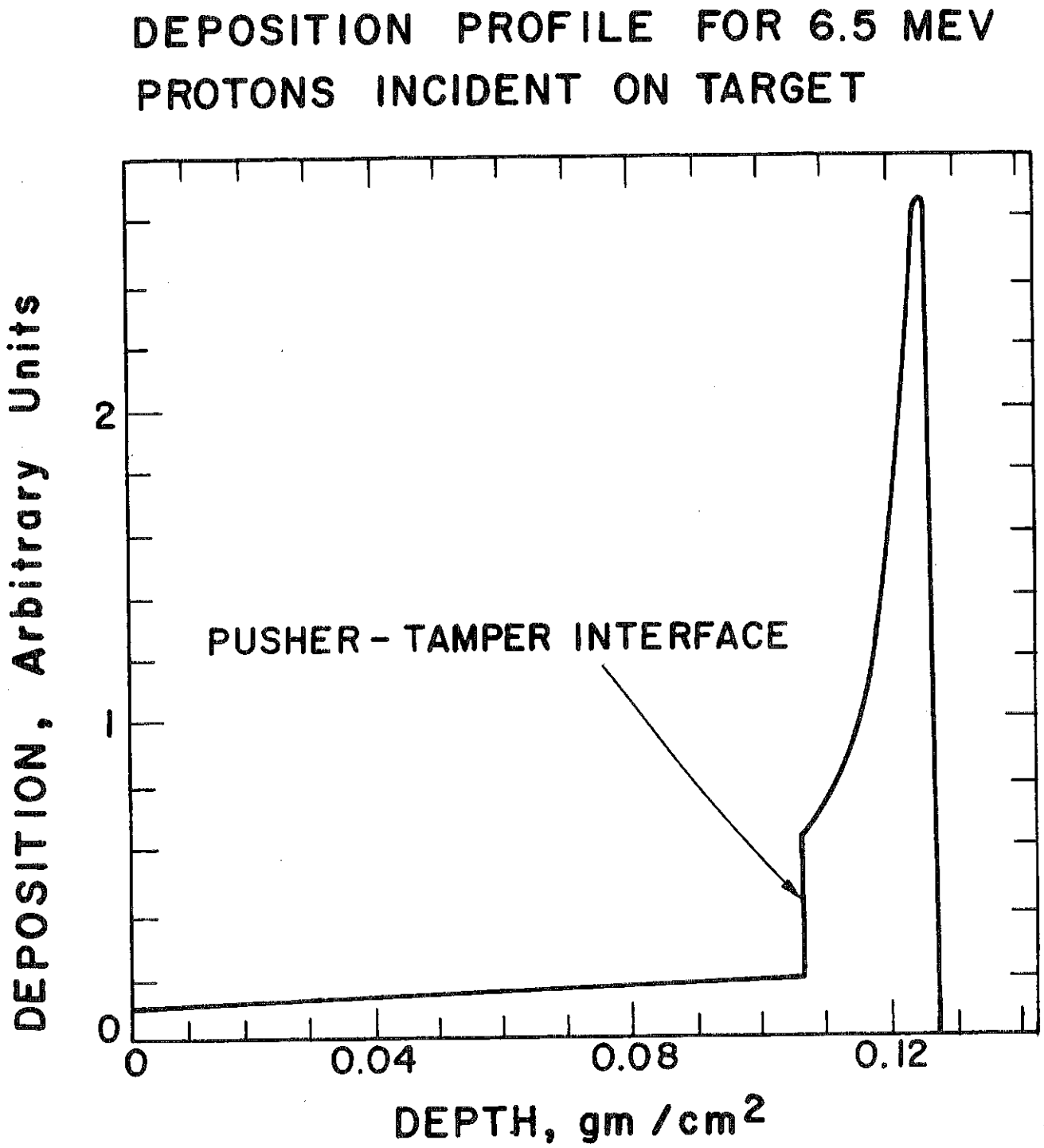
DEPOSITION PROFILE FOR 6.5 MEV PROTONS INCIDENT ON TARGET
DEPOSITION, Arbitrary Units
0
1
2
PUSHER - TAMPER INTERFACE
0
0.04
0.08
0.12
DEPTH, gm / cm2

Fig. III.1-4

This target design is modified in several ways for the HIBALL study. The TaCOH ablator-pusher is replaced with a Pb-Li mixture that gives the same mass density, 1.26 g/cm^3, as in the Bangerter design. This will not greatly perturb the implosion dynamics. It has a very beneficial effect on the target material recovery problem because now the target materials are the same as the PbLi coolant. Thus the materials separation problem is eliminated. The HIBALL target must produce a yield of 400 MJ, hence there must be more than the 1 mg of fuel used in the Bangerter design. This is straightforwardly solved by multiplying all target masses used in the Bangerter design by a factor of four. This allows us to do all of our calculations using the 1 mg target. Intrinsic quantities such as neutron, X-ray and ion spectra are assumed to be the same for the two targets while absolute quantities such as neutron, X-ray and ion yield are all scaled by a factor of four. This is admittedly a crude approximation. However, there are equally serious questions about the details of such a target design for heavy ions. For instance the heavy ions, with a flatter range-energy relation, will not deposit such a large amount of energy at the inner surface of the LiPb absorber. A total reoptimization of the design is required for applications to heavy ions. With all of these shortcomings we believe that this design will provide us with representative values for neutron, X-ray, and ion spectra and yields for heavy ion targets.

The target design used for the HIBALL analysis is shown in Fig. III.1-5 in both its initial configuration and its configuration at the time of ignition. This second configuration was not obtained from an implosion calculation but was derived from the gain reported by Bangerter and a previous knowledge of conditions required for ignition and propagating burn.[4] It is

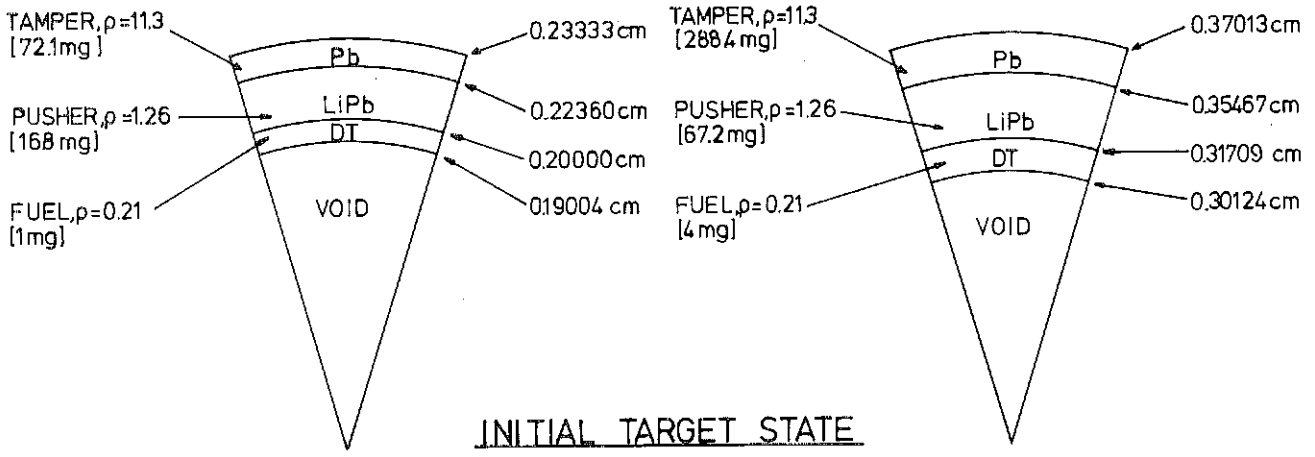

INITIAL TARGET STATE

MODIFIED BANGERTER DESIGN

HIBALL DESIGN
(SCALED UP BANGERTER DESIGN)

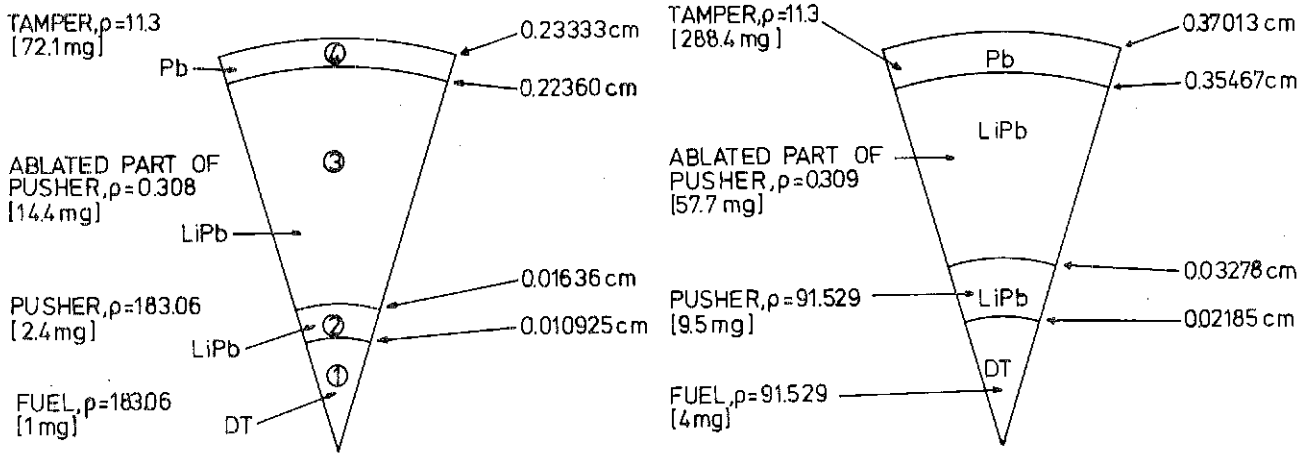

FINAL TARGET STATE

Fig. III.1-5

this target configuration that is used for calculating the neutron, X-ray, and ion spectra.

III.1.1 X-ray and Ion Spectra

The X-ray spectra for the HIBALL target were computed with the PHD-IV hydrodynamics code.[5] The features of this code are given in Table III.1-2. The code was used to simulate the ignition, burn, and disassembly phases of the target dynamics. No attempt was made to simulate the implosion. (See section III.3 for a simulation of the implosion by the MEDUSA code at KfK.) The output X-ray spectrum was computed by collapsing the 33 group Los Alamos astrophysical multifrequency opacity data into 11 coarse groups. No multifrequency opacity data is available for either $Li_{95}Pb_5$ or Pb. In our calculations the $Li_{95}Pb_5$ equation of state and opacity properties were replaced with those of neon and the lead was replaced by iron. The justification for these substitutions is: (1) neon has the same electron number density as $Li_{95}Pb_5$ and (2) iron is the highest-Z material for which we have data. Approximations such as these are quite crude. However, the results of the calculations qualitatively demonstrate some phenomena that would be similar if the correct data were used. Furthermore, the partitioning of the energy between X-rays, ions, and neutrons is very likely to be most dependent on the masses and ρR values of the various materials and not on their specific properties. This is not true for the implosion calculations where such details are extremely important to the compression process. Figures III.1-6 and III.1-7 show the time integrated X-ray spectrum at 0.0312 ns and 3.51 ns following ignition. At 0.0312 ns the thermonuclear burn phase is already completed and the spectrum is characterized by a hard component ($h\nu > 30$ KeV) and a small thermal component. The hard component results from photons from the

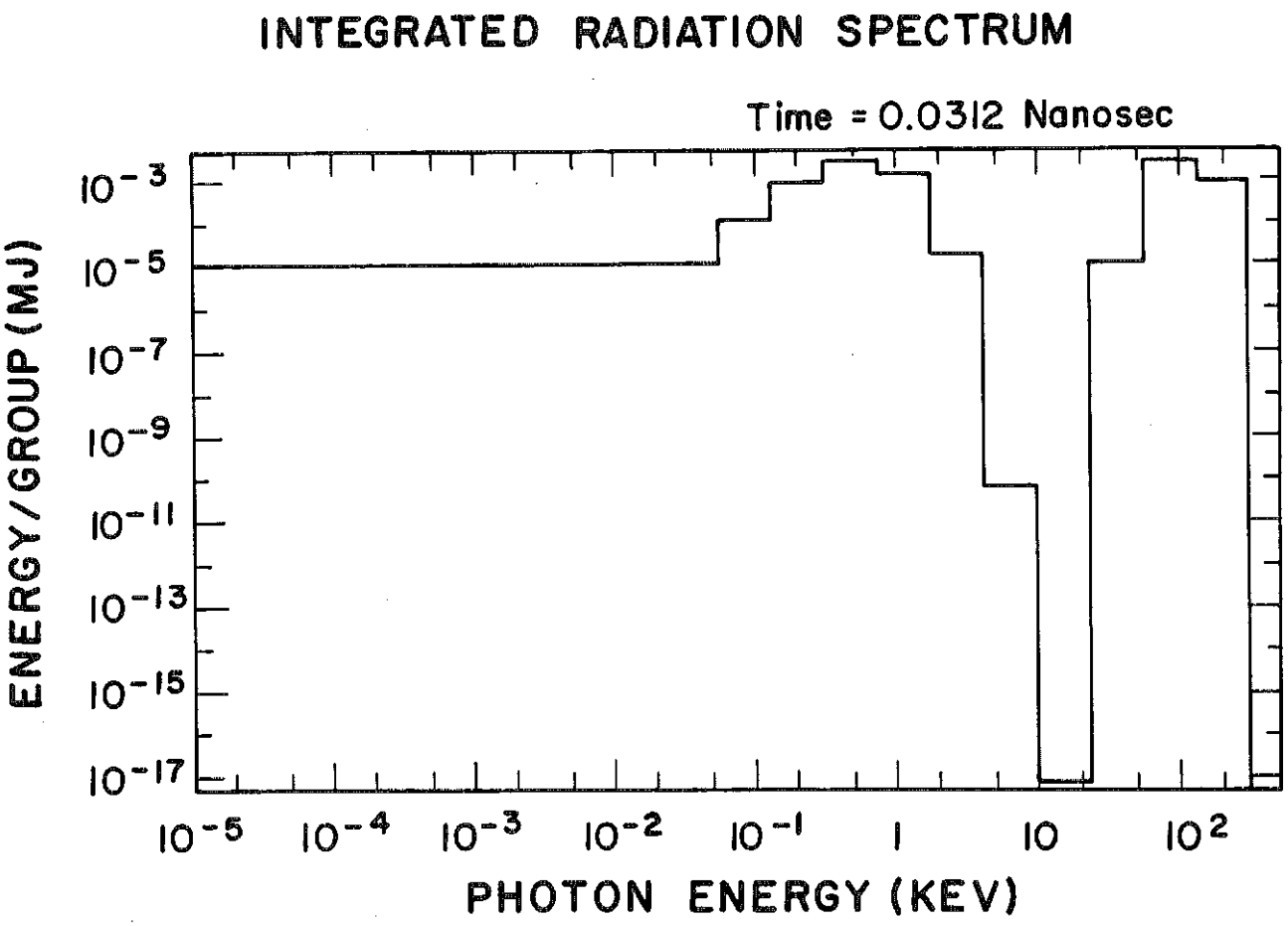
INTEGRATED RADIATION SPECTRUM
Time = 0.0312 Nanosec
ENERGY/GROUP (MJ)
10^-3
10^-5
10^-7
10^-9
10^-11
10^-13
10^-15
10^-17
10^-5
10^-4
10^-3
10^-2
10^-1
1
10
10^2
PHOTON ENERGY (KEV)

Fig. III.1-6

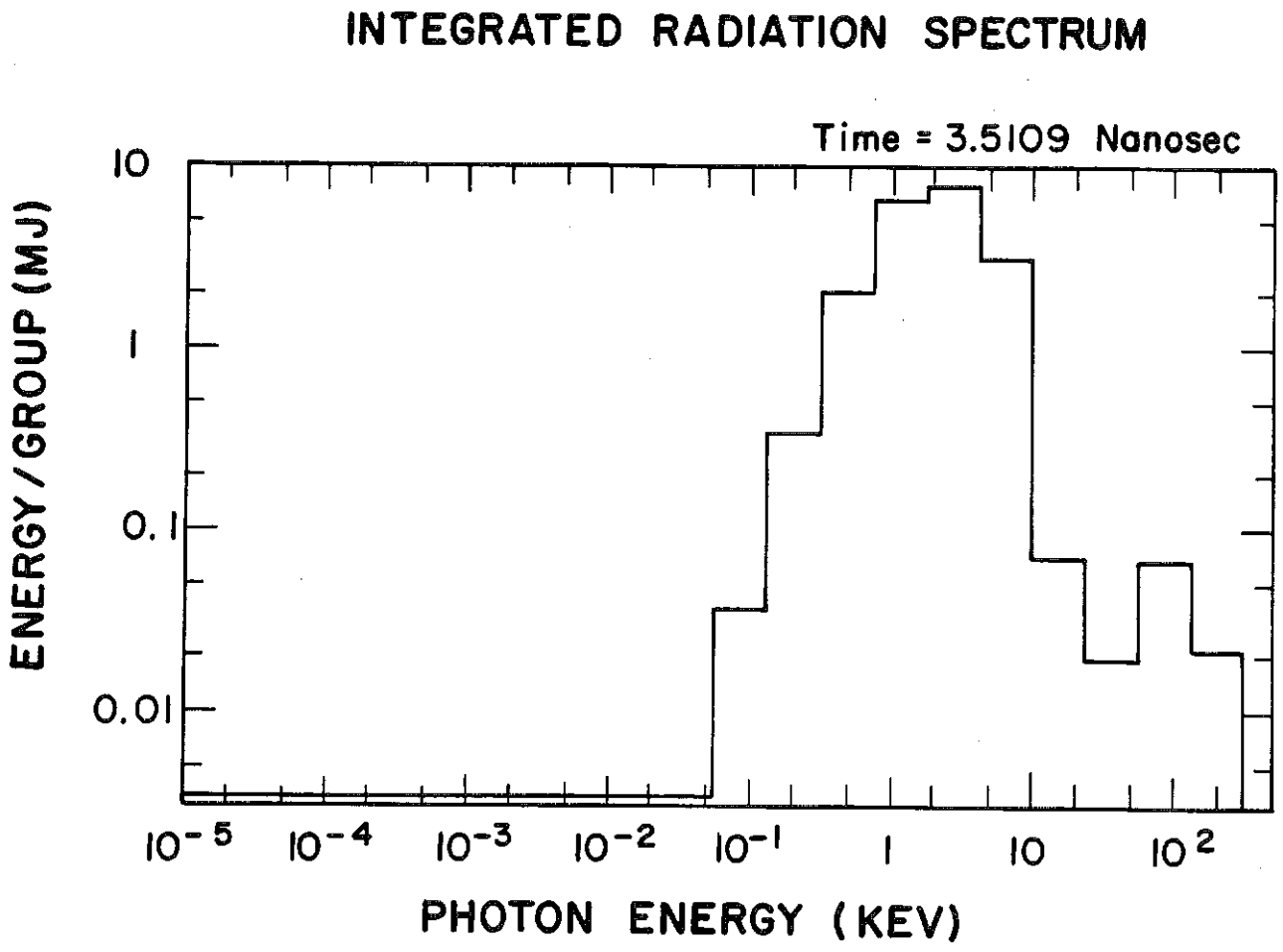
INTEGRATED RADIATION SPECTRUM
Time = 3.5109 Nanosec
ENERGY / GROUP (MJ)
10
1
0.1
0.01
10^{-5}
10^{-4}
10^{-3}
10^{-2}
10^{-1}
1
10
10^{2}
PHOTON ENERGY (KEV)

Fig. III.1-7

Table III.1-2 Major Characteristics of PHD-IV

One-dimensional (planar, cylindrical, spherical) Lagrangian coordinates.

One fluid equation-of-motion with pressure contributions from electrons, ions, radiation, and thermonuclear reaction products.

Two-temperature (electron and ion) energy flow with separate ion and flux limited electron thermal conduction, electron-ion energy exchange, PdV work, radiation emission and absorption coupling terms, and energy sources from ion beam absorption and thermonuclear energy redeposition.

Radiation transport using the multifrequency variable Eddington technique with tabulated opacities for materials of interest.

Thermonuclear reaction rate and species depletion equations for DT, DD, and DHe^3 reactions.

Transport and slowing down of charged-particle thermonuclear reaction products using the time-dependent particle tracking algorithm.

Tabulated SESAME equations-of-state for materials of interest.

Ion beam attenuation by classical slowing down theory.

Execution time of 3 ms/zone-cycle (UNIVAC 1110).

6000 card images (not including EOS data).

78,000 words of storage on UNIVAC 1110.

Written in FORTRAN IV to execute on any large computer.

burning DT fuel with energies above the K-edge of the surrounding high-Z material (8.5 keV for iron and 95 keV for lead). The "hole" in the spectrum is due to the strong absorption of photons with energies above the K-edge of the material. These absorbed X-rays and the alpha particle reaction products heat the target material to temperatures of about 1 keV. The bulk of the target then radiates at this temperature as shown in Fig. III.1-7. At 3.5 ns, the target has reached a quasi-steady state expansion phase. It is cold enough that it has essentially stopped emitting X-rays. At this point, the time

integrated spectrum shows a large thermal component with an effective blackbody shape of about 1 keV. The high frequency tail from the initial burning of the DT fuel is still apparent. The total frequency integrated emission is displayed in Fig. III.1-8 as a function of time. We see that most of the X-ray yield is released by 3.5 ns. The total X-ray yield in this calculation (4 times the computed yield) is 89.5 MJ or 22% of the overall target yield.

The ion spectrum is much more difficult to compute using our lagrangian hydrodynamics model. The ions are treated as a single fluid so no spectral information is available. To obtain the values shown in Table III.1-3 we divide the total kinetic plus thermal energy remaining in the disassembling target at 3.5 ns by the total number of atomic mass units, amu's, in the target. From this value of 0.85 keV/amu we compute the energies of individual ionic species. The ion yield is 21.0 MJ or 5.1% of the overall target yield.

Table III.1-3 Ion Spectra

Normalized Energy	0.85 keV/amu
D	1.70 keV
T	2.55 keV
He-4	3.40 keV
Li-natural	5.90 keV
Pb-natural	176.0 keV

The 14.1 MeV neutron interactions in the target account for the X-ray + ion yield fraction of 27% rather than the 20% coming from the DT fusion reaction. For the purposes of the X-ray and ion yield, as well as spectrum calculations,

X-RAY POWER DENSITY FROM 400 MJ PELLET AT 5 METERS

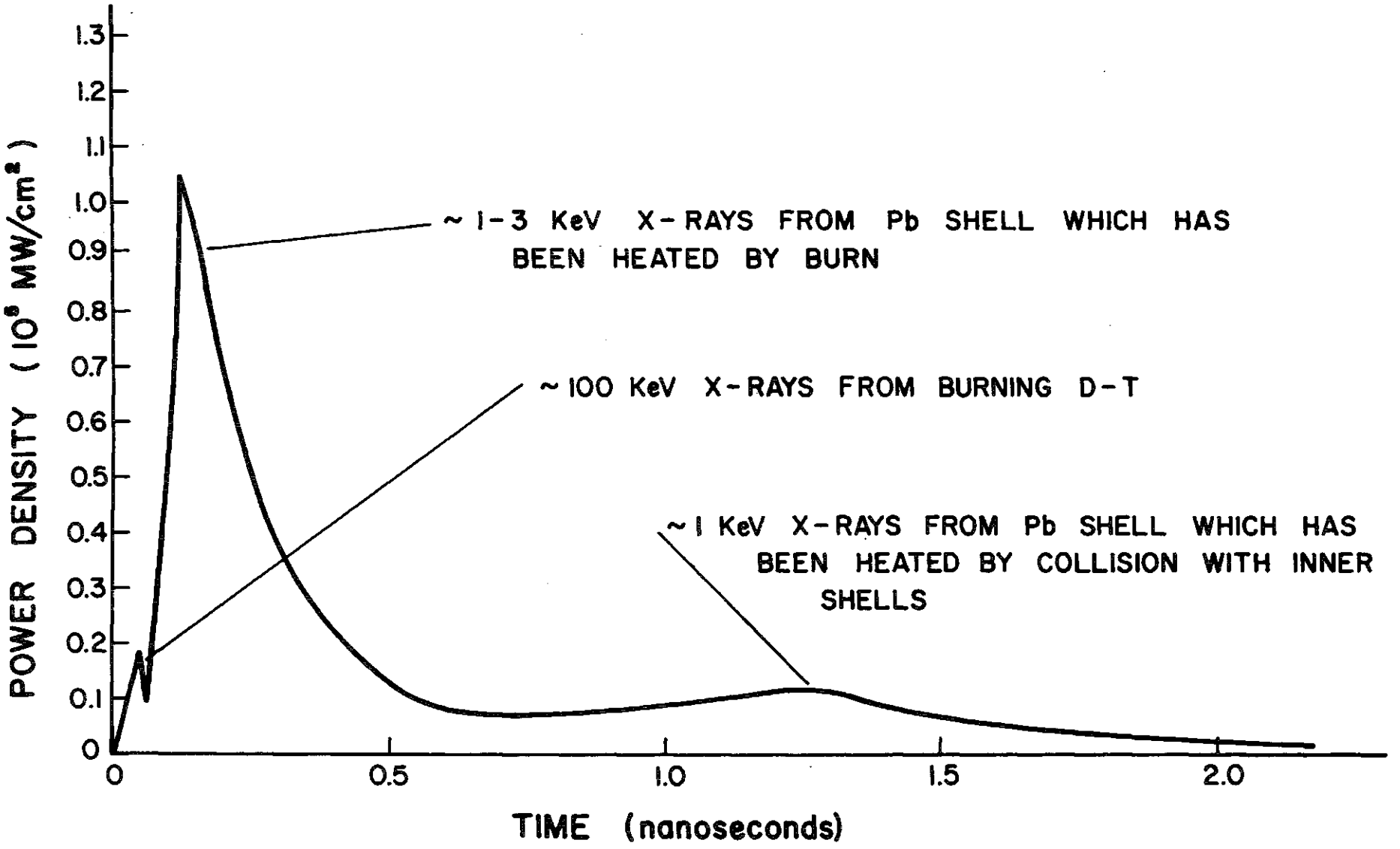

Fig. III.1-8

we did not add this deposited neutron energy. Instead, we adjusted the X-ray and ion yields so that the overall energetics is treated consistently.

III.1.2 Target Neutronics and Photonics

Neutronics and photonics calculations are required to determine important fusion reactor parameters such as tritium breeding, nuclear heating, and radiation damage. No neutron-fuel interactions occur in the low density ($\sim 10^{14}/cm^3$) plasma of a magnetic confinement fusion reactor. In an inertial confinement fusion reactor, the DT fuel is heated and compressed to extremely high densities ($\sim 10^{25}/cm^3$) before it ignites. Therefore, neutron-fuel interactions cannot be neglected. The spectrum of emerging neutrons is softened as a result of elastic and inelastic collisions with the target constituent materials. Neutron multiplication also occurs as a result of (n,2n) and (n,3n) reactions. This affects the performance of the blanket, first wall, reflector and shield. Neutron-fuel interactions produce gamma photons which contribute to nuclear heating in the blanket. A consistent neutronics and photonics analysis must, therefore, account for neutron target interactions. This is done by performing multigroup neutronics and photonics calculations within the target and coupling them to the blanket calculations.

The target used in the HIBALL fusion reactor design is shown in Fig. III.1-5. Neutronics and photonics calculations are performed within the target at ignition. The multi-group discrete ordinates code ANISN gives time integrated results. An isotropic source of 14.1 MeV neutrons is distributed uniformly in the DT fuel region. A coupled 25 neutron-21 gamma group cross section library is used throughout this work. The library consists of the RSIC DLC-41B/VITAMIN-C data library and the DLC-60/MACKLIB-IV response data library. The same calculations were performed using the ONETRAN finite

element code implemented at KfK. The results of the two calculations are compared later in this section.

Table III.1-4 lists the density data for the final target state used in this work. The target design used in the neutronics and photonics calculations utilizes 1 mg of DT fuel which produces an energy yield of 100 MJ per shot. Since a DT energy yield of 400 MJ is proposed for HIBALL, the results are scaled by a factor of 4. Assuming that the ρR values for the 100 MJ and 400 MJ targets are the same, the neutron and gamma spectra obtained for the 100 MJ yield case can be used for a yield of 400 MJ.

The calculated spectrum of neutrons escaping from the target, which represents the neutron source for the blanket calculations, is given in Fig. III.1-9. The large peak at 14.1 MeV is due to the uncollided flux of neutrons escaping the target. This amounts to 70.75% of neutrons leaking from the target. Local peaking of the flux at 2 and 4 MeV is caused by backward elastic scattering of 14.1 MeV neutrons with D and T, respectively. The lower energy range contains neutrons that have been elastically and inelastically scattered and those produced by (n,2n) and (n,3n) reactions. The average energy of emerging neutrons is 11.98 MeV. The results show that a target neutron multiplication of 1.046 is obtained. This results mainly from (n,2n) reactions in the dense DT fuel and LiPb pusher. The (n,2n) and (n,3n) reactions per fusion obtained using the ANISN and ONETRAN codes are given in Table III.1-5 for the different target regions. Very good agreement between the two codes is obtained.

The spectrum of gamma rays leaking from the target is given in Fig. III.1-10. The spectrum peaks around 0.6 MeV. The average energy of the gamma photons emerging from the target is 1.533 MeV.

Neutron interactions with Li in the target are found to produce 0.0146 tritium atoms per DT fusion reaction. Most of this tritium is produced in ^{7}Li because of the relatively hard spectrum of neutrons in the target. Tritium production in the target is very small compared to that in the blanket.

Table III.1-4 Target Data at Ignition

Region	Composition	Density [g/cm^3]	ρR [g/cm^2]	Atomic Density [atoms/b-cm]
1	D	183.06	2	22.225
	T			22.225
2	^{6}Li	183.06	1	0.4656
	^{7}Li			5.809
	Pb			0.32166
3	^{6}Li	0.308	0.0638	7.834×10^{-4}
	^{7}Li			9.774×10^{-3}
	Pb			5.412×10^{-4}
4	Pb	11.3	0.11	3.2831×10^{-2}

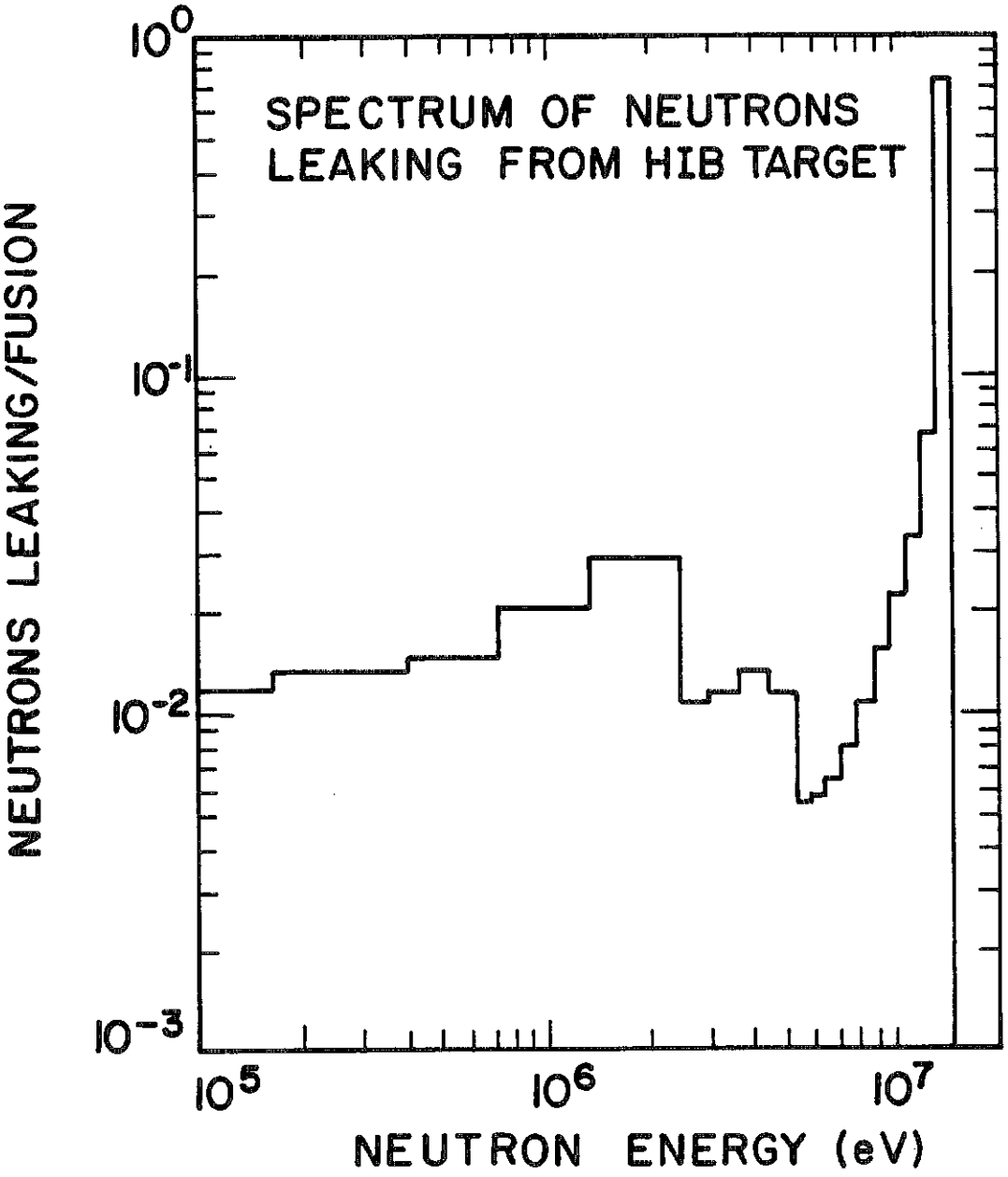

Fig. III.1-9

Neutron Spectrum (The ordinate is the integral in each energy group.)

Table III.1-5

Region	Reactions/Fusion event 1 mg Target (ANISN, S_4P_3) (n,2n)	(n,3n)	Reactions/Fusion event 1 mg Target (ONETRAN, S_8P_3) (n,2n)	(n,3n)
1	4.0432×10^{-2}	0.0	3.9704×10^{-2}	0.0
2	5.0972×10^{-3}	5.6370×10^{-5}	4.8606×10^{-3}	5.3895×10^{-5}
3	3.6479×10^{-4}	4.0026×10^{-6}	2.5559×10^{-4}	2.8105×10^{-6}
4	6.336×10^{-4}	8.5960×10^{-6}	6.1183×10^{-4}	7.9566×10^{-6}
TOTAL	4.6658×10^{-2}	6.8969×10^{-5}	4.4532×10^{-2}	6.4662×10^{-5}
Neutrons leaking/ per source neutron	1.04589		1.04482	
Gammas leaking/ per source neutron	0.01752		0.01639	

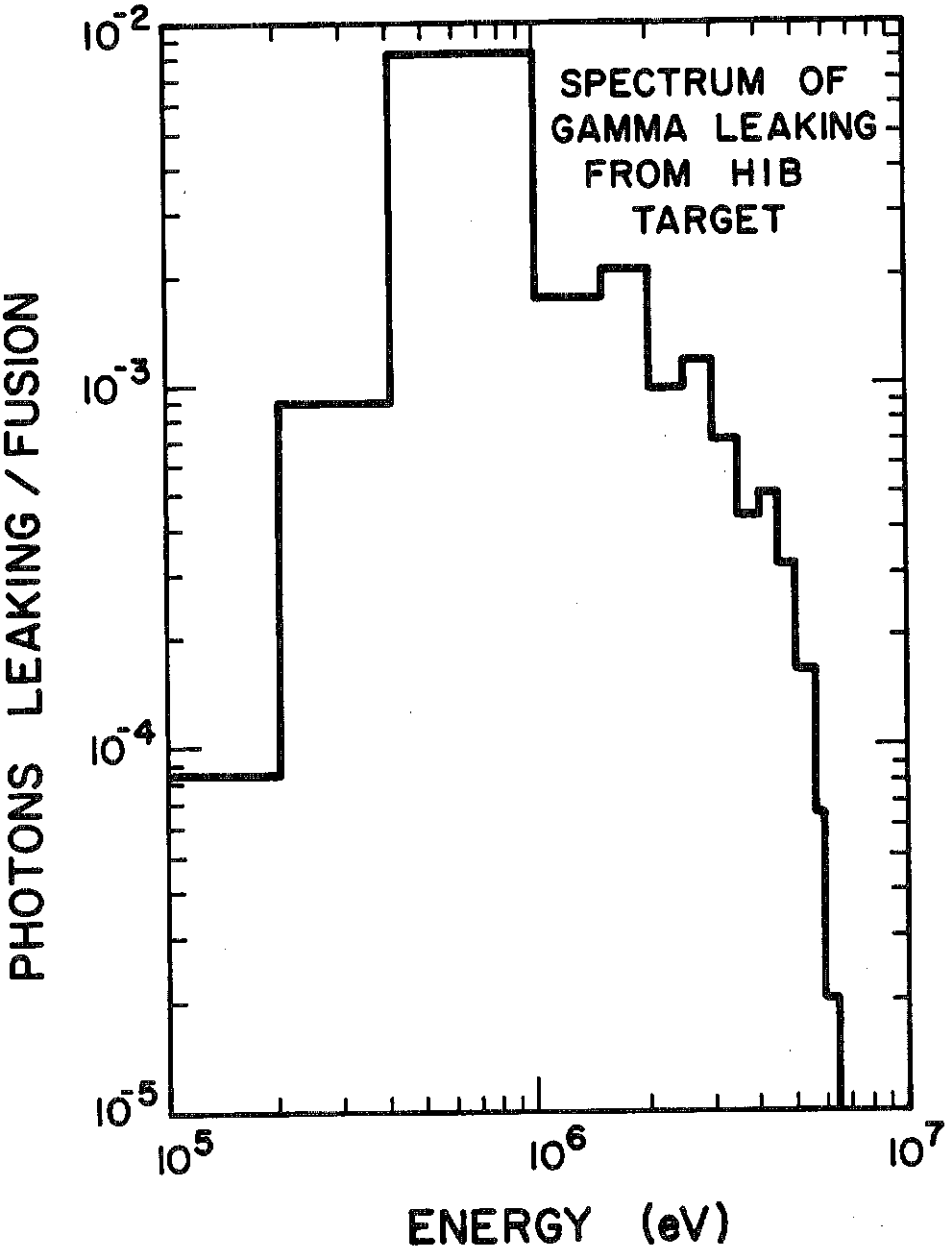
SPECTRUM OF
GAMMA LEAKING
FROM HIB
TARGET
PHOTONS LEAKING / FUSION
10^{-2}
10^{-3}
10^{-4}
10^{-5}
10^{5}
10^{6}
10^{7}
ENERGY (eV)

Fig. III.1-10

Neutron and gamma energy deposition in the target, blanket, first wall, and reflector are calculated using the neutron and gamma spectra and the appropriate kerma factors. Table III.1-6 gives neutron and gamma energy deposition in the different regions of the target. Most of this energy is deposited by neutrons in the DT fuel core. The energy deposited in the target by neutrons and gamma photons is 1.3615 MeV per fusion. When the 3.5 MeV energy carried by the alpha particle emerging from the fusion reaction is added, a total energy of 4.8615 MeV per fusion is found to be carried by X-rays and target debris following the target microexplosion. The energy carried by emerging neutrons is found to be 12.532 MeV per fusion or 71% of the total yield and the energy carried by gamma photons is found to be 0.027 MeV/fusion. The remaining energy of 0.179 MeV/fusion is lost in endoergic neutron reactions with the target materials.

III.1.3 Radioactivity in the Target

Induced radioactivity in the target can be very substantial, depending on the target materials. Radioactivity calculations were performed using the DKR code[7] developed at the University of Wisconsin. Results are displayed in Fig. III.1-11. The DKR code post processes ANISN fluxes to compute the initial activation and then follows the important decay chains to determine how the radioactivity changes with time.

The very high initial activity of 10^5 curies is due to $^{6}Li(n,p)^{6}He$ and $^{7}Li(n,\gamma)^{8}Li$ reactions. These products β-decay with half-lives of 800 ms. The very long term activity is due to ^{205}Pb with a 3×10^7 year half-life. The activity between these two extremes is mostly due to ^{205}Hg and ^{203}Pb with half-lives of 5.5 minutes and 52 hours.

This target radioactivity is a negligible part of the total coolant activity. The target materials are the same as the $Pb_{17}Li_{83}$ coolant that

Table III.1-6 Neutron and Gamma Energy Deposition in the Target

Region	Element	Neutron Heating [eV/fusion]	Gamma Heating [eV/fusion]
1	DT	1.168×10^{6}	0.0
2	^{6}Li	1.70129×10^{4}	2.07881×10
	^{7}Li	1.62950×10^{5}	2.5936×10^{2}
	Pb	6.1056×10^{2}	9.06526×10^{2}
	Region Total	1.805734×10^{5}	1.18667×10^{3}
3	^{6}Li	1.20695×10^{3}	1.26611×10^{0}
	^{7}Li	1.16287×10^{4}	1.57965×10
	Pb	4.35637×10	5.4128×10
	Region Total	1.2879214×10^{4}	71.19061
4	Pb	9.38872×10	1.53527×10^{2}
Total		1.3615×10^{6}	1.14114×10^{3}

protects the first wall, consequently no special separation and handling of the target materials is required in HIBALL.

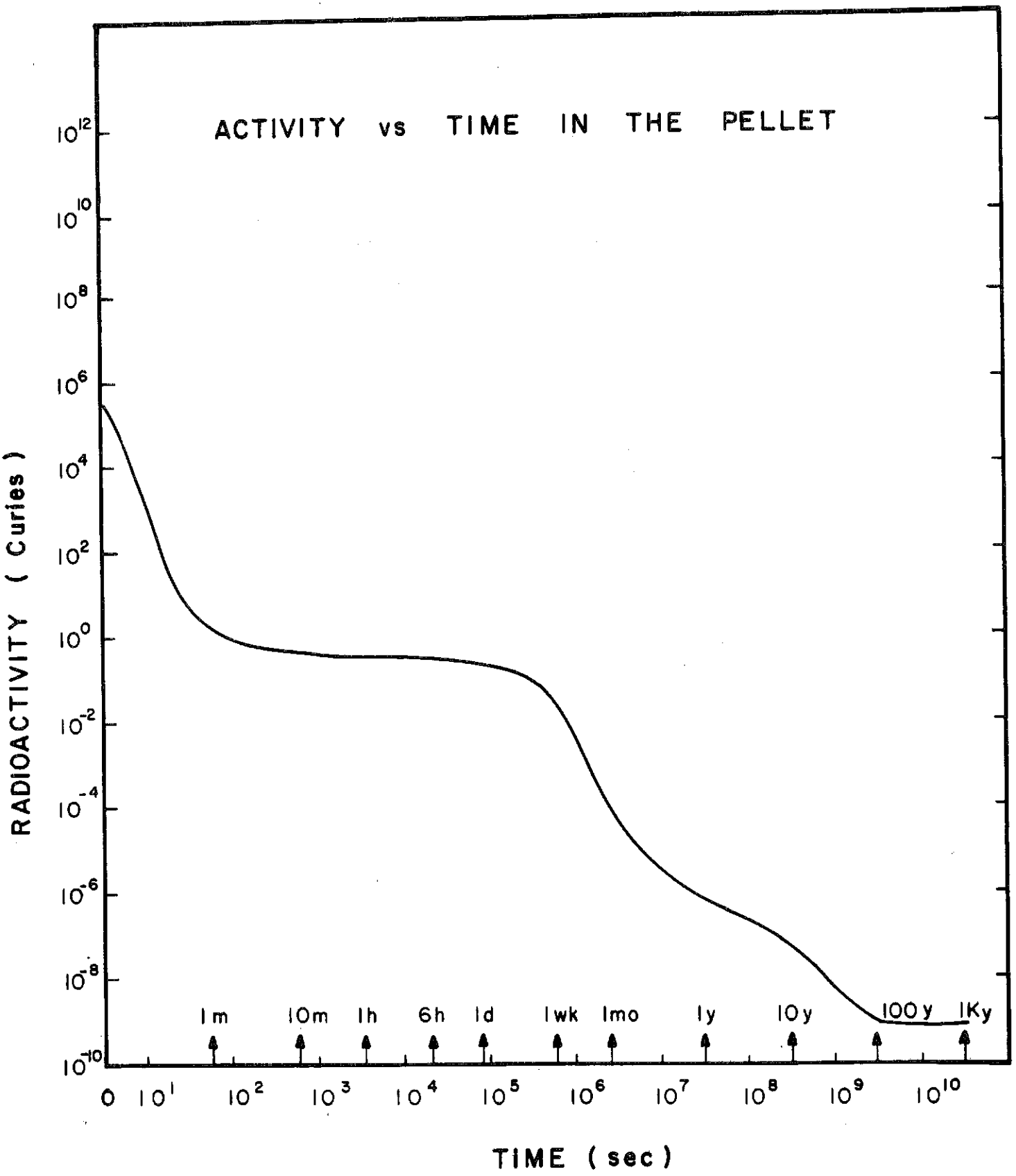
ACTIVITY vs TIME IN THE PELLET
RADIOACTIVITY (Curies)
10^{12}
10^{10}
10^{8}
10^{6}
10^{4}
10^{2}
10^{0}
10^{-2}
10^{-4}
10^{-6}
10^{-8}
10^{-10}
1m
10m
1h
6h
1d
1wk
1mo
1y
10y
100y
1Ky
0
10^{1}
10^{2}
10^{3}
10^{4}
10^{5}
10^{6}
10^{7}
10^{8}
10^{9}
10^{10}
TIME (sec)

Fig. III.1-11

References for Section III.1

1. S.E. Bodner, "Critical Elements of High Gain Laser Fusion," NRL Memo Report 4453, Naval Research Laboratory, Washington, D.C., January 1981.

2. R.O. Bangerter, Laser Program Annual Report - 1976, Lawrence Livermore Laboratory Report UCRL-50021-76, June 1977, p. 4-44.

3. R.O. Bangerter and D. Meeker, "Ion Beam Inertial Fusion Target Designs," Lawrence Livermore Laboratory Report UCRL-78474 (1976).

4. G.A. Moses et al., "The SOLASE Conceptual LaserFusion Reactor Study," Proc. of the 3rd Top. Mtg. on the Tech. of Cont. Nuclear Fusion, Vol. 1, Santa Fe, NM, May 1978, p. 448.

5. G.A. Moses and G.R. Magelssen, "PHD-IV, A Plasma Hydrodynamics-Thermonuclear Burn-Radiative Transfer Computer Code," University of Wisconsin Fusion Engineering Program Report UWFDM-194 (unpublished).

6. W. Engles, "A Users Manual for ANISN," RSIC Code Package CCC-254, Radiation Shielding and Information Center, Oak Ridge National Laboratory, Oak Ridge, TN.

7. T.Y. Sung and W.F. Vogelsang, "DKR Radioactivity Calculation Code for Fusion Reactors," University of Wisconsin Fusion Engineering Program Report UWFDM-170 (Sept. 1976).

III. 2 Target Design at MPQ

The work on target design presented in this chapter has been performed at the Max-Planck-Institut for Quantum Optics (MPQ) in Garching / FRG. It includes a parameter study for pellet gain, an investigation of heavy ion stopping in hot dense plasma and a detailed discussion of a typical heavy ion induced pellet implosion selecting a single-shell design. Strong emphasis has been put on the underlying physics, but all results are directly related to HIBALL and are used to check the "frozen" parameter list for consistency with actual HIF target behaviour. This work represents a first step and leaves important aspects untouched. The effect of irradiation asymmetry on target performance, consideration of double-shell and more complicated designs and optimization between beam and target parameters are some of these aspects. To a certain extent, they will be discussed in chapter III. 4 and in the final HIBALL report.

The parameter study is based on a modified version of the Kidder-Bodner model for pellet gain. The modification consists in a more realistic assumption about the fuel configuration at ignition than used by Kidder and Bodner. The model provides a physical interpretation of the Livermore "conservative" gain curves (see Fig. III.1-1) and reproduces the HIBALL working point (E_{Beam} = 4.8 MJ, Gain 83) with reasonable choices for hydrodynamic efficiency, cold fuel isentrope and fuel pressure at ignition. The theory of heavy ion stopping in hot dense plasma is outlined and used to calculate ranges and deposition profiles for 10 GeV Bi-ions in Pb, Li, and PbLi-alloy relevant for the HIBALL target. Finally, a 1D-implosion of the chosen

target configuration yields a detailed picture of the pellet dynamics. Special attention is given to the shock sequence leading to the ignition configuration and how it is related to the pulse shape. Also the growth of Rayleigh-Taylor instability at the absorber-pusher interface is estimated.

III.2.1 Modified Kidder-Bodner model for pellet gain

Pellet gain as a function of beam energy is one of the crucial relations for inertial confinement fusion. Although the dynamics of pellet implosion are very complex, the gain curve can be expressed in terms of a few physical parameters. This has recently been pointed out by S. Bodner.[1] The underlying model had been formulated before by R. Kidder [2]. The fuel configuration at ignition is assumed to consist of a central hot region (spark) surrounded by highly compressed fuel at low entropy as shown schematically in Fig. III.2-1. Ignition will occur in the centre, and burn then propagates into the cold fuel. Propagating burn is essential to achieve high gain. The question of how to achieve such an ignition configuration dynamically is addressed in section III.2.3.

As an important modification of the Kidder-Bodner model, we assume constant pressure p over the total (hot and cold) fuel region. Kidder and Bodner had assumed constant density implying a sharp pressure jump from the hot to the cold fuel region. However, typical implosion runs (see e.g. ref. 3 and section III.2.3) show that the ignition point with maximum fuel ρR and maximum central temperature T_s is generally reached only after the shock, emerging from the centre after shell collapse,

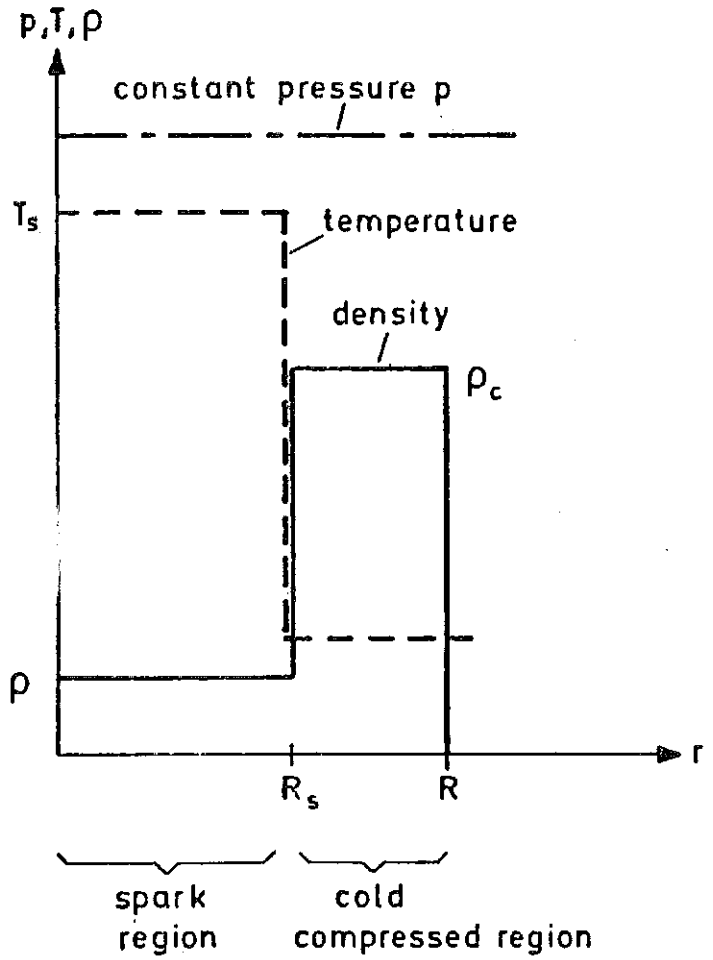

Fig. III.2-1: Profiles of pressure p, temperature T, and density for the schematic ignition configuration

has passed through fuel and pusher. At this time, almost all the inward going kinetic energy has been converted to internal energy, and the pressure is nearly constant over the fuel. This is the realistic ignition situation. Replacing constant density by constant pressure leads to less optimistic gain curves than those discussed by Bodner. This is because now more energy goes into the compressed fuel part.

The model is defined by the following equations. The spark region is described as an ideal gas. Taking as ignition conditions

$$kT_s \geq 5\ keV \tag{1a}$$

$$H_s = \varrho_s R_s \geq 0.4\ g/cm^2 \tag{1b}$$

one obtains for the density ϱ_s, the radius R_s, the mass M_s, and the internal energy E_s of the spark

$$\varrho_s = \frac{\mu_{DT}}{2kT_s} \cdot p \tag{2a}$$

$$R_s = H_s / \varrho_s \tag{2b}$$

$$M_s = \frac{4\pi}{3} R_s^3 \varrho_s \tag{2c}$$

$$E_s = 2 \cdot \frac{3}{2} kT_s \cdot \frac{M_s}{\mu_{DT}} \tag{2d}$$

Here, the atomic weight of DT $\mu_{DT} \cong 4 \times 10^{-24}$ g, and p is the overall pressure.

The highly compressed region is described as a degenerate electron gas with the pressure

$$p = \alpha \cdot \frac{2}{5} n_e \varepsilon_F = 2.34 \cdot 10^{12} \cdot \alpha \varrho_c^{5/3} \quad (\text{cgs units}) \qquad (3a)$$

and the internal energy

$$E_c = \alpha \cdot \frac{3}{5} \varepsilon_F \cdot \frac{M}{\mu_{DT}} = 1.55 \cdot 10^{13} \cdot \alpha M_c \varrho_c^{2/3} \quad (\text{cgs units}) \qquad (3b)$$

The isentrope parameter α denotes the deviation from the completely degenerate expressions and labels different isentropes. Obviously, one has $\alpha \geq 1$. The Fermi energy is given by $\varepsilon_F = \hbar^2 (3\pi^2 n_e)^{2/3} / (2 m_e)$ with the elctron mass m_e and the electron density $n_e = \varrho_c / \mu_{DT}$. In the model, the density ϱ_c of the highly compressed region is obtained from eq. (3a) and its mass M_c from eq. (3b). The total fuel energy $(E_s + E_c)$ is related to the input beam energy

$$E_{Beam} = (E_s + E_c)/\eta \qquad (4)$$

via the hydrodynamic efficiency η. The total fusion energy

$$E_{Fusion} = q_{DT} \cdot M \cdot \phi \qquad (5)$$

is given by the specific DT fusion energy $q_{DT} = 3.34 \times 10^{11}$ J/g, the total fuel mass $M = M_s + M_c$, and the burn rate

$$\phi = H_F/(H_o + H_F) \qquad (6)$$

with the burn parameter $H_o \cong 7$ g/cm^2, the total fuel (ϱR)

$$H_F = \varrho_s R_s + \varrho_c (R - R_s) \qquad (7)$$

and the fuel radius $R^3 = 3M/(4\pi\varrho_c) + (1 - \varrho_s/\varrho_c) R_s^3$. The value for H_o corresponds to a freely expanding DT sphere. In actual pellet implosions, pusher material tamps this expansion and increases the burn rate. On the other hand, asymmetry effects will degrade the burn so that the chosen H_o may effectively describe a realistic situation. Finally, the pellet gain is given by

$$G = E_{Fusion} / E_{Beam}$$

Results for $G(E_{Beam})$ are shown in Figs III.2-2 to III.2-4. If the input energy is not sufficient for ignition

$$E_{Beam} < E_s^{ign}/\eta \qquad (8)$$

the model assumptions are $E_c = 0$, $M_c = 0$, $E_s = \eta E_{in}$, $M_s = E_s \mu_{DT} / 3kT_s$, and $R_s = (3M_s/4\pi\varrho_s)^{1/3} < H_s/\varrho_s$. The break in the gain curves marks the point of ignition and the onset of propagating burn. The hydrodynamic efficiency η, the isentrope parameter α, and the central pressure p are chosen as free model parameters. A standard set obtained for these parameters from explicit code calculations in section 3 is

$$\eta = 0.05, \quad \alpha = 2, \quad p = 0.2\ Tb \qquad (9)$$

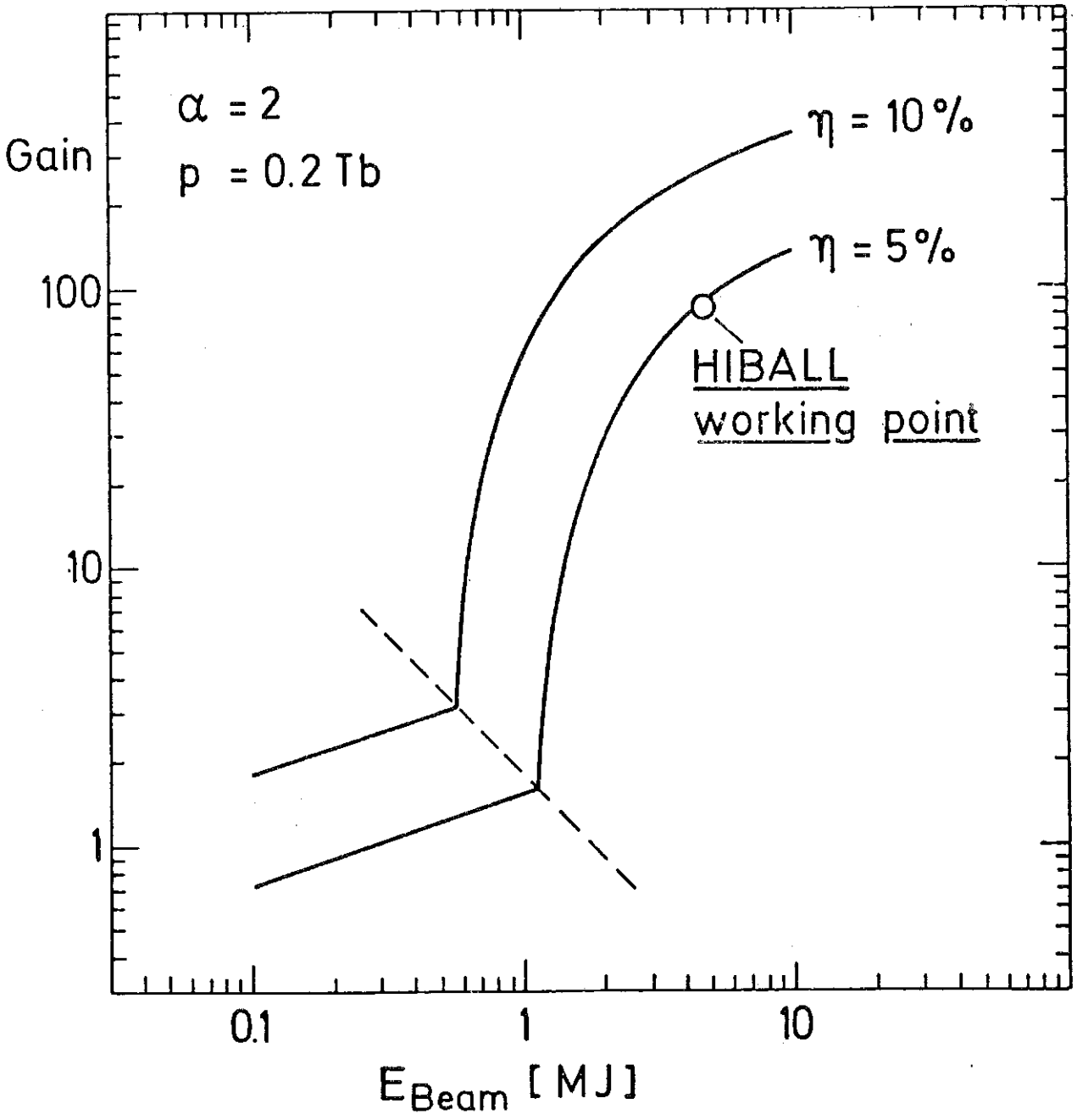

Fig. III.2-2: Gain curves for different hydrodynamic efficiencies, α and p are kept fixed.

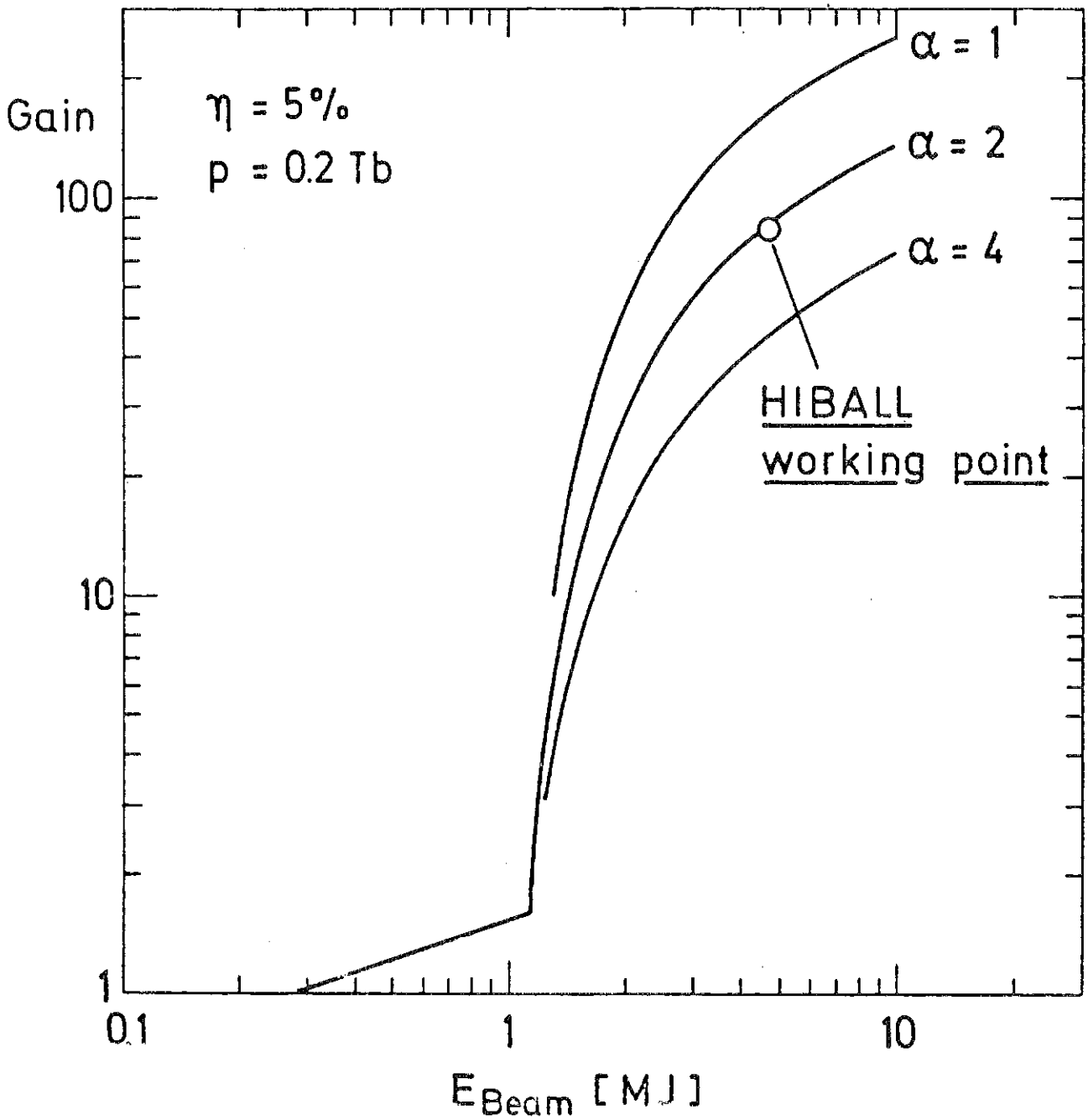

Fig. III.2-3: Gain curves for different cold fuel isentropes, η and p are kept fixed.

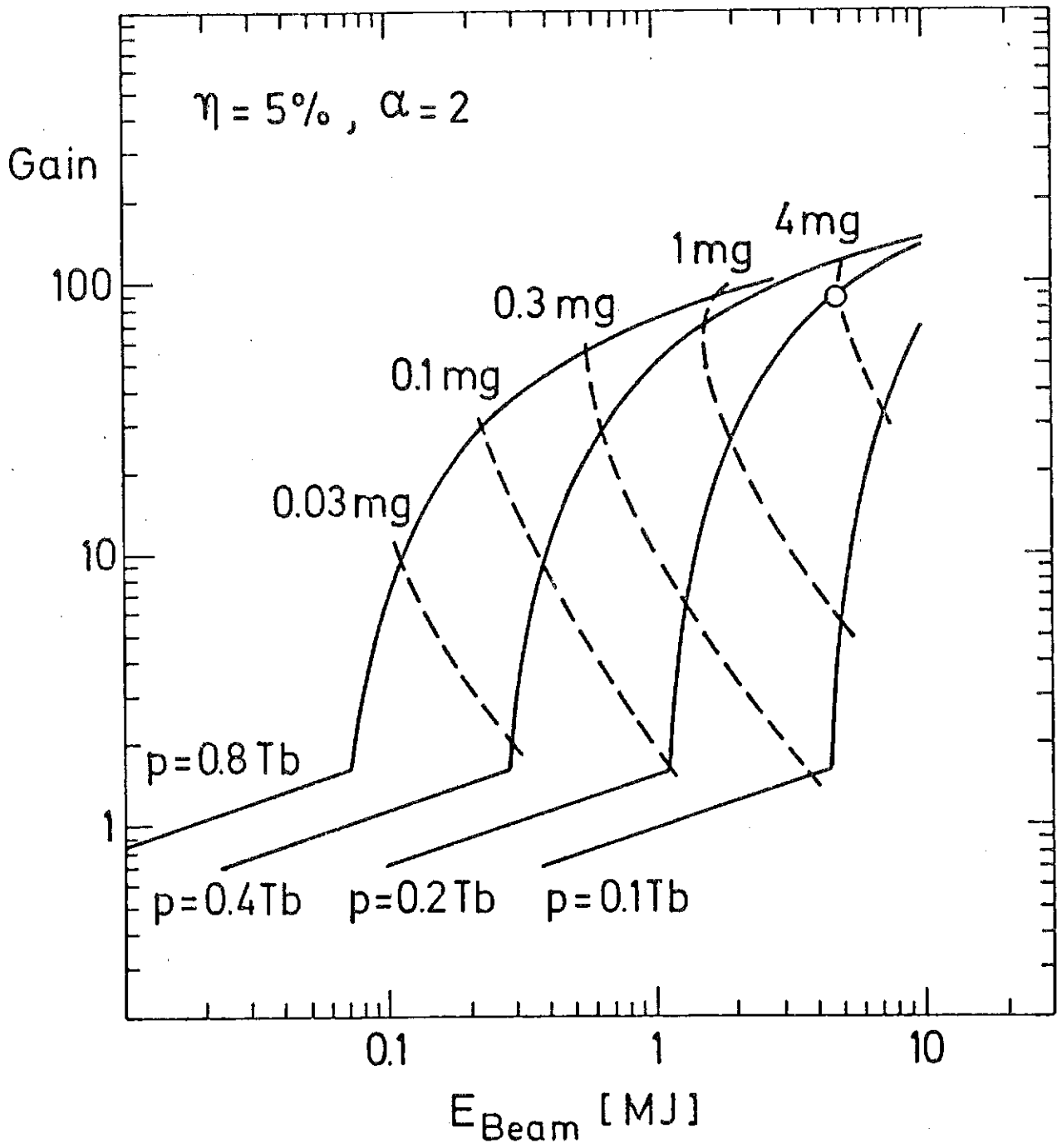

Fig. III.2-4: Gain curves for different central pressures, η and α are kept fixed. The broken lines are curves of equal fuel mass.

The gain curve for these standard parameters as well as neighbouring curves when varying η, α, and p are shown in Figs. III.2-2, -3, and -4, respectively. The standard curve has its ignition point at about 1 MJ. Changing the hydrodynamic efficiency from 5 % to 10 % in Fig. III.2 2, a gain band is obtained which almost reproduces the 'conservative' gain region predicted by the Livermore group.[4] Targets for heavy ion beam fusion have relatively low η and are located at the lower edge of this band. The gain is also lowered by going to higher cold fuel isentropes as seen from Fig. III.2-3; in the region of propagating burn one has $G \sim 1/\alpha$. High central pressures strongly decrease the ignition energy $E^{ign}_{Beam} \sim \rho^{-2}$, but are less important in the high gain regime. This is seen in Fig. III.2-4, where also lines of equal fuel mass are given. At high pressures, the ignition conditions can be achieved with exceedingly small masses. Such small targets may be an option for laser fusion, where sharp focussing and high beam power are possible. For heavy ion beam fusion, however, both these points are difficult to achieve. Therefore one is bound to take relatively large targets.

The working point of the HIBALL reactor design has been chosen as

$$G = 83 \qquad (10)$$
$$E_{Beam} = 4.8 \text{ MJ}$$

which lies on the reference gain curve with the parameters (9). Within the model, one then finds the other pellet parameters as given in Table III.2-1. The spark contains 2.5 % of the fuel mass, but 25 % of the fuel energy. Its density is less than one tenth of the compressed fuel density.

Table III.2.-1 HIBALL Pellet Parameters

total fuel	mass	M	= 4 mg
	confinement	(ϱR)	= 3.4 g/cm^2
	burn rate	ϕ	= 30 %
	radius	R	= 124 µm
	pressure	p	= 0.2 Tb
	energy	E	= 240 kJ
spark	temperature	T_s	= 5 keV
	mass	M_s	= 0.1 mg
	confinement	$\varrho_s R_s$	= 0.4 g/cm^2
	radius	R_s	= 77 µm
	density	ϱ_s	= 52 g/cm^3
	energy	E_s	= 57 kJ
compressed fuel	density	ϱ_c	= 630 g/ cm^3
	compressed ratio	ϱ_c/ϱ_o	= 3000
	isentrope	α	= 2
	energy	E_c	= 183 kJ

In the next section, the stopping of heavy ions in hot dense matter is discussed, and stopping powers of Bi-ions are calculated for the absorber materials of the pellet described in section III.2.3. The dynamic design parameters as pulse shape, maximum beam power, absorber pressure, implosion velocity etc. which are needed to achieve the ignition configuration are then discussed.

III.2.2 Heavy ion stopping powers in hot dense matter

III.2.2.1 General considerations

One of the advantages to use heavy ion beams for pellet fusion consists in the high stopping powers. The 10 GeV Bi-ions considered for HIBALL, e.g., are stopped in less than 0.5 mm of a Pb surface layer. So far, however, there exist no precise measurements for ion energies and target regimes of interest for pellet fusion. Stopping data in some cold target materials and for ion energies up to 5 MeV/nucleon have been measured recently at GSI.[5,6] In some cases, these data differ considerably from tables of Northcliffe and Schilling[7]. Tables extrapolated from the new data and covering the range of ion energies 2.5 - 100 MeV/nucleon and various projectile/target combinations have been published by Hubert et al.[8] No experimental information is available for stopping powers in hot dense matter. For pellet applications, one has therefore to rely on theoretical extrapolations.

Fortunately, there are good reasons to believe that classical stopping theory is applicable. As pointed out by Bangerter[9], the typical heavy ion beam for fusion (HIBALL values: 10 GeV Bi-ions, ion velocity $v_B/c \cong 0.3$, particle current at target $\cong$ 25 kA/cm^2) has an ion density of 10^{14} - 10^{15}/cm^3 as compared to a target electron density of $\cong 10^{23}$/cm^3. In this sense, it has to be considered as a dilute beam. The Debye screening length λ_D is 2 - 3 orders of magnitude smaller than the average ion seperation distance. One may therefore hope that anomalous collective effects can be ignored.

The dominant stopping mechanisms are then energy loss due to binary collisions with electrons at distances $r < \lambda_D$ and due to plasmon excitations at distances $r > \lambda_D$. For stopping in partially ionized plasma, it has been claimed that bound electrons at $r > \lambda_D$ do not contribute to the stopping power because of Debye screening[12, 13]. This is incorrect. It would have the consequence that stopping powers first decrease when a target is heated and increase only later at higher temperatures (> 50 eV) when the stopping contribution from the free electrons themselves becomes larger than their assumed screening effect. However, a careful analysis of the energy flow at distances $r > \lambda_D$ (see e.g. Jackson's book[10]) shows that bound electrons in this region contribute to the energy loss just as the free electrons do. Therefore, as long as the ion velocity is large compared to the thermal velocity ($v_{el}^{th}/c \cong 0.003$ for T = 200 eV), the stopping power will monotonically increase with temperature. This is because the number of free electrons increases and energy is more easily transferred to free electrons than to bound ones. As an important result for ion pellet design it follows that ion ranges in cold material represent upper bounds and decrease when the target is heated.

III.2.2.2 The theoretical model for ion stopping

In this subsection, the basic equations for ion stopping in hot dense matter are given. The theoretical frame is kept as simple as possible. Standard stopping theory[10] is generalized and applied to partially ionized dense plasma. The topic has been discussed recently in detail by Mehlhorn[11] and others [12, 13]. The present work basically follows Mehlhorn's description except for a few points explained below.

The electronic stopping power for non-relativistic beams has the general form

$$S = - \frac{4\pi e^4 Z_B^{eff\,2} n_e}{m_e v_B^2} \ln\left(\frac{b_{max}}{b_{min}}\right) \qquad (11)$$

where e and m_e are charge and mass of the electron, Z_B^{eff} is the effective charge of the beam ion and v_B its velocity, $n_e = (\varrho_T Z_T)/(A_T m_p)$ is the electron density with the mass density ϱ_T, the charge number Z_T and the mass number A_T of the target atoms, and m_p is the proton mass. The minimum and maximum impact parameters are given by

$$b_{min} = Max\left\{ \frac{Z_B^{eff} e^2}{m_e v_B^2} \,,\, \frac{\hbar}{m_e v_B} \right\}$$

$$b_{max} = \begin{cases} v_B/\bar{\omega} & \text{for bound electrons} \\ v_B/\omega_p & \text{for free electrons} \end{cases}$$

For the average ionization potential, we have used the expression

$$\hbar\bar{\omega} = 9\,eV \cdot Z_T \cdot (1 + 1.8/Z_T^{1/2}) \cdot \exp\{2.7 \cdot (Z_T^{ion}/Z_T)^2\}$$

which represents a fit to results of ref. 11. The plasma frequency of the free electrons $\omega_p = (4\pi e^2 n_e Z_T^{ion}/m_e Z_T)^{1/2}$, Z_T^{ion} is the average ionization state of target atoms, and $\hbar$ Planck's constant. In the case of 10 GeV Bi-ions, the minimum impact parameter b_{min} is found to be equal to the Coulomb distance ($Z^{eff} e^2/m_e v^2$) over the whole stopping range implying that Bohr's classical stopping formula is valid. For most heavy ion applications, it is incorrect to use the quantum value $b_{min} = \hbar/(m_e v_B)$ which leads to Bethe's stopping formula. This point has been overlooked in a number of papers including Mehlhorn's[11]. Our choice for b_{max} takes into account binary collisions as well as plasmon excitations as discussed in the preceding section.

An important quantity is the effective charge Z_B^{eff} of the beam ion inside the stopping medium, since the stopping powers depend on $Z_B^{eff\,2}$. It is difficult to measure Z_B^{eff} directly, and it has therefore in general been determined indirectly from measured stopping powers on the basis of eq.(11). It is found that Z_B^{eff} is approximately a function of the ion velocity alone and independent of target properties. A good parametrization of existing data has been given by Nikolaev and Dmitriev[14] in the form

$$Z_B^{eff} = Z_B \cdot \left[1 + \left(Z_B^{\alpha} v_o / v\right)^{1/k}\right]^{-k} \qquad (12)$$

with the parameters $\alpha = 0.45$, $k = 0.6$, and $v_o = 3.6 \times 10^8$ cm/sec. We have used this formula taking for the relative velocity between beam ion and electrons $v = (v_B^2 + v_{el}^{th\,2})^{1/2}$ where $v_{el}^{th} = (2kT/m_e)^{1/2}$ is the thermal electron velocity and kT the temperature. The total stopping power is finally obtained by adding the contributions from bound and free electrons

$$\frac{dE}{dR} = \frac{1}{\varrho_T}\left(1 - \frac{Z_T^{ion}}{Z_T}\right) \cdot S_{bound} + \frac{Z_T^{ion}}{\varrho_T Z_T} G(v_B / v_{el}^{th}) \cdot S_{free} \qquad (13)$$

Here, the function $G(x) = (\mathrm{erf}(x) - 2x \exp(-x^2)/\sqrt{\pi})$ accounts for the temperature dependence of the Coulomb cross section in the case that the thermal velocity v_{el}^{th} becomes comparable or larger than the ion velocity v_B. It is well known that the description given above breaks down for low ion energies. The Lindhard theory, applicable at low energies, gives for the bound electron contribution

$$S_{bound} = -k\sqrt{E_{ion}/A_B} \qquad (14)$$

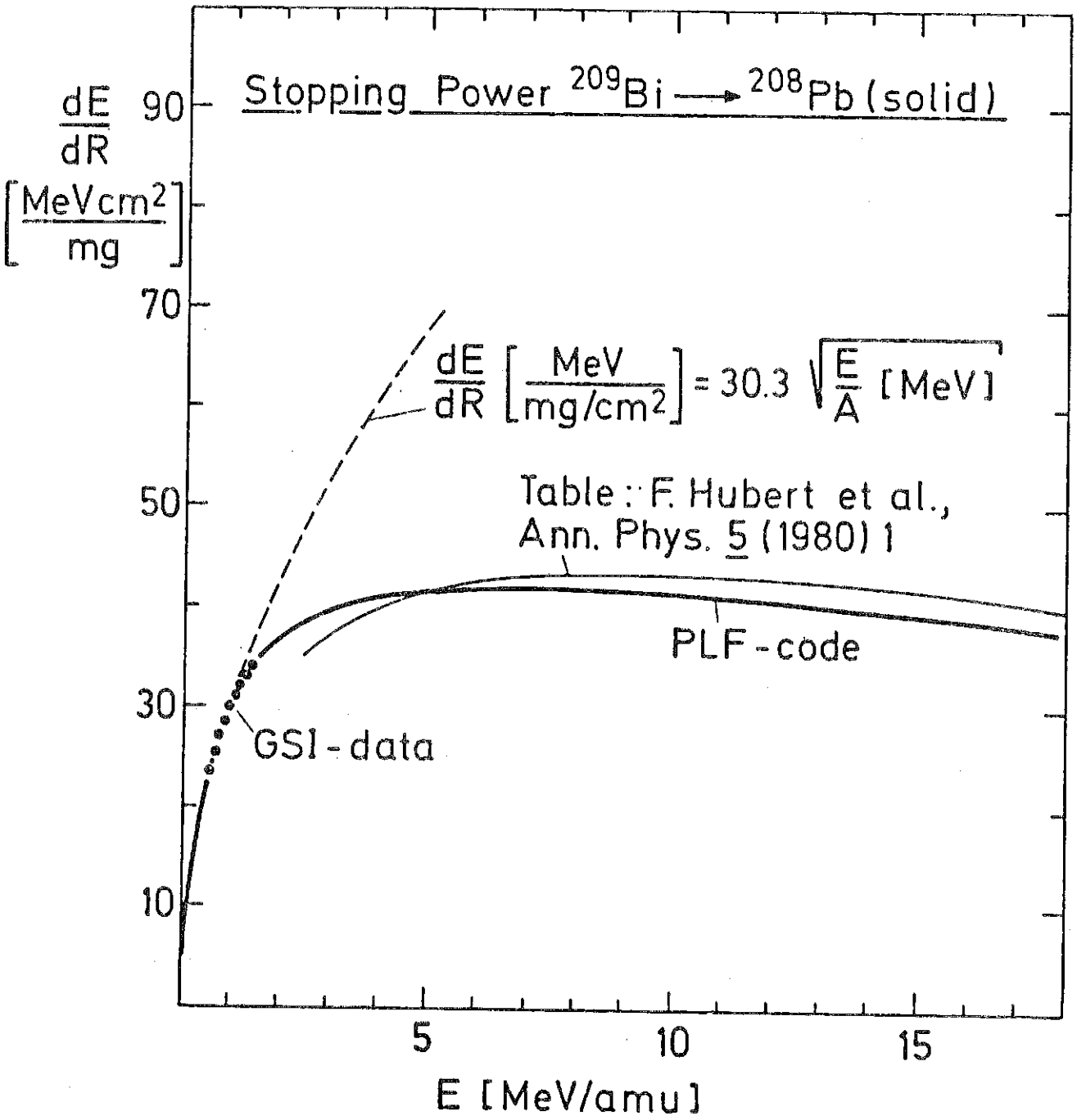

Fig. III.2-5: Stopping powers of Bi on solid PB at low energies.

In order to insure a correct treatment of the energy deposition near the end of the beam range, we have smoothly replaced expression (11) for S_{bound} by the Lindhard expression (14) at small energies, taking the parameter k from recent GSI measurements.[5] The calculated stopping power at small energies for Bi on solid lead is shown in Fig. III.2-5 together with GSI-data and values from the tables in ref. 8.

III.2.2.3 Calculated ranges and stopping powers

As a central result of this study, ranges of Bi-ions on solid Pb, solid Li, and solid PbLi alloy as considered in the HIBALL pellet design are given in Fig. III.2-6 as a function of ion energy in the relevant energy region. The range of 10 GeV Bi on solid Pb is found to be

$$R.(10\,GeV\ Bi \rightarrow Pb) \cong 0.30\ g/cm^2$$

in solid Li, it is

$$R(10\,GeV\ Bi \rightarrow Li) \cong 0.13\ g/cm^2$$

For stopping powers at finite temperature, the average ionization Z_T^{ion} of the target plasma has been calculated from the Saha equation using ionization energies derived within Thomas-Fermi approximation. As an example the ionization of Pb-plasma as a function of temperature and density is shown in Fig. III.2-7. Based on these results, deposition profiles of 10 GeV Bi-ions in different materials and at various temperatures relevant for pellet fusion have been calculated as shown in Figs. III.2-8 to III.2-10. With increasing temperature, range shortening is found in all cases. The deposition profile in solid Pb is rather flat, and pronounced Bragg peaks only develop at higher temperatures. In a

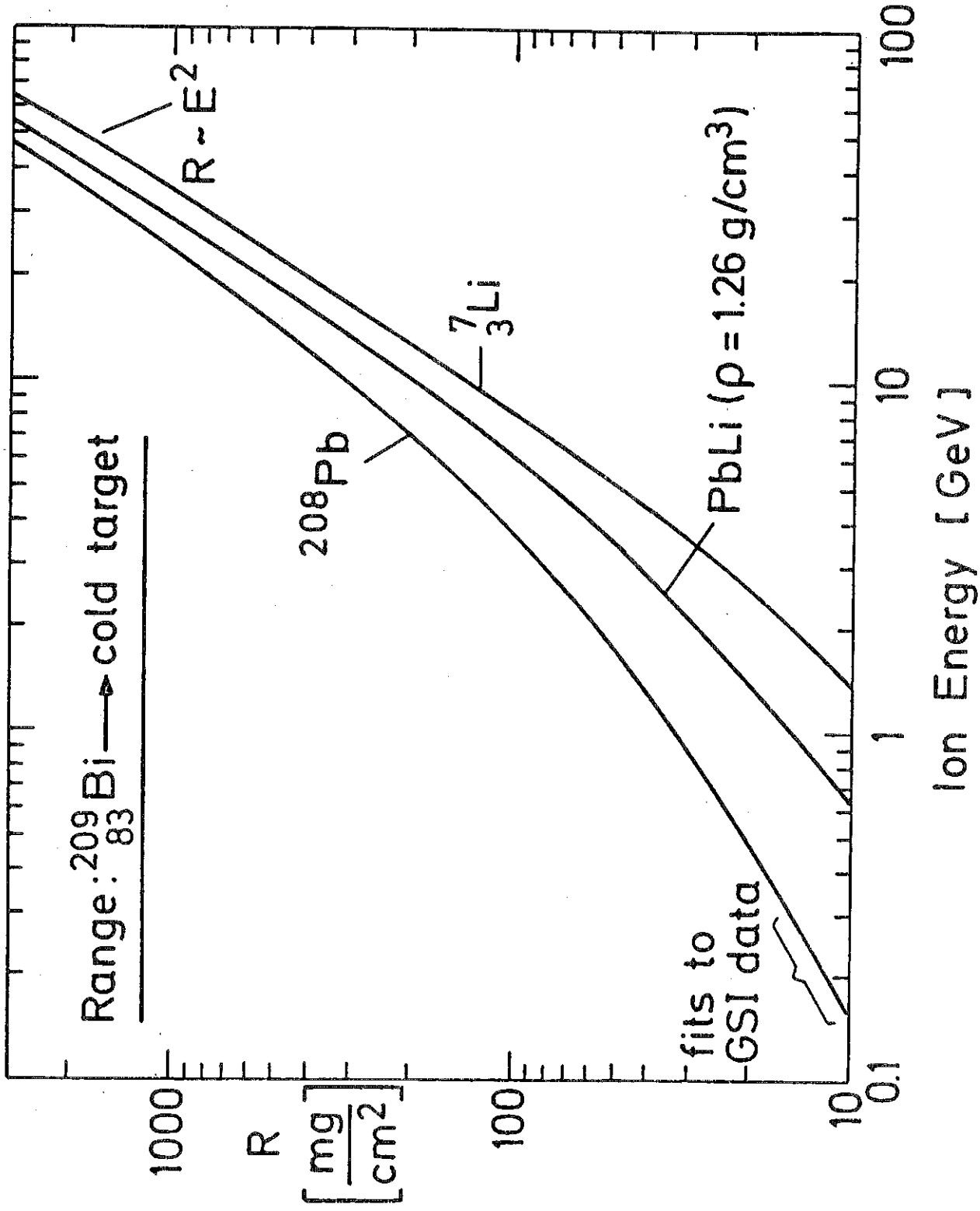

Fig. III.2-6:. Ranges of Bi-ions in different solid materials as a function of ion energy.

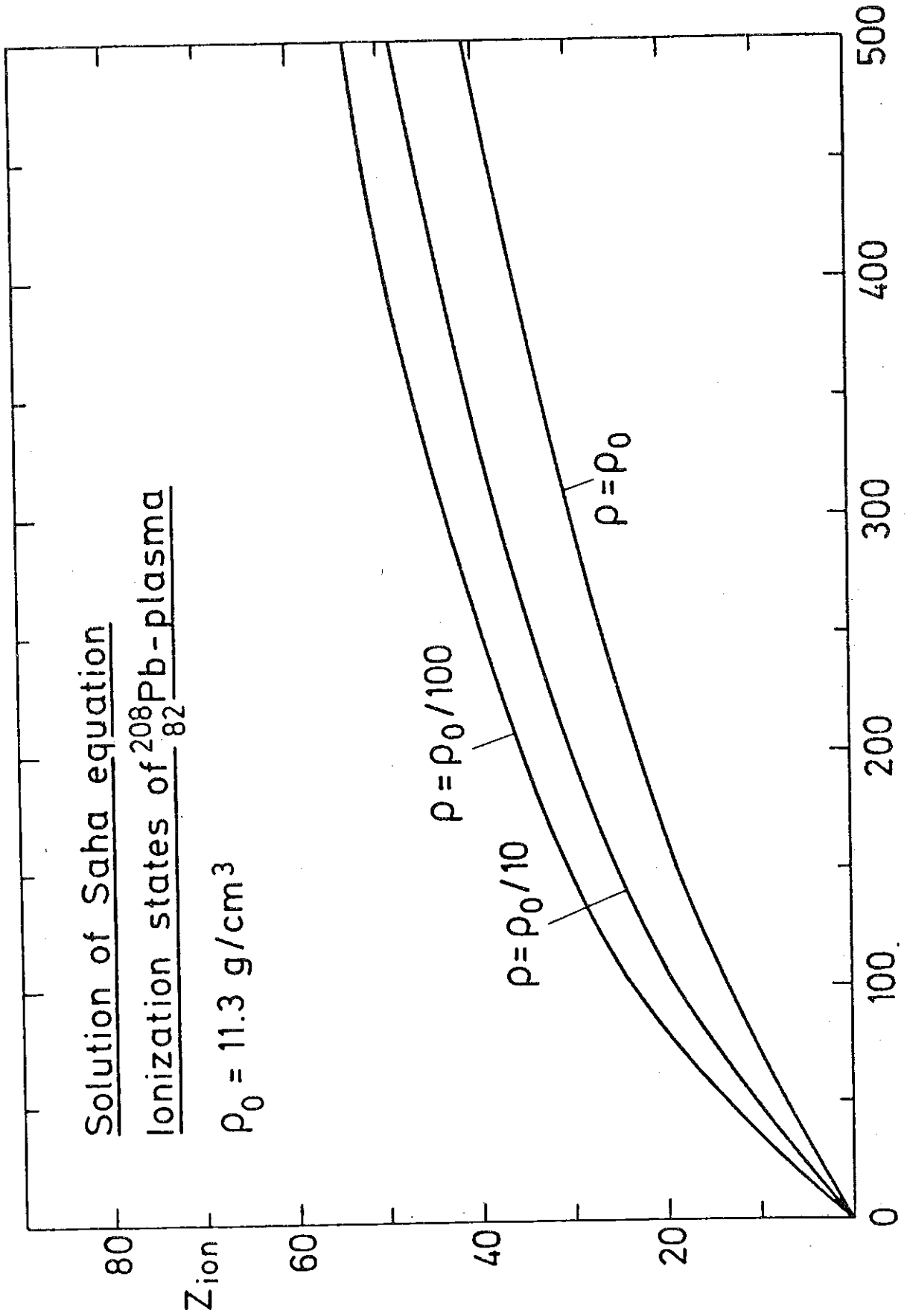

Fig. III.2-7: Average ionization of Pb-plasma as a function of temperature and density.

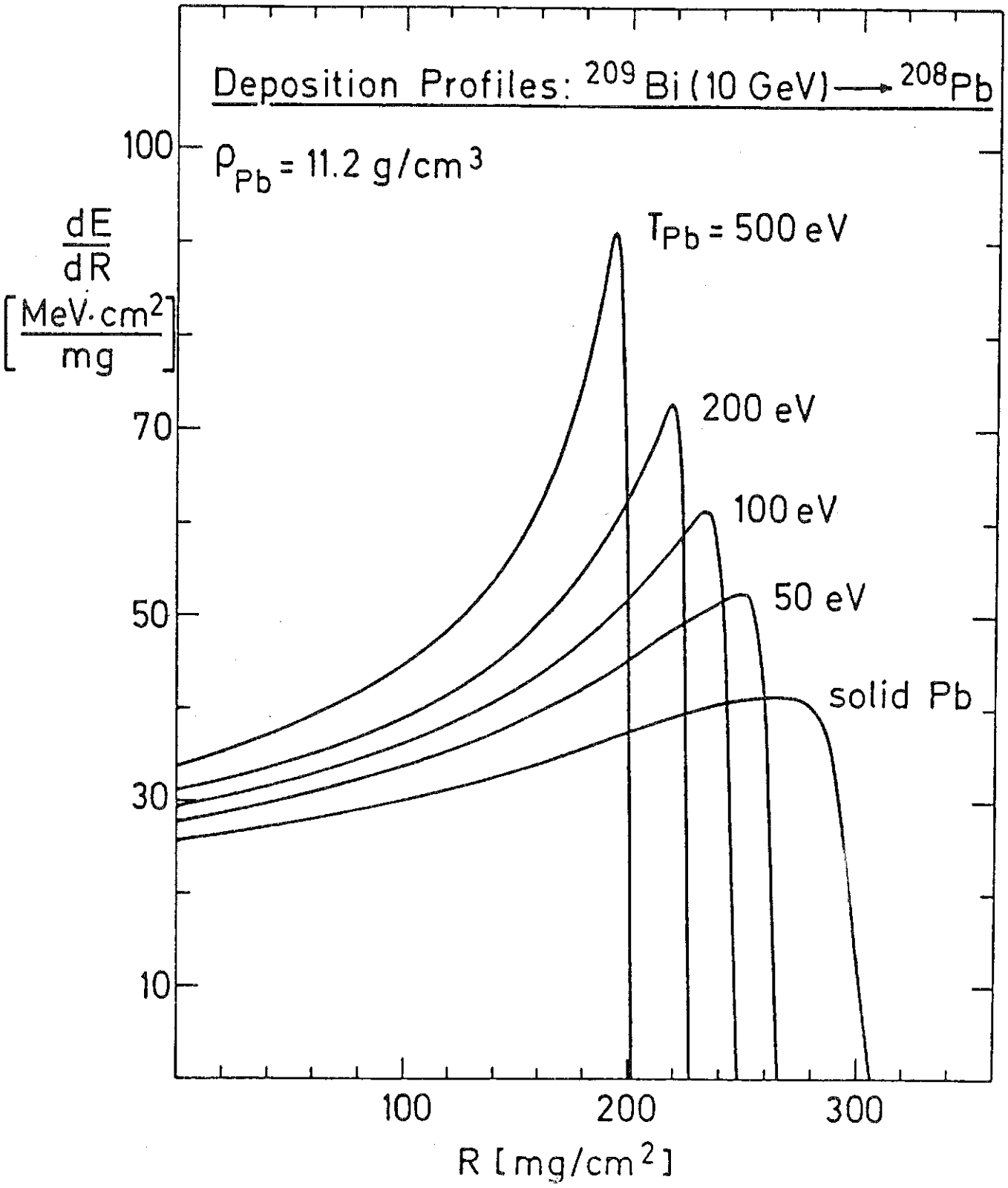

Fig. III.2-8: Stopping power as a function of range for Bi on Pb for different target temperatures.

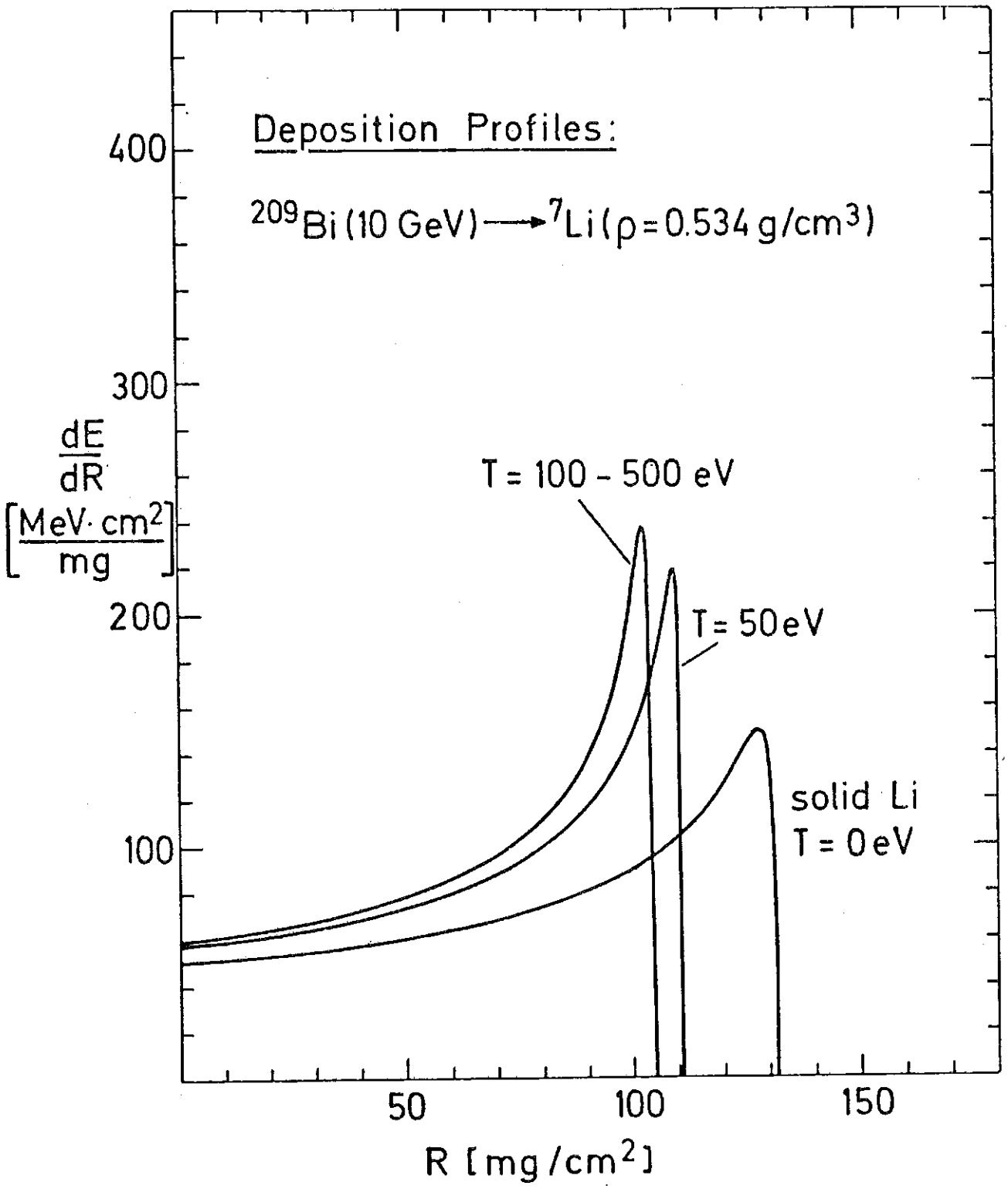

Fig. III.2-9: Same as Fig. III.2-8, but for Bi on Li.

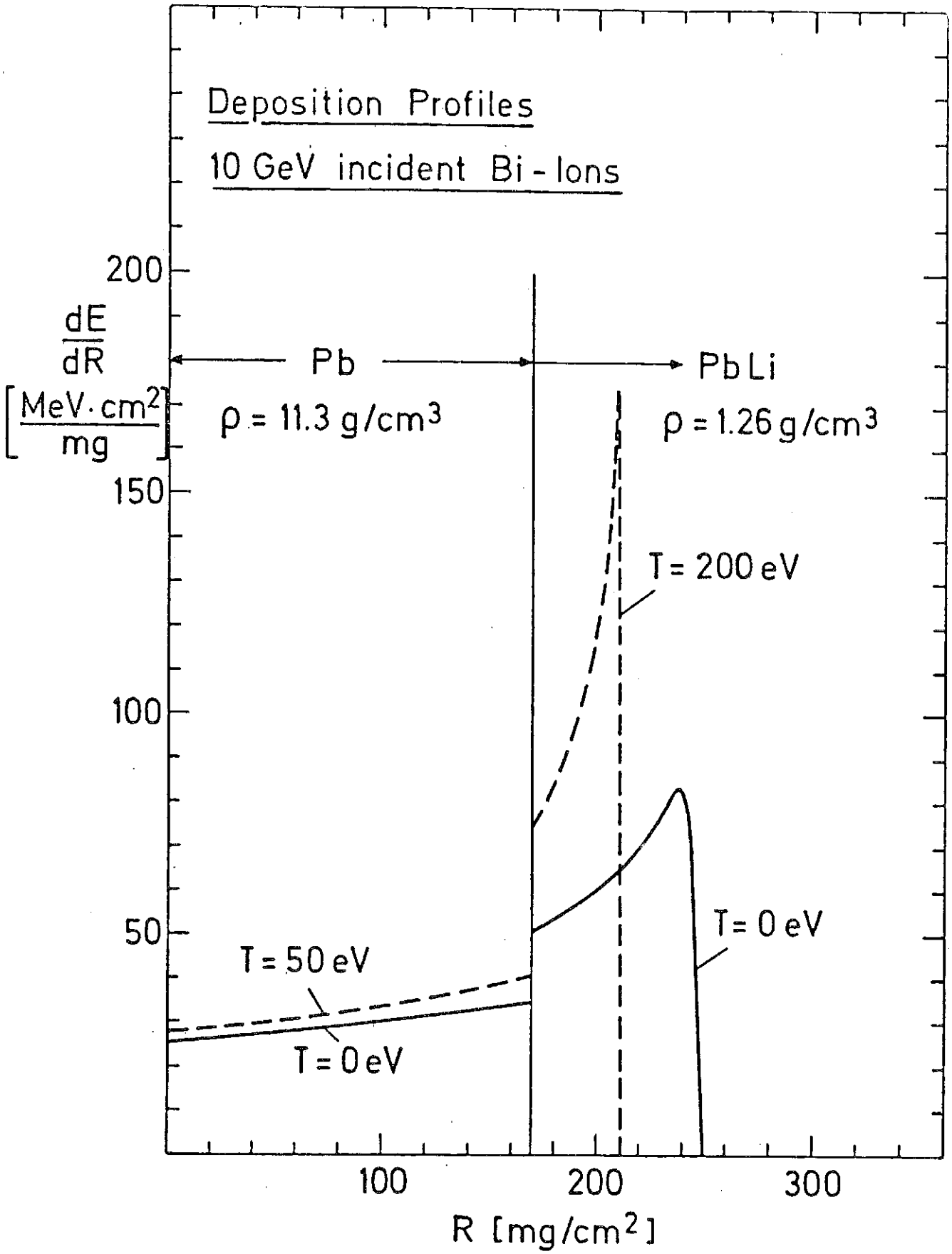

Fig. III.2-10: Energy deposition of 10-GeV Bi-Ions in the absorption layers of the HIBALL pellet. Solid line for cold target, broken line for typical temperatures during implosion.

light material like Li, the average stopping is higher than in Pb and the effect of range shortening saturates at a temperature of about 100 eV as seen in Fig. III.2-9. At this temperature, the material is fully ionized.

In Fig. III.2-10, deposition profiles are shown for the HIBALL pellet. The beam first passes through a heavy Pb layer with relatively low stopping power. This layer serves as a tamper. The rest of the beam energy (almost 50 %) is then absorbed in a PbLi layer with low density and high stopping power. It is heated to higher temperatures than the Pb layer. For simplicity, constant temperatures are chosen in Fig. III.2-10 for each layer. They correspond to typical values of the implosion calculation discussed in the next section. It should be noted that deposition profiles of light ion beams show a much more pronounced Bragg peak than the heavy ion beams discussed here. Light ion beams are therefore more suited to create an implosion configuration with a heavy cold tamper outside and a light hot absorber inside which pushes the fuel with high efficiency. The advantage of this design is somewhat reduced when used for heavy ion beam fusion as in the present study.

A further degradation of coupling efficiency between beam and implosion dynamics is due to the fact that, in a realistic situation, the beam arrives at the pellet surface not perfectly focussed (see e.g. ref. 15) The effect of defocussing has been studied in ref. 16. It tends to wash out any Bragg peak in the deposition profile. Since the exact beam properties at target are still uncertain, we have chosen box deposition profiles with constant dE/dR in the following implosion calculation.

III.2.3 A specific pellet design

III.2.3.1 General consideration

In this section, a single shell pellet design is considered, and the results of an implosion calculation are presented in detail. The intention is to provide insight into the dynamics of a heavy ion induced pellet implosion, to check the consistency of the general HIBALL parameters with the requirements of the pellet and to discover critical points. The results indicate that the beam parameters assumed so far are not consistent. Most critical points are ignition and symmetry. The assumed power of 240 TW is too low to insure a stable and igniting implosion, at least for the envisioned single shell design. The presented calculation achieves ignition with 240 TW, but only at the price of a highly optimized pulse shape, a thin pusher (6 mg) and a reduced amount of fuel (2 mg). The required output energy of 400 MJ is obtained due to a high burn rate. However, a rough estimate then shows that the implosion symmetry will be destroyed due to Rayleigh-Taylor (RT) instability. A thicker pusher that survives RT-instability is needed as well as 4 mg fuel to allow for a more realistic burn rate. This will require considerably more beam power for ignition, probably in the order of 500 TW. An alternative approach may be a double shell pellet design which has been found to require less power for ignition due to a central igniter[17].

It should be kept in mind that the present calculations are based on a simple hydrodynamic code (see description below) and are subject to large uncertainties on top of those inherent to pellet design in

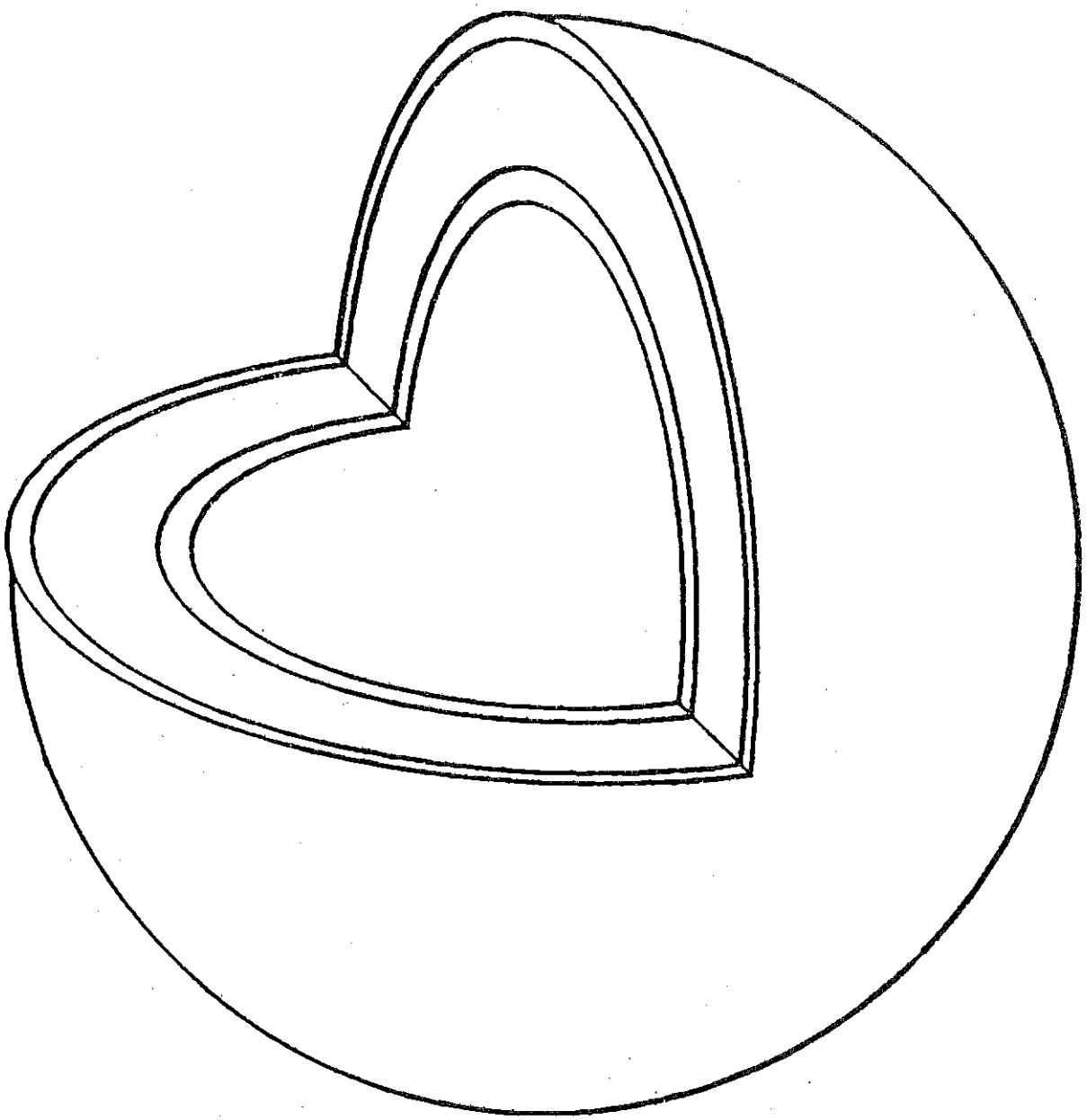

Fig. III.2-11: Perspective view of the HIBALL pellet.

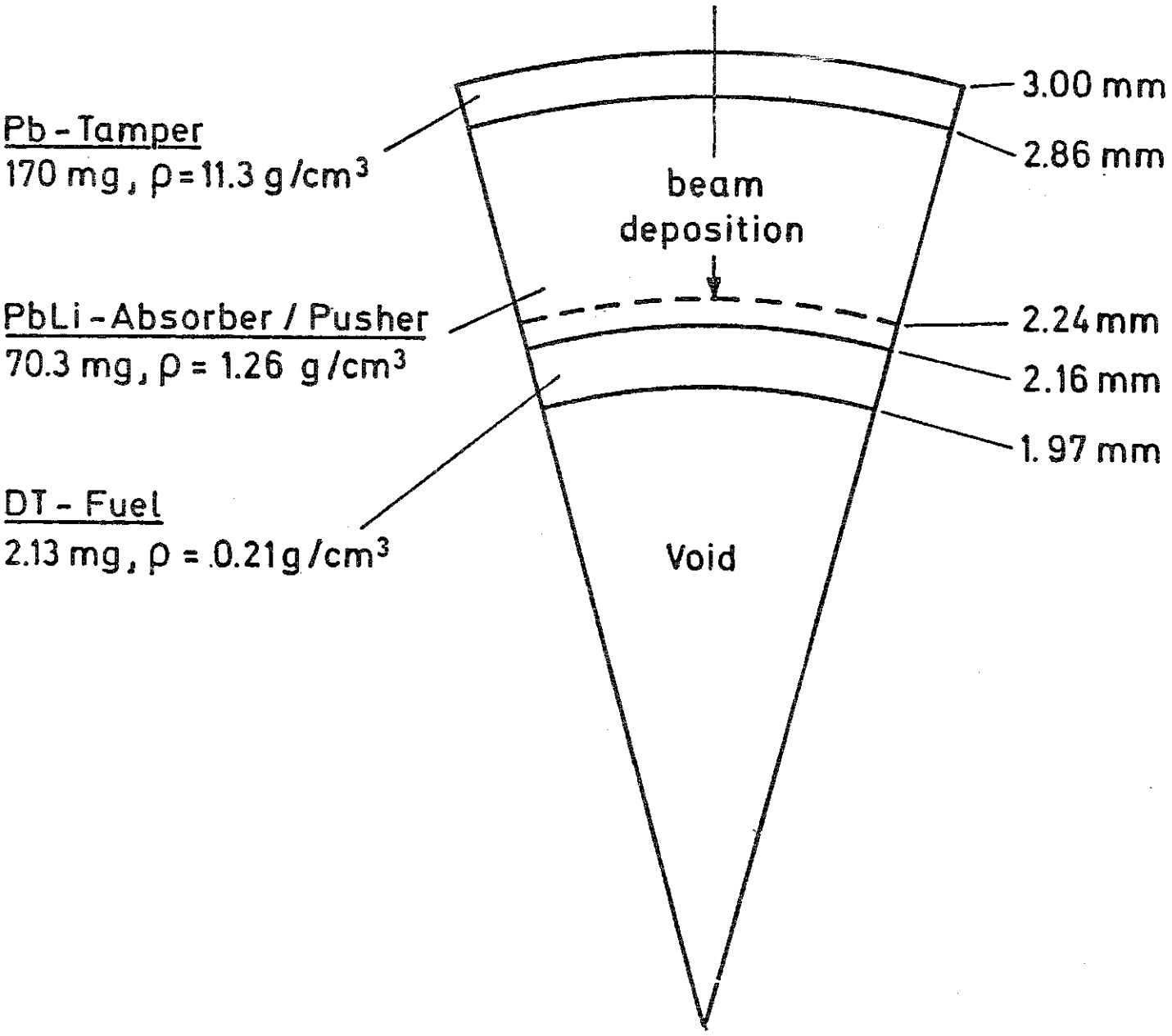

Fig. III.2-12: Sector of the HIBALL pellet

general. A particular problem not further addressed in the following is related to asymmetric irradiation of the pellet in the HIBALL reactor. Due to high density and relatively low temperature in the beam deposition region, lateral heat conduction will be rather ineffective to smooth out these asymmetries, at least in the present design.

III.2.3.2 The pellet configuration

The pellet considered in this work closely follows a design proposed by Bangerter and Meeker[18] for light ion beam fusion. A perspective view is given in Fig. III.2-11. The pellet consists of a spherical hollow shell made of three layers as shown in Fig. III.2-12. The cryogenic fuel is contained in the inner layer, the outer layers are made of low density PbLi alloy and high density Pb. They serve as pusher/absorber and tamper, respectively. The PbLi-alloy replaces the TaCOH material of the Bangerter-Meeker design and has been chosen for reasons of chemical compatibility with the environment in the HIBALL reactor cavity. The main reason for choosing a low density layer in the middle is to have a low density pusher in order to prevent RT-instability at the pusher-fuel interface during the final stage of implosion. The other advantage in having a heavy tamper outside and a light absorber material inside is related to beam target coupling and has already been discussed in the section III.2.2.3.

The masses of the Pb and PbLi layer have been determined such that the interface between these layers is approximately stationary during the implosion and, secondly, by the requirement that beam ions have stopped

in the cold absorber 80 μm before reaching the fuel. This inner region of the PbLi layer is not directly heated by the beam and forms the pusher. The pusher mass (6 mg) as well as the fuel mass (2 mg) have been chosen such that ignition is achieved at a beam power of 240 TW (compare discussion in section III.2.3.1). The outer radius of the pellet has been fixed to 3 mm. This is a minimum value set by the requirements of final beam focussing.

III.2.3.3 The pellet code MINIHY

The 1D-Lagrangian hydrodynamic code MINIHY used for the implosion calculation is characterized by the following physical features:

A. One temperature for electrons and ions

It has been checked that this is sufficient for ion beam driven implosions[19], since energy deposition occurs in dense material and temperatures are typically below 500 eV. This is different from the situation in laser fusion where electron and ion temperatures decouple in the corona.

B. Spitzer thermal conductivity, no flux limit

This is sufficient for the same reasons as mentioned under point A.

C. DT burn with local deposition and free neutron escape

Since this treatment may overestimate ignition, fusion processes are switched on only when the central temperature reaches 5.6 keV. At this temperature, fusion energy production overtakes losses by bremsstrahlung. Fuel depletion is accounted for during burn.

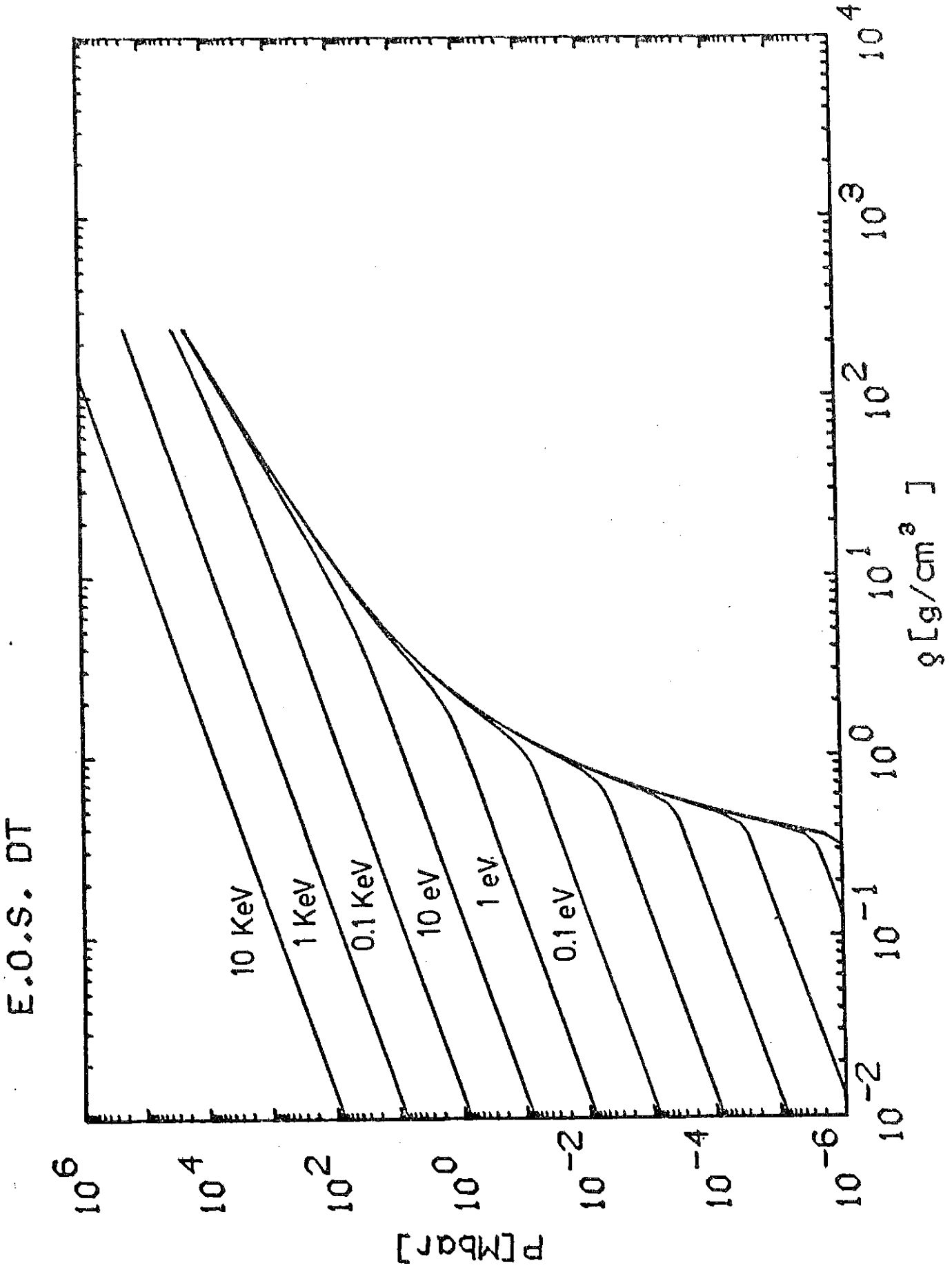

Fig. III.2-13a: Equation of state for DT used in the calculation.

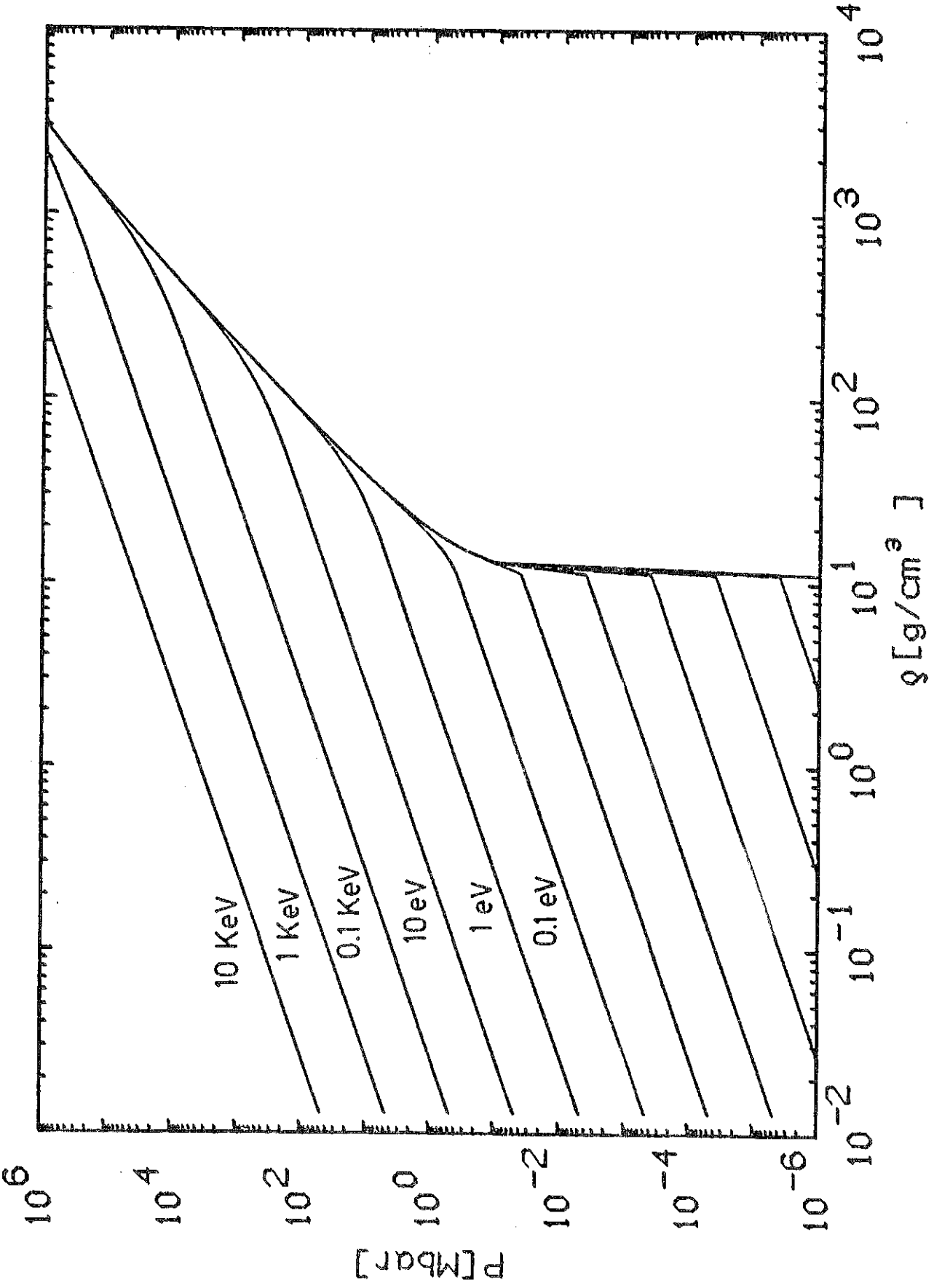

Fig. III.2-13b: Same as Fig. III.2-13a, but for Pb

D. Ideal gas equation of state allowing for electron degeneracy

A crucial point is that the Fermi temperature which controls the transition to the degenerate state is not calculated from the total electron density n_e in the medium (as e.g. in the original version of the Medusa code[20]), but from an effective density of unbound electrons n_e^* which is determined by an ad hoc description of pressure ionization in the form

$$n_e^* = n_e \cdot \exp\left\{-1/(V_0 n_e)\right\}$$

for DT, where $V_0 = 4\pi/3 \quad (\hbar^2/m_e e^2)^3$ is the volume occupied by a bound electron, and for heavier materials in the form

$$n_e^* = \begin{cases} n_e \cdot [1 - \exp(-(\varrho - \varrho_0)/(\beta\varrho_0))] & \text{for } \varrho > \varrho_0 \\ 0 & \text{for } \varrho \leq \varrho_0 \end{cases}$$

where ϱ_0 is the solid density and β an adjustable parameter. In the present calculation, $\beta = 200$ has been chosen for Pb, and $\beta = 50$ for PbLi. To be definite, the isotherms for DT and Pb in the (p, ϱ) plane have been plotted in Figs. III.2-13a and 13b. They show at least qualitatively a reasonable behaviour, in particular near the limiting degeneracy curve which is most important for a correct description of the high compression regions in the implosion.

With a more realistic equation of state, one would have to deposit more energy to create the same driving pressure in the absorber. Also, absorber temperatures would be higher at the same pressures. A critical point will be radiation transport which has not been included in the code, so far. The high-Z Pb layer is optically thick, and radiation

losses through the surface may be estimated by black body radiation. For the proposed pellet design, one finds a loss of 6 kJ for 50 eV surface temperature, 100 kJ for 100 eV, and 1.6 MJ for 200 eV. These are upper limits, but they demonstrate that a careful treatment of radiation as well as a more realistic equation of state are needed in the future development of this work. Nevertheless, no dramatic changes are expected for the overall implosion results. Concerning the beam energy deposition, it has been assumed $dE/\varrho\, dx$ = const (see discussion in section III.2.2.3). The implosion calculation has been performed on a Lagrangian mesh with 100 zones (36 for DT) and with progressively finer zoning towards the inner interface of each layer.

III.2.3.4 The pellet implosion

III.2.3.4.1 The general view

The optimized pulse shape to implode the described pellet configuration and to drive it to ignition is displayed in Fig. III.2-14. It consists of a 20 nsec prepulse at a power level of 2.4 TW and a 10 nsec main pulse at 240 TW with a 2 nsec rise time in between. The pulse is cut off at 32 nsec, since a further continuation would not improve the implosion result. The total pulse energy is 2.7 MJ. The corresponding r-t-diagram of the imploding shell is shown in Fig. III.2-15. The solid lines describe the motion of the outer pellet surface, the interfaces between the Pb, PbLi, and DT layer, and the inner DT surface, respectively. The broken lines display the temperature evolution in the deposition region. Ignition and burn occurs at about 37.7 nsec near R = 0.

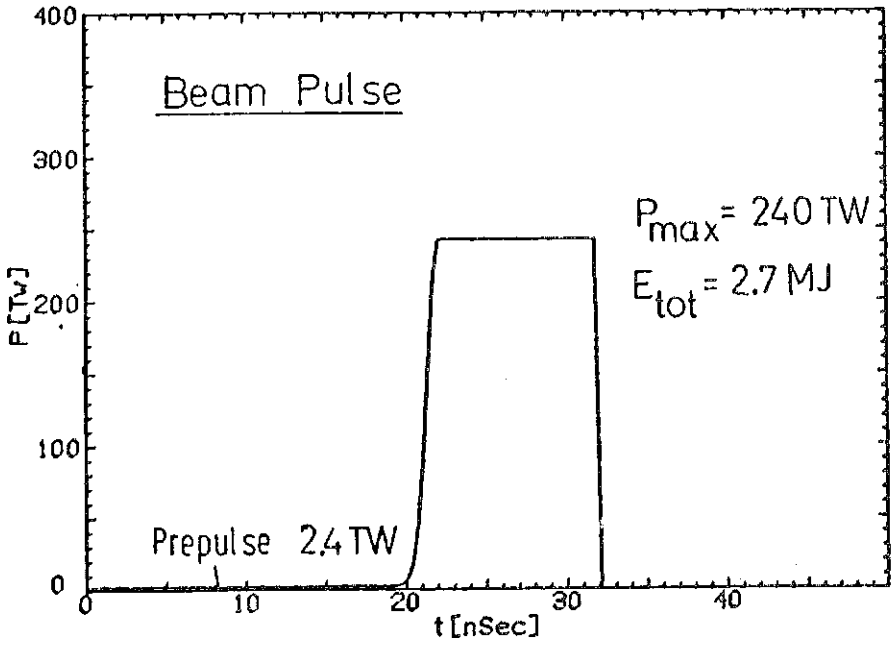

Fig. III.2-14: Pulse shape of the HIBALL design

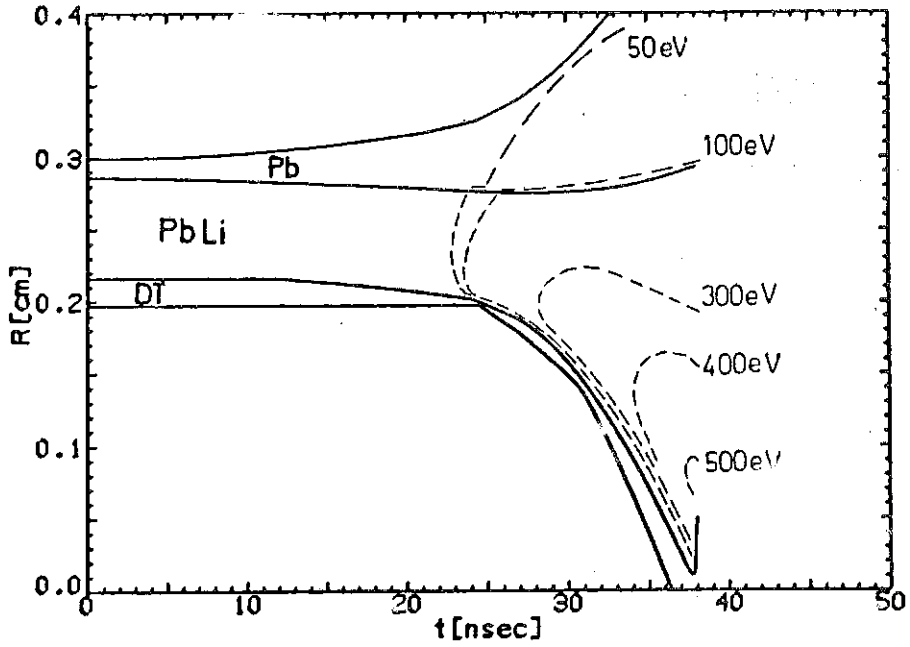

Fig. III.2-15: Implosion of the HIBALL pellet driven by pulse shown in Fig. III.2-14

The ion driven implosion looks rather different from that driven by a laser. It is essentially the explosion of a massive metal shell pushing the fuel at its inner front. The 10 GeV Bi-ions pass through 97.5 % of the shell's mass and deposit their energy deeply inside the volume, whereas laser deposition occurs far outside in a low density corona and the imploding material is driven by an ablating surface. As a consequence, the temperatures in the ion deposition region remain rather low ($\lesssim$ 500 eV) as compared to corona temperatures in laser fusion, and no problem with hot electrons is expected to occur. A disadvantage of the low temperatures is that heat conduction is slow and therefore ineffective to smooth out irregularities due to asymmetric irradiation of the pellet.

III.2.3.4.2 Absorber, pusher, and fuel during implosion

It is instructive to look at the profiles of temperatures Θ, density ρ, and pressure p given in Figs. III.2-16a-j for different times in conjunction with the r-t-diagram. Fig. III.2-16a shows the unperturbed pellet. The solid points in the broken line for the density mark the interfaces. The profiles at 18 nsec are seen in Fig. III.2-16b. The prepulse has heated the absorber to about 5 eV, the tamper interface stands like a rigid wall, the heated PbLi is flowing inwards, and a sharp density and temperature jump has built up at the border to the unheated PbLi which now forms the pusher. The steep gradients at this interface, formed at early times, stay on through all stages of the implosion. It is subject to severe RT-instability, a point further discussed in section III.2-3.4.5. At 18 nsec, the first shock generated by the prepulse has

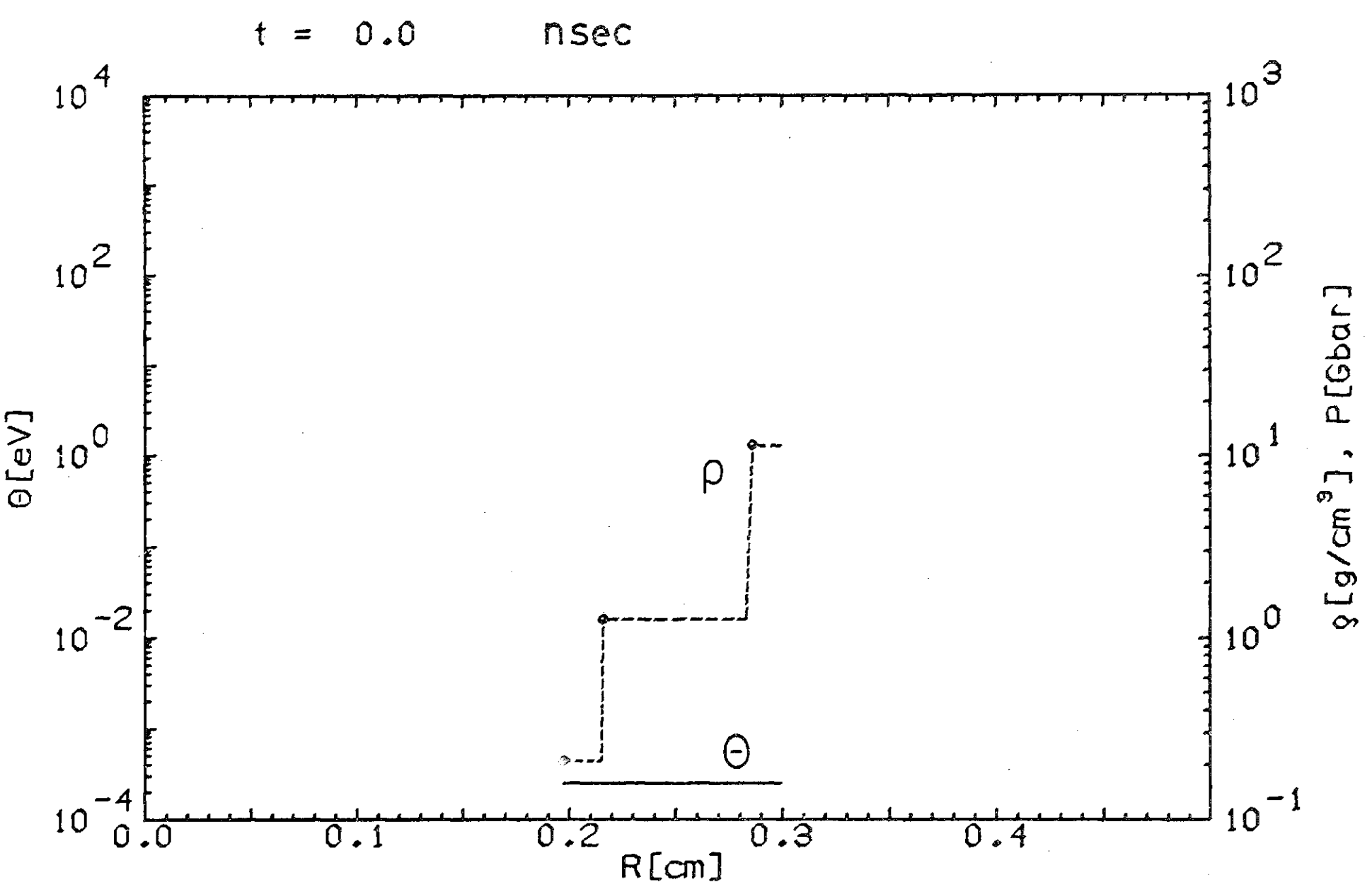

Fig. III.2-16a: Distribution of density ϱ, temperature Θ, and pressure p in the pellet at time t = 0. The solid points in the density line mark the interfaces. The pressure is still too low to be seen at this time.

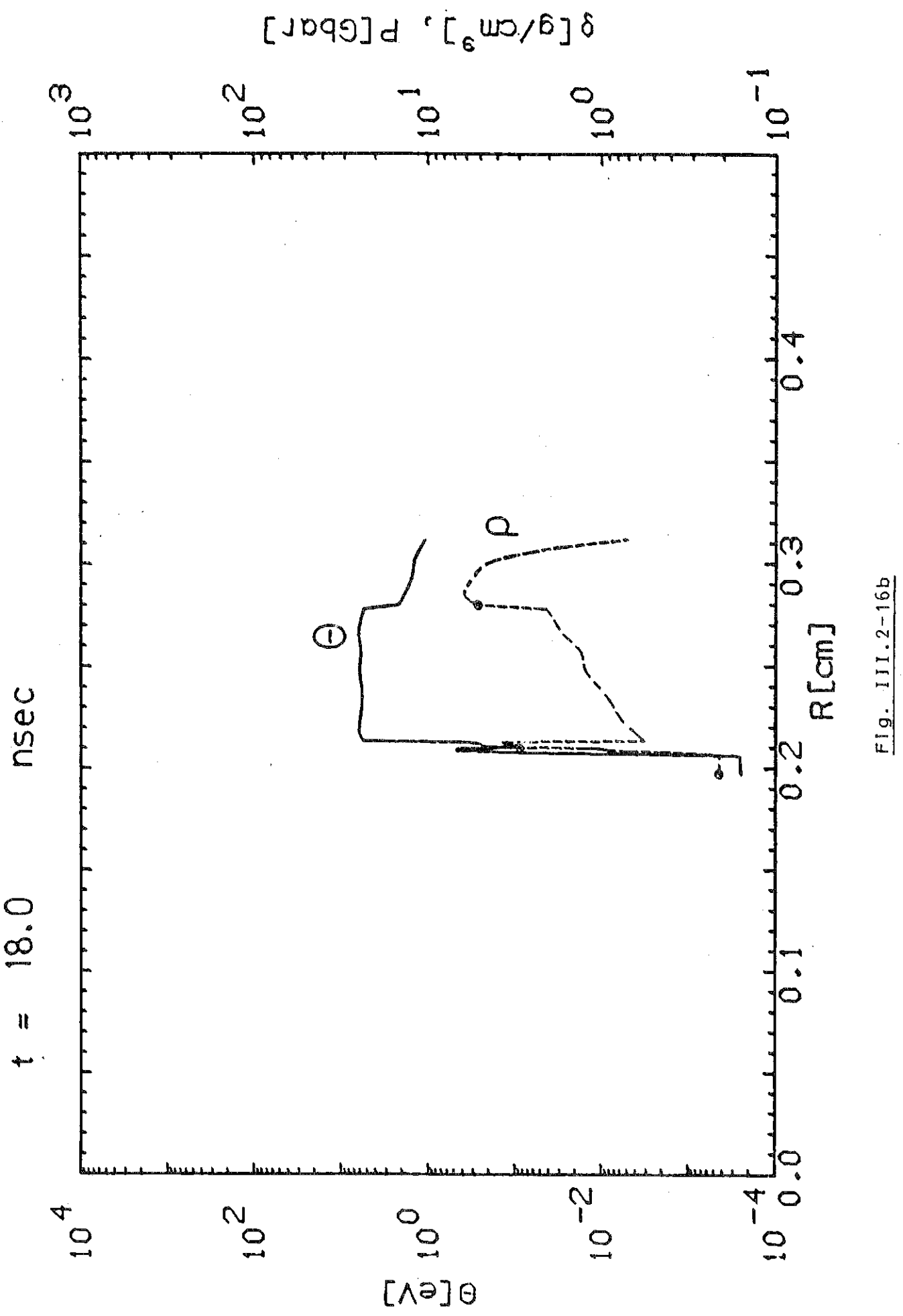
ϱ [g/cm³], P [Gbar]
10³
10²
10¹
10⁰
10⁻¹
Θ [eV]
10⁴
10²
10⁰
10⁻²
10⁻⁴
0.0
0.1
0.2
0.3
0.4
R [cm]
t = 18.0 nsec
Θ
ϱ
1

Fig. III.2-16b

just entered into the unperturbed fuel. At 24.5 nsec, it has almost reached the inner surface of the fuel closely followed by the second strong shock launched by the main pulse which was switched on at 21 nsec. This is seen from Figs. III.2-16c and 16d. The importance of these two shocks and their relative timing for forming the ignition spark will be discussed in section III.2.3.4.6. Here, one should again pay attention to the r-t-diagram (Fig. III.2-15) and to the way the inner fuel surface is set into sudden fast motion upon arrival of the shocks. It then travels at almost constant speed until the accelerated pusher catches up at about 31 nsec and gives the fuel another kick involving the passage of a third shock through the fuel. This fuel bouncing has been described before by Kidder[3]. It is also important for ignition.

At 36.40 nsec, the inner surface arrives at the centre (void closure). The fuel has now an average velocity of 2.5×10^7 cm/sec. Its kinetic energy amounts to 2.3 % of the input beam energy, whereas its internal energy is only 0.2 %, at this moment. The profiles are plotted in Fig. III.2-16e. A remarkable feature is the temperature distribution in the fuel which steeply rises towards the centre and is forming the ignition region. The pressure has now increased to more than 100 Mbar in the central region and appears on the scale chosen in the diagrams. Typical pressures in the absorber at main pulse time range between 10 and 100 Mbar.

III.2.3.4.3 Ignition and burn

Ignition (defined here as time when the central temperature reaches 5.6 keV) occurs at 37.647 nsec, about 1.2 nsec after void closure. During

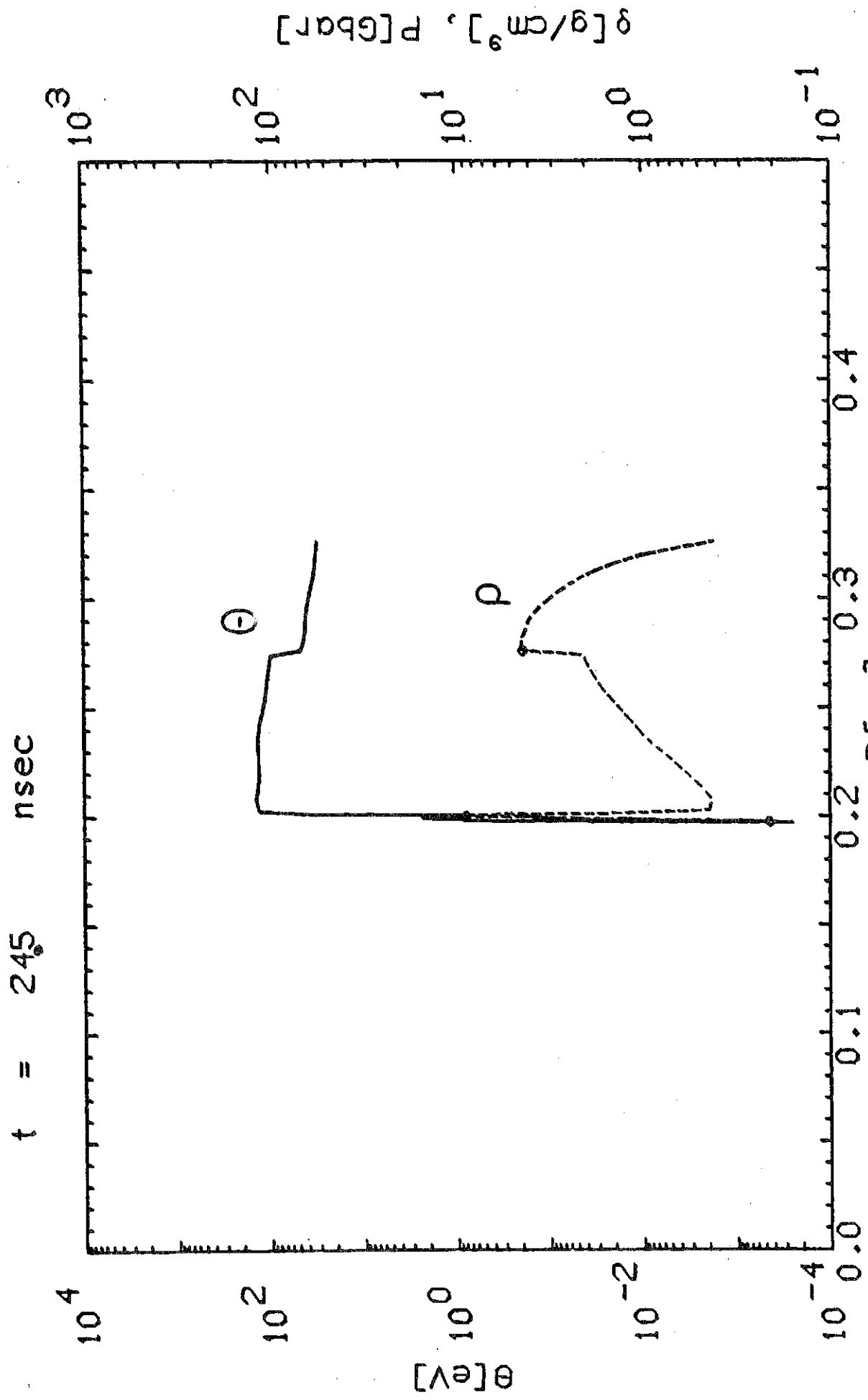

Fig. III.2-16c

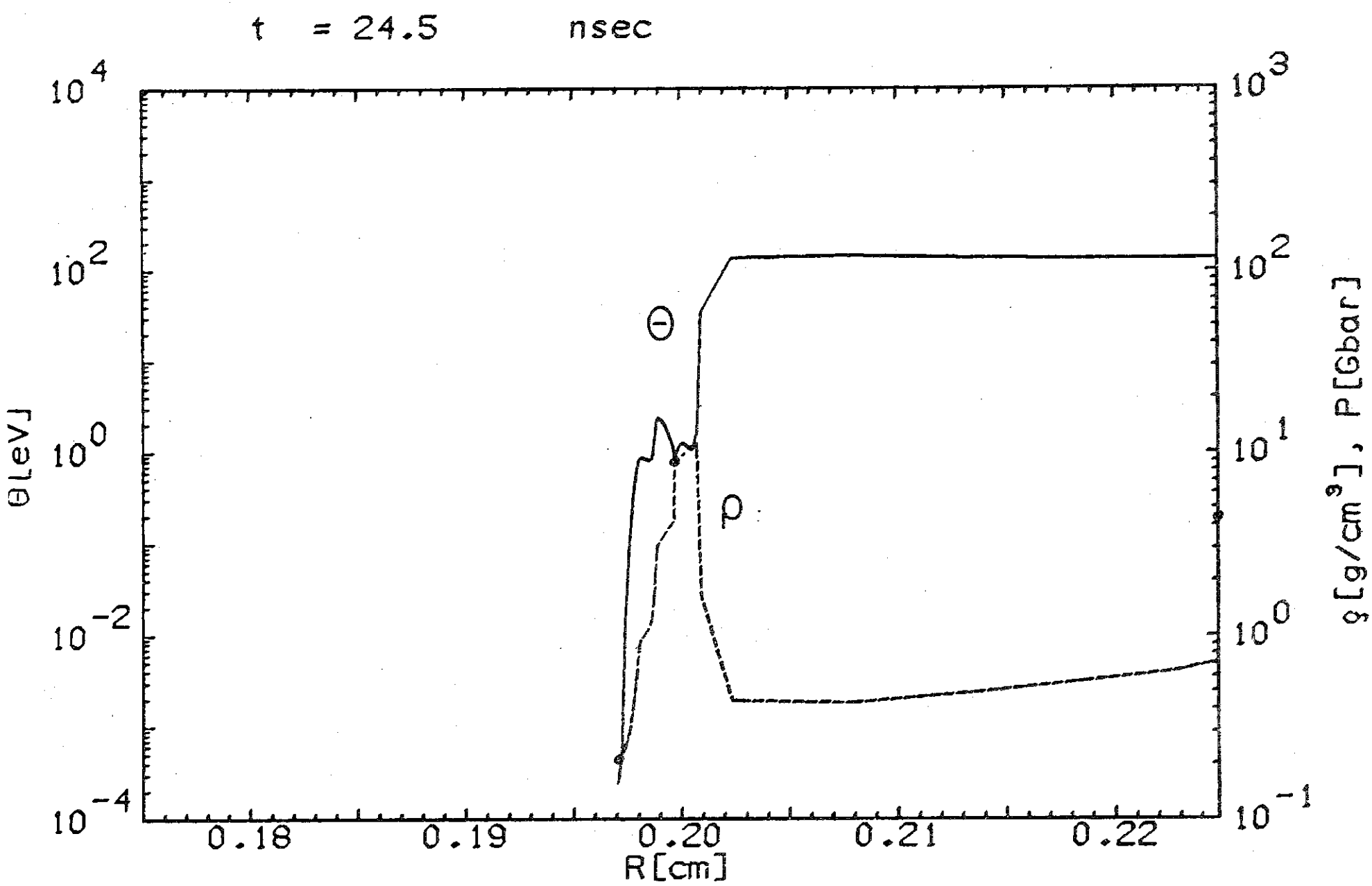

Fig. III.2-16d: Enlarged view of Fig. III.2-16c. First two shocks are seen in fuel.

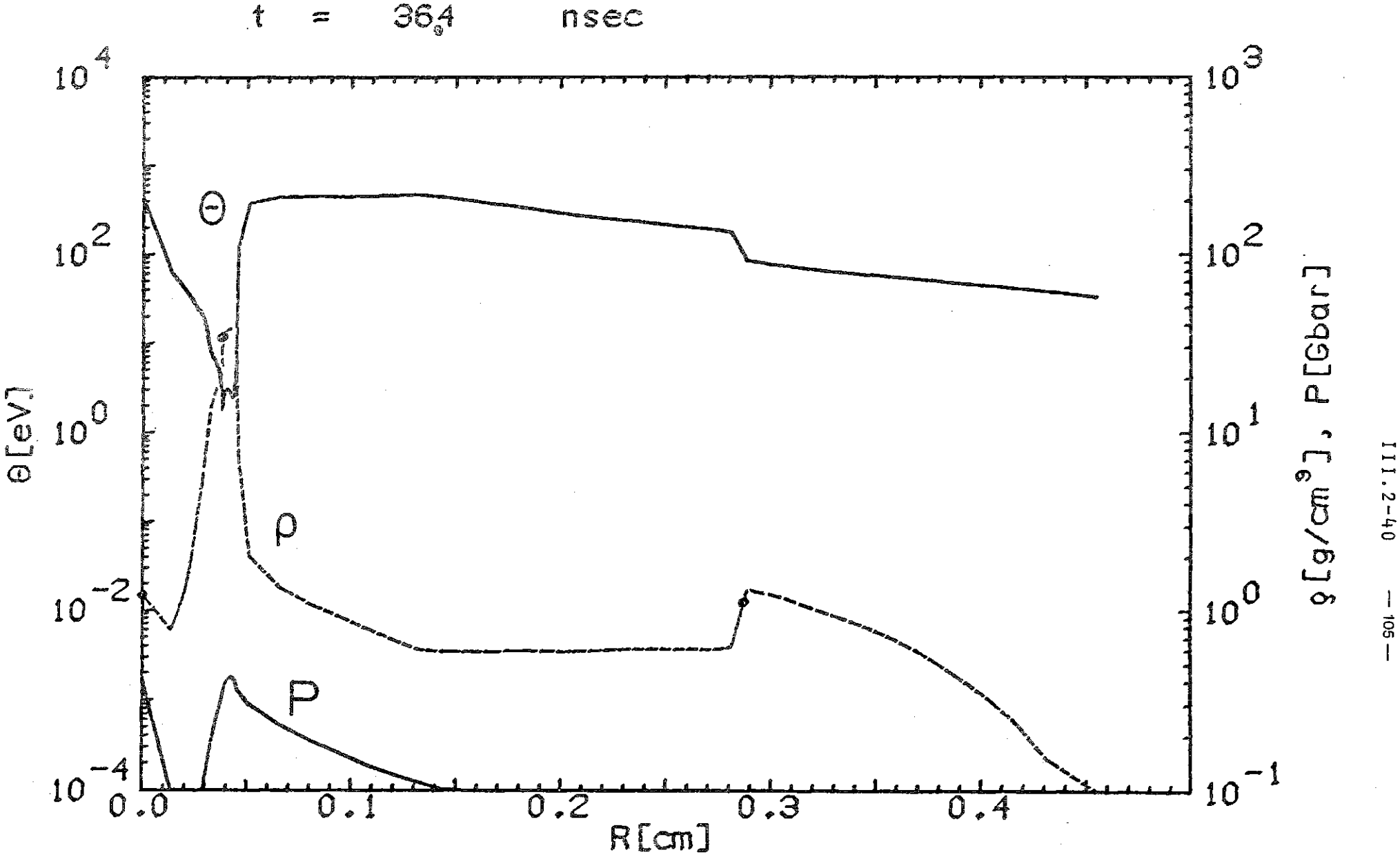

Fig. III.2-16e: Distributions at void closure time. Region of high fuel temperature seen in the centre.

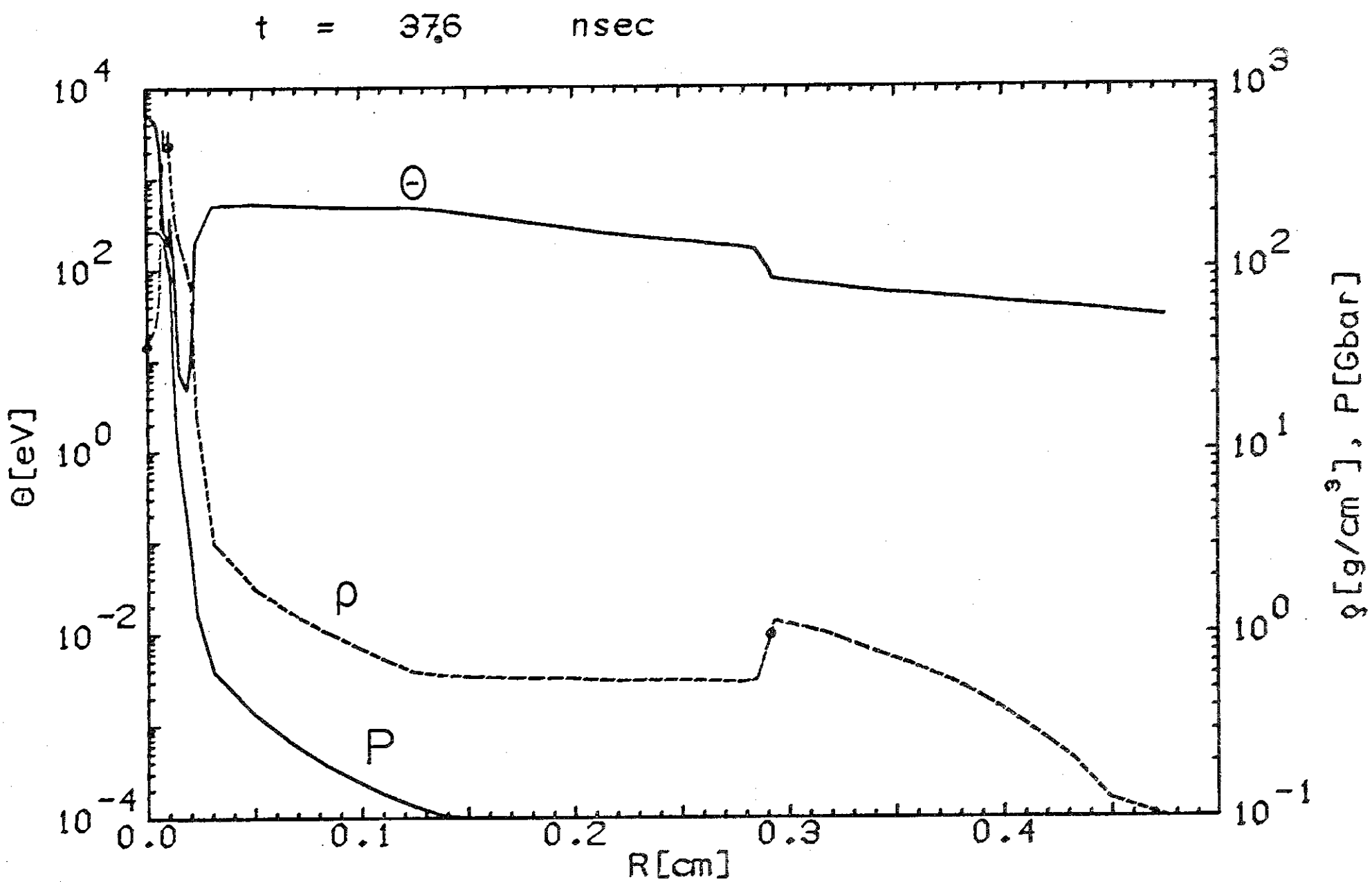

Fig. III.2-16f: Distributions at ignition time.

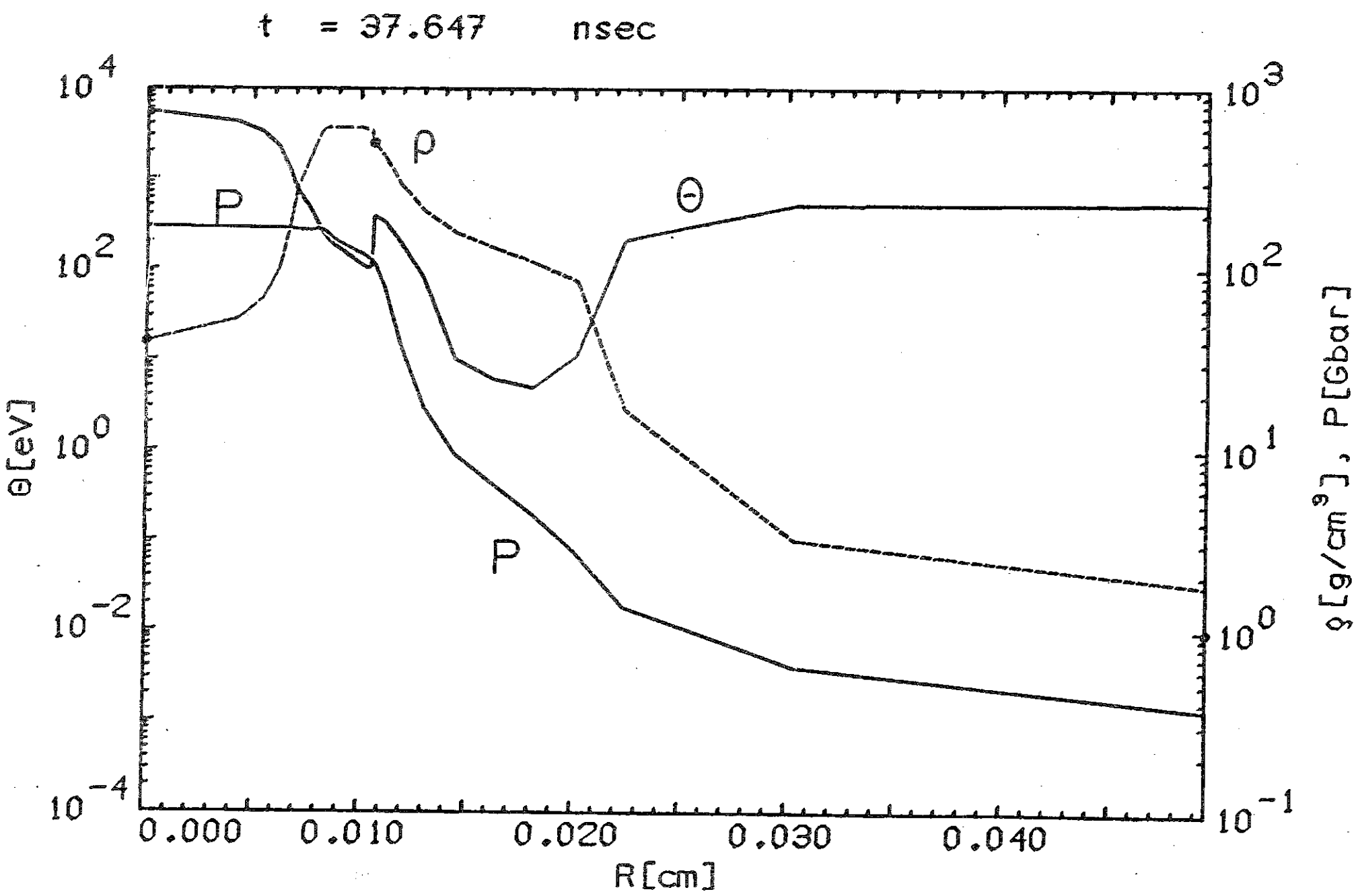

Fig. III.2-16g: Enlarged view of Fig. III.2-16f. The ignition configuration with constant pressure over the fuel is seen for R ≅ 110 µm.

this time, a strong reflected shock has traveled outwards through the fuel and is clearly seen in the pressure profile of Figs. III.2-16f and -16g at a position of 120 μm. (Note that a von Neumann viscosity is used in the hydrodynamic code, and shocks do not appear as sharp discontinuities, but smeared out over several Lagrangian cells). The return shock has finally brought the fuel into the ignition configuration. In Fig. III.2-16g, one should notice

(a) the constant pressure over the fuel of $p \cong 0.17$ Tbar,

(b) the spark region extending to 70 μm with a temperature near 5 keV, a density around 50 g/cm^3 and $(\varrho R)_{spark} \cong$ 0.4 g/cm^2,

(c) the highly compressed fuel region extending from 70 μm to 105 μm with a density plateau at 600 g/cm^3 and a temperature around 150 eV; the total fuel $\varrho R \cong 2.3$ g/cm^2.

These values are very near to those of the HIBALL working point which have been determined within the simple gain model of section III.2.1 and have been listed in Table III.2-1. The present calculation shows that the ignition configuration postulated there can actually be achieved dynamically. In particular, it confirms the key assumption of constant fuel pressure in which our model differs from that of Kidder and Bodner.

At ignition time, the fuel has come almost to rest. The fuel kinetic energy now amounts to 0.07 % of the total input energy, but the internal energy has increased to 4.2 % or 113 kJ. At the same time, there

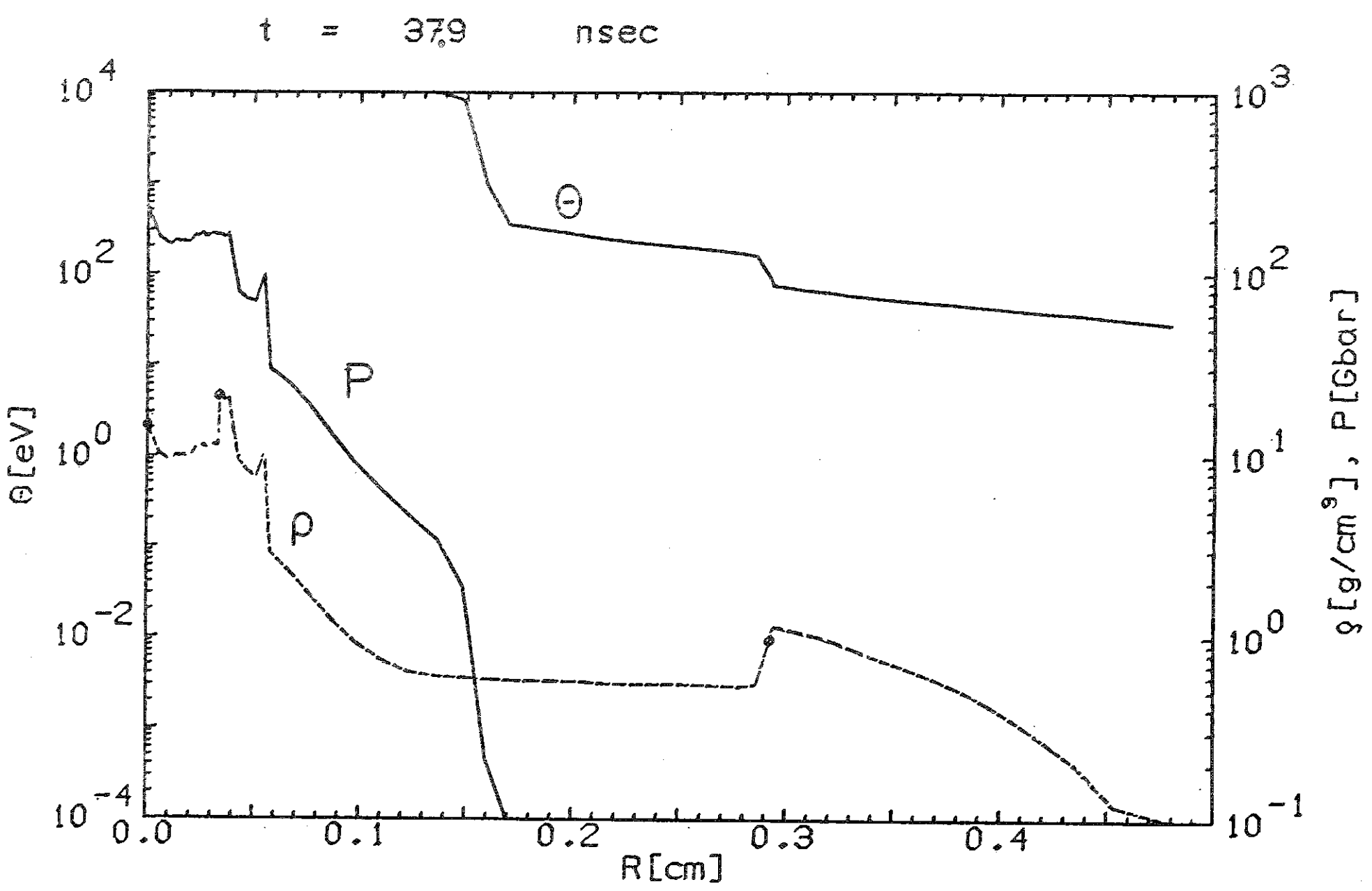

Fig. III.2-16h: Distribution after burn. A heat wave at 0.15 cm is seen travelling to the right far ahead of the burn shock wave at 0.06 cm.

still exists 4.5 % of the energy in form of inward going kinetic energy, mainly located in the massive pusher. The bulk of the energy occurs as internal energy of PbLi (≈ 43 %) and as energy of the tamper (18 % internal, 30 % kinetic). The absorber/tamper interface has hardly moved during the implosion, but about half of the beam energy has been deposited in the tamper and Pb is strongly flowing outwards at this time.

After ignition, it takes roughly 200 psec until burn has spread into the dense fuel region, and fusion energy is released in a short burst of about 20 psec. Fig. III.2-16h displays the situation shortly after burn. The central temperature is now above 10 keV, the burned up fuel is expanding, the outgoing burn shock sits at 0.6 mm, but has been left far behind by a fast moving heat wave with the front located at 1.5 mm. The calculated gain is 212, corresponding to a burn rate of 80 %. Such a high burn rate is probably unrealistic and expected to be degraded by effects (e.g. nonsymmetric implosion) not simulated in our code. In the present calculation, it is explained by the strongly tamping effect of the pusher ($(\varrho R)_{Pusher} \approx 3$ g/cm^2) and its high, inwards directed kinetic energy during burn time.

III.2.3.4.4 Pulse shape, shocks, ignition

The formation of the ignition spark and how it is related to the pulse shape is now discussed in some more detail. The problem is to drive a certain inner part of the fuel to a much higher isentrope than the rest of the fuel, the entropy of which should be kept as low

as possible. In pure gas dynamics, which are approximately valid for the imploding fuel, the entropy of a fluid element is a constant of motion as long as no shock passes through. The amount of entropy increase due to a shock depends on its strength in a non-linear way. The concept followed in the present design work to achieve an optimal ignition configuration is schematically outlined below and then illustrated by showing the fuel entropy evolution in the code calculation. It involves a sequence of 4 shocks passing through the fuel.

I. Prepulse shock

The prepulse (few TW) launches a 1. shock S1 which homogeneously heats the cryogenic fuel to a temperature of about 0.5 eV.

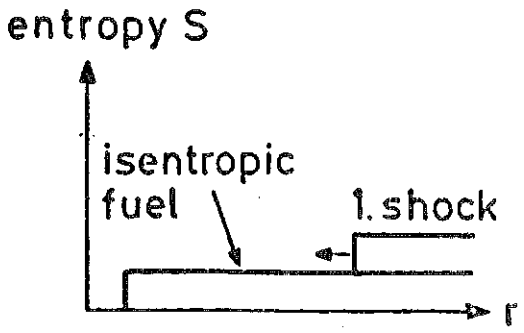

II. Main pulse shock

The main pulse (some 100 TW) launches a second shock S2 into the fuel which is timed to overtake S1 near the inner fuel surface.

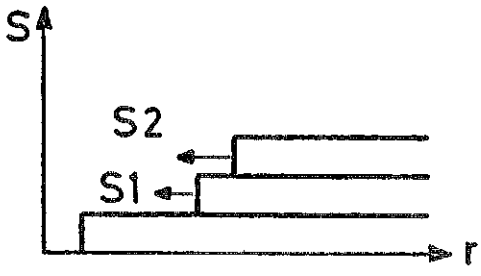

The combined shock S12 is much stronger than the sum of the original shocks and produces a region of higher entropy.

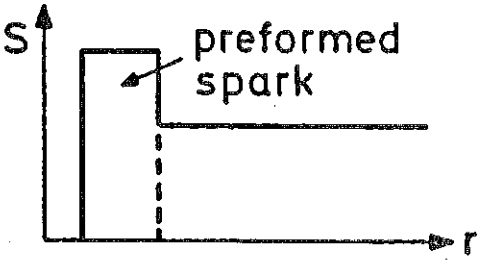

III. The bounce shock

The bounce shock (see section III.2.3.4.2) passes through a sloping density profile near the inner fuel surface and selectively adds entropy to this region.

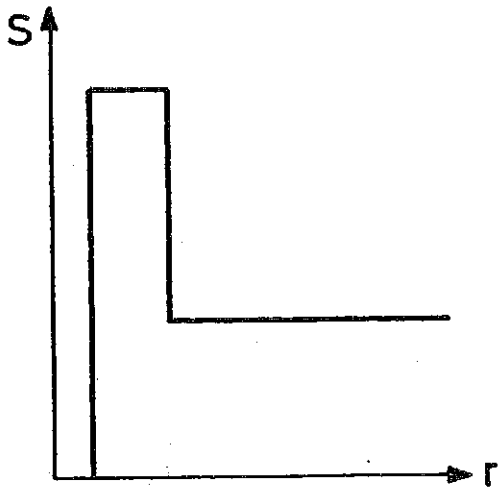

IV. The return shock

The return shock from central collapse finally shapes the spark and brings it to ignition temperature.

In Fig. III.2-17, it is shown to which extent this schematic ignition concept works in the actual code calculation. The ratio ($p/\rho^{5/3}$) normalized to its value for a degenerate electron gas has been chosen as an approximate measure for the entropy and has been plotted over the fluid cells of the Lagrangian mesh for different stages of the implosion Cell. 1 is located at the inner surface of the fuel, cell 36 at the interface with the pusher. For 24 nsec, one observes the first two shocks S1 and S2 as jumps in the entropy distribution (compare the corresponding density jumps in Fig. III.2-16d). At 27 nsec, both shocks have passed the fuel. The timing has been such that S2 has caught up with S1 at Lagrange cell 6, and then the combined shock S12 has propagated further to the left and has generated a region of increased entropy over the last few cells. The preformed spark is clearly seen in the 27 nsec curve. The next increase in entropy is due to the third shock created by fuel bouncing. At 31 nsec,

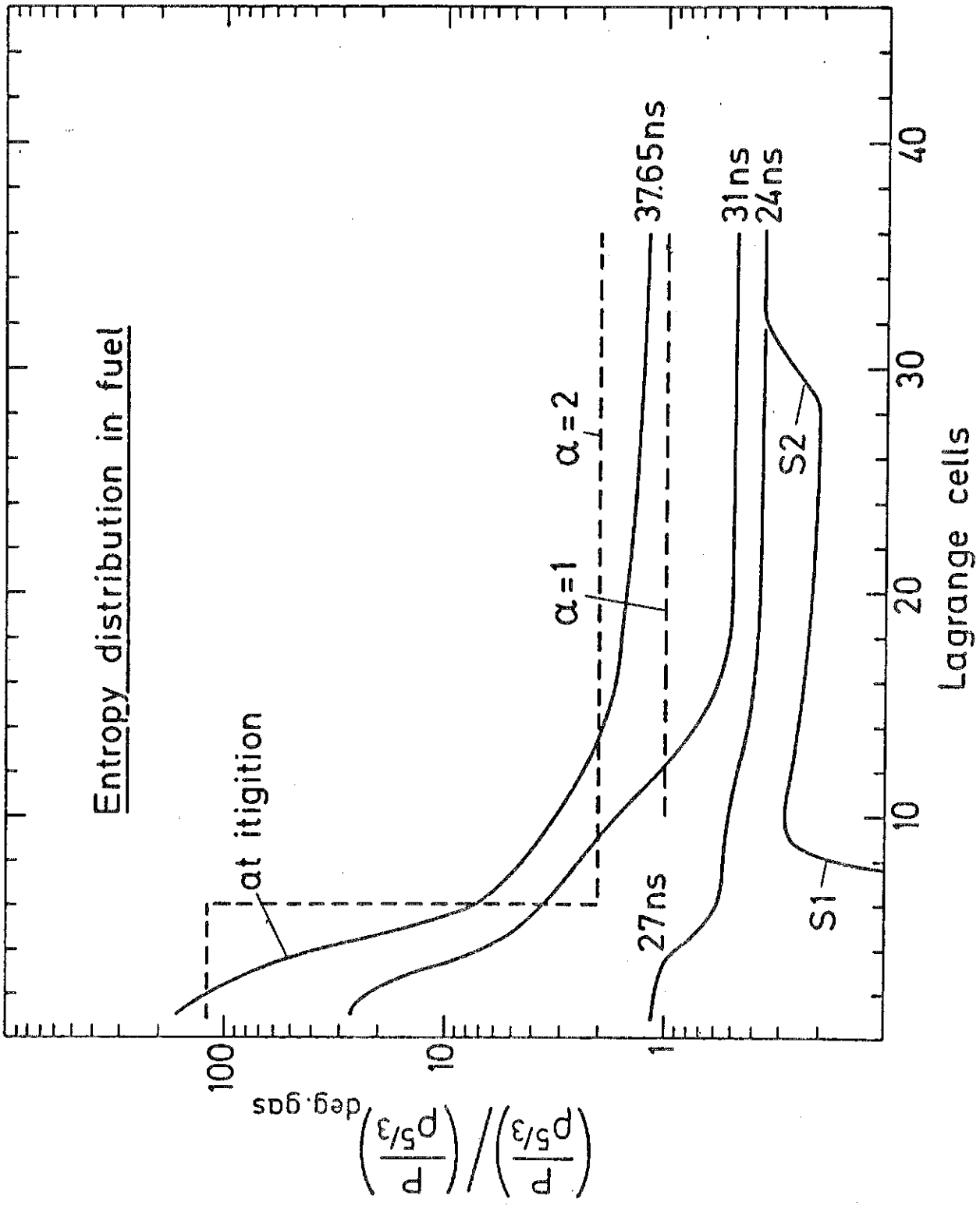

Fig. III.2-17: Time evolution of $(p/\rho^{5/3})$ distribution in fuel.

it has already passed the fuel, but the entropy curve at this time shows what has happened. In propagating through the fuel to the left, the bounce shock has met at Lagrange cell 16 with a rarefaction wave running to the right. This has caused the sharp entropy increase towards the inner surface. Finally, at 37.65 nsec, after passage of the return shock, the $p/\varrho^{5/3}$ curve for the ignition configuration (compare Fig. III.2-16g) is obtained. Its lower part corresponds to the highly compressed, electron degenerate fuel. Notice that this part cannot be directly compared with the other curves of the plot due to the electron degeneracy. Entropy is calculated differently in this case. This becomes clear from the broken curve labelled by $\alpha = 1$ which represents the lowest isentrope possible for the degenerate gas. However, it is interesting that the degenerate branch lies very close to the optimal isentrope $\alpha = 1$. This is indeed an optimal run: Not withstanding the 4 shocks which have gone through the fuel, the overall compression has been almost adiabatic. The $p/\varrho^{5/3}$ distribution assumed in the gain model of section III.2.1 for the HIBALL pellet is given in Fig. III.2.-17 by the broken line $\alpha = 2$, including the spark region at the left with a much higher isentrope. It compares well with the code run.

It is concluded that the idealized ignition configuration assumed by the gain model can approximately be obtained by implosions with optimized pulse shape. With the ignition concept described above, size and form of the spark is mainly determined by the timing of the first 2 shocks which is related to the length of the prepulse and to the power of prepulse and main pulse. The exact values to be chosen also depend on the actual pellet configuration. One problem has been to make the second shock strong enough for reaching final ignition. It has been solved by taking

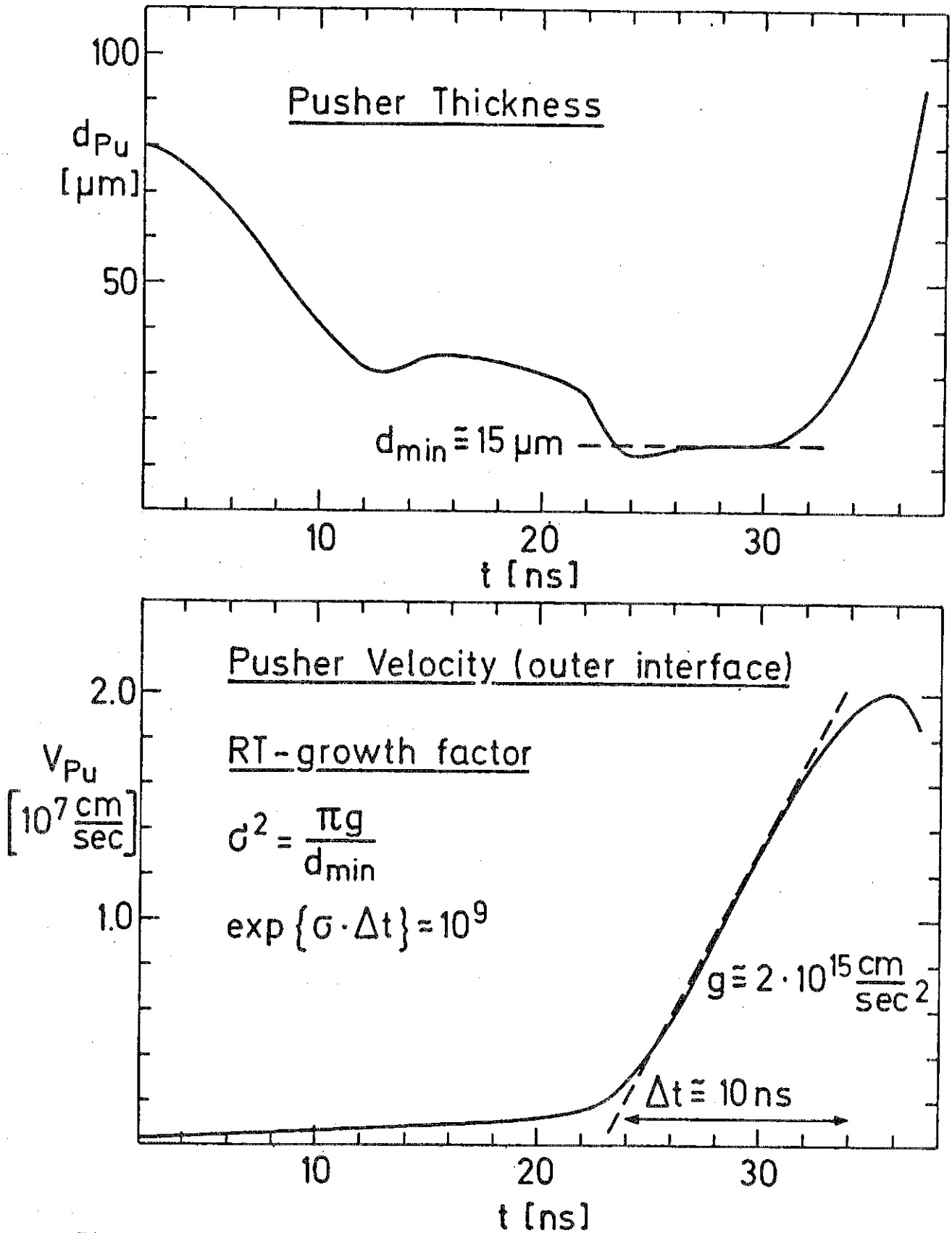

Fig. III.2-18: Pusher thickness and velocity of the pusher/fuel interface as a function of time.

a short rise time of the main pulse. A general experience with these heavy reactor targets is that it is easy, at least in 1D-calculations, to obtain high compression in terms of (ϱR), but it is difficult to achieve high enough temperatures in the centre. The ignition requirement sets the lower bound for the beam power. Certainly more power than 240 TW is needed to make the present design less sensitive to the pulse shape.

III.2.3.4.5 Estimated growth of Rayleigh-Taylor instability

Symmetry is an even more critical point than ignition. A rough estimate shows that the present design fails due to RT-instability. The pusher region is probably not thick enough to survive this fluid instability. Since no 2-dimensional code was available to follow the evolution of the instability in detail, the growth rate has been estimated by applying linear RT-theory for an incompressible fluid. The ingredients for our analysis are given in Fig. III.2-18. The upper plot shows the evolution of pusher thickness with time. It is seen that the pusher is strongly compressed during implosion and has a thickness $d_{min} \cong 15$ µm at the time of maximum acceleration which amounts to $g \cong 2 \times 10^{15}$ cm/sec^2 as seen from the velocity plot in Fig. III.2-18. The pusher is subject to RT-instability, since it has high density and is accelerated by low density absorber material. The density gradient at the interface is very steep (compare Figs. III.2-16b-e), and the Atwood number is $\cong 1$. We have chosen $k_{crit} \cong \pi / d_{min}$ for the wave number of the most critical mode. The exponential growth rate

$$\sigma = (\pi g / d_{min})^{1/2}$$

then leads to an estimated growth factor

$$\exp\{\sigma \cdot \Delta t\} \cong 10^9$$

taking as the relevant implosion time $\Delta t \cong 10$ nsec. Such a growth rate will certainly destroy the symmetry of the pusher during implosion and will prevent burn. According to the simple analysis, a pusher 4 times as thick would lead to a growth factor of $\approx 10^5$ which might be tolerable.[21] It may be that these formulas of linear RT-theory overestimate the growth of the instability and that nonlinear effects (see e.g. ref. 22) not taken into account here improve the situation. But there is little doubt that symmetry is a most critical issue in this design. A more massive pusher may help, although it will be compressed to higher densities and the thickness at maximum acceleration will not increase linearly with mass. Also, a more massive pusher will require more beam power for implosion. The symmetry problem has to be studied in much more detail including the question of initial perturbations and irradiation asymmetry.

III.2.4. Conclusion

A pellet design for heavy ion beam fusion has been presented displaying the different stages of implosion and describing the physical mechanisms such as beam deposition, the relation between pulse shape, shock evolution and ignition, and also pusher dynamics and implosion symmetry. An elementary version of heavy ion stopping theory has been outlined, studying in particular the temperature dependence of stopping powers and ranges. In addition, a gain model has been developed which is based on the results of the explicit design and allows for scaling

of various parameters. It produces gain curves similar to those obtained by the Livermore group and provides a physical interpretation. The model differs from that of Kidder and Bodner in the assumption of constant pressure over the fuel at ignition.

With respect to HIBALL, the gain model yields the HIBALL working point with a gain of 83 at an input energy of 4.8 MJ in a natural way. It corresponds to a hydrodynamic efficiency of 5 % and a compressed fuel isentrope of $\alpha = 2$ in close agreement with the explicit design. Concerning the beam power, however, the code calculation indicates that 240 TW, assumed for HIBALL so far, are insufficient to insure a stable and igniting implosion. The present design achieves ignition at 240 TW only with a highly optimized pulse and will not survive RT-instability. It requires more beam power to improve on both points. Also, consideration of a more realistic equation of state and of radiation losses will increase the requirements on beam power, probably to a level of 500 TW. A final remark should be made with respect to the pulse shape. It has turned out that a carefully timed prepulse is important for effective ignition and should be taken into account in the general HIBALL design.

References

1. S. Bodner, NRL Memorandum Report 4453 (1981).

2. R.E. Kidder, Nucl. Fus. 16 (1976) 405.

3. R.E. Kidder, Nucl. Fus. 19 (1979) 223.

4. J.H. Nuckolls, in LLL Laser Program Annual Report 1979, vol. 2, p. 3-2.

5. H. Geissel, T. Kitahara, Y. Laichter, and P. Armbruster, 'Stopping powers of 0.2-1.4 MeV/u heavy ions in solids', preprint GSI Darmstadt (1980).

6. R. Bimbot, D. Gardes, H. Geissel, T. Kitahara, P. Armbruster, A. Fleury, F. Hubert, Nucl. Instr. Meth. 174 (1980) 231.

7. L.C. Northcliffe and R.F. Schilling, Nuclear Data Tables A7 (1970) 233.

8. F. Hubert, A. Fleury, R. Bimbot, D. Gardes, Ann. Phys. (Fr.) 5 (1980) 1.

9. R.O. Bangerter, Proc. Heavy Ion Fusion Workshop, Report ANL-79-41, p. 415 (1979).

10. D. Jackson, 'Classical Electrodynamics' p. 641ff, Wiley, New York (1975).

11. T.A. Mehlhorn, Report Sand 80-0038 (1980).

12. K.A. Brueckner and N. Metzler, 'Stopping power for energetic ions in solids and plasmas', preprint UCSD (1980).

13. J.E. Rogerson, NRL Memorandum Report 4485 (1981).

14. V.S. Nikolaev and I.S. Dmitriev, Phys. Lett. 28A (1968) 277.

15. K.A. Brueckner, N. Metzler, and R. Janda, Phys. Fluids 24 (1981) 964.

16. K.A. Brueckner and N. Metzler, 'Targets for heavy ion fusion', preprint UCSD (1980).

17. J.D. Lindl and R.O. Bangerter, Report UCRL (1980).

18. R.O. Bangerter and D.J. Meeker, Report UCRL 78474 (1976).

19. S. Jorna, N. Metzler, and P. Hammerling, Phys. Lett. 80A (1980) 308.

20. J.P. Christiansen, D.E.T.F. Ashby, and K.V. Roberts, Comp. Phys. Commun. 7 (1974) 271.

21. R.O. Bangerter, J.D. Lindl, C.E. Max, and W.C. Mead, Report UCRL 77 048 (1975).

22. Ril. McCrory, L. Montierth, R.L. Morse, C.P. Verdon, Phys. Lett. 46 (1981) 336.

III.3 Target Design at KfK

III.3.1 Introduction

At the Institute for Neutron Physics and Reactor Technology, an advanced and extended version of the MEDUSA code is being used to design targets for the ICF reactor study, HIBALL. The design of targets for ICF is a very complicated and involved problem and therefore use of a large computer code such as MEDUSA is essential. In order to be credible such a code must be carefully written and extensively tested on benchmark problems. The original version of the MEDUSA code was written by Christianson, Roberts, and Ashby [3] at the Culham Laboratory, England. The code has been extended by Evans and Bell[4,5] of the Rutherford Laboratory (EOS, fast electron transport, etc.), and Tahir and Laing[6,7] of Glasgow University (radiation transport, ionization, etc.). Further extensions have been made by Tahir and Long[1,2] at KfK, Karlsruhe, in order to transform the code into a fusion design code (multi-shell hollow targets, radiation transport, ionization for heavy elements, etc.) for ion beam fusion, and heavy ion beam fusion in particular. In section III.3.2 the physics and numerical techniques of MEDUSA are presented. In this section the importance of realistic physics for accurate and meaningful simulations is stressed, in particular the fact that a realistic EOS is essential. In section III.3.3 the effect of radiation transport on target simulations is discussed. The energy deposition of ions in hot plasmas is treated in section III.3.4, and in particular the deposition profile in the HIBALL target is presented. Extensive simulation studies of various targets have been carried out during the last year. First of all calculations of a target proposed by Bangerter for light ions are presented. The computer code MEDUSA has been used to reproduce these calculations done at Livermore around 1976, which establishes the credibility of the code as a target design code.

Finally, the HIBALL target has been simulated and first results are presented in section III.3.5. Various conclusions are drawn from these calculations and these are given in section III.3.6.

III.3.2 The Physics and Numerical Methods in MEDUSA

The MEDUSA codes is a well-known and well-tested code, because an intermediate version of the code has been published. The code, however, has been improved and extended in many ways since this version appeared. The physics in the code is as follows,

1. The code is a one-dimensional Lagrangian code which calculates plane, cylindrical and spherical geometry.
2. It is a THREE temperature code, one temperature each for ions, electrons, and thermal radiation. The ions and electrons need separate temperatures in order to give a correct treatment of shock heating. During the burn phase the ion temperature becomes considerably higher than the electron temperature, so this is very important for an accurate study of the physics of the burn phase. It is important also that the radiation field have a separate temperature for reasons explained in section III.3.3.
3. The thermal conduction is due to electrons and radiation and both are flux limited. Flux limited conduction is vital in regions where there are very large temperature gradients, for instance at the outside of the shell and during the burn phase.
4. The code treats any type of multi-shell, multi-material spherical pellet, and can calculate single and double shell targets.
5. Fast electron transport is included as well as a treatment of the ponderomotive force. These facilities are necessary in laser driven targets.

6. Absorption routines for both laser and ion beam fusion are incorporated. At the present time the ion beam deposition is calculated using analytic formulae, in which the range and the deposition profile can be changed.
7. The energy deposition of α-particles produced during the burn is treated locally and the neutrons produced during the burn are allowed to escape freely.
8. The equation of state of the ions is the classical ideal gas EOS. The EOS of the radiation is that of blackbody radiation. The equation of state of the electrons is in general more important than that of the ions because there are more of them. In the original version of MEDUSA the electron equation of state was either that of an ideal gas or of a degenerate or non-denerate (as the case may be) Fermi-Dirac gas. These equations of state have been replaced (although they are still available as options within the code) because they cannot handle problems such as ionization and motion of electrons within the atomic potentials of the ions plus bound electrons. The ionization energy, for instance, represents an important sink of energy which is then not available for compression. Radiation is another such sink, and both these points have been made very strongly by D. Henderson(*) in discussing the dangers of using over-simplified codes. A Thomas-Fermi EOS has therefore been made available and as further sophistication, a corrected Thomas-Fermi model which includes quantum and exchange forces is available. The EOS produces a very good fit to the Los Alamos EOS tables (see Fig. III.3-0), and further allows for the total pressure to be zero at solid densities, so that materials do not expand unphysically when they are cold. Studies that we

*Private communication, "Simple H.I.F. targets are sensitive to physical models".

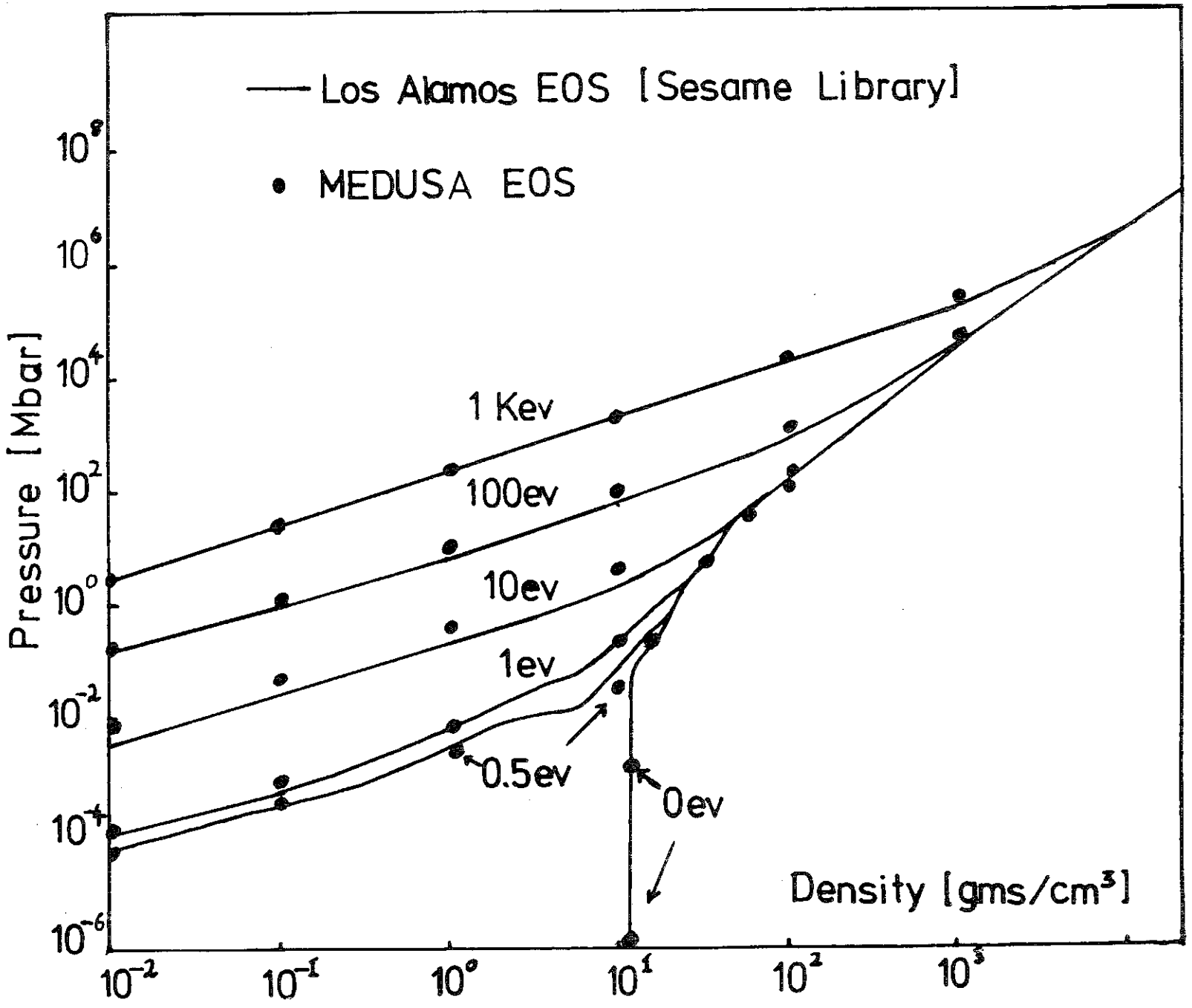

Fig. III.3-0. Equation of state of Lead

have made show that with the use of an ideal EOS, unrealistically high gains can be produced (even without much tuning), which then disappear when the corrected Thomas-Fermi EOS is used.

9. Ionization states are calculated by use of the SAHA equation, and the average ionization $\langle Z \rangle$ and average squared ionization $\langle Z^2 \rangle$ used in various transport coefficients are also calculated by the SAHA routine. The TRIP time dependent ionization and atomic physics package is also incorporated in the code.

The hydrodynamic and energy equations are solved numerically in MEDUSA. The equation of motion is treated explicitly while the energy equations are solved by the Cranck-Nicolson implicit method and Gauss's elimination scheme. Since the energy equations are non-linear, an iterative scheme is used to check the convergence of the numerical solution. Typically 5 to 10 iterations are required for convergence. Since the equation of motion is solved explicitly, the time step must be restricted by the C.F.L. (Courant, Friedrichs, and Levy) condition. For reasons of accuracy, the time step is also monitored by the time variation of T_e and T_i.

A typical MEDUSA run without radiation transport takes up to 15 minutes of CPU time on an IBM 3032 computer when calculating the 4 mg DT HIBALL target. With radiation transport a typical run takes up to 30 minutes.

III.3.3 The Importance of Radiation Transport in ICF Target Simulations

Radiation effects can be of considerable importance in the ICF target simulations for the following reasons.

The thermal radiation produced by the thermal electrons in the absorption region can preheat the fuel and set the compression on a higher adiabat. This could degrade the final fuel density, which in turn, could reduce the target yield.

The thermal radiation may be helpful in smoothing out irradiation asymmetries.

The radiation losses from the target surface can be significantly large and may be reduced by an appropriate target design.

Radiation may be helpful to propagate thermonuclear burn from the ignition region into the surrounding dense and relatively cold fuel.

From the above considerations it is clear that the radiation can influence the compression and the burn propagation in an ICF target. It is, therefore, very important to include a radiation transport model in the hydrodynamic code, when designing a target for a reactor study. The updated version of the computer code MEDUSA used at KfK includes a steady state, single group radiation diffusion model which can simulate transport of total continuum radiation arising from free-free and free-bound transitions taking place in the plasma. This model has been developed by Tahir et al.[6,8] to simulate radiative preheat effects in laser-compression experiments performed at the Central Laser Facility, Rutherford Laboratory. Some typical results are published in ref. 9 and 10.

It is to be noted that the applicability of the above model requires that the radiation field is in local thermal equilibrium with the electrons. This assumption is valid in the target core but does not hold in the corona region. In the latter region the radiation field may be accurately represented by a multi-group radiation model. In general, multi-group radiation transport models involve a large amount of CPU time. When such a model is included in a hydrodynamic code, the CPU time requirements for the target simulations become prohibitively large. Tahir et al.[12] have proposed a multi-group treatment of radiation transport which will make use of the ICCG[11] numerical methods and will be very efficient compared to the standard

multi-group models. The entire radiation field in this model is divided into a large number of groups (typically 20) which transport radiation energy in real space as well as in energy space. Diffusion in energy space takes place via electron-radiation interaction.

This model is being developed at KfK in collaboration with the Central Laser Facility, Rutherford Laboratory. We will incorporate this model into MEDUSA in order to take account of various radiation effects and to design a target for the HIBALL II reactor study.

III.3.4 Energy Deposition in the HIBALL Target. The Energy Deposition Code GORGON

The distinguishing feature of ion beam fusion is, of course, that the energy is deposited by ions rather than from a laser. The original MEDUSA code was written as a laser fusion code and therefore modifications have to be made in order to transform it into an ion beam target design code. This is being done in two stages. The first stage consisted of using simple analytic formulae for $\frac{1}{\rho}dE/dx$ and these formulae are cold formulae. However, one could expect that energy deposition would change considerable as the material heats up and forms a plasma consisting of free electrons and partially ionized atoms, since scattering from ions and electrons could be expected to be different than from neutral atoms. Hence one needs to develop a code based on a definite physical model that can calculate $\frac{1}{\rho}dE/dx$ as a function of density and temperature within the ranges of interest namely, 0 to 500 eV and ρ_s and $\rho_s/100$. Then as a beam of ions is incident on a target, energy loss in each cell can be calculated as a function of the thermodynamic state of that cell, and this energy loss is then subtracted from the ion energy and the new energy is used to calculate dE/dx in the next cell. This procedure is continued until the ion energy is zero which then defines the range. The ranges of protons

in the 2 to 10 MeV range and heavy ions in the range 5 to 20 GeV are such that they are very well-suited to imploding targets of the size to be encountered in I.C.F. This is not really surprising when one realizes that the lower bound of the mass of DT in the target is fixed by the requirement that the hot burning target should re-absorb the α-particles emitted in the DT reaction.[29] The upper bound is of course fixed by the size of the micro-explosion that can be contained in a reactor chamber. A typical range for Bi^{++} in lead is ~ 0·3 g/cm^2 or 0.3 mm, for a 10 GeV ion, whereas shell thicknesses for fusion targets are of the order of 0.5 mm.

An energy deposition code, GORGON, based on refs. 14 and 15 has been developed including modifications and extensions described below which are designed to deal with various physical effects. An ion travelling through a charged plasma loses energy mainly to the electrons,[16] by a series of small angle collisions. In each individual collision the amount of energy lost is very small, but because of the long range of the electrostatic forces, there are very many such collisions, so the total energy loss is quite large. The mass of the ion is much larger than the mass of the electron, so that the ion is deflected through small angles and one can consider the ion as travelling in a straight line. The projectile ion is further considered to be a point charge with specified energy, mass and charge (which may change with velocity, see below). The plasma is considered to be either degenerate or non-degenerate as the case may be.

The physical model used in the calculation is based on the distinction between the contribution of bound and free electrons in the target plasma. Free electrons are those having a wave function that extends to infinity (i.e., $\sim e^{i\underline{k}\,\underline{r}}$) and bound electrons are those whose wave function goes as e^{-kr} at large r, therefore not having infinite extent.

The contribution of the bound electrons to the stopping power is calculated according to Bethe's theory[17], taking into account the differences in characteristic excitation energies between a neutral atom and a plasma ion via the Thomas-Fermi model. The contribution of the free electrons is calculated using the dielectric theory for non-degenerate electrons with a more simplified theory being used if the electrons are degenerate.

Calculation of the plasma parameters:

In the model used in this calculation knowledge of the average degree of ionization in the plasma is required, because of the separate treatment of bound and free electrons. This is done using the Thomas-Fermi model of the atom at finite temperature. For this purpose the Thomas-Fermi model is solved using the methods described by Latter[18], which yields values for the electron density distribution in the atomic sphere n(r) for a given density and temperature of the target material, as well as the potential V(r) and the chemical potential α. The number of bound electrons which yields the average degree of ionization is given in the Thomas-Fermi model by,

$$N_b = \frac{32\pi^2}{h^3} \int_{-\infty}^{0} \frac{dE}{[\exp(E-\alpha)/kT + 1]} \int_0^{r(E)} m[2m(E+eV(r))]^{1/2} r^2 dr \qquad \text{(III.3-1)}$$

where E is the total electron energy, m is the electron mass, T is the temperature, k is Boltzmann's constant, h is Planck's constant and r(E) is the radius which satisfies the condition,

$$eV(r(E)) = - E \qquad \text{(III.3-2)}$$

i.e., where the kinetic energy of the electron just equals its potential energy. From the number of bound electrons the number and density of the free

electrons are determined and used in the calculation of the stopping power due to the plasma free electrons. The calculated structure of the ions is used to determine the bound electrons contribution to the stopping power.

Stopping power due to bound electrons:

The contribution of bound electrons to the stopping power is calculated by Bethe's theory[19], including corrections due to the differences between a plasma ion and a neutral atom. The basic physical parameter is the average excitation energy I, defined by

$$\ell nI = \frac{1}{N} \sum_i \ln(\hbar\omega_i) \qquad \text{(III.3-3)}$$

where N is the number of bound electrons participating in the slowing down process and $\hbar\omega_i$ are the characteristic excitation energies. In these calculations the ω_i's are interpreted as the frequencies of revolution, following Bohr's model[20]. In order to calculate I within the framework of the Thomas-Fermi model one notes that at each radius r, a spectrum of revolution frequencies is determined by the Fermi energy distribution at this radius

$$\omega(r) = [(2/m)\{E + eV(r)\}]^{1/2}/r \qquad \text{(III.3-4)}$$

Here E is the total electron energy. The number of electrons per unit frequency having a revolution frequency ω is,

$$n(\omega) = (32\pi^2\omega^2m^2/h^3)$$

$$\times \int_0^{r_{max}(\omega)} r^5 \left(\exp\{[\tfrac{1}{2} m\omega^2r^2 - eV(r) - \alpha]/kT\} + 1\right)^{-1} dr \qquad \text{(III.3-5)}$$

Here $r_{max}(\omega)$ is the radius beyond which the energy which corresponds to ω yields a free electron, i.e.,

$$eV(r_{max}(\omega)) = - E \qquad \text{(III.3-6)}$$

The effective excitation energy is given, within the framework of this model, by

$$\ln I = \frac{1}{N} \int_0^\infty n(\omega) \ell n(\hbar\omega) d\omega \qquad \text{(III.3-7)}$$

A shell correction is included in the calculation by eliminating from the integration in Eqn. (3-7) those electrons for which

$$2mv^2 < \hbar\omega \qquad \text{(III.3-8)}$$

where v is the projectile velocity.

The solution of the Thomas-Fermi model, provides the required values of V(r) (the potential), α (the chemical potential) and n(r) the electron density required in the above integrations.

Stopping power due to free electrons:

The free electron contribution to the stopping power is calculated using the plasma dielectric theory[21,22,23]. The energy loss is given by,

$$\frac{dE}{ds} = - \frac{2e^2 Z^2_{eff}}{\pi\rho} \int_0^\infty k dk \int_0^1 \mu d\mu \ \mathrm{Im} \left(\frac{1}{D(k, \omega = k\mu v)}\right) \qquad \text{(III.3-9)}$$

where ρ is the density, $s = \rho x$ where x is a distance into the material, v is the projectile velocity, k is the wave number, $\mu = \cos\Theta = \underline{k} \cdot \underline{v} / |\underline{k} \cdot \underline{v}|$ D is the dielectric function of the plasma and ω is the frequency. In calculating the

dielectric function a classical, non-degenerate plasma is assumed and collisions in the plasma are taken into account. The collision time is given by,

$$\tau = 3m^{1/2}(kT)^{3/2}\,[4(2\pi)^{1/2}e^4 Z_{eff} n\ell n\Lambda]^{-1} \qquad \text{(III.3-10)}$$

where n is the free electron density, Z_{eff} is the average ion charge, $\ell n\Lambda$ is the Coulomb logarithm. The dielectric function is given by

$$D(k,\omega) = 1 + 2x^2\{1 + xZ(\xi)\}\omega_p^2/\omega^2 \qquad \text{(III.3.11)}$$

where $\xi = x+iy$, $Z(\xi)$ is the plasma dispersion function, $x = \omega/kV_t$, $y = \nu/kV_t$, ν is the collision frequency, V_t is the free electron thermal velocity, $V_t = (\frac{2kT}{m})^{1/2}$. An upper cutoff wave number is used in the integration in eqn. 3-9 following Bethe[19],

$$k_B^{-1} = e^{-\gamma}\hbar/mV_t$$
$$\gamma = 0.5772 \qquad \text{(III.3-12)}$$

Certain additions have been made recently in order to improve the physics in the code and to allow the code to calculate stopping powers for heavy ions. The model now includes an option which allows the calculation of the stopping power of ions in degenerate electrons. This is an important factor for calculating the cold range in metals where up to 5 electrons/atom can be degenerate. Experimental results exist only at room temperature, so the calculations are calibrated on cold material, and it is therefore important to calculate correctly in this limit. The code, as described above, calculates the stopping power of protons very well because the charge on the proton does not change as it passes through the plasma. In principle it could capture an

electron to become a neutral hydrogen atom but since the binding energy is only 13 eV collisions with electrons would prevent this. However for heavy ions say Bi^{++}, entering a plasma, collisional ionization occurs, as does recombination. This is a dynamic process and it takes time for the ion to reach a steady state effective charge when it is travelling at a constant velocity. However, since the velocity is changing continuously it is not clear that the charge state ever reaches a steady state, and it is likely that the effective charge problem should be treated as a dynamic problem. For simplicity in the code at the moment a steady state effective charge formula is used, which is derived by comparing the "cold" experimental results to the Bethe formula. The effective charge is the given by,(24)

$$Z_{eff} = Z_B[1 - 1.034 \exp(-137\beta/(Z_B)^{0.69})] \qquad \text{(III.3-13)}$$

where Z_B is the charge on the ions on the beam, v is the velocity of the ion, and $\beta = v/c$, where c is the velocity of light.

A general formula for dE/dx has the form (from bound electrons),

$$\frac{dE}{dx} = Z_{eff}^2 \omega_p^2 \frac{e^2}{v^2} \quad L \qquad \text{(III.3-14)}$$

where ω_p is the plasma frequency, v is the velocity of the ion, and e is the electron charge. In Bethe's formula L has the form,

$$L_{BETHE} = \ell n \{\frac{2mv^2}{\hbar\omega}\} - \ln(1 - \beta^2) - \beta^2 \qquad \text{(III.3-15)}$$

where $\hbar\omega = I$ is defined above, and m is the electron mass. On the other hand, the classical expression derived by Bohr is given by,

$$L_{BOHR} = \ell n \left(\frac{1.123mv^3}{Z_{eff}e^2\omega}\right) - 1n(1 - \beta^2) - \beta^2/2 \qquad \text{(III.3-16)}$$

A quantum mechanical expression derived by Bloch[13] who attempted to reconcile the two approaches is given by,

$$L_{BLOCH} = \ln \frac{2mv^2}{\hbar\omega} - \frac{1}{2} \ln(1 - \beta^2) - \beta^2/2$$

$$+ \psi(1) - Re\psi\ (1 + iZ_{eff}\alpha/\beta) \qquad \text{(III.3-17)}$$

where ψ is the diagamma function, and α is the fine structure constant.

The Bohr approach is one which uses classical mechanics, and is based on the use of any impact parameter b. For b greater than some impact parameter b_1 collisions are treated as electromagnetic excitations of harmonic oscillators in a constant electric field produced by the passing ion. For $b < b_1$, ions are assumed to scatter from the electrons as if the electrons were free. The Bethe approach uses quantum mechanics and therefore uses momentum transfer to characterize collisions. It considers the ion wave function to be a plane wave of given momentum and treats the ion-atom scattering within the Born approximation. The Bloch approach reconciles these two theories. Block demonstrates that the distant collision part of the Bohr theory is valid quantum mechanically within the dipole approximation. Bloch again assumed that for $b < b_1$ the electrons are free, but relaxed the assumption that the ion should be described by a plane wave. The confinement of the electron within a cylinder of radius b_1 introduces transverse momentum components which interfere with each other under the influence of the scattering potential.

This leads to a scattering cross section which can be very different from the Coulomb cross sections for plane waves.

For very weak scattering b_1 can be large, and plane waves can be used and the Bloch formula tends to the Bethe formula. In the limit of strong scattering wave packets can be constructed which scatter as classical objects and the Bloch formula gives the same results as obtained by Bohr. This happens especially when Z_{eff} is large. In the code the problem is solved by using the larger of two minimum impact parameters, one the quantum impact parameter $\frac{h}{2mv}$ and the other the Bohr impact parameter $(\frac{e^2 Z_{eff}}{mv^2})$, where v is the relative speed between ions and electrons. This effectively changes the Bethe formula over to the Bohr formula.

Another change to the code that has been made, is to include the scattering of the ion off the ions in the plasma. The standard expression originally developed by Chandrasekhar[25] is used. The code can calculate for any type of ion (from hydrogen to uranium) and on any type single element target material, and can be extended to treat mixtures in a simple approximation. Since the code can calculate energy deposition for an ion passing through a degenerate plasma, it can also calculate the energy loss of α particles in degenerate and non-degenerate DT.

The results presented here are confined to those relevant to the HIBALL reactor, and complete results illustrative of the working of the code will be presented elsewhere.[1,26] Figure III.3-1 shows the energy deposition profile of 10 GeV Bismuth ions on lead at 200 eV and in Figure III.3-2 the deposition profile of 10 GeV Bismuth ions in lithium at 200 eV is shown. The deposition profile in the HIBALL target for 10 GeV ions is shown in Figure III.3-3. The range of the ions decreases as the temperature increases from room temperature. Also the deposition profile becomes more peaked at the end of

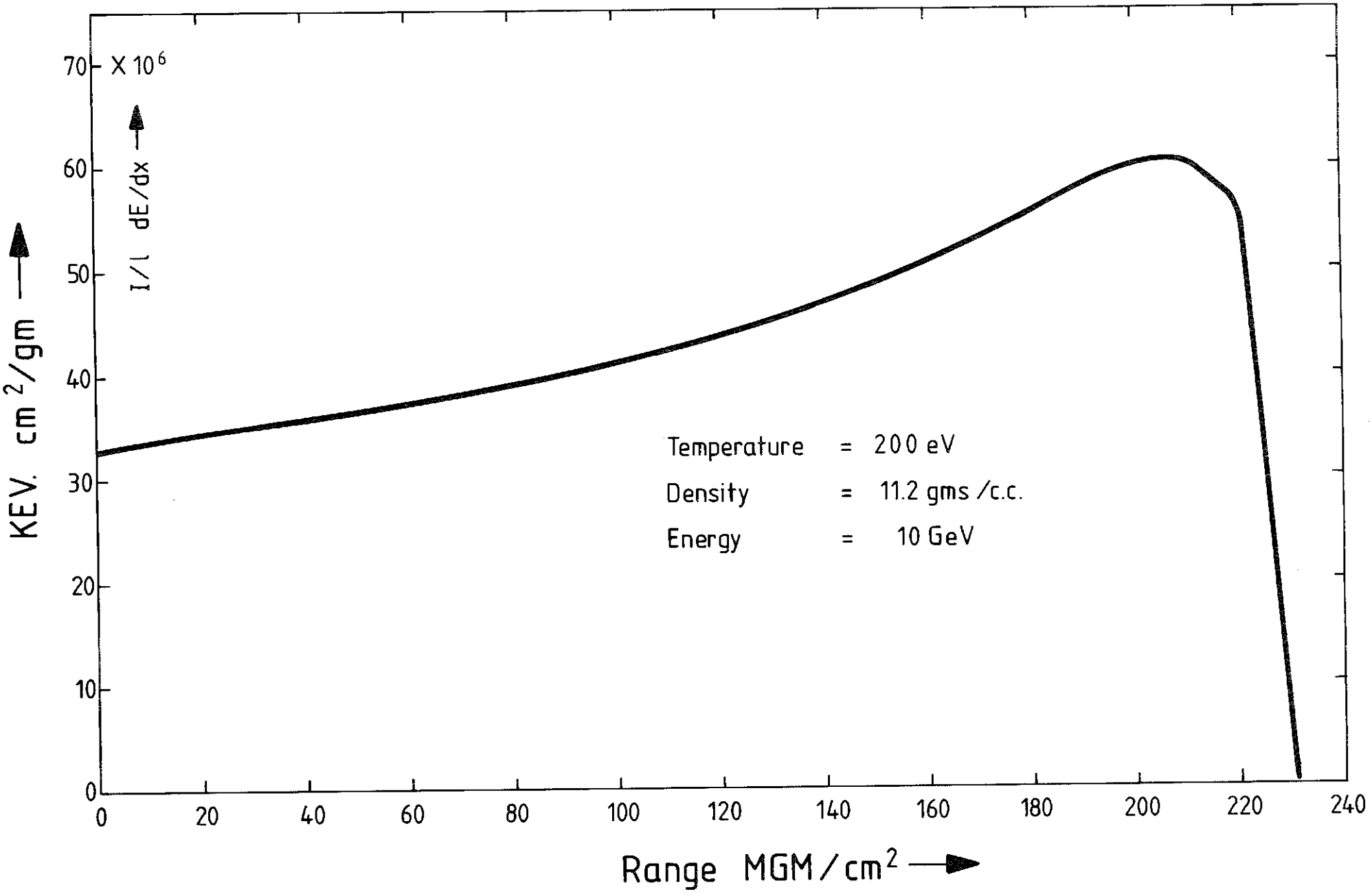

Fig. III·3-1
Stopping power of bismuth ions on lead

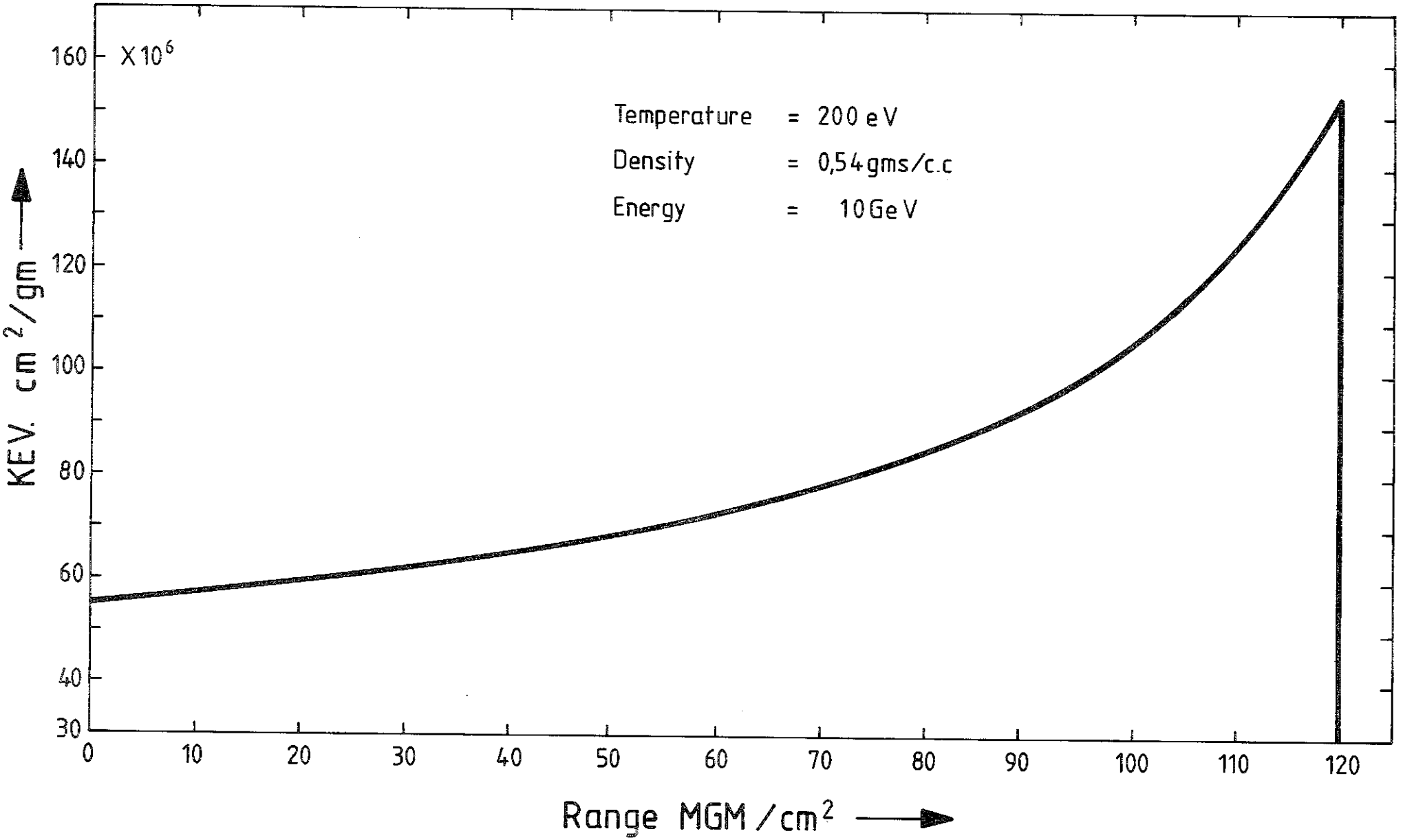

Fig. III·3-2
Stopping power of bismuth ions on lithium

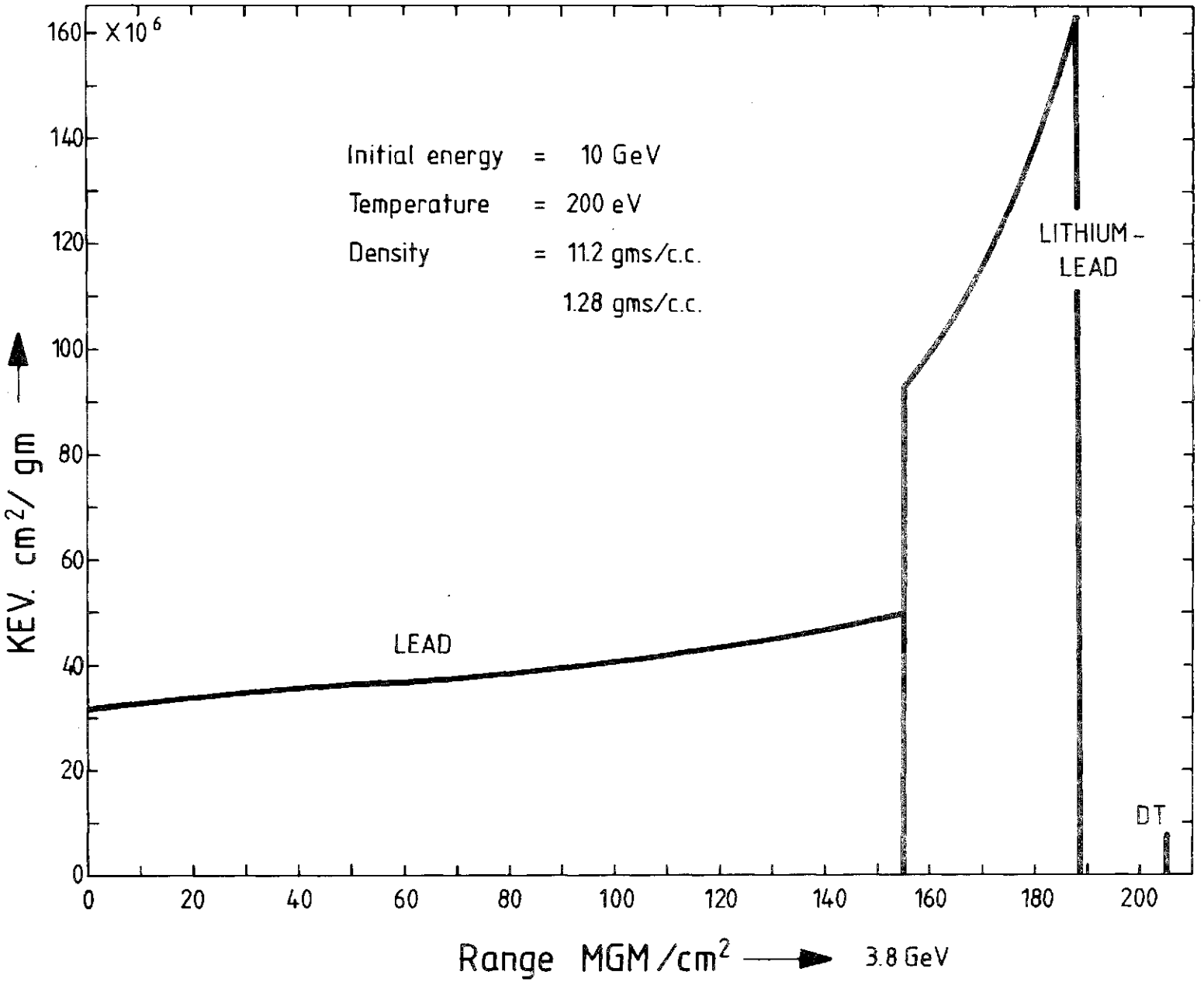

Fig. III·3-3

Bismuth ions on lead and lithium - lead

Hitball pellet

the range as the temperature increases. The reason for this is as follows: At room temperature the energy deposition profile is relatively flat and this comes about because the Bragg peak type profile which would be calculated using Z_B^2 is flattened out by the decrease in Z_{eff}^2 as a function of velocity. As the range is shortened the cutoff occurs at larger values of Z_{eff}^2, so that the flattening effect is much reduced and the Bragg peak starts to reappear. It should be noted here that the peak in the distribution curve always occurs when $V_B \sim V_{el}^{Th}$(the electron thermal velocity), and as the temperature increases so does V_{el}^{Th}, so V_B becomes greater at this point and so does $Z_{eff}(V)$.

In conclusion the assumptions that are inherent in these calculations are briefly considered. The ion is assumed to travel in a straight line and lose energy by small angle scattering to the electrons by excitation and ionization. Hence large angle scattering events are ignored, as these are important only at lower energies. The ions are assumed to slow down independently of each other, that is collective effects (of the beam interaction) are assumed to be absent. This is justified by an argument proposed by Melhorn.[27] For typical beam parameters the interparticle spacing is >100Å, while the relevant shielding distance in both solid and plasma is of the order of 1Å. Hence, in some sense, the particles should not see each other. However this is not the whole story, since one should also consider the time domain. Ions going through a plasma emit plasmons which vibrate with a period $\sim 10^{-17}$ secs. Ions travel typically with a velocity $\sim 3 \times 10^9$ cm/sec, so the time taken to travel 100Å is $\sim 10^{-16}$. Therefore as long as the plasmons are not damped out in ~ 10 oscillations the next ion will see the perturbation produced by the ion in front. Under certain circumstances this could lead to bunching and a coherent motion of the ions, leading to the unstable growth of large amplitude plasma

waves. This could then lead at least to enhanced energy deposition. This effect is currently being investigated to see if such an instability can occur within the parameter space relevant to ICF fusion.

III.3.5 Target Gain Calculations for the HIBALL Reactor Study Using MEDUSA

An ICF target should have a high gain, but there are several other requirements that it should fulfill. The target should be hydrodynamically stable and it should have a reasonable tolerance of irradiation asymmetries. It should also need as low an energy and power as possible to ignite it. Further certain other requirements should be met which do not directly involve target physics considerations. For instance the target should be easy to fabricate and should be made out of relatively cheap materials. It would be desirable that the target produces a minimal amount of radioactivity, that it should be compatible with other materials of the reactor coolant system and finally it should be large enough that the beam can be focussed onto it.

Many of the above requirements impose contradictory constraints. For example, power requirements can be reduced by using shells with large aspect ratio, but such shells are usually unstable.

Bangerter and Meeker[28] proposed a target which fulfills most of the above requirements and is shown in Fig. III.1-2. This is a single shell multi-layered target with a low density, low Z pusher sandwiched between a high density, high Z tamper and the fuel. The heavy tamper serves as a confinement shell to increase the efficiency of implosion. The pusher is seeded with a high Z material to reduce radiative preheat of the fuel. The use of a low density pusher has a number of advantages over a high density pusher. For instance, the pusher can be made relatively thick to reduce hydrodynamic instabilities and yet contain little mass. Also the hydrodynamic instabilities causing pusher-fuel mixing during the final stages of

compression may be eliminated because of the very small density difference between the fuel and the pusher. In addition, this target has a simple structure and is made from inexpensive materials. The simulations of Bangerter and Meeker[28] indicate that in the case of a high Z pusher target comparable to the one shown in Fig. III.1-2, the ρR in the pusher is 10 gm/cm^2. On the other hand, in the present calculations the bulk of the high Z material remains uncompressed and the total ρR of both the pusher and the tamper is less than 1 gm/cm^2. Therefore the latter target would produce less than 10% as much high Z radioactive debris as a target with high Z pushers.

As a first step towards designing the HIBALL target the 1 mg DT Bangerter-Meeker[29] target was simulated at KfK (INR) with the updated version of MEDUSA. To make these calculations computationally simpler the TaCOH pusher was replaced by PbLi, the two have the same mass density and approximately the same electron number density. These results show good agreement with the Bangerter-Meeker results. It is, however, to be noted that a target with 4 mg of DT is required for the HIBALL reactor study. For this purpose the above target has been scaled to a bigger one which contains 4.3 mg of DT in such a way that the two targets have the same aspect ratios. From now on this bigger target will be referred to as the "HIBALL TARGET". Compression, ignition and the burn propagation in this HIBALL target have been simulated. A comparison between the KfK and Bangerter results and results for the 4 mg target are discussed below.

Results

a) 1 mg DT target (Comparison between Bangerter-Meeker and KfK results)

A target very similar to the Bangerter-Meeker[28,29] target, but with PbLi pusher instead of TaCOH, has been simulated using the updated version of MEDUSA. The two materials have the same mass density and approximately same

number of electrons/unit volume. We have used approximately the same deposition profile as in Fig. III.1-4. The pulse shape used in these calculations is shown in Fig. III.3-4 and is relatively simpler compared to the one shown in Fig. III.1-3. A comparison between the KfK results and the Bangerter-Meeker results is given in the following table.

Table III.3-1 Comparison between Livermore and KfK results

	Bangerter-Meeker	KfK
Pulse Energy (MJ)	1.28	2.0
Peak Power (TW)	240	250
Output Energy (MJ)	113	164
Gain	88	84

From the above table it is seen that Meeker and Bangerter have obtained a gain of 88 by using less input energy and practically the same peak power. To get a gain comparable to their value it was necessary to use somewhat higher input energy. The reason for this is that they have used a shaped pulse in their calculations which is designed to minimize shock heating of the fuel. Their target is compressed on a lower adiabat and the input energy requirement is reduced. On the other hand, in the KfK calculations a relatively simpler pulse, shown in Fig. III.3-4 has been used. This pulse shape gives rise to more shock heating of the target and so the compression is placed on a higher adiabat. Consequently, one would require more energy to achieve a high pellet gain. In these calculations 2 MJ input energy is used which compresses the target to give a higher value of ρR as compared to the Bangerter-Meeker calculations. As a consequence one gets larger fractional burnup of DT and more output energy.

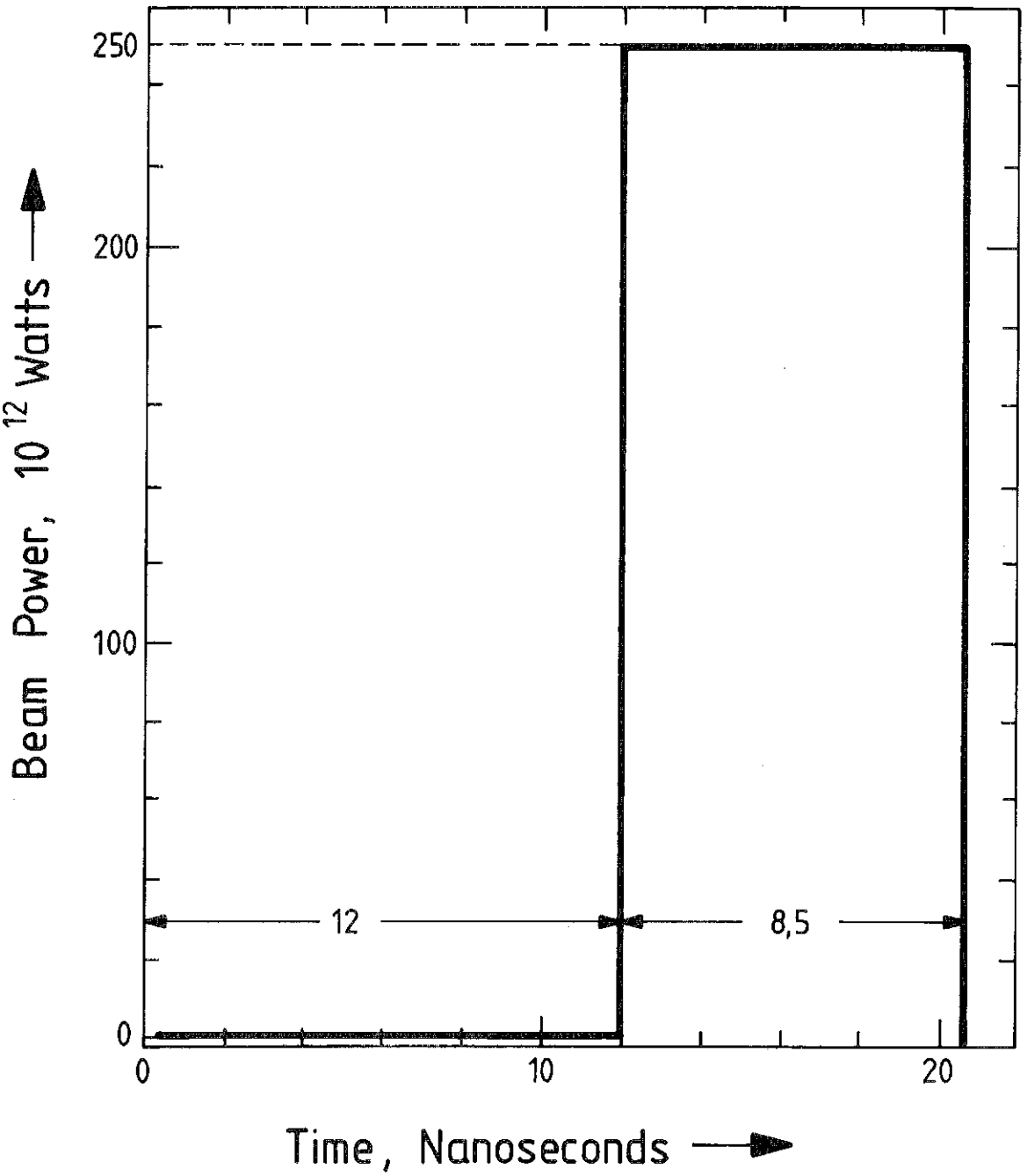

Fig. III·3-4
Beam power as a function of time

It should also be noted that during the final stages of compression the fuel density becomes comparable to the pusher density which is very good for the stability of the pusher-fuel interface. This effect has also been mentioned by Bangerter and Meeker.[28,29]

b) The HIBALL target with 4.3 mg DT

Using the updated version of MEDUSA described in section III.3.2, compression and ignition of the HIBALL target shown in Figure III.3-5 has been simulated. The problem of burn propagation from the central spark region into the surrounding dense and cold fuel has also been studied.

To design an ICF target and tune it for maximum output energy for a possible minimum input energy and power is a very complicated and time consuming problem. The reason for this is that the designer has to work in a multi-dimensional parameter space. The most basic parameter in this space is the type of the target itself which can either be a single shell multi-layered or a composite shell multi-layered target. For the HIBALL target a single shell multi-layered target with the same structural design and aspect ratio as the 1 mg target shown in Fig. III.1-2 has been chosen. The next set of variables which one has to select, are the input energy, the pulse shape and the pulse parameters. Bangerter[29] has mentioned an approximate energy mass scaling relationship according to which one should use 20 to 25 MJ/gm for good target compression. Applying this scaling law the HIBALL target would require 7.5 MJ input energy.

A pulse shape similar to the one shown in Fig. III.3-4 has been used. The choice of correct pulse parameters is another difficult problem. Since each computer run takes about 15 - 20 minutes of the IBM 3032 computer at KfK, it was not possible to vary these parameters blindly (to tune the target). The prepulse and the main pulse lengths were guessed to scale according to

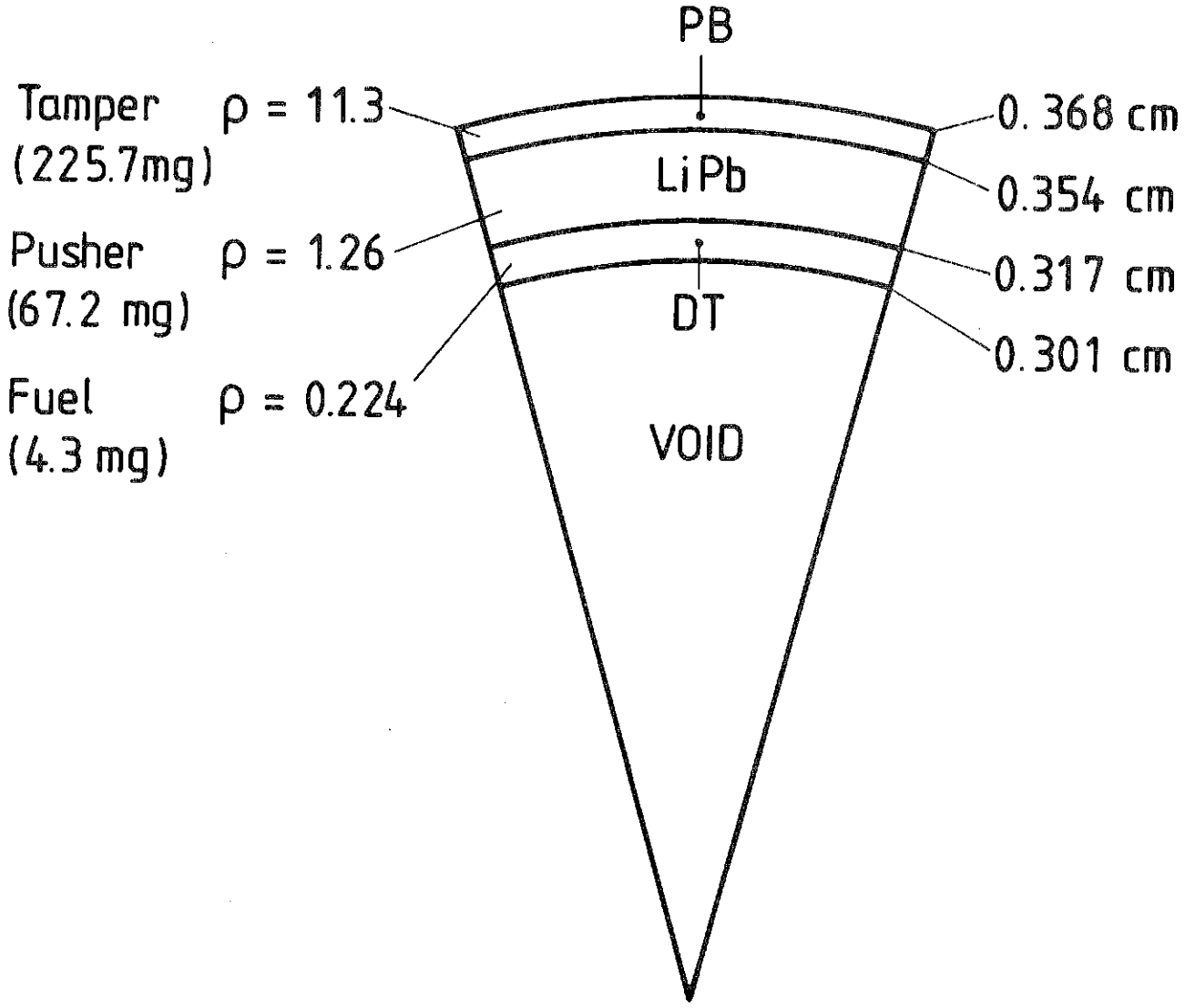
PB
Tamper ρ = 11.3
(225.7mg)
Pusher ρ = 1.26
(67.2 mg)
Fuel ρ = 0.224
(4.3 mg)
LiPb
DT
VOID
0.368 cm
0.354 cm
0.317 cm
0.301 cm

Fig. III · 3-5

$m^{1/3}$ times the corresponding values for 1 mg target. The pulse parameters used in these calculations and the target yield are given in Tables III.3-2 and III.3-3 respectively.

Simple analytic formulae have been used to simulate heavy ion deposition in the pellet. The target conditions at the time of ignition are shown in Fig. III.3-6.

Table III.3-2 Pulse Parameters

Prepulse Power	10 TW
Main Pulse Power	600 TW
Prepulse Length	19 ns
Main Pulse Length	12 ns

Table III.3-3 Input Energy and Target Yield

Pulse Energy (MJ)	7.38
Gain	97
Output Energy (MJ)	715

It is to be noted that these calculations are initial and the performance of this target could be improved substantially by further fine tuning. The target yield can be optimized with less input energy and lower peak power by using a shaped pulse.

It should also be noted that one-dimensional codes cannot treat the hydrodynamic instabilities and the effects arising from non-uniform target illuminations. These effects can be studied by two-dimensional codes. Inclusion of the above two effects may degrade the compression substantially

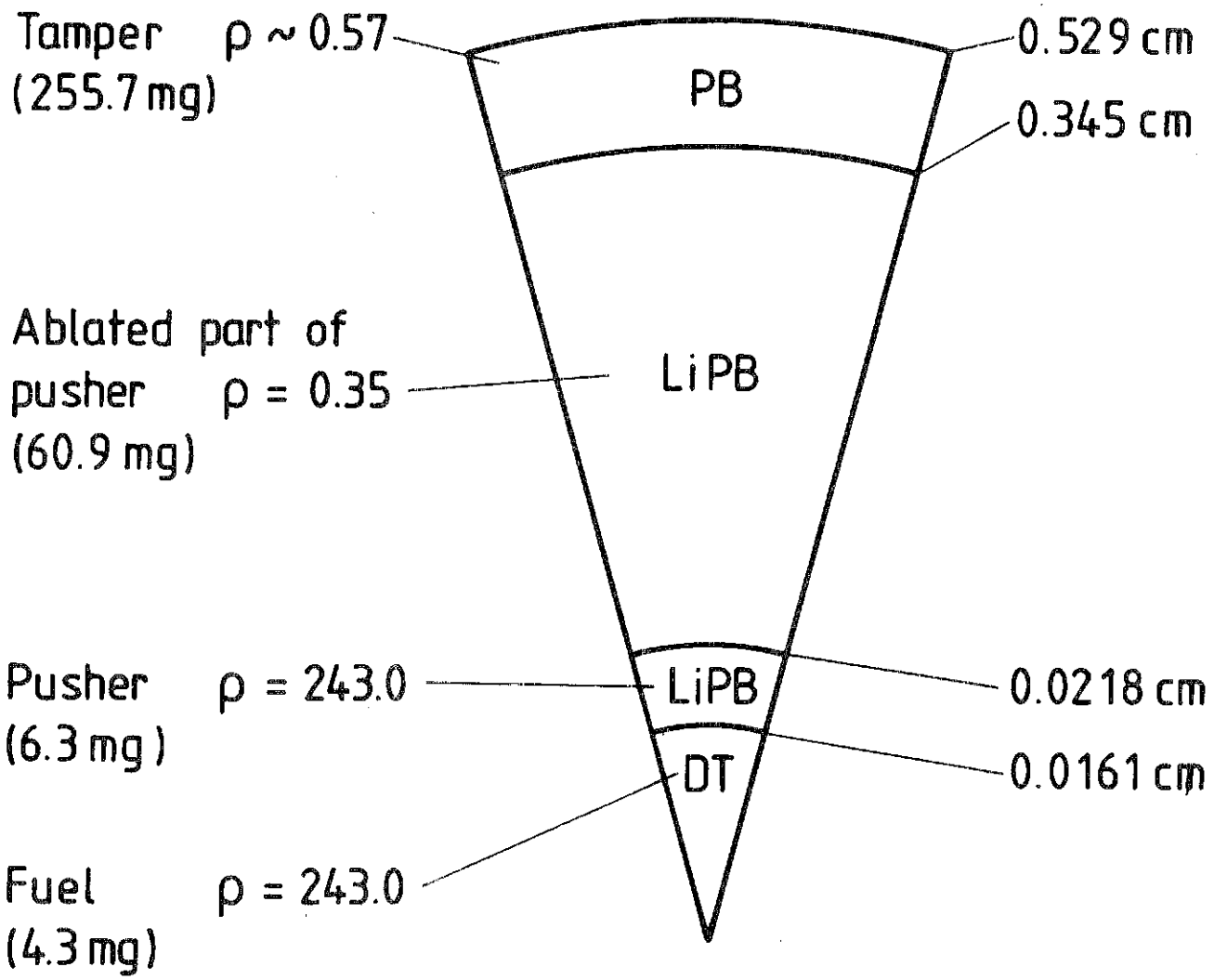
Tamper ρ ~ 0.57
(255.7 mg)
PB
0.529 cm
0.345 cm
Ablated part of
pusher ρ = 0.35
(60.9 mg)
LiPB
Pusher ρ = 243.0
(6.3 mg)
LiPB
0.0218 cm
DT
0.0161 cm
Fuel ρ = 243.0
(4.3 mg)

Fig. III · 3-6

which in turn would reduce the target output. According to Meeker* two-dimensional simulations of a typical target show a reduction in gain by up to a factor of 10 compared to the gain obtained by one-dimensional calculations for the same target.

In Fig. III.3-7 the coordinates for the tamper-pusher and pusher-fuel interfaces are plotted as a function of time, respectively. It is seen that the pusher-fuel interface moves inwards as the target gets compressed and ignition starts at about t = 31.0 ns. This is the time when compression achieves its maximum value and corresponds to the switch off time of the pulse. On the other hand, the tamper-pusher interface maintains a steady position during the burn phase and then moves outwards as the target expands. This is because the tamper is very heavy and it does not move in but holds the pusher and the fuel together for a long enough time for nuclear fusion to take place.

The ignition and burn conditions are given in Figs. III.3-8 to III.3-10. We plot log ρ, log P and log T_i as a function of the target radius at three different times. The solid and broken vertical lines represent the pusher-fuel and the pusher-tamper interfaces, respectively. Fig. III.3-8 is plotted at t = 31 ns when the compression has achieved its maximum value. It is seen that the inner 10% of the fuel is heated to ignition temperature but is at a relatively lower density such that the total pressure in the fuel is constant. Figure III.3-9 is plotted after 130 ps and it shows a pressure peak in the ignited fuel region. This is because the charged particles produced in the nuclear reactions deposit their energy and heat up the fuel to temperatures $\sim 10^8$ K. This pressure peak sends a shock wave into the surrounding fuel and the burn spreads radially throughout the fuel. It is seen from Fig. III.3-10

*D. Meeker, private communication.

III.3-28

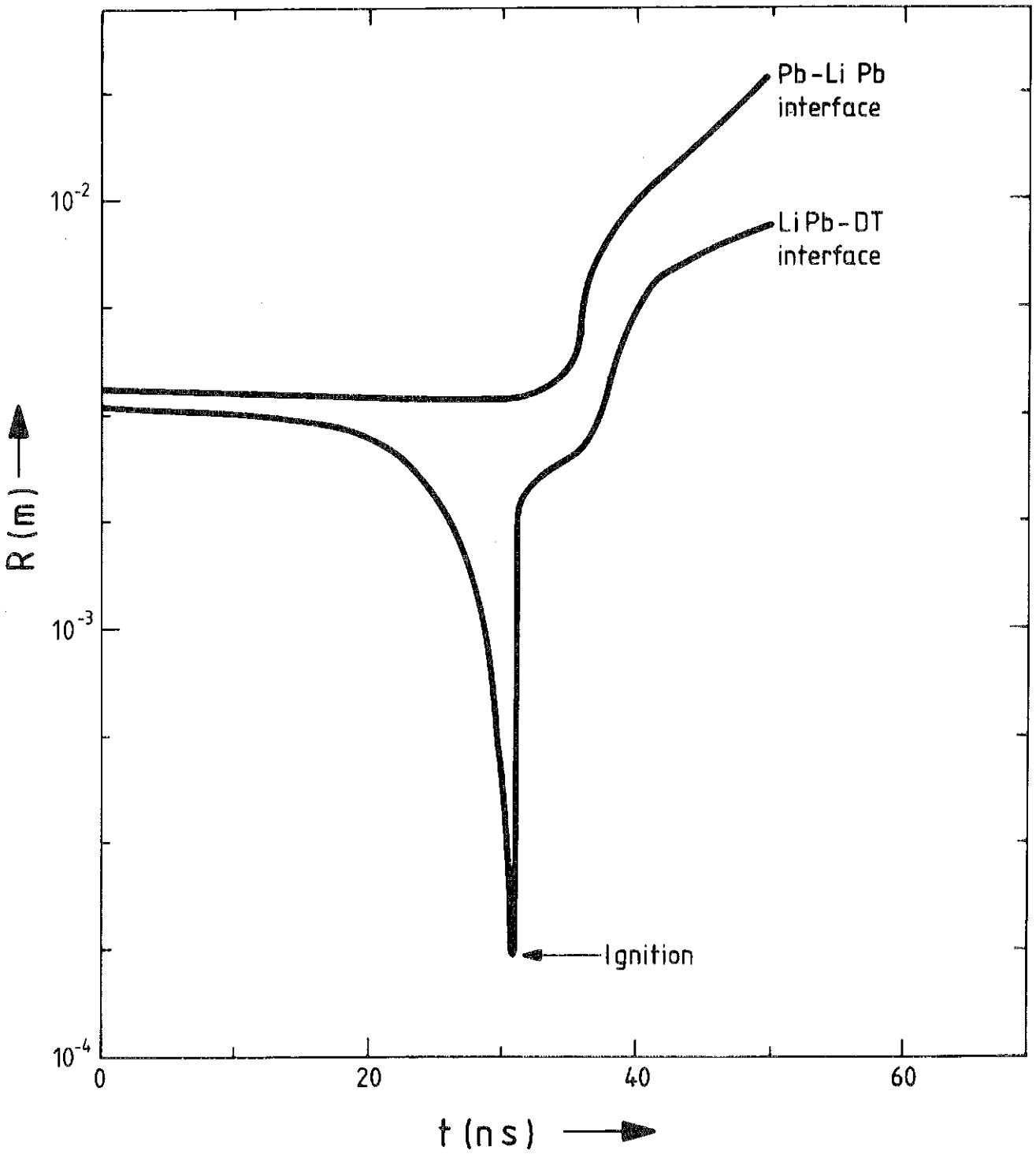

Fig. III·3-7

III.3-29

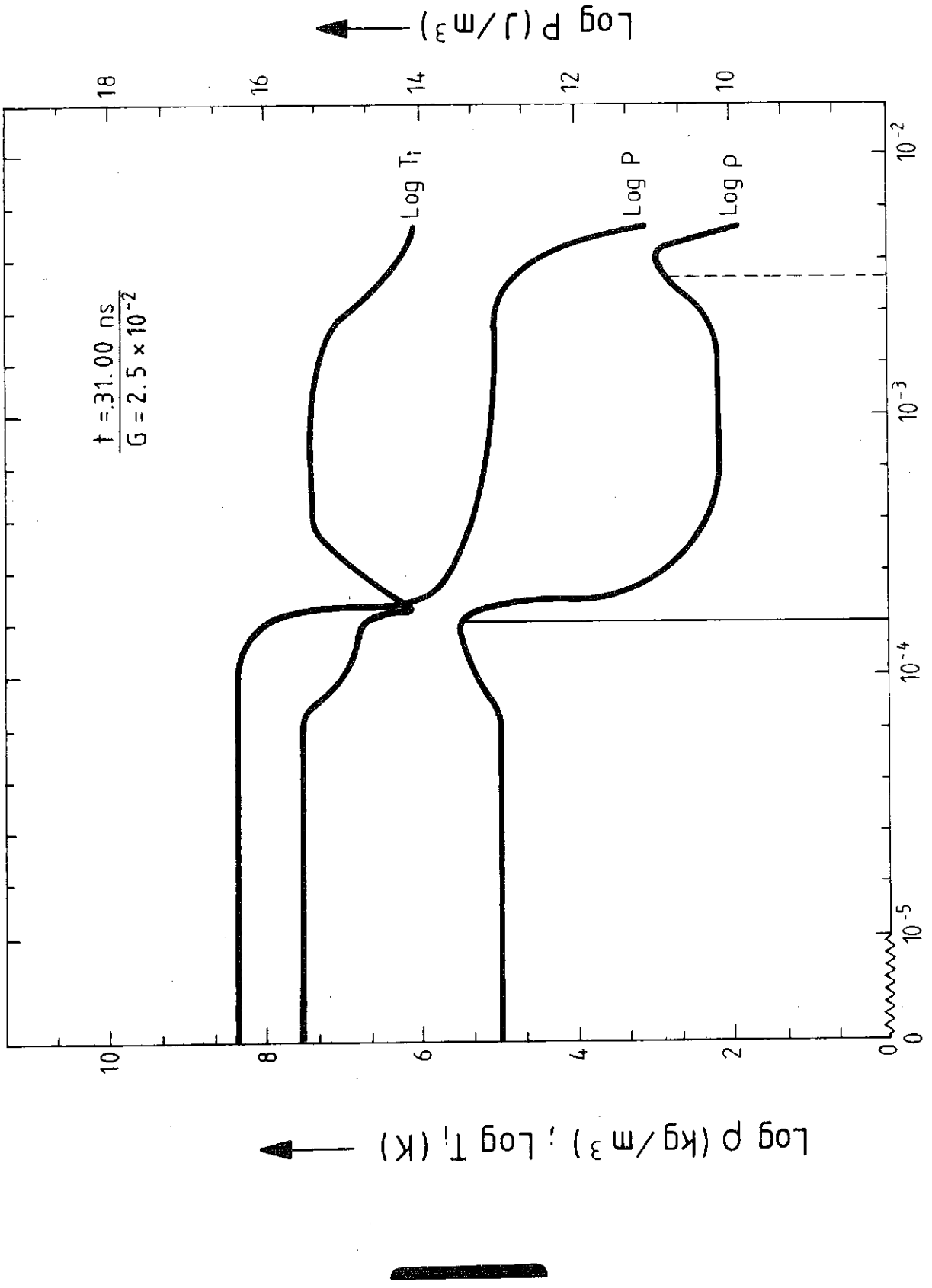

Fig. III·3-8

III.3-30

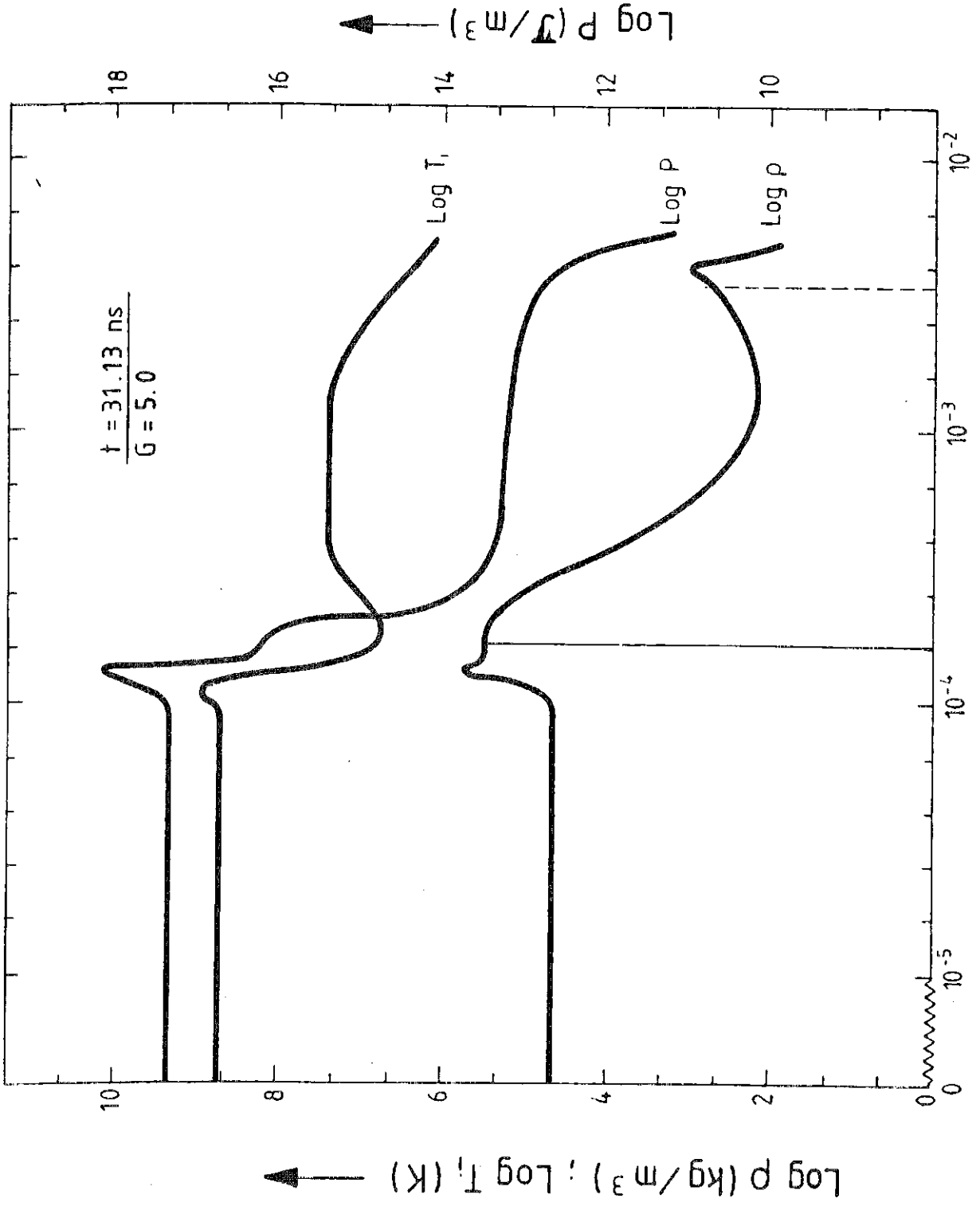

Fig.III.3-9

III.3-31

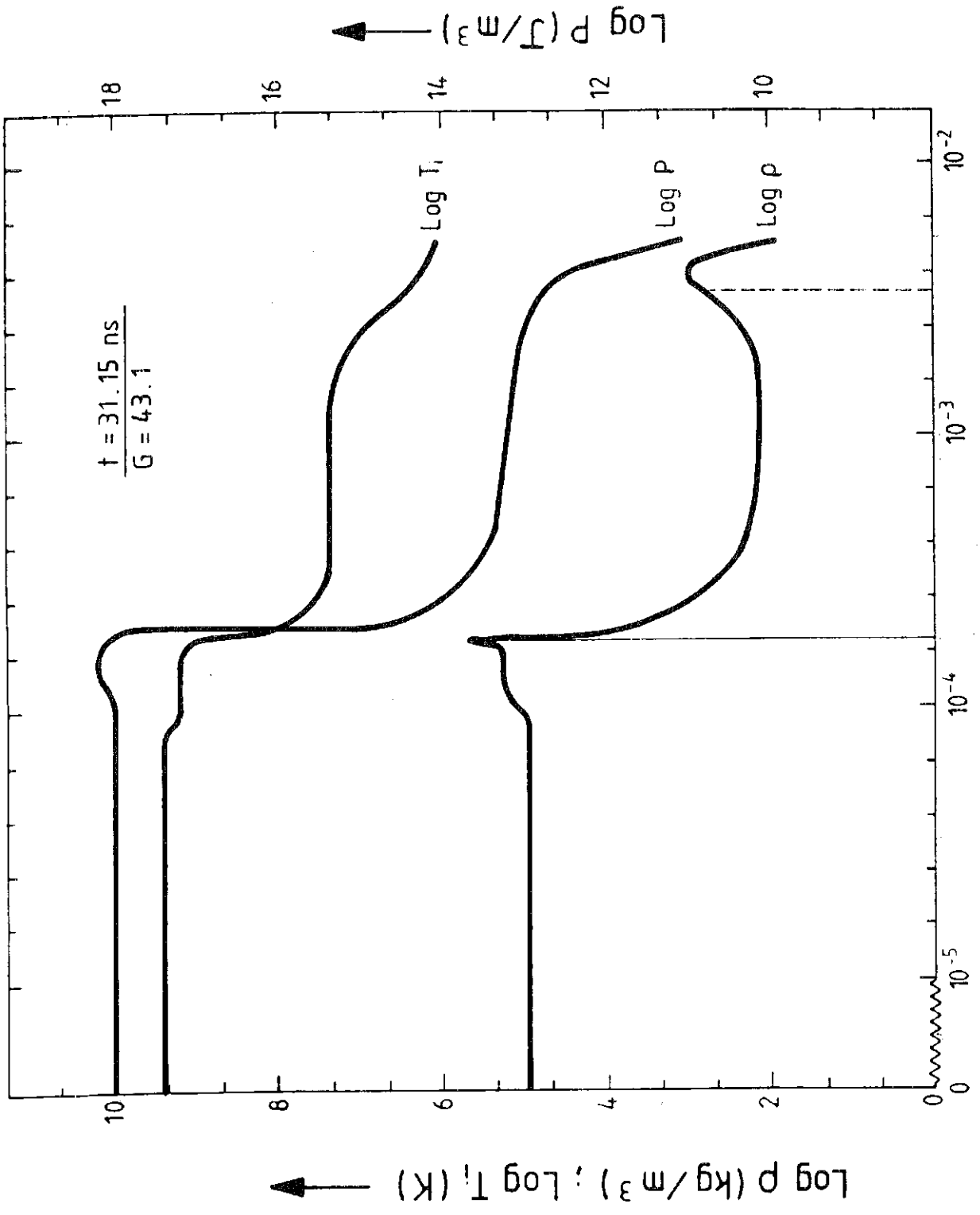

Fig.III.3-10

that after 20 ps the whole of the fuel is heated to a temperature ~ 10^9 K. It should be noted that in these calculations radiation transport effects are excluded because of inavailability of opacities for lead. Since the pusher in this pellet is seeded with a high Z element, the radiative preheat effects will be reduced. Also the surface temperature of the target is ~ 100 eV and so the radiation losses will be small. In these calculations we have neglected radiation losses. However, inclusion of radiation transport will help the burn propagation. We expect to include radiation effects in our future calculations of the HIBALL target.

Figure III.3-11 shows the Atwood number at the pusher fuel interface as a function of time. It is seen that towards the end of the implosion the Atwood number decreases rapidly and even becomes negative. This indicates that while the pusher is being decelerated by the high pressure in the fuel, the fuel density becomes comparable to the pusher density. This indicates that our target should be stable to hydrodynamic instabilities which cause pusher-fuel mixing during the final stages of implosion.

III.3-6 Discussion and Conclusion

An advanced and extended version of the well-known MEDUSA code has been transformed into a target design code suitable for heavy ion beam fusion targets. The EOS is vital because it determines to which extent matter can be compressed, and how much energy is needed to do this. Also because the sound velocity is determined from the EOS, the EOS determines the time scale of the whole implosion. The detailed behavior of strong shocks is also determined by the EOS. Hence with a false EOS, targets of the wrong size and structure are likely to be designed. Radiation transport is also important in the design of targets as this can cause preheat of the DT, losses from the surface of the

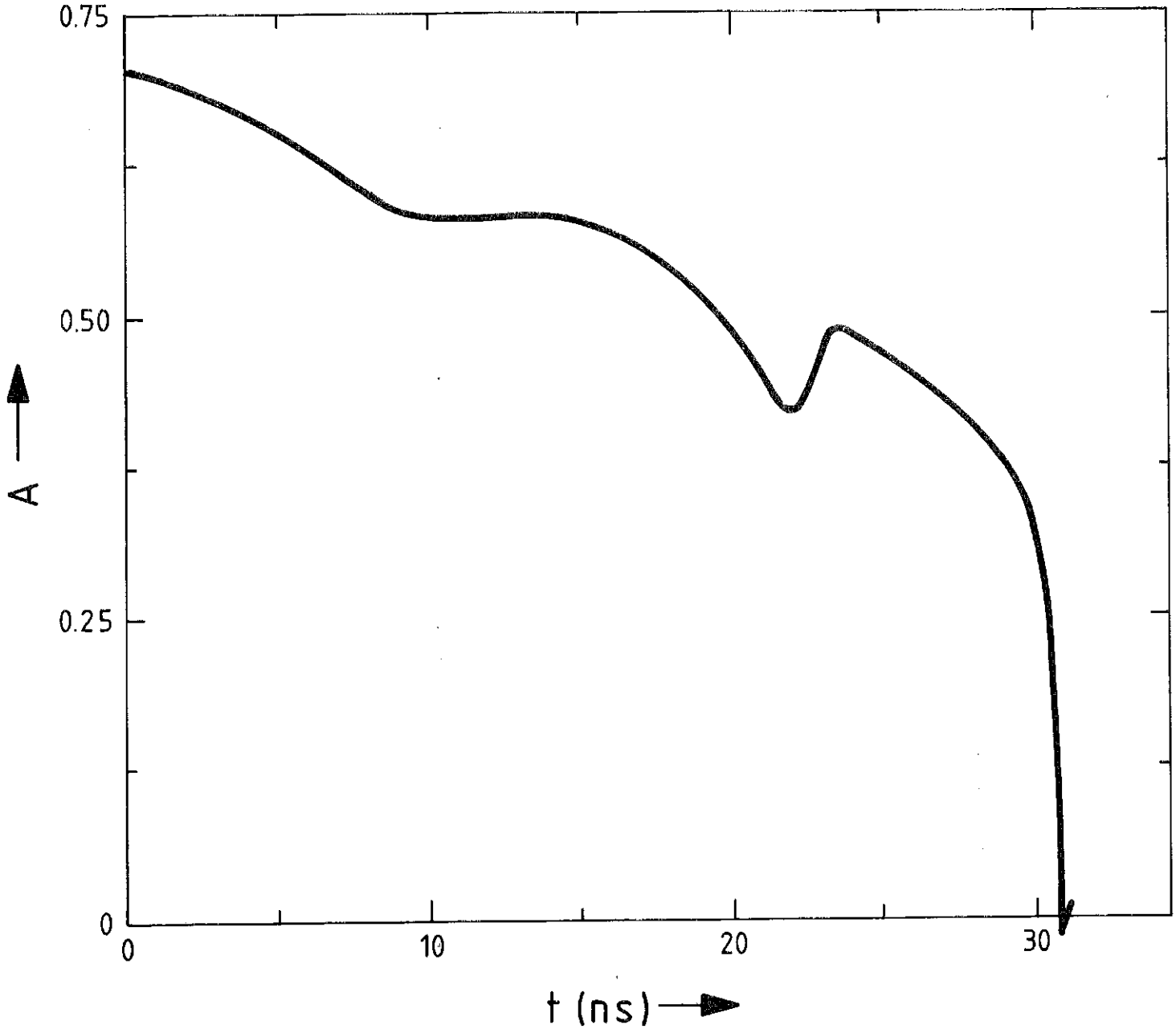

Fig. III·3-11

targets and is important for the propagation of the burn. The HIBALL target has been designed to minimize the deleterious effects of radiation transport.

The energy deposition of ions in ICF target materials has been calculated. A code has been developed which is suitable for the deposition of light and heavy ion beams. Detailed calculations show that range shortening by up to a factor 2 occurs for both heavy and light ions. For heavy ions the deposition profile becomes more peaked as the temperature of the material rises. Typical deposition profiles for the HIBALL target materials and the HIBALL target itself are presented.

The credibility of the MEDUSA code as a target design code has been established by reproducing results obtained by Bangerter for a 1 mg target design. This target has then been successfully scaled up using an $m^{1/3}$ law, to 4 mg of DT. Detailed implosion, ignition and burn phase calculations are presented for this 4 mg HIBALL reactor study target. The gain of this target is 97, with an input energy of 7.4 MJ and an output energy of 715 MJ which is easily sufficient for the designed fusion reactor. Further, detailed tuning and use of a more carefully tailored pulse is expected to increase the gain and decrease the input energy, while still producing over 500 MJ of energy. We found that the gain of the 4 mg target is less sensitive to changes in the ion beam range and the pulse parameters than the 1 mg target. Larger targets are hence less sensitive to parameter changes such as ion beam range, so that range shortening will not have such an effect. Range shortening could be compensated for by ramping the voltage of the incoming ions.

The HIBALL target design has therefore many attractive features. It is a high gain target, and needs reasonable values of input energy and power. It is a relatively simple target, which would make construction reasonably easy, and would also keep the cost down because it contains no expensive material.

The target materials are compatible with the rest of the reactor design, in particular the coolant materials. Since the density of the high Z tamper is low, it produces minimal radioactivity. The target is over 7 mm in diameter and so focussing problems will not be too hard to overcome. The target is stable to pusher-fuel instabilities, and by use of a thick pusher could be made stable to Rayleigh-Taylor instabilities.

References for Section III.3

1. K.A. Long and N. Tahir, "Ion Beam Fusion: Energy Deposition in and Simulations of ICF Pellets," to be published.

2. N.A. Tahir and K.A. Long, "Pellet Simulations for the HIBALL Reactor Study," to be published.

3. J.P. Christiansen, D.E.T.F. Ashby, and K.V. Roberts, "MEDUSA, a One-Dimensional Laser Fusion Code," CPC 7, 271, (1974).

4. R.G. Evans, "Improvements to the MEDUSA Code," Rutherford Laboratory Report, unpublished, June 1980.

5. A.R. Bell, "New Equation of State for MEDUSA," Rutherford Laboratory Report, RL-80-091, (1980).

6. N.A. Tahir, "Simulation Studies of Laser Compression of Matter," PhD Thesis, Glasgow University, 1978.

7. N.A. Tahir and E.W. Laing, Phys, Lett. A, 79A, 321, (1980).

8. N.A. Tahir, E.W. Laing, and D.J. Nicholas, Rutherford Laboratory Report, RL-80-048, (1980).

9. N.A. Tahir and E.W. Laing, Plasma Physics, 22, 1113, (1980).

10. N.A. Tahir and E.W. Laing, Phys. Letts, 77A, 430, (1980).

11. D. Kershaw, J. Comp. Phys. 26, 43, (1978).

12. N.A. Tahir, E.W. Laing, D.J. Nicholas, Rutherford Laboratory Report, RL-80-083, (1980).

13. S.P. Ahlen, Rev. Mod. Phys. 52, 121, (1980).

14. E. Nardi, E. Peleg, and Z. Zinamon, Phys. Fluids 21, 574, (1978).

15. E. Nardi and Z. Zinamon, Phys. Rev. A 18, 1246, (1978).

16. L.D. Landau and E.M. Lifschitz, Quantum Mechanics, Permagon Press, Oxford (1965).

17. H.A. Bethe, in Handbuch der Physik, Springer, Vol. 24, 273, (1933).

18. R. Latter, Phys. Rev. 99, 1854, (1955).

19. H.A. Bethe, Ann. Phys. 5, 325, (1930).

20. N. Bohr, Phil, Mag. 25, 10, (1913).

21. D. Pines and P. Nozières, "The Theory of Quantum Liquids," Benjamin, N.Y., (1966).

22. D. Pines, "Elementary Excitations," Benjamin, (1965).

23. S. Doniach and E. Sondheimer, "Green's Functions for Solid State Physicists," Benjamin, (1972).

24. M.D. Brown and C.D. Moak, Phys. Rev. B6, 90, (1972).

25. S. Chandrasekhar, Principles of Stellar Dynamics, Dover, P. 251, (1960).

26. K.A. Long, "Energy Deposition of Ions and α-particles in ICF Targets," GSI Report 81-3, (1981).

27. T.A. Mehlhorn, SAND80-0038, (1980).

28. R. Bangerter and D. Meeker, LLL Report, UCRL-78474, (1976).

29. R. Bangerter, LLL Report, UCRL-82026, (1978).

III.4 Target Design - University of Wisconsin

There is little question that the key element of inertial confinement fusion is the target. The fortunes of ICF ride on the target performance, thermonuclear yield as a function of driver energy. For commercial applications (i.e., production of electricity) the target gain, or ratio of thermonuclear yield to driver energy, must be large enough to compensate the major inefficiencies of the power plant such as the electrical efficiency of the driver. Furthermore, this minimum gain must be achievable for economically-sized drivers.

A very simple systems analysis of the power cycle within an ICF power plant will predict this value of minimum gain. This cycle is shown in Fig. III.4-1 where the three major components are the target, the energy conversion system, and the driver. The following terms are defined for this system:

η_D = driver efficiency = $\frac{\text{driver energy on target}}{\text{energy into driver}}$

Q = target gain = $\frac{\text{thermonuclear yield}}{\text{driver energy on target}}$

η_t = thermal to electric conversion efficiency

f = recirculating power fraction.

Multiplying these factors around the closed loop of Fig. III.4-1 gives

$$\eta_D Q \eta_t f = 1 \quad . \tag{III.4-1}$$

It is clear from the Fig. III.4-1 that the cost of electricity is proportional to

$$\$ \sim (1 - f)^{-1} \quad . \tag{III.4-2}$$

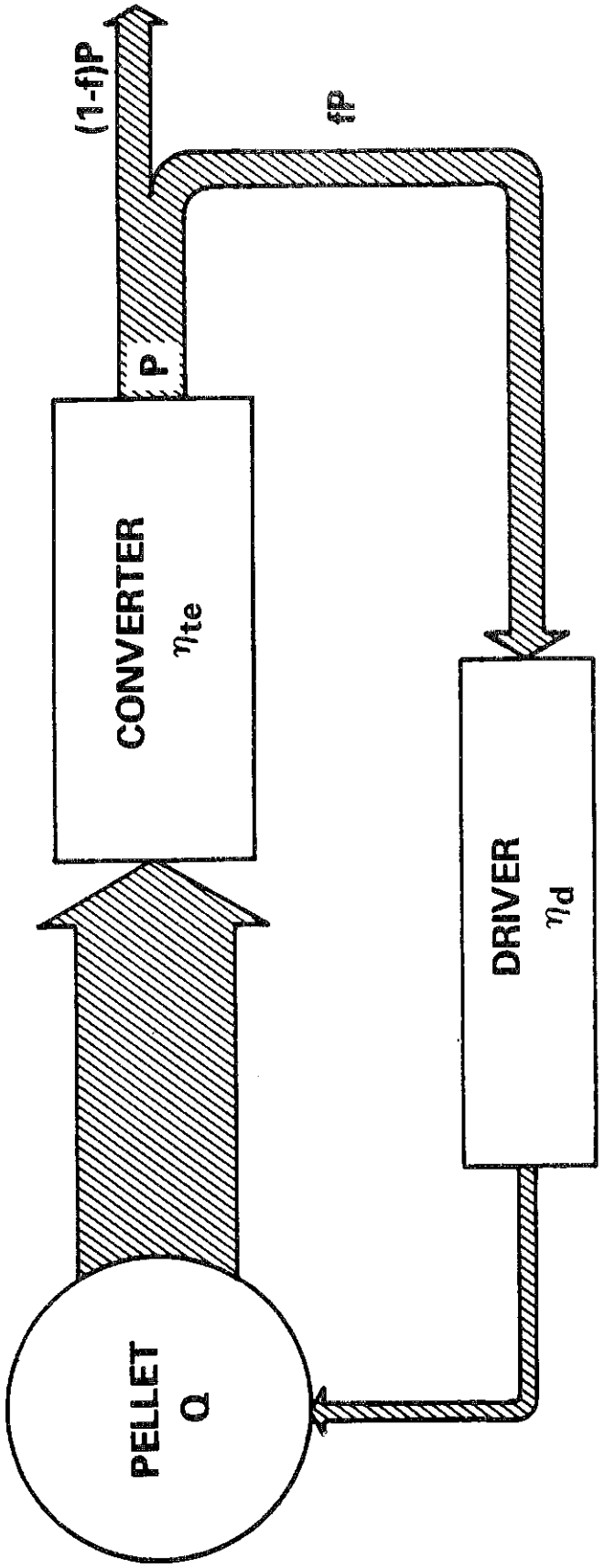

Fig. III.4-1

Power flow in ICF reactor.

This of course is a strong incentive to minimize the recirculating power fraction, f. Historically, a maximum value of f has been taken as 25%, although this value is most certainly quite arbitrary. (We might note that the recirculating power fraction in a nuclear fission reactor is about 5%.) For the sake of specificity we will adopt the 25% convention for our analysis. If we further assume

$$\eta_t = 0.4 \quad , \tag{III.4-3}$$

a reasonable value for a conventional thermal steam cycle, then we are left with a relationship between the target gain and driver efficiency

$$Q\eta_D > 10 \quad . \tag{III.4-4}$$

This product has been labelled the "fusion gain" of the system. The acceptable target gain is therefore dependent on the efficiency of the driver. In our case of ion beam drivers this efficiency may be in a range of 10-40%. Hence the minimum target gain is in a range of 25-100. Any situation where the target gain is much greater than this will naturally lead to smaller recirculating power fractions and more economical electricity production.

We have now established the range of minimum target gain that must be achieved. We next face the question: How much ion beam energy is required to produce this gain? This is a question that is based to a large extent on detailed target design calculations. This is unfortunate because the principle target design tools, large two-dimensional radiation-hydrodynamics computer codes and equation of state and opacity data, are unavailable to all except those working at the three principle nuclear weapons design laboratories, Lawrence Livermore Laboratory, Los Alamos Scientific Laboratory, and Sandia Laboratory. Furthermore, many target designs are classified as secret

restricted data on the grounds that they are somehow related to nuclear weapons design. This problem is partially alleviated by the fact that Lawrence Livermore Laboratory has published general information regarding the performance of ICF targets. An example of their so-called target gain curves is shown in Fig. III.4-2. The solid lines indicate the best possible performance of single and double shelled targets. Single and double shelled target designs are shown schematically in Fig. III.4-3 parts (a) and (d). By "best possible performance" we mean that (1) the target shell configuration is very accurately matched to the intensity profile of the incident pulse of driver energy, and (2) the calculations are performed using a one-dimensional implosion model. Each of these two conditions are in fact unrealistic. First of all, the precise matching of hydrodynamic response to the input pulse of energy is an exercise in "numerical gymnastics." The high gains predicted by the curves in Fig. III.4-2 are often nearly a "delta function" in the target design parameter space. By this we mean that small variations in shell thickness, density, etc., can seriously degrade the result. Critical tolerances are often smaller than the quite sizable uncertainties in the calculational model. Secondly, one-dimensional calculations always over-predict the target gain. Because the actual implosion will not converge to a point, as the one-dimensional model would predict, the ignition condition is generally much more severe than would be indicated by these results.

As a correction to these unrealistic results, the LLL target designers also include a band of performance in Fig. III.4-2 that they label "conservative." This represents a degradation of the idealized results to account for two- dimensional and other unspecified effects that make up the difference between the one-dimensional computer world and the real physical world. The band or range of gain vs. driver energy is meant to represent the uncertainty

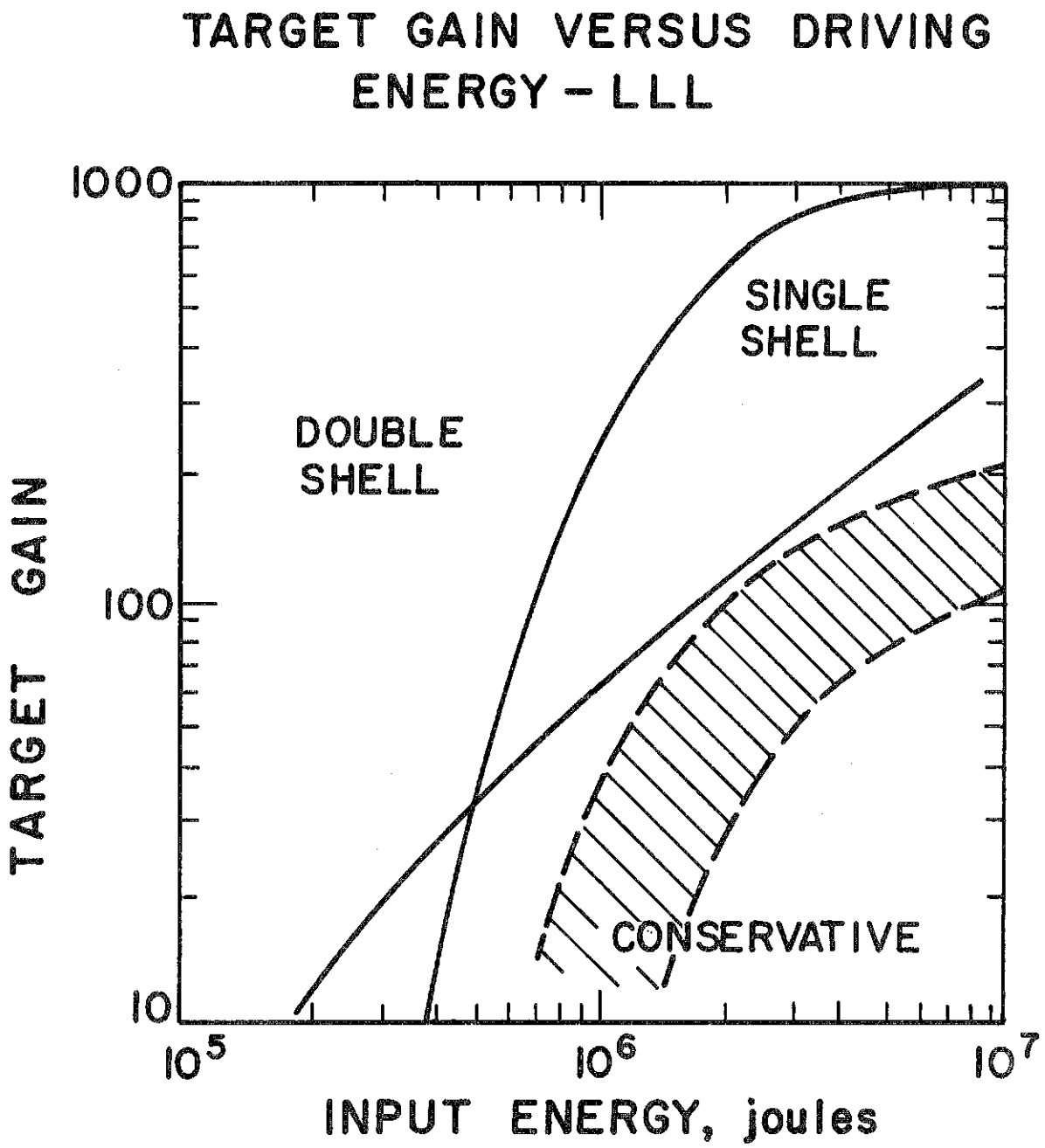
TARGET GAIN VERSUS DRIVING ENERGY - LLL
1000
100
10
TARGET GAIN
SINGLE SHELL
DOUBLE SHELL
CONSERVATIVE
10^5
10^6
10^7
INPUT ENERGY, joules

Fig. III.4-2

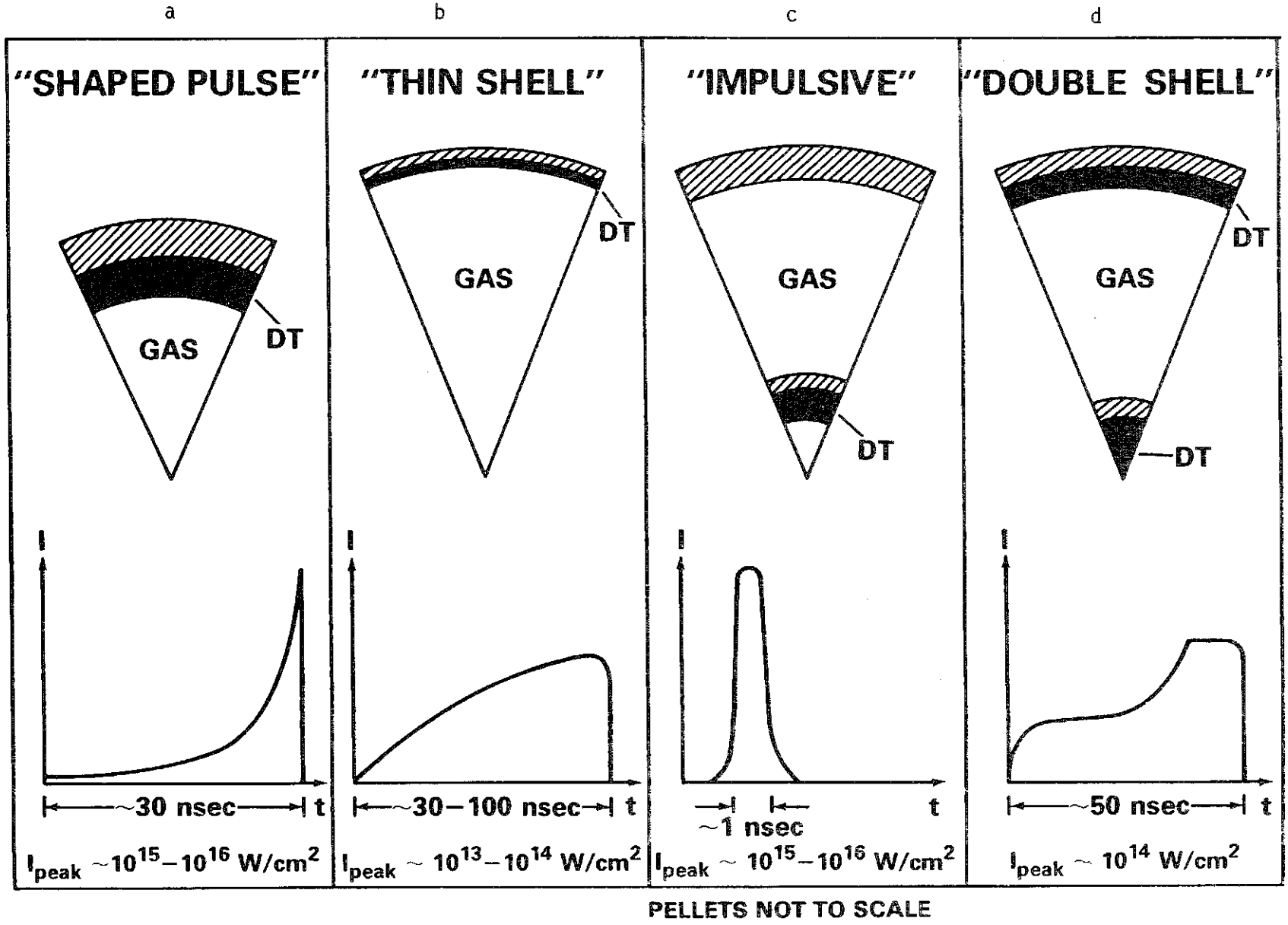

Fig. III.4-3

Different ICF target designs.

in the calculations. It is important to note that this uncertainty is substantial.

With this valuable information the reactor designer can now determine a range for the driver energy. From our earlier values of Q = 25-100 we get

$$Q = 25 \quad \rightarrow \quad E_D = 0.85 - 2 \text{ MJ}$$

$$Q = 100 \quad \rightarrow \quad E_D = 2 - 8 \text{ MJ} \ .$$

Such large ranges of driver energy are very disquieting. The precise value chosen for a reactor study seems almost arbitrary and in fact it is! To understand this we must ask: How conservative is this band and what does it really mean from the point of view of target design?

This question is answered in section III.2.1 where a simple parameter analysis is used to reproduce the gain curves shown in Fig. III.4-2. To achieve high gain the fuel must be nearly isentropically compressed to high densities (hundreds of times liquid DT density). To achieve this high compression and an efficient hot-spot ignition configuration the fuel must be very symmetrically imploded.

The problem of implosion symmetry cannot be over-emphasized. This symmetry can be destroyed in two ways, (1) nonuniform driving pressures, and/or (2) fluid instabilities. The first is a macroscopic effect. Some parts of the shell are accelerated to greater or lesser velocities and therefore the entire shell does not reach the center of the implosion at the same time. The second problem is much more subtle. In this case, the fluid at the ablation surface during the implosion and the fuel-pusher interface at ignition time are hydrodynamically unstable. Small perturbations in the fluid density tend to grow. This complex subject will not be discussed here in detail. These fluid instabilities can be mitigated by rapid acceleration of

the shells so that the instabilities do not have time to grow and by very narrow tolerances on the surface finish of the various shells in the target.

Symmetric implosion is a very troublesome problem for directly driven ion beam targets as compared to laser driven targets. This comes from the fact that the ions are depositing their energy very close to the ablation surface whereas laser beams deposit energy at the critical density of the blow-off plasma, Fig. III.4-4. This region between the critical density surface and the ablation surface allows nonuniformities to be smoothed due to lateral conduction. Two-dimensional hydrodynamics calculations by Emery, Gardner and Boris of NRL[1] on thin slab targets demonstrate this smoothing effect. In these calculations they irradiate a slab target with 1.06 μm laser light with a nonuniform spatial profile, Fig. III.4-5. Under extreme circumstances they see very nonuniform density and pressure profiles as shown in Figs. III.4-6 and III.4-7. This study was done parametrically for differing laser intensities (and consequently, different spacing between ablation and critical density surfaces) and these results are summarized in Fig. III.4-8. Here the nonuniformity of ablation pressure is plotted as a function of the ablation-critical density surface spacing for different nonuniformity scale lengths. We clearly see that to hold the pressure variation to a few percent, the scale length of the nonuniform laser profile must be less than or equal to the distance between the critical density surface and the ablation surface. For ion beam targets the ablation surface is directly adjacent to the energy deposition region, because the ions penetrate to such high densities. This implies that ion beam targets such as the one proposed by Bangerter require extremely uniform illumination. Symmetry may possibility be improved by target designs that are beyond the scope of this discussion.

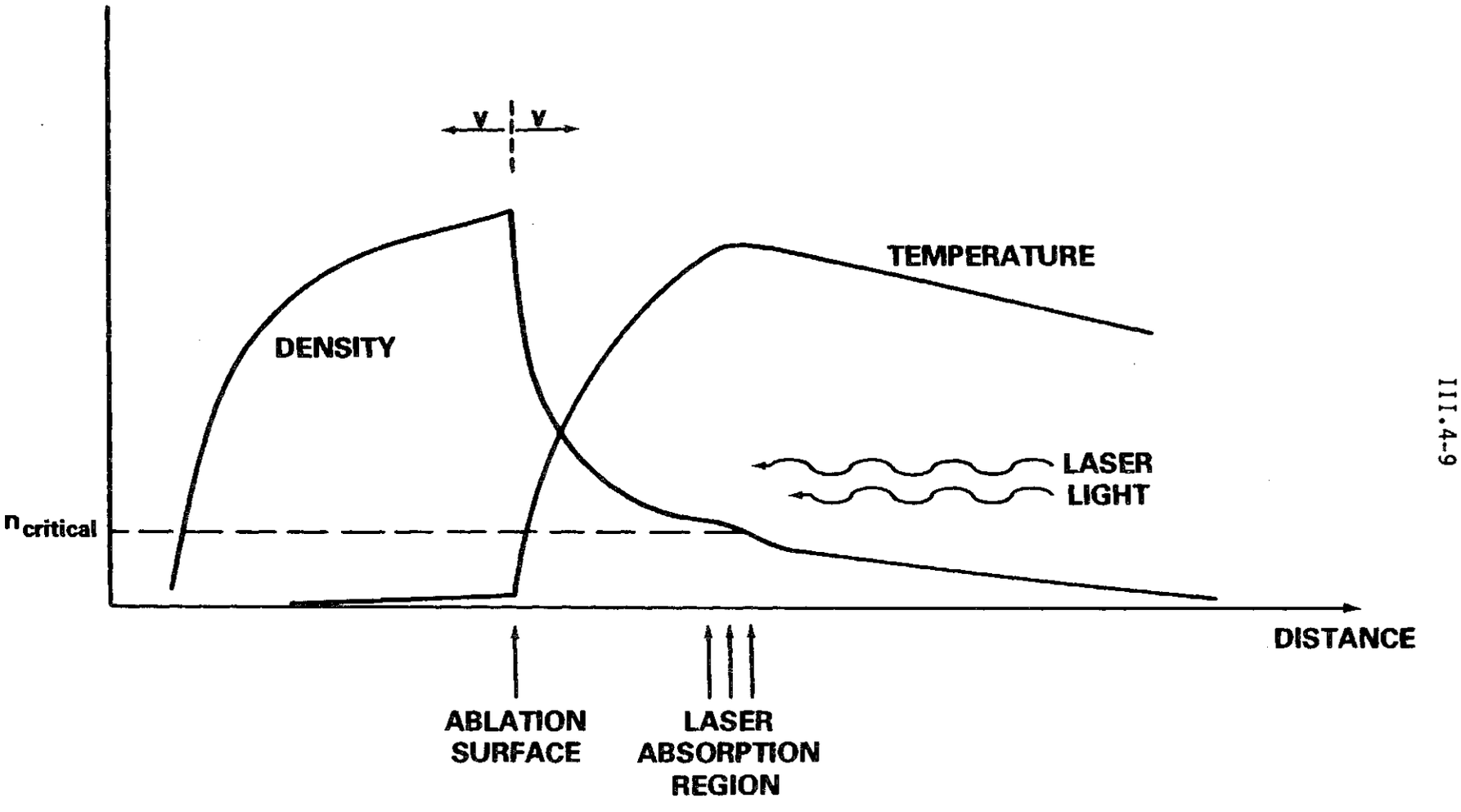

Figure III.4-4

Temperature and density profiles in laser ablated target.

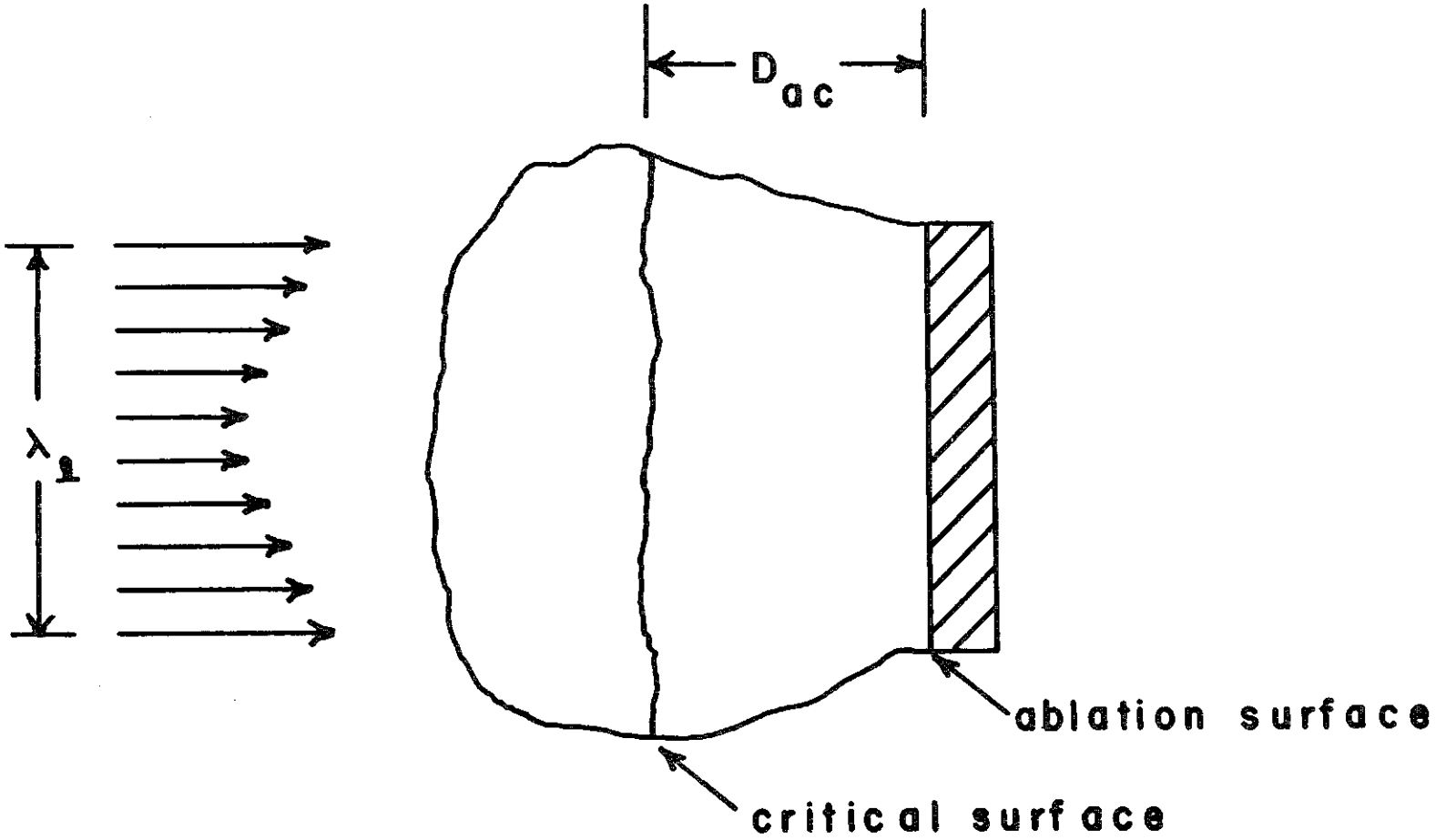

Figure III.4-5
Non-uniform laser spatial profile.

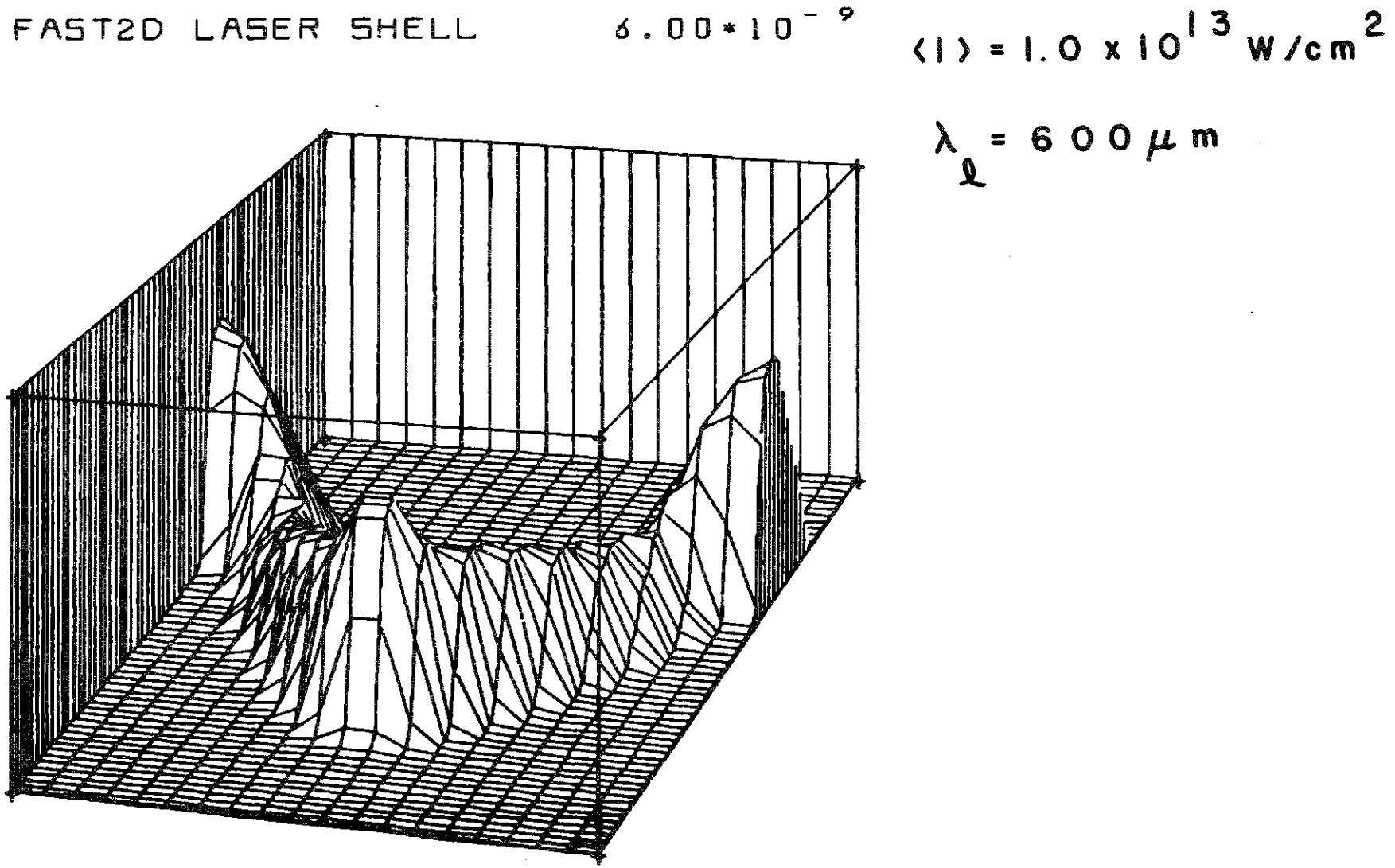

Figure III.4-6
Pressure vs. position for non-uniform laser profile.

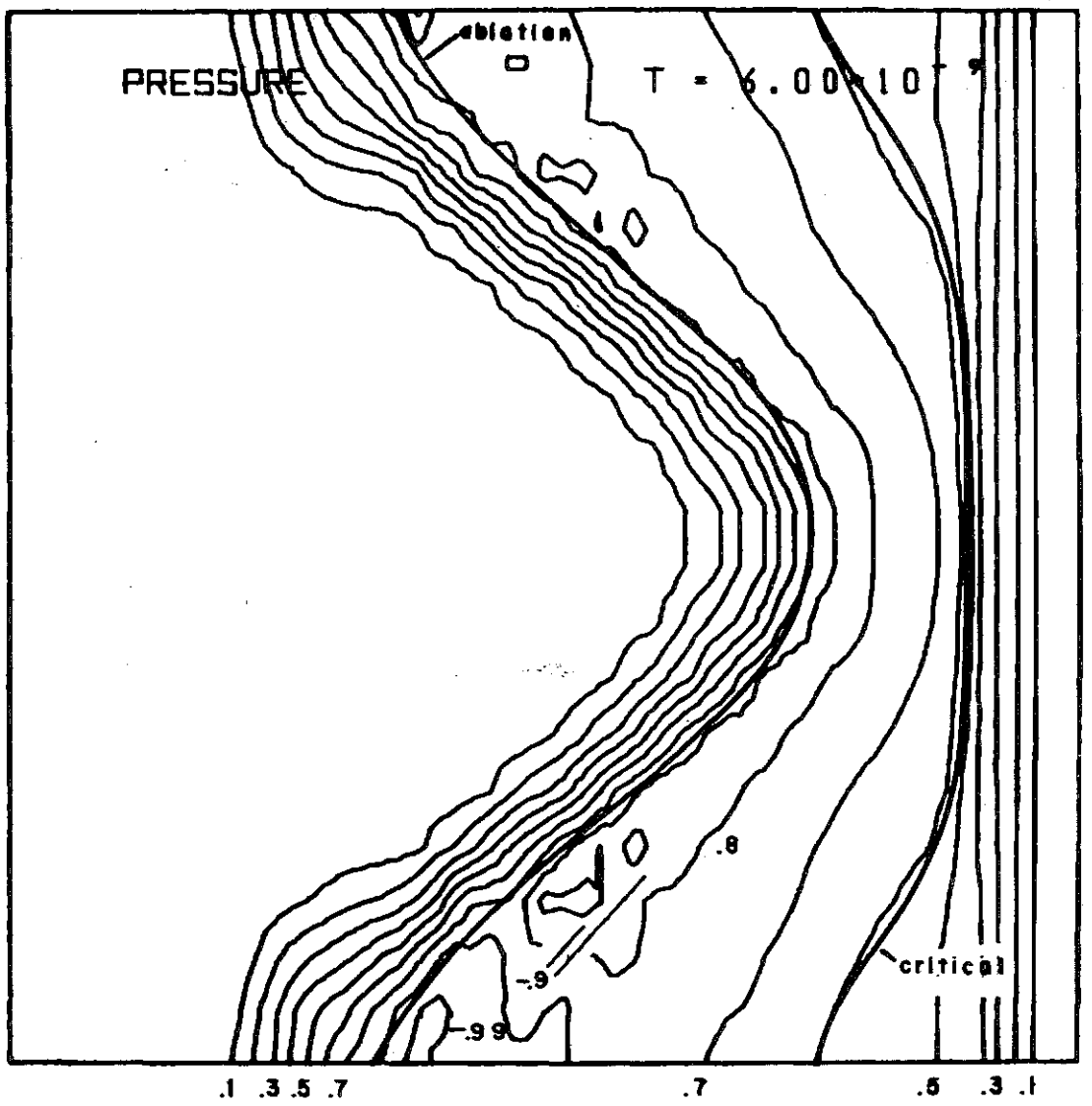

$\langle I \rangle = 1.0 \times 10^{13}$ W/cm^2

$\lambda_\ell = 600\ \mu m$

Figure III.4-7
Pressure contours for non-uniform laser profile.

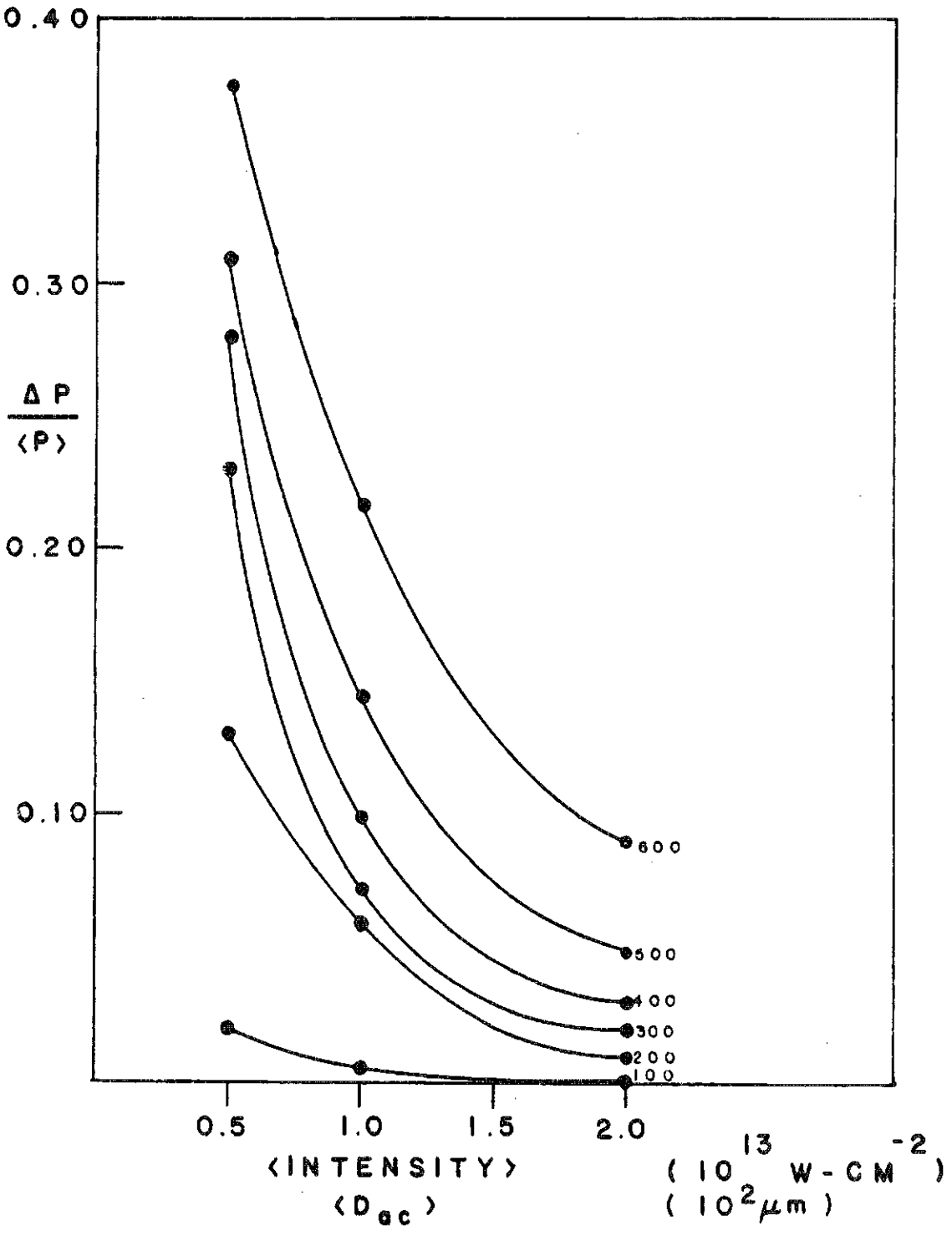

Figure III.4-8

Fractional ablation pressure variation vs. laser intensity.

We have studied the deposition of ions in hot material using the model of Mehlhorn.[2] This analysis is based on the Bethe stopping theory at high ion energy and Lindhard stopping theory at low ion energy. In the transition between these two we interpolate as shown in Fig. III.4-9. Finite temperature effects are then added to these standard models. The theory will not be reproduced here. Instead we show results of calculations for heavy ions stopping in low and high Z material at different temperatures. Figures III.4-10 and III.4-11 show the ranges of 10 GeV bismuth ions in 0.01 solid density gold and aluminum. The range is shortened at higher temperatures. In the case of protons the range begins to re-lengthen at temperatures higher than about 100 eV. Hence the shortest range is associated with about 100 eV material. However, in the heavy ion case, the range is still becoming shorter at 300 eV in both gold and aluminum. The ranges of 10 GeV heavy ions are very much longer than those of 2 MeV protons. In fact, at an aluminum density of 0.027 g/cm^3 the proton energy would be in excess of 10 MeV to have a range that is equivalent to the 10 GeV heavy ions. Heavy ions have a much shorter range in low-Z material than in high-Z material. However, the Bragg peak is not very large and therefore it is more difficult to concentrate energy in a localized region of the target. Figures III.4-12 and III.4-13 show the ranges of 10 GeV uranium ions in gold and aluminum. These are presented for comparison with other researchers since U ions seem to be an unofficial standard for heavy ion beam fusion.

Finally, Fig. III.4-14 and III.4-15 show a comparison between calculations done at the University of Wisconsin using Mehlhorn's model and those done at KfK by Long. His model is discussed in section III.3 of this report. We see remarkably good agreement between these two code calculations.

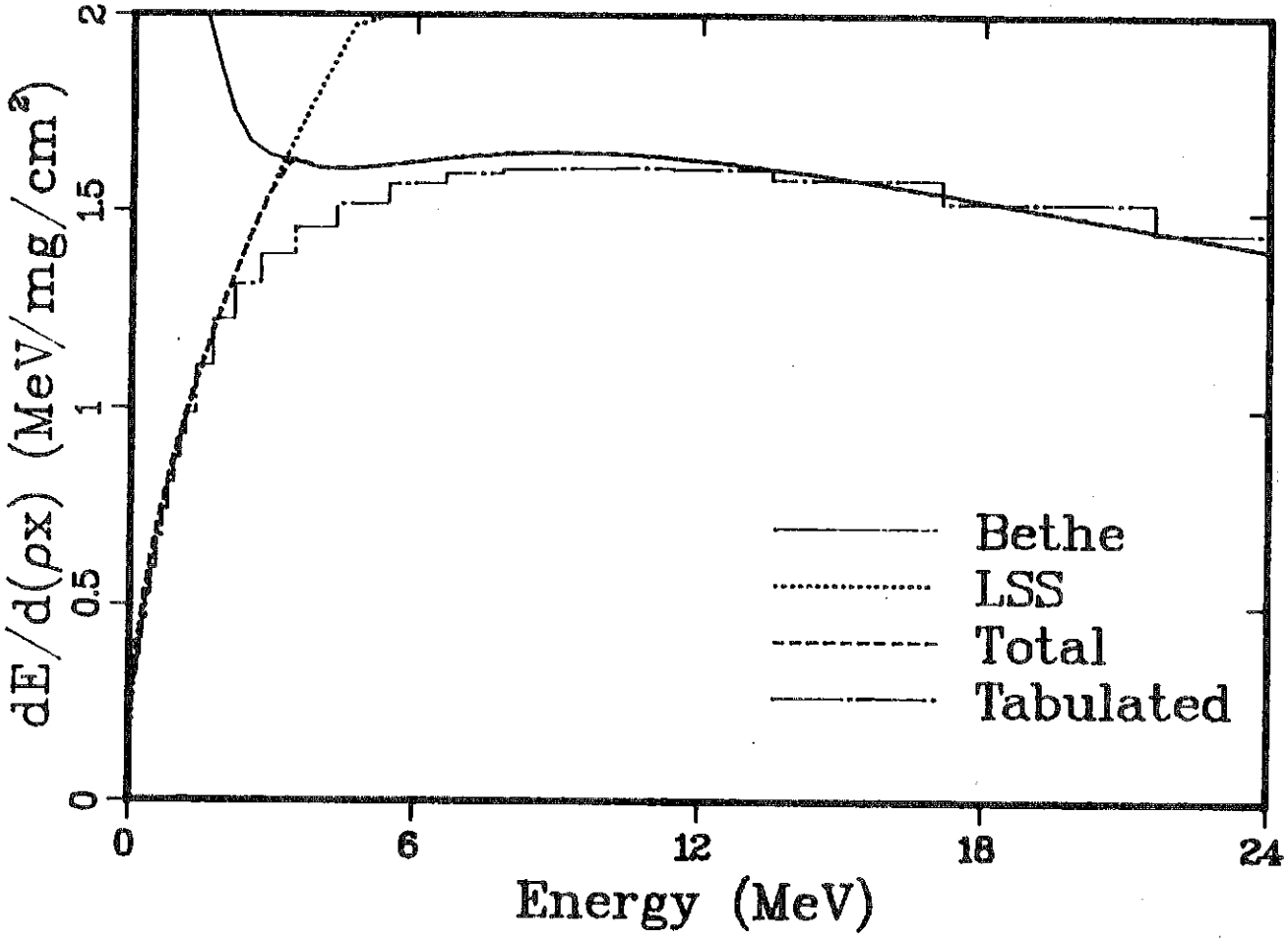

Figure III.4-9

Interpolation of Bethe and LSS theories.

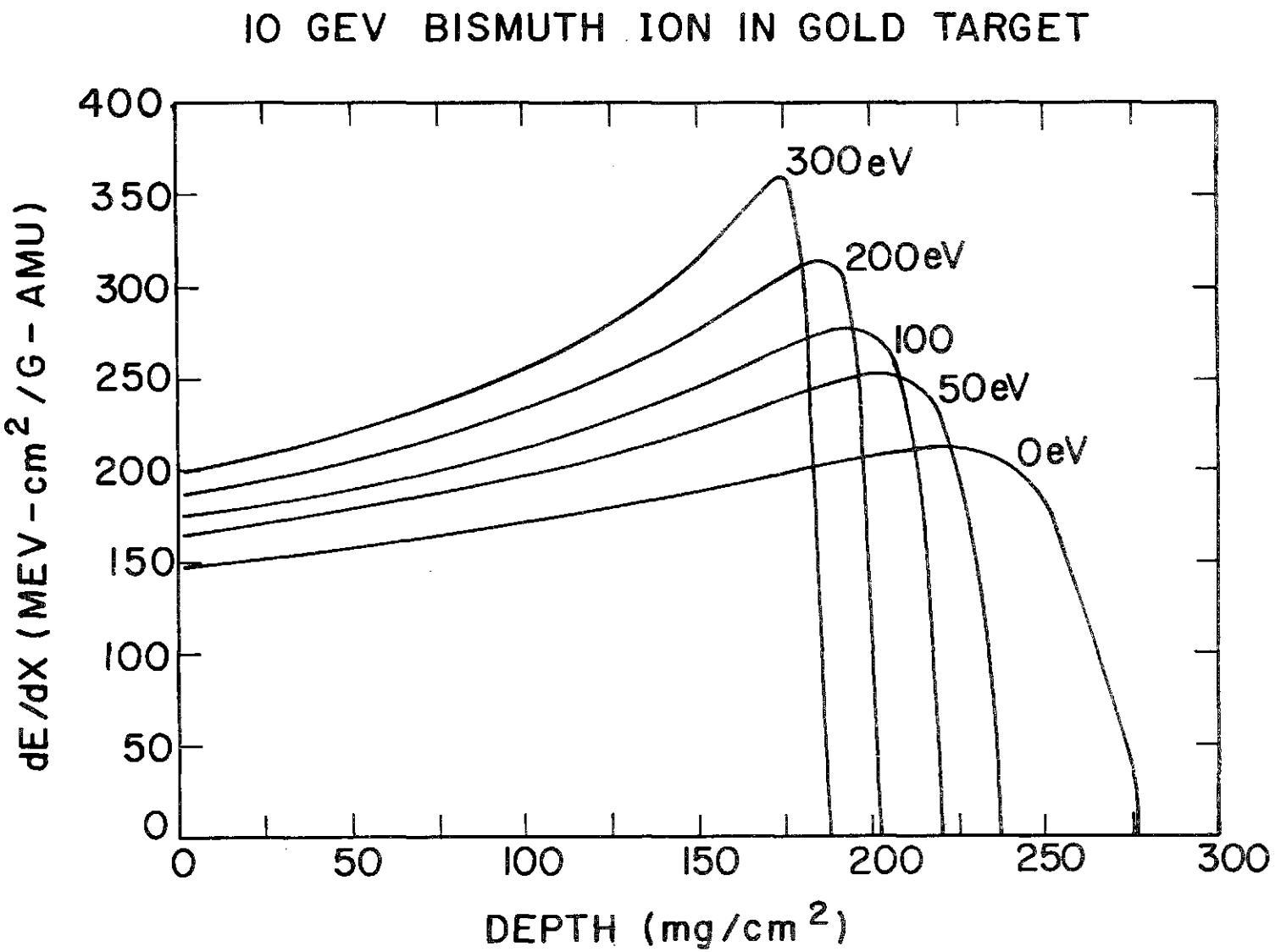

Figure III.4-10

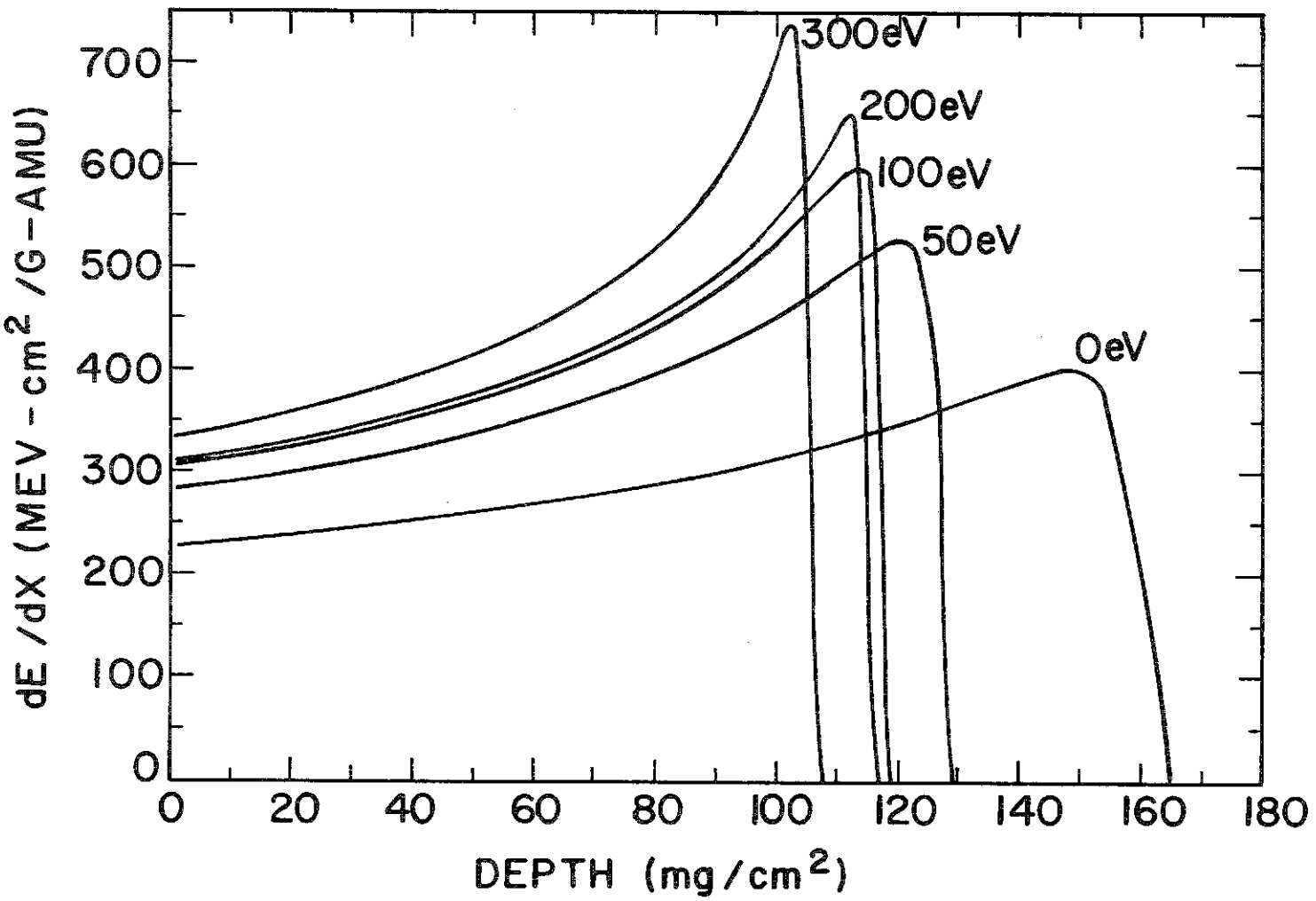

Figure III.4-11

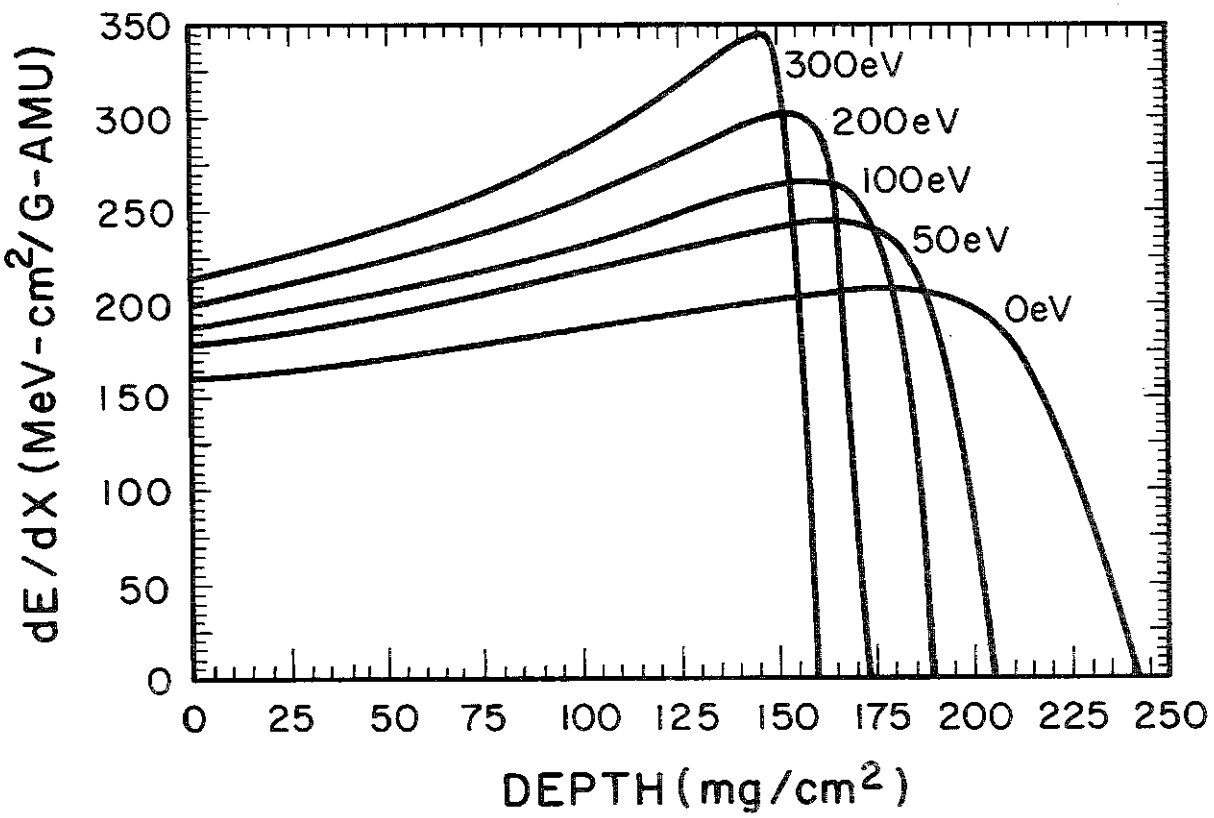

Figure III.4-12

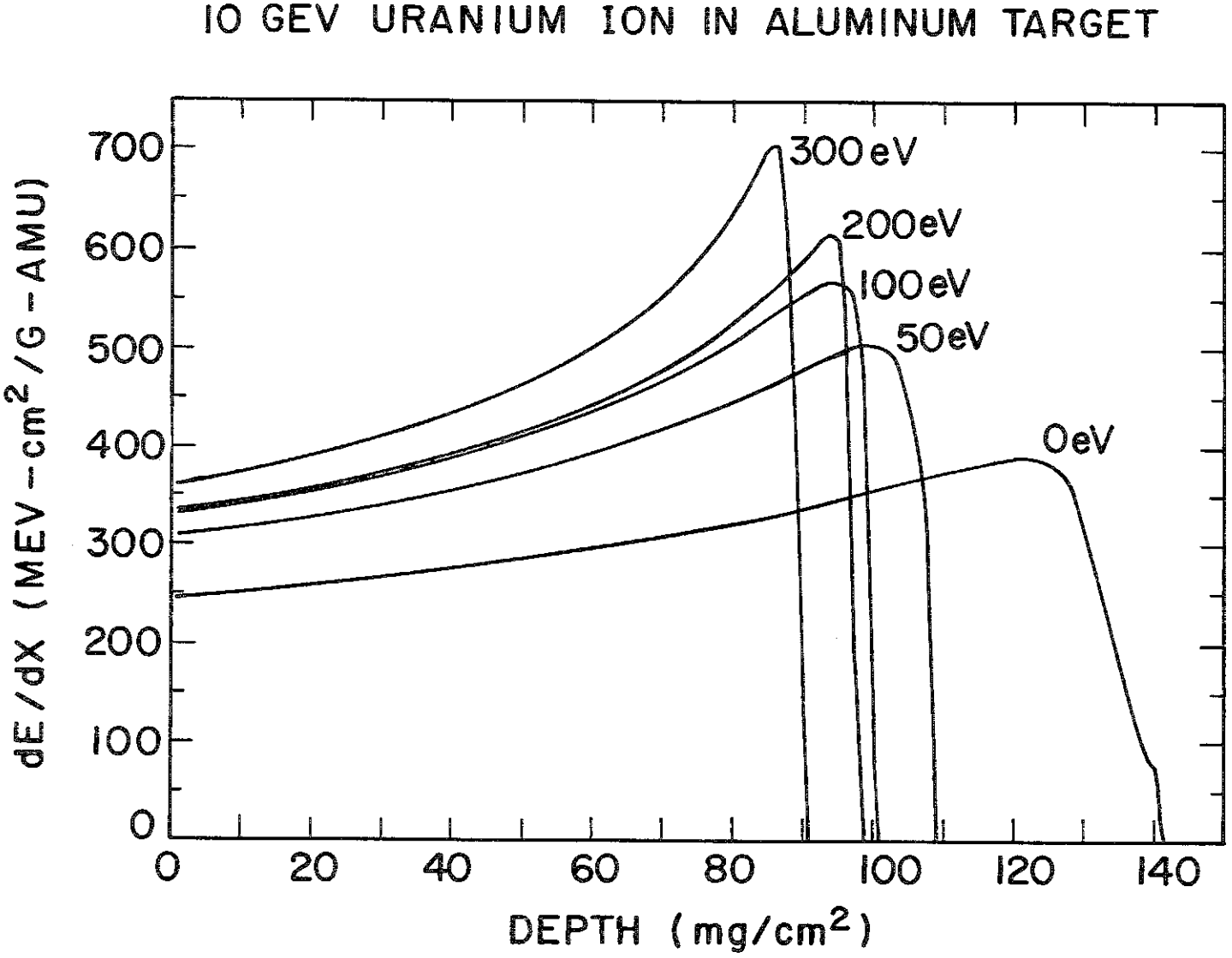

Figure III.4-13

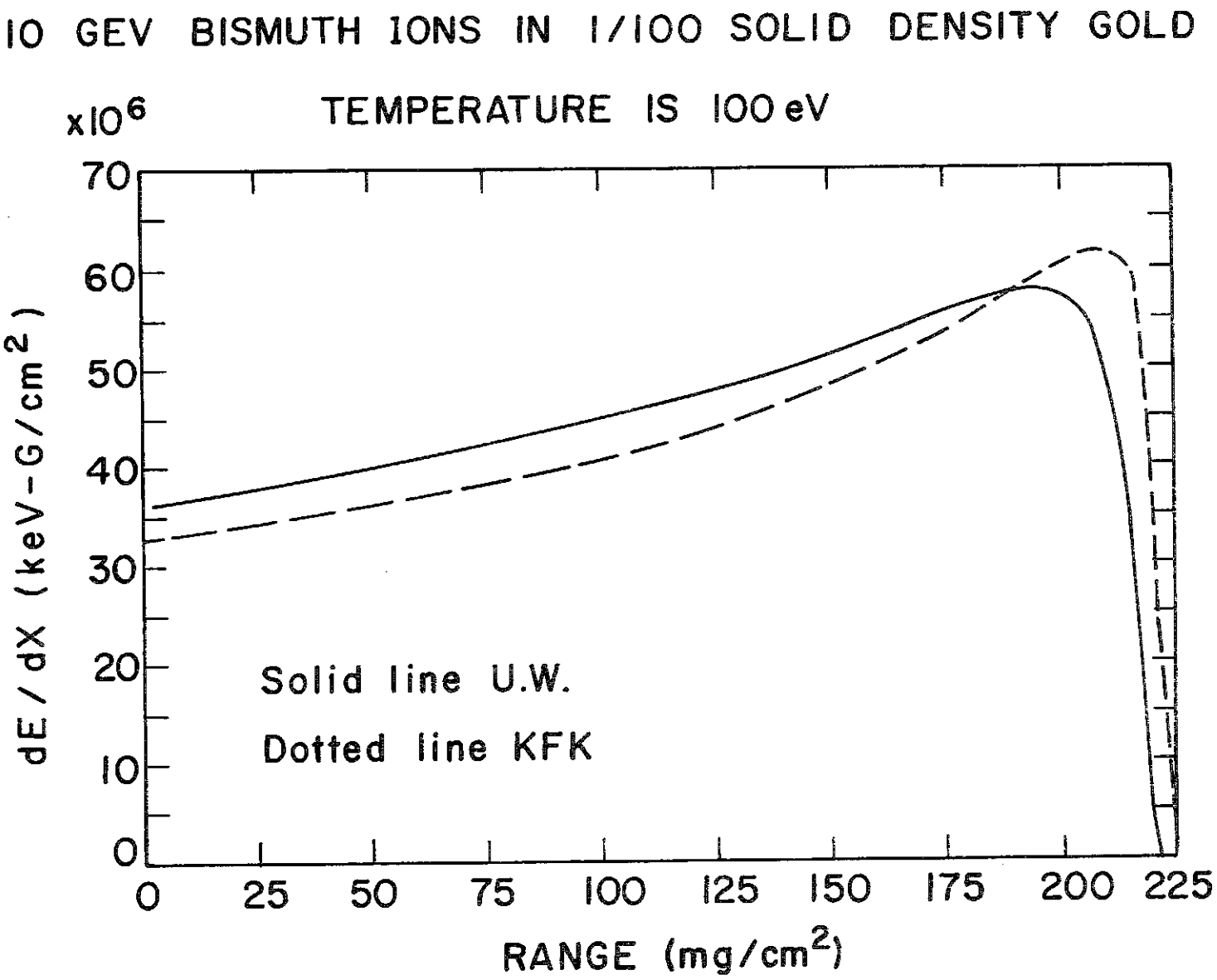

Figure III.4-14

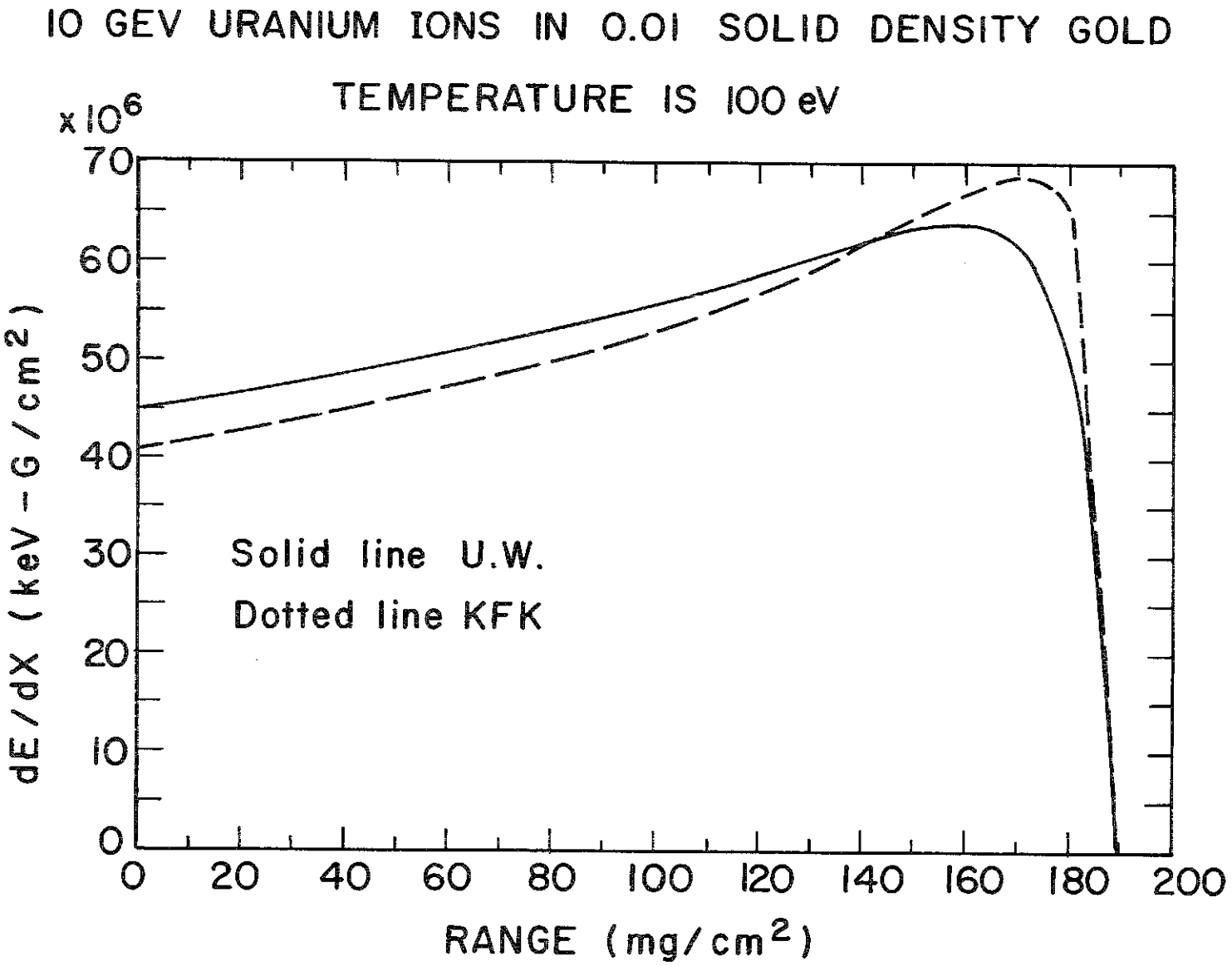

Figure III.4-15

References for III.4

1. M.H. Emery, J.H. Gardner, and J.P. Boris, "Simulation of Laser Beam Nonuniformity Effects," Naval Research Laboratory Report NRL Memo Report 4500, April 1981.

2. T.A. Mehlhorn, "A Finite Material Temperature Model for Ion Energy Deposition in Ion-Driven ICF Targets (U)," Sandia National Laboratory Report SAND80-0038, May 1980.

III.5 Target Delivery

III.5.1 Introduction

The term target delivery comprises two tasks: injecting the cryogenic target into the reactor chamber, and synchronizing the target motion and the ion pulse so that they both reach the focus location at the same time.

General conditions on the injection process are that the target must not be altered to such a large degree that it will not properly implode. This includes limiting the physical damage to the outer shell and, more importantly, the heating during delivery causing the DT fuel to sublimate or melt.

The HIBALL-I design uses ballistic injection, i.e., the target is not guided up to the focus location but travels in free motion for a substantial, final part of its flight time. During this time neither the direction nor the velocity can be corrected. Therefore, lateral deviations (the "scatter circle" of the injector) must be small enough, and the total target travel time must either be very precisely reproducible or the ion pulse has to be timed individually according to the measured target motion rather than by a clock frequency. In this latter case, the intervals between successive explosions will slightly scatter about the nominal value.

The injector described in section III.5.6 meets the scatter circle requirement but not the requirement on total travel time precision. Therefore, the design uses an optical system for longitudinal target tracking. From the results of the tracking the arrival time of the target is predicted and the ion pulse released accordingly.

Alternative "guided" ways of injection are possible and will be mentioned in section III.5.5. Lateral deviations of the target could in principle be compensated for by lateral ion-beam steering (see remark in III.5.9).

III.5.2 Target Positioning Tolerance

The tolerance (admissible inaccuracy) of the target position at ion pulse arrival clearly depends on the target size and on the geometry and intensity distribution of the ion focus. At the focus, each of the twenty beams is assumed to have a circular cross section with a Gaussian radial intensity profile and 80% of the ions within a 3 mm radius (see chapter V). Thus a perfectly positioned 3 mm-radius target will be hit by 80% and missed by 20% of the ions. For a target misplaced by 0.5 mm these figures change to about 78% and 22%, respectively. Since the target is injected along the chamber axis, roughly at right angles with all twenty beams, the same figures will apply approximately to the splitting of the total ion current in case of a longitudinal misplacement (i.e., along the flight path). The current missing the target and thus the power fraction recirculating in the installation would therefore increase by 10% relative if every target were misplaced 0.5 mm upward or downward. For lateral misplacements, the effect is smaller as it obviously multiplies by $|\sin\phi|$ where ϕ is the azimuthal angle between the direction of misplacement and the respective beam. The average of $|\sin\phi|$ over all angles is $2/\pi = 0.64$. Therefore, tolerances of 0.5 mm for the longitudinal and 0.7 mm for the lateral direction are adopted.

Any target misplacement, besides increasing the recirculating power fraction, will also decrease the symmetry of target illumination. We presume the above tolerances to be sufficient also in this respect but the question should be kept in mind for physics considerations.

III.5.3 Target Velocity

The choice of target velocity is clearly related to the longitudinal positioning tolerance. Another important condition is the fact that the ion beams are formed into bunches in the storage rings before being extracted into

the transport lines. Consequently, the ion pulse cannot be released at an arbitrary time but only when the two bunches in each ring are passing the kicker magnets (see chapter IV), i.e., at discrete instants 2.5 μs apart. The easiest way to deal with this difficulty is to choose a velocity low enough so that the distance traveled by the target in 2.5 μs is less than the longitudinal positioning tolerance. The 0.5 mm tolerance then leads to a maximum velocity of 0.5 mm/2.5 μs = 200 m/s.

From the pneumatic injector design point of view a low target velocity is favorable because it relaxes the requirements on the acceleration pressure and length and on the quantity of propellant gas leaving the injector per shot.

A condition leading to a lower bound for the velocity is given by the heating processes before ignition. The target is heated by radiation during the flight time it spends inside the chamber. In addition, with a low velocity the target may have to enter the chamber so soon after the preceding explosion that it finds a sufficiently dense atmosphere for conductive heating and/or vapor condensing on its surface.

The calculations of the following section show that radiative heating at 200 m/s is tolerable (there is a safety margin because a perfectly black target surface was assumed). The flight time spent in the chamber is 33 ms so that the new target enters 167 ms after the explosion of the preceding one. At this time the PbLi vapor density is below 10^{11} atoms/cm^3 (see chapter VI) corresponding to a pressure below 10^{-4} Torr or 13 mPa. The thermal conductivity of the vapor at this pressure should be negligible.

Considering all the above conditions the velocity of v = 200 m/s appears the best choice.

III.5.4 Target Heating During Injection

Since it is importance to keep the fuel in a cryogenic target frozen, the

heating of a target during injection into the chamber should be considered. Using the target shown in Fig. III.5-1, we have studied the transfer of heat from the surface through the DT fuel with a Crank-Nicholson finite difference code. The result of this calculation is the temperature profiles in the target versus time.

The heat flux on the surface of the target is assumed to be due to the blackbody radiation from the cavity surface, which we assumed to be at the maximum first-surface temperature 500°C. This leads to a heat flux of 2.02 W/cm^2. Another possible source of heat is the cavity gas itself, but since this gas reaches a temperature at 167 ms very close to the INPORT tube temperature we have just used the blackbody temperature of the first surface. We have assumed that the target is a perfect absorber and have neglected its re-radiation because its temperature is so far below that of the blackbody radiation, but these are obviously worst-case assumptions. Heat conduction from the gas to the target has also been neglected (see preceding section).

Temperature dependent thermal properties have been used[10,11] with the finite-difference code to obtain the maximum fuel temperatures versus time shown in Fig. III.5-2. In the pusher region we have assumed the PbLi to be entirely Li. Here the maximum fuel temperature of the target was found to be less than 13.7 K after 32.5 ms in the cavity. If the target must travel 6.5 m at 200 m/s, this is the amount of time it remains in the cavity before it is exploded.

The temperature of 13.7 K at the DT-PbLi interface is still below the melting temperature of DT (19.7 K)[1] so that a slight lowering of the injection velocity will not lead to melting of the fuel. Furthermore, the

Fig. III.5-1 HIBALL Cryogenic Target

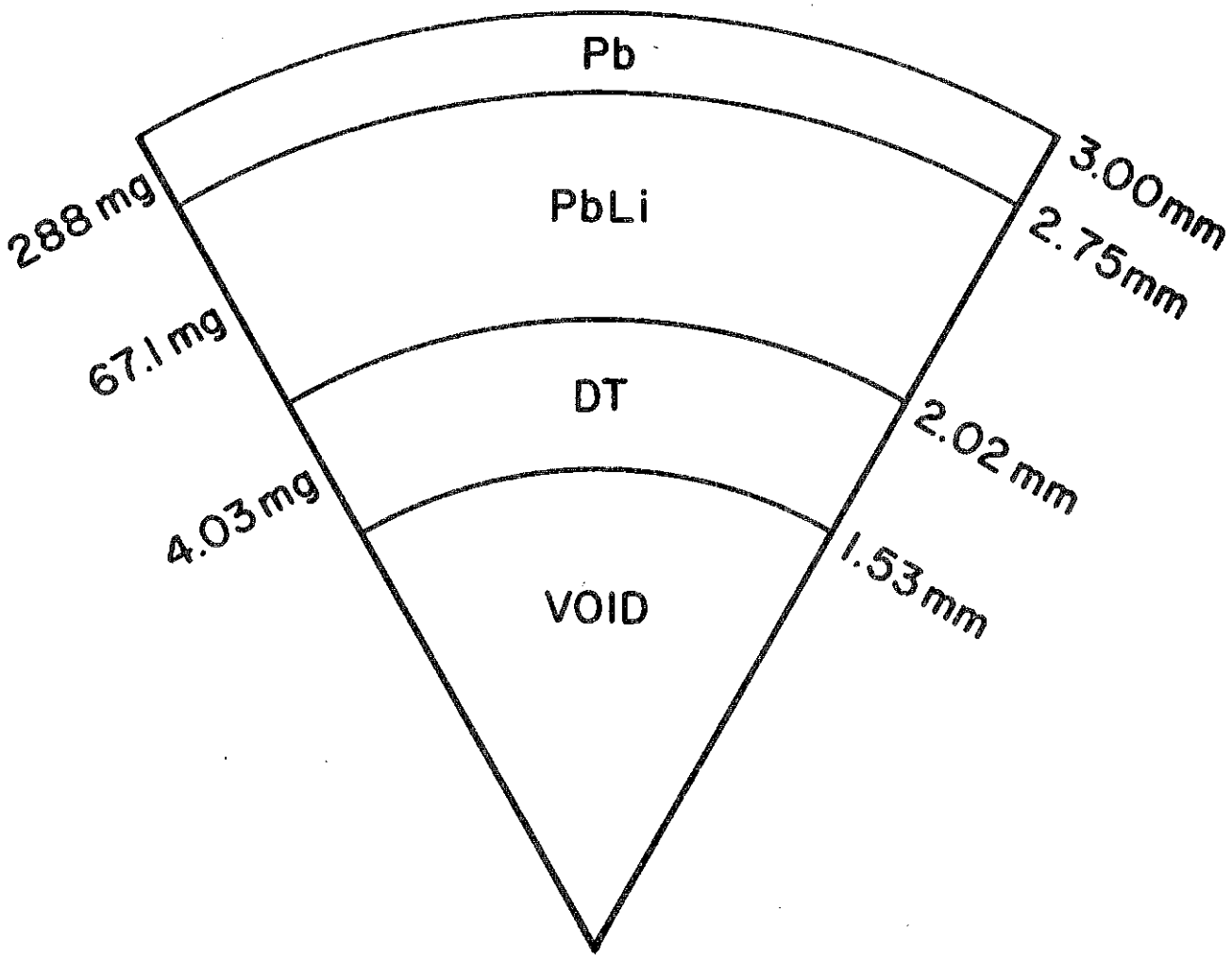

Fig. III.5-2 Maximum Target Fuel Temperature versus Time

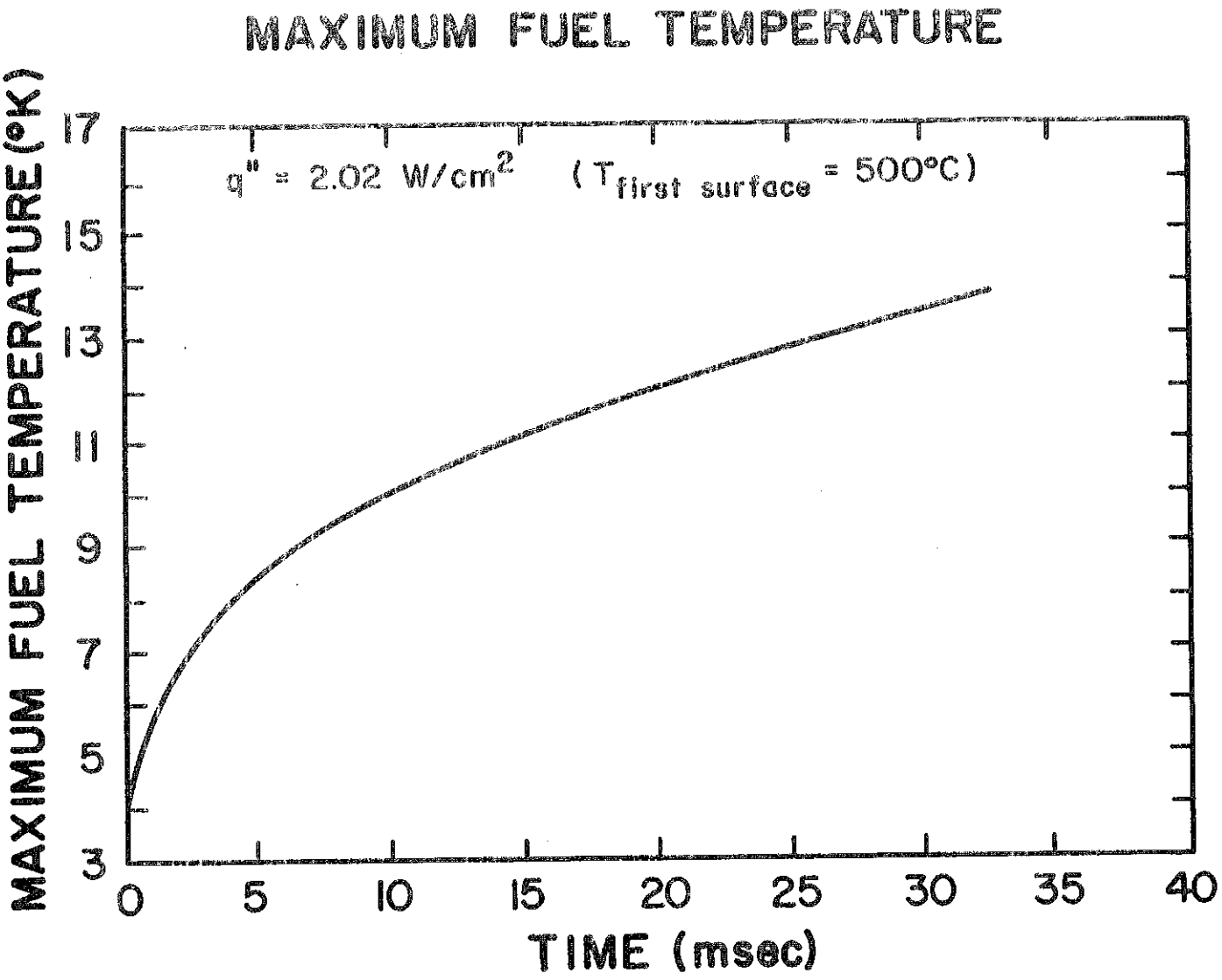

temperature of 11.3 K at the inner boundary of the fuel layer is below the sublimation temperature of DT (14 K)[2].

Temperature profiles in the target are plotted for a few times in Fig. III.5-3. The temperature is found to be almost uniform across the Pb and PbLi shells and to fall off sharply in the DT. This occurs because of the relatively high thermal diffisivity of Pb and Li at low temperatures. Because of the sharp temperature gradient in the fuel, melting will occur at the fuel-PbLi interface long before the whole fuel shell melts. Whether a small amount of melting at this interface is detrimental to the implosion and ignition is an open question, but we avoid controversy by keeping the maximum fuel temperature significantly below the melting point.

There are improvements that can be made to this calculation. Additional sources of heat should be considered as should different initial conditions. The target may have some non-uniform initial temperature distribution due to tritium decay, cooling during storage and heating due to friction during target acceleration. Additional sources of heat on the surface of the target during injection may include laser energy which guides the target to the focus of the ion beams (see III.5.5). In the future, these considerations must be dealt with as more information about them becomes known.

III.5.5 Injection Methods

There are several techniques that can be proposed for target acceleration to high velocity of 100 to 1000 m/s needed for ICF purposes: gravitational, pneumatic, electrostatic, electromagnetic techniques.

The gravitational acceleration is not suited for velocities of this order because the total vertical flight distance would be too large (some hundreds of meters).

Fig. III.5-3 Temperature profiles in the target

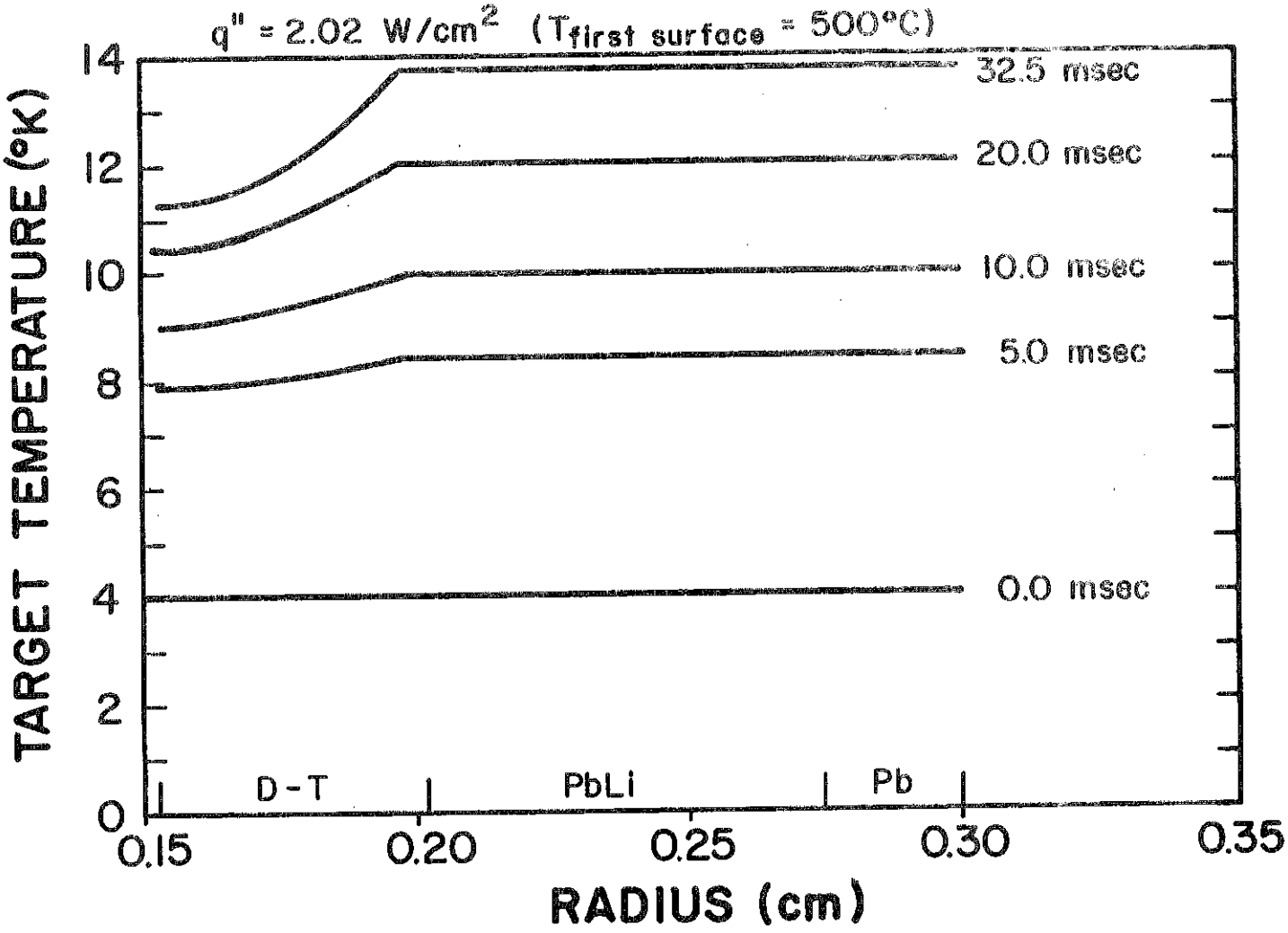

The use of the electrostatic method requires the placement of a high electric charge on the target. To accelerate masses of the order of 1 g and several millimeters diameter to velocities of about 100 m/s a charge-to-mass ratio of roughly 10^{-3} Coulomb/kg and an acceleration field of 10^{6} V/m would be necessary.(3) The experimental basis for such a scheme is too poor at the moment.

To employ the electromagnetic technique the target has to be placed into a conducting carrier driven through an induction tube. Masses of several grams could be accelerated to 100 m/s over a few meters with feasible induction currents.(4) There is, however, the problem of stability of the target carrier motion within the induction tube and the stopping of the carrier after reaching the final velocity. No experiments have been made for such an acceleration scheme. Another problem is the thermal insulation of the target from the carrier material which will be heated by the induced currents.

Pneumatic injection seems to be the most promising method at the moment because there is experience on injection systems used for refueling magnetic-confinement fusion installations.(4,5) Gas gun type injectors are used on the ORMAK and the ISX-B tokamak at Oak Ridge and the WENDELSTEIN VII A stellarator at Garching. Further work in this field is done at Risö and Culham. The purpose of these injection systems is to shoot small cylinders of solid deuterium, called pellets, into a magnetically confined plasma. A high repetition frequency is intended and pellet velocities up to 10 km/s are envisaged. Up to now deuterium masses of the order of 10^{-4} g have been accelerated to 100 m/s by helium or hydrogen gas at 30 to 40 bars at room temperature. Due to the small pellet mass an acceleration length of only some decimeters is necessary.

For each of these injection methods the aiming accuracy must be evaluated. It decides whether projectile guiding (and/or ion-beam lateral steering) is needed.

Some methods have been proposed for target (or projectile) guidance. Electrostatic trajectory corrections are suitable if electrostatic acceleration is used because the target is already charged. In any case, devices performing electrostatic trajectory corrections must be arranged outside the reactor chamber to avoid their direct irradiation.

Another class of methods for projectile guidance uses laser beams for trajectory corrections inside the reactor cavity. If a laser beam hits the target and ablates some surface material the target moves in the direction of the resulting recoil momentum. Via the illumination intensity and duration, the amount of ablated matter can be controlled so that the magnitude of the trajectory correction is adjustable.

A method by which the target is laterally guided into the desired position by only one laser beam is proposed by Chang.[6] The target drifts through a conical laser light tube which is adjusted to the aiming point where its inner diameter is just as large as the tolerance of lateral target positioning. The greatest effect of this on target performance should be mainly through additional target heating (see III.5.4).

III.5.6 HIBALL-I Pneumatic Injection System

The injection method which is most suitable from its present technological basis is pneumatic injection. The HIBALL target is vertically injected by a gas gun. Trajectory corrections are not provided. With presently available high-precision air guns a scatter circle radius of less than 0.7 mm at a distance of 12 m can be realized even for horizontal injection.[7] This distance corresponds to just the proposed injection system

(see distance scale of Fig. III.5-4). So the lateral target positioning tolerance of 0.7 mm adopted in section III.5.2 for the given illumination scheme is probably feasible by pneumatic injection without lateral guidance.

High repetition frequencies of several shots per second are also feasible with pneumatic devices.[7] Fast electromagnetic valves with a gas delivery time of the order of 10 ms are available for pressures of the order of MPa (10 Bar).[8]

A 5% reproducibility of the total target travel time, 80 ms, is needed and appears feasible.

The main components of the HIBALL-I injection system are the high pressure propellant gas reservior, the gas gun loader, the gun barrel, the fast gas valve between the reservior and the barrel, the buffer cavity between the barrel and the injection channel which penetrates the top shield of the reactor cavity, and the vacuum pumps providing the low pressure of the buffer cavity. Figure III.5-4 gives a scheme of the system together with the design parameter values.

As a cryogenic target is used in this study it is important that the fuel is not heated to a temperature above 19 K, neither in the cavity nor by friction during acceleration. To avoid heating by the latter source it is appropriate, if not necessary, to put the cryogenic target into a carrier, called a sabot in the following,[9] which is cooled to the cryogenic temperature. Thus, cryogenic sabots, each containing a target, are delivered from a factory to the gas gun. Handling sabots within the injection system requires fewer precautions than the handling of bare targets, especially with regard to the loading of the gun. Furthermore, the sabot protects the target from damage and friction during acceleration. It provides for straight guiding within the gun barrel and isolates the target from the friction heat. The

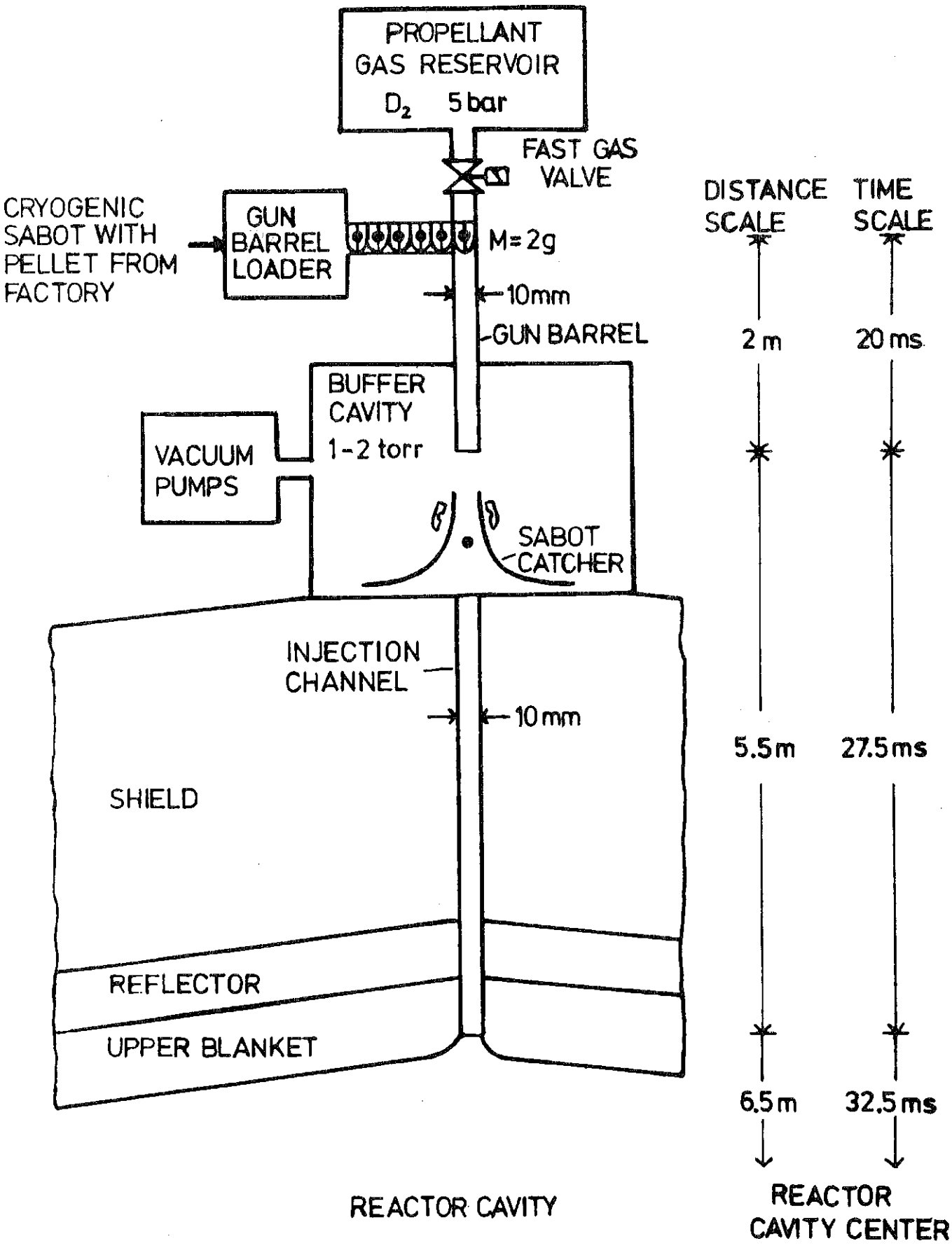

FIGURE III 5-4 SCHEME OF HIBALL-I PNEUMATIC INJECTION SYSTEM AND DESIGN PARAMETER VALUES, PELLET VELOCITY = 200 m/s

latter property requires a low thermal conductivity of the sabot material. The sabot could be made of plastic having a low friction coefficient in contact with the barrel and a high tensile stress allowing for a high acceleration. It consists of two halves separated longitudinally and is removed from the target behind the gun muzzle by a spin given to it during acceleration. To avoid a high mass, the sabot should be hollow with a suitable support structure for the target inside where a contact surface as small as possible should be provided to minimize heat transmission. If the sabot halves do not fit together very tightly the propellant gas, which should be at a low temperature in this case, will enter the sabot so that the halves will be pushed apart when the target enters the low-pressure region behind the gun muzzle. This scheme has to be avoided, however, if a momentum is transferred to the target. Otherwise, target guidance must be provided.

The sabot halves are finally collected by catcher baffles. It would be favorable to choose a sabot material which could be recirculated.

The results of sections III.5.3 and III.5.4 favor a target velocity of 200 m/s, so this value is chosen for this study. Using the sabot concept the dimensions and the mass of the sabot have to be specified. We choose a sabot diameter of 10 mm and a length of about 15 mm. Providing for a hollow, shell-like sabot structure, the sabot mass could be kept at about 1 g (even for a sabot material with mass density of several grams per cubic centimeter). As a reference value for the projectile mass, i.e., the sum of the sabot and target masses, we choose 2 g. To accelerate this projectile to a velocity of 200 m/s a minimum energy of 40 J (0.4 bar-liters) has to be provided by the propellant gas. This corresponds to a minimum gas quantity of 304 Torr-liters per shot. Accounting for the difference between the effective pressure on the projectile and the pressure of the gas reservoir, which generally depends on

the ratio of the specific heats and the temperature of the propellant gas, for the resistance due to the residual deuterium in the gun barrel, and mainly for the energy loss due to friction, we choose an overall efficiency for the kinetic energy transfer to the projectile of 0.5 as a reference value. This means that a propellant gas amount of 608 Torr liters per shot must be provided. Since a certain quantity of the gas will enter the reactor cavity we choose deuterium as a propellant gas for reasons of compatibility. A deuterium amount of 141 mg must be provided for each shot.

The deuterium quantity streaming into the reactor cavity depends on the pressure difference between the buffer cavity and the reactor cavity and on the diameter of the channel cennecting both. The buffer cavity will be kept at 1 Torr before each shot. A volume of 0.88 m^3 is sufficient to keep the pressure below 2 Torr after the shot assuming adiabatic expansion of the gas. For a mean pressure of 1.5 Torr in the buffer and an injection channel diameter of 10 mm, we obtain a maximum of 1.6 mg dueterium per shot streaming into the reactor cavity, assuming a reactor cavity pressure some orders of magnitude lower that 1.5 Torr.

From the total quantity $(pV)_o$ of 608 Torr liters per shot (or 80 J) a value for the product of the working pressure p_o and the acceleration distance L_a can be derived by dividing $(pV)_o$ by the cross section q of the gun barrel. In our case q = 0.785 cm^2 which gives $p_o L_a$ = 10.2 Bar·m. We choose L_a = 2 m so that the working pressure delivered by the gas reservoir must be about 5 Bar. The actual acceleration corresponds to 2.5 Bar due to the overall acceleration efficiency of 0.5. For L_a = 2 m and v = 200 m/s we obtain a mean target acceleration of 10000 m/s^2. For many materials and the given sabot dimensions this does not imply an intolerable stress on the sabot. The acceleration time is about 20 ms.

The energy loss of the projectile during acceleration due to friction can only be calculated if the sabot is completely designed because the contact area A_s between sabot and the gun barrel, the pressure p_f by which the sabot is pressed against the gun barrel and the materials of sabot and gun barrel must be known. A mean value for the friction power $\dot{Q}_f$ can be estimated using the following expression:

$$\dot{Q}_f = f \cdot p_f \cdot A_s \cdot \bar{v} \qquad \text{(III.5-1)}$$

where f is the friction coefficient and $\bar{v}$ the mean velocity of the projectile during acceleration. Assuming that only 10% of the sabot surface touches the gun barrel which gives in our case a value for A_s of about 50 mm^2, we obtain with p_f = 1 Bar and v = 100 m/s:

$$\dot{Q}_f = f \cdot 500\ W \qquad \text{(III.5-2)}$$

If we use a combination of plastic (for the sabot) and metal with f = 0.05 (Teflon on steel) the friction power is 25 W; taking two metals it may be greater by a factor of ten.

In any case the gun barrel has to be cooled and the target has to be isolated from the friction heat by using a sabot material of low heat conductivity. Furthermore a small contact surface between sabot and target should be provided.

III.5.7 Target Tracking

Longitudinal target tracking means the measurement of two quantities, the target velocity and the time at which the target passes through a fixed plane.

The simple device we propose consists of a laser beam observed by a photosensitive detector and intercepted by the passing target. A beam of 0.2 mm diameter, obtainable by simple lens focussing, is completely intercepted at $v \simeq 200$ m/s within 1 μs. It is therefore certainly possible to derive a timing signal from the light detector with an uncertainty $\Delta t \leq 0.3$ μs. Two of these devices are provided at 5.5 m and 3.0 m above the focus plane (Fig. III.5-5) and furnish the times t_1 and t_2. The distance $s_{12} = 2.5$ m between them is traveled in $T = t_2 - t_1 \simeq 12.5$ ms, and this interval is measured with an uncertainty $\Delta T \leq 0.6$ μs or $\Delta T/T \leq 5 \cdot 10^{-5}$. If $s_{23} = 3$ m is the distance between the second measurement plane and the focus plane the predicted time of target arrival at focus is

$$t_3 = t_2 + (s_{23}/s_{12})T \qquad \text{(III.5-3)}$$

with a maximum uncertainty of

$$\begin{aligned} \Delta t_3 &= \Delta t_2 + (s_{23}/s_{12})\Delta T \\ &= \pm\,(0.3 + (3/2.5) \cdot 0.6)\mu s \simeq \pm\ 1\ \mu s\ . \end{aligned}$$

This precision is sufficient as it is less than the interval between two successive possible ion-pulse instants (see III.5.3). The 0.7 mm lateral tolerance of the target trajectory is not a problem since such a deviation in the worst case will cause the interception to start only about 0.1 μs late.

In the last equation the uncertainty of s_{23}/s_{12} has been neglected. In practice this ratio of two fixed distances has to be kept constant within about $5 \cdot 10^{-5}$ which may require temperature control of the respective mechanical supports.

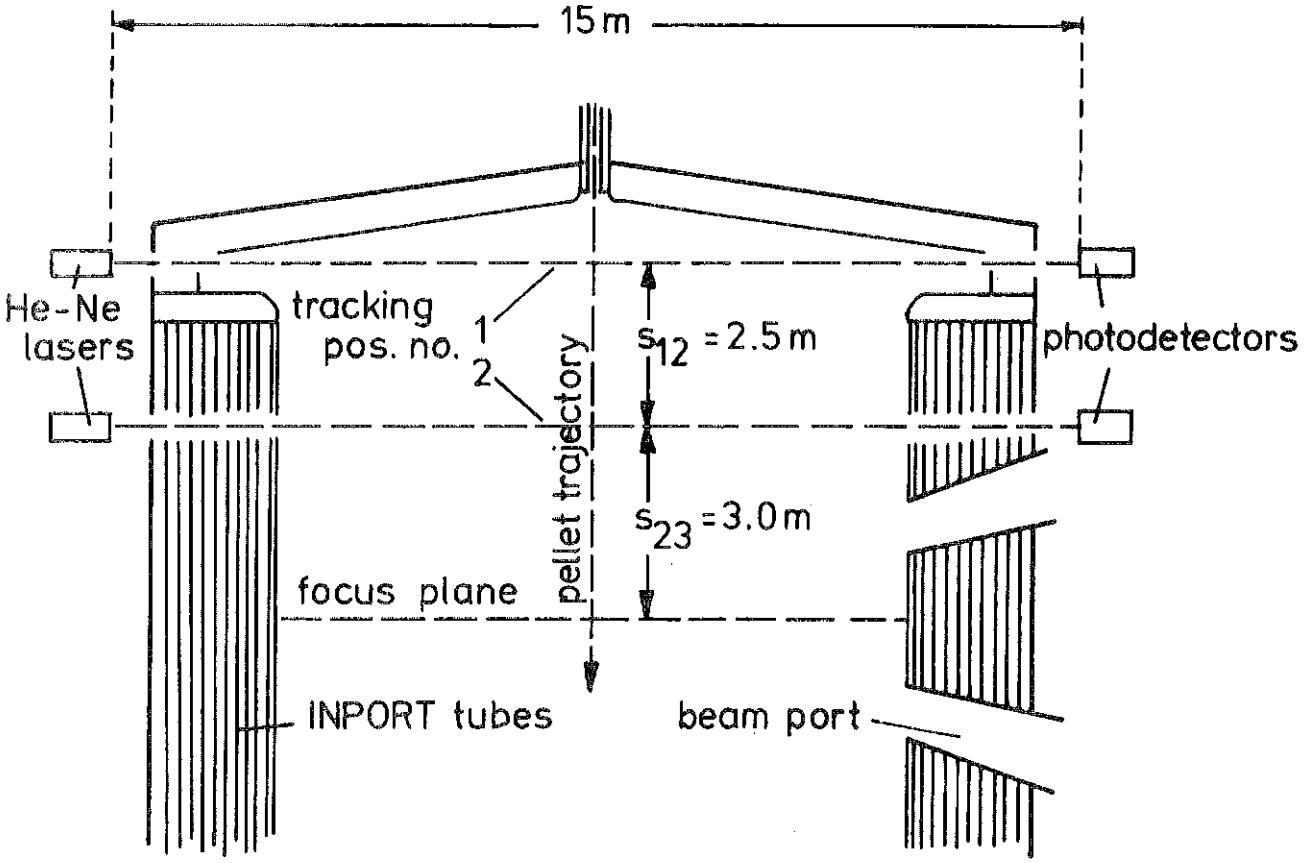

Fig. III.5-5 PELLET TRACKING

The tracking system needs optical windows that have to be protected from condensing vapor as well as from excessive radiation damage. This might be accomplished by a combination of wiping devices and rotating shutters. The lasers and detectors might also be removed out of line of sight with the cavity by using metal mirrors which could be heated to prevent condensation.

III.5.8 Synchronization

Synchronization is achieved basically as follows. Both the target injection and the ion-pulse buildup procedure are started by signals from the master clock of the facility. The ion-pulse buildup procedure is interrupted again by the clock after part of the adiabatic bunching process in the storage rings, and continues upon a signal from the synchronization circuit which evaluates the target tracking information.

Four reactor chambers, denoted A to D, each with a 200 ms average interval between shots, are served by the common driver which therefore works in a 50 ms cycle. The average duration of pulse buildup and delivery is fixed at 45 ms to allow for a maximum deviation of ±5 ms due to target injection scatter.

Figure III.5-6 is an attempt at visualizing the evolvement with time. The target being delivered to chamber B, the driver, the master clock, and the synchronization circuit are each represented by a horizontal line. Every dot means a signal created by the respective component and passed to another component as indicated by a vertical arrow. The start of the driver procedure for a shot to chamber B has been chosen arbitrarily as t = 0. The adiabatic bunching is started at 7.5 ms and interrupted at 36 ms. This interval of 28.5 ms suffices to reach about half the final compression of the bunches. In that state the beam is stable enough to be stored for a buffer time period which may be varied arbitrarily from zero to 10 ms in steps of 2.5 μs.

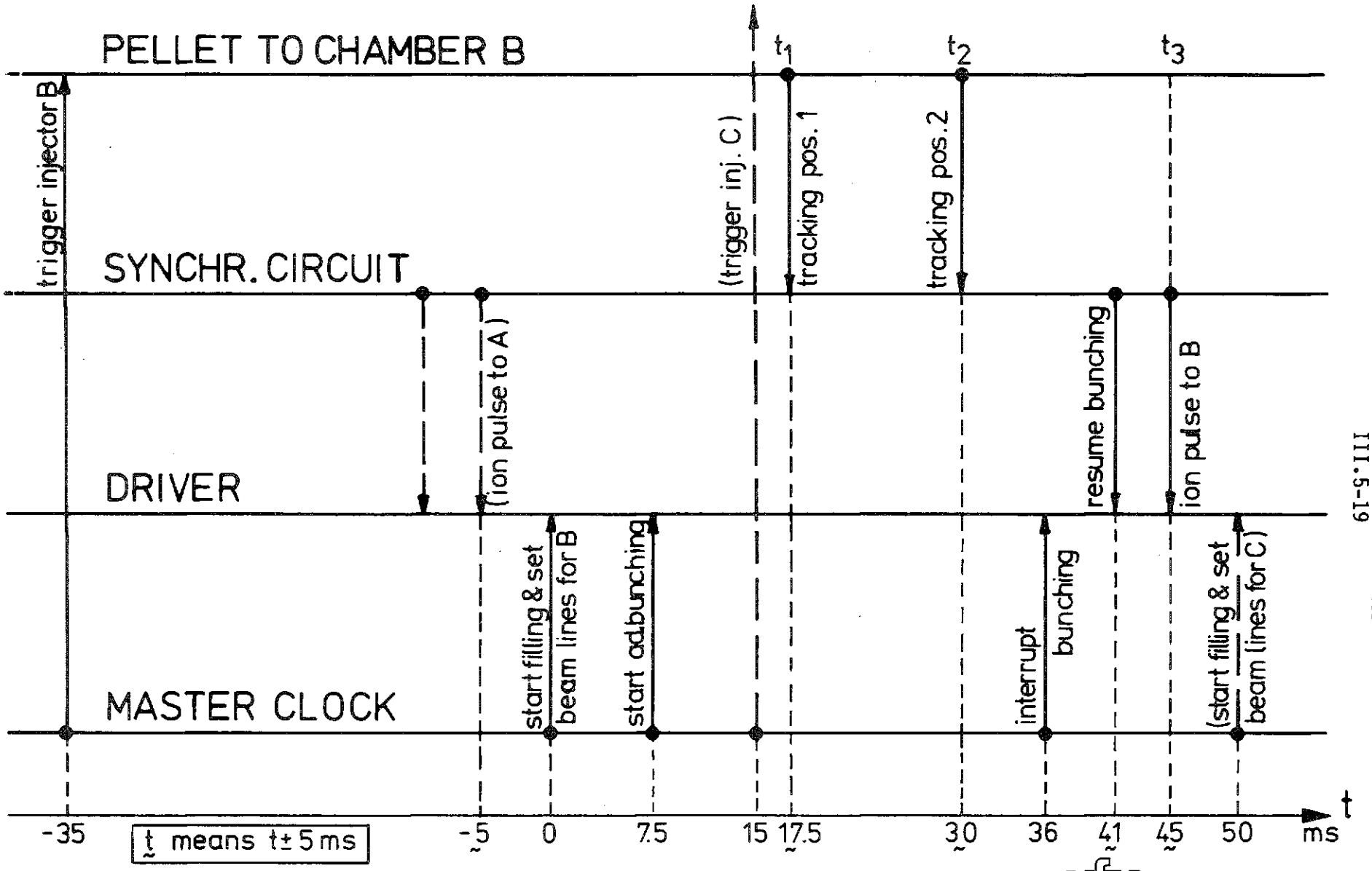

Fig. III. 5-6 SYNCHRONIZATION

At about 30 ms (35 at the latest) the target has passed the second tracking position. Allowing 1 ms for signal processing and computation, the t_3 prediction information is thus available before or at the onset of the buffer period. The synchronizing circuit issues the continuation signal which ends the buffer period by resuming the bunching. After another 4 ms the ions are extracted into the beam transport lines. The subsequent passage to the reactor chamber, including the final fast compression, takes only about 10 μs.

III.5.9 Possibilities of Fine Synchronization

It was shown in sections III.5.3 and III.5.4 that by present knowledge, a target velocity as low as 200 m/s can be used and that in this case the ion-pulse arrival time need not be fixed to better than 2.5 μs so that the discretization introduced by the bunching in the storage rings does not present a problem. However, the safety margin with respect to target heating is not large. If a higher velocity such as 500 or 1000 m/s had to be used one or the other of the possibilities described subsequently that offer a fine adjustment within the 2.5 μs interval would be needed in addition to the "coarse" synchronization described above.

The discrete, periodic points in time at which the ion bunches reach the kicker regions are in principle determined as soon as the bunching RF voltage is switched on. That instant, situated at about 7.5 ms on the time scale of Fig. III.5-6, might be shifted arbitrarily within a 2.5 μs interval so as to make one of the possible pulse arrival instants coincide exactly with a given time t_3. However, this would require the t_3 prediction to be known already 37.5 ms before t_3. For example, at 500 m/s and a 12 m distance to be traveled from the muzzle, the target would not even have left the barrel at that time. Therefore, this is hardly a useful method.

There is also a way to shift the pattern of pulse instants when the bunches are already existing. It consists in varying, for a limited time, the ion energy. As the ion velocity is in the relativistic domain this will change the revolution period even though the magnetic fields would have to be kept constant for practical reasons. However, the beam trajectory is displaced radially, and the storage ring clearance admits only a very limited variation, corresponding e.g., to a relative change of 10^{-4} in the revolution period. Since the necessary shift is at most ±1.25 μs the t_3 prediction would now be needed 12.5 ms in advance.

The third possibility is ion beam steering in the vertical plane. In this case the necessary shift of the ion arrival time is replaced by a shift of the focus location in space, up or down the target trajectory. At a target velocity of 1000 m/s, a ±1.25 μs change in arrival time can obviously be effectuated by a ±1.25 mm focus shift. The corresponding deflection angle of e.g., 1.25 mm/12.5 m = 0.1 mrad can be produced by air-coil magnets. These magnets and their power supplies are less ambitious components than the storage ring kickers as the deflection angle is smaller and the rise time can be much longer. On the other hand, the magnetic field has to be continuously adjustable by a feedback-loop regulating circuit.

Since a few milliseconds would suffice to adjust the steerer fields the t_3 prediction would not be needed any earlier than it is needed for the coarse synchronization.

It may be noted that similar steerers for the horizontal plane could be used, together with target tracking for lateral deviations, to compensate for excessive direction scatter of an injector.

When considering the cost and energy consumption of a steering system it should be noted that such a system may be necessary anyway for a general,

quasistationary adjustment of the twenty beams so that only the feature of individual shot-to-shot adjustment would have to be added.

References for Section III.5

1. C.K. Briggs, R.G. Hickman, R.T. Tesugawa, P.C. Souers, "Estimated Values of Some Cryogenic Properties of Hydrogen Isotopes," IV-12 to IV-21, Radiation Effects and Tritium Technology for Fusion Reactor, Gatlinburg, Tenn. (Oct. 1979).

2. K.A. Brueckner et al., "Assessment of Drivers and Reactors for Inertial Confinement Fusion," AP-1371, Research Project 1346-1, La Jolla Institute (Feb. 1980).

3. R.G. Tomlinson et al., "Pellet and Laser Beam Space-Time Interaction System Study," R 79-954373-1, United Technologies Research Center, Conn. (Nov. 1978).

4. C.T. Chang, L.W. Jorgensen, P. Nielsen, L.L. Lengyel, "The Feasibility of Pellet Re-Fuelling of a Fusion Reactor," Nucl. Fus., 20, 859 (1980).

5. S.L. Milora, "Review of Pellet Fueling," J. Fus. En., 1, 15 (81).

6. F.R. Chang, "Laser Guided Pellets for Inertial Fusion," Nucl. Fus. 20, 537 (1980).

7. R.W. Conn et al., "SOLASE, A Laser Fusion Reactor Study," University of Wisconsin, UWFDM-220 (Dec. 1977).

8. MPP-Mitteilungen, 103, 2 (1981).

9. M.J. Monsler, "Laser Fusion: An Assessment of Pellet Injection, Tracking and Beam Pointing," Proceedings of the 3rd Topical Meeting on The Technology of Controlled Nuclear Fusion, Santa Fe, New Mexico (May 1978).

10. Y.S. Touloukian, R.W. Powell, C.Y. Ho, M.C. Nicolaou, "Thermophysical Properties of Matter," Vol. 10, Thermal Diffusivity, New York-Washington (1973).

11. H.M. Roder, G.E. Childs, R.D. McCarthy, P.E. Angerhofer, "Survey of the Properties of the Hydrogen Isotopes Below Their Critical Temperatures," NBS Technical Note 641 (Aug. 1973).

III.6 Conclusions and Recommendations

The framework of the target design effort for HIBALL is outlined at the beginning of this chapter. Three separate groups at MPQ, KfK, and UW have participated. The parameters used for this HIBALL study are:

Target Gain	83
Target Yield	400 MJ
Ion Beam Energy	4.8 MJ
Beam Power	240 TW
DT Fuel Mass	4 mg
Target Radius	0.3 cm
Ion Energy	10 GeV
Ion Type	Bi^{2+}

These were fixed at the beginning of the study. Subsequent target design efforts at MPQ and KfK have produced target designs that may differ from these fixed parameters. However, in the process we have learned where changes must be made and future HIBALL designs will reflect the increasing capabilities of the MPQ and KfK target design groups. The future overall reactor designs will be based on their specific target design results.

At this stage we are able to make the following specific statements and conclusions:

1. The ICF target gain model of Bodner has been modified to account for the constant pressure fuel configuration at ignition rather than a constant density configuration. Parametric curves generated by this new model are consistent with the target parameters chosen for HIBALL.

2. The one-dimensional Lagrangian hydrodynamics code MINIHY has been implemented at MPQ as a heavy ion beam target design code. This code includes a heavy ion beam deposition package that includes temperature effects.
3. Implosion studies with MINIHY indicate that the maximum beam power of 240 TW chosen for HIBALL is likely to be too low and a power of approximately 500 TW may be necessary to stably implode a target.
4. Implosion studies with MINIHY also indicate that careful pulse shaping is important to efficient implosions.
5. At KfK, the one-dimensional Lagrangian hydrodnamics code, MEDUSA, has been implemented for use as a heavy ion fusion target design code. The MEDUSA code contains analytic equations of state that match very closely with the SESAME equation-of-state tables from LANL.
6. The MEDUSA code has been tested by successfully reproducing the results of a published light ion target design from LLNL.
7. Calculations with MEDUSA indicate that accurate equations of state at high density and low temperature are very important to the accurate simulation of the implosion process.
8. Temperature dependent energy deposition of heavy and light ions can now be computed by a code developed at KfK. Code results were compared to yet another code at UW with remarkably good agreement.
9. From two-dimensional computer simulations of laser irradiated planar targets at NRL we infer that achieving uniform driving pressures with ion beams requires very good illumination uniformity. Much more work is needed in this area.
10. Target injection at 200 m/s is consistent with the switching of the ion beams out of the final storage rings. At this velocity, the target can

be hit within tolerance by switching the ions out at one of the discrete available instants (2.5 μs apart) without any finer adjustment.

11. An injection velocity of 200 m/s allows the target to reach the center of the cavity without any melting of the cryogenic DT fuel.

In the future, the one-dimensional hydrodynamics codes will continue to be developed. However, they have now reached the stage where useful target design information can be produced so more implosion calculations should also be done. More attention should be paid to multidimensional effects such as target illumination uniformity and Rayleigh-Taylor instabilities during the implosion. Some benchmarking of the various codes used in the HIBALL study could also be attempted.

IV Heavy Ion Beam Driver

IV.1 General Philosophy

IV.1.1 Choice of Ion Species

The mass-to-charge ratio of the ions A/q is chosen so that there are no excessive difficulties impeding the deposition of the energy of these ions into the target ablator, without taking into account the compensating effects of any electrons. The basic criterion is that the target, at its "cold" dimensions will not be charged up to a voltage higher than the accelerating sum voltage (kinetic energy/ion charge), or that the ratio of the pulse charge Q over the sum voltage U_Σ, which quantity may be called "beam capacity", be substantially smaller than the electric capacity of the cold target, $4\pi\varepsilon_0 r_{target}$. Formulating two more relations, one for the particle range depending on the kinetic energy and the particle mass, which should be a certain fraction of the target radius r_{target}, and one equation for the required pulse energy QU_Σ, this set of three equations or inequalities has a solution for $A/q > 100$.

If the target would keep its original dimensions during irradiation, at $A/q = 100$ one half of the pulse energy would be invested into electrostatic field energy rather than into ablator heating. The ablating target, however, will send out ions forming a charge sphere which is substantially larger than the cold target, so that indeed the target voltage will be $< U_\Sigma$. Also all the electric fields within the reactor chamber will be so low that the ion motion remains "ballistic" until the ions arrive at the target surface, although these fields are still a matter of concern. Since the occurrence of free electrons is unavoidable, at least within the ablator corona, the electric fields created by the converging and ultimately stopped ion beams have to be a matter of concern and investigation in the future. These free electrons tend to undergo collective acceleration towards the symmetry center (into the target).

Other points of view in the search for a suitable ion species are: low charge-changing cross-sections against collisions with residual gas atoms, or with other ions in the bunches; it should be naturally mono-isotopic, as a matter of costs; easy handling and ionization in the source. For all these reasons we would prefer $^{209}Bi^{2+}$; other choices are $^{133}Cs^{+}$, $^{127}I^{+}$, $^{181}Ta^{+}$ or $^{181}Ta^{2+}$, $^{197}Au^{2+}$. $^{209}Bi^{2+}$ is preferred over Bi^{+} mainly because of the costs for the final focusing lenses which would be nearly prohibitive for an ion stiffness of 200 Tesla-meters, but also because of a slightly lower probability of charge exchange for Bi^{2+} during intra-beam ion-ion collisions.

IV.1.2 Pulse Energy Accumulation

Target implosion requires a driving power of 10^{14} to 10^{15} watts, i.e. a pulse energy of 5 MJ delivered within 10 to 20 nanoseconds. In contrast to the induction linac scheme, this pulse power in HIBALL is not generated in "real time", but a long beam pulse (some milliseconds) is stored, compressed, and then delivered to the target. In the papers of the early HIF workshops[1], this scheme has been called "RF accelerator scenario" (see Fig. IV.1-1).

All the pulse energy is generated in a long RF linac with $U_{\Sigma} = 5 \times 10^{9}$ volts, $I_{beam} = 160$ mA, and $P_{beam} = 800$ MW. Since some short beam pauses are programmed within the pulse, simply by switching the ion current off/on, the pulse has to last 7.5 msec, with a net on-time of 6.3 msec. The particle momentum has to be within a band of a relative width of $\pm 5 \times 10^{-5}$; therefore the beam requires careful debunching. If this band were larger, one would run into difficulties with chromatic aberrations of the final lenses which have to focus the beam onto the target, and a high fraction of the beam would miss the target. The longitudinal emittance of the beam, i.e. the product of beam energy half-width and the pulse time half-width, is critical throughout the scenario, and is more critical than the transverse emittances. While the beam energy is

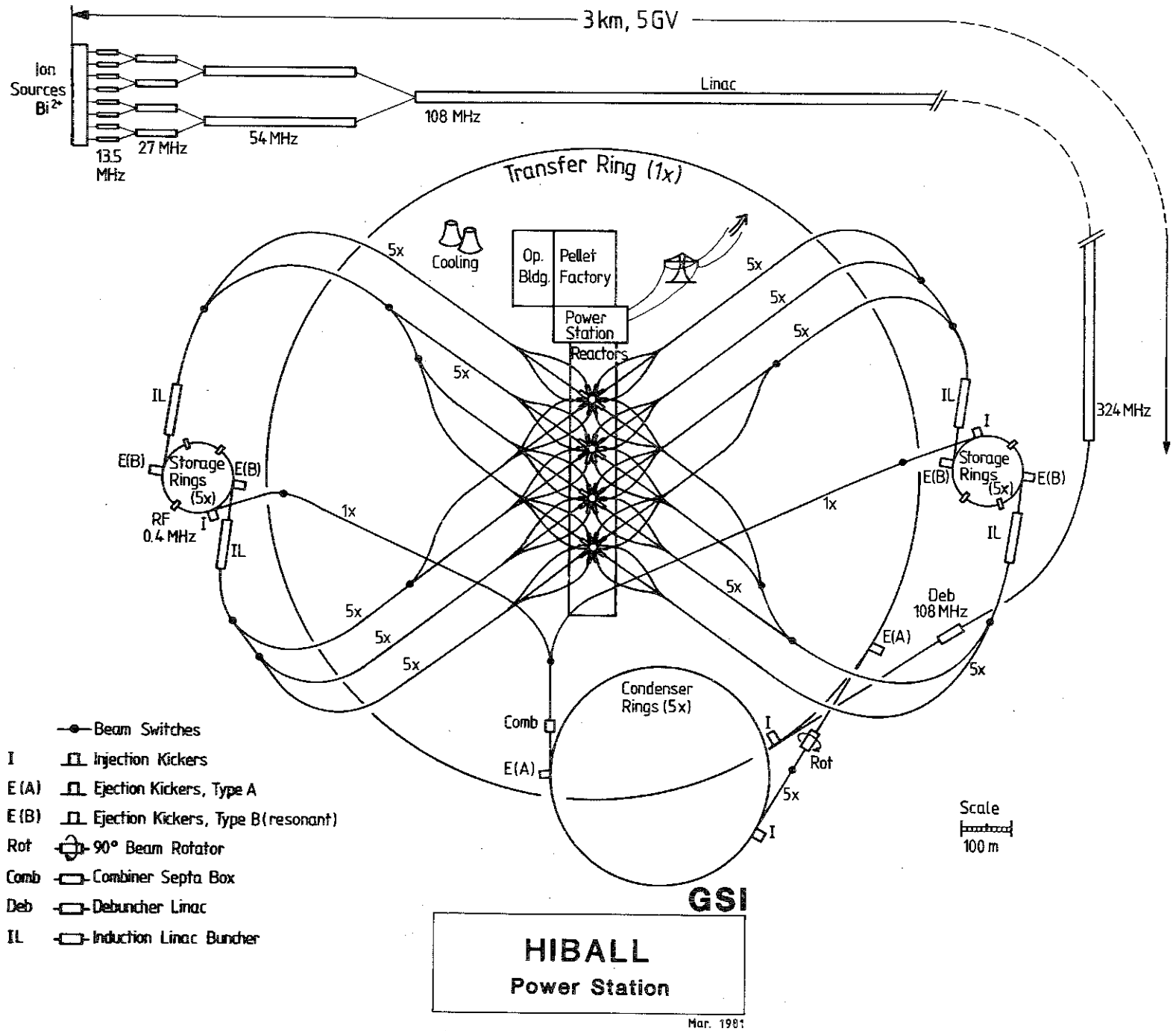
3km, 5GV
Ion Sources Bi2+
13.5 MHz
27 MHz
54 MHz
Linac
108 MHz
Transfer Ring (1x)
Cooling
Op. Bldg.
Pellet Factory
Power Station
Reactors
324 MHz
IL
E(B)
Storage Rings (5x)
RF 0.4 MHz
I
1x
5x
Deb 108 MHz
E(A)
Condenser Rings (5x)
Comb
Rot
Beam Switches
Injection Kickers
Ejection Kickers, Type A
Ejection Kickers, Type B (resonant)
90° Beam Rotator
Combiner Septa Box
Debuncher Linac
Induction Linac Buncher
Scale
100 m
GSI
HIBALL
Power Station
Mar. 1981

Fig. IV.1-1

being generated in the linac, it is piecewise stored in a set of storage rings. It is convenient to think of the storage rings in terms of electric capacitors. The "coherent" space charge limit, which indicates at which stored electric charge Q an allowable tune shift $\Delta\nu$ (difference of betatron oscillation numbers per revolution) occurs, is proportional, among other factors, to the accelerator voltage U_Σ. For long-term storage, $|\Delta\nu|$ is restricted to values < 0.25, or even lower. For a few turns, $|\Delta\nu|$ of even a few units may be tolerated. Other important factors are the transverse emittances ε_H or ε_V of the stored beam, and the bunching factor $B_F = \bar{I}/\hat{I}$, where $\hat{I}$ is the spatial maximum and $\bar{I}$ the average circulating beam current. Non-relativistically, the coherent space charge limit can be expressed as

$$Q = 8\pi^2 \varepsilon_o \, \Delta\nu_H \, \varepsilon_H \left(1 + \sqrt{\frac{\varepsilon_V}{\varepsilon_H}}\right) B_F \, U_\Sigma$$

$$= 1400 \text{ pF/m} \cdot \Delta\nu \, \varepsilon_T \, B_F \, U_\Sigma \qquad \text{for } \varepsilon_H = \varepsilon_V = \varepsilon_T \ .$$

(Shape factors quoted in the original literature (CERN) are in the order of unity in the cases considered here.)

Again, aberrations of the final lenses determine the allowable transverse emittances ε_T. For a target of 3 mm radius, the emittance should not be greater than 60 mm mrad = 6×10^{-5} m per channel or per storage ring, or at least a product of $\varepsilon_H \varepsilon_V = 3600$ (mm mrad)^2 should not be surpassed. Therefore, the electric charge of 10^{-3} Coulomb per pulse has to be distributed into 10 storage rings, of a capacity of 0.02 pF each, to ensure that in none of them $\Delta\nu = 0.25$ is surpassed at $B_F = 1$, or $\Delta\nu = 0.5$ at B_F at 0.5, and so on. For more precise numbers, refer to Fig. IV.1-2. The limits for $\Delta\nu$ which are really safe are not well established; they may be even higher.

Fig. IV.1-2

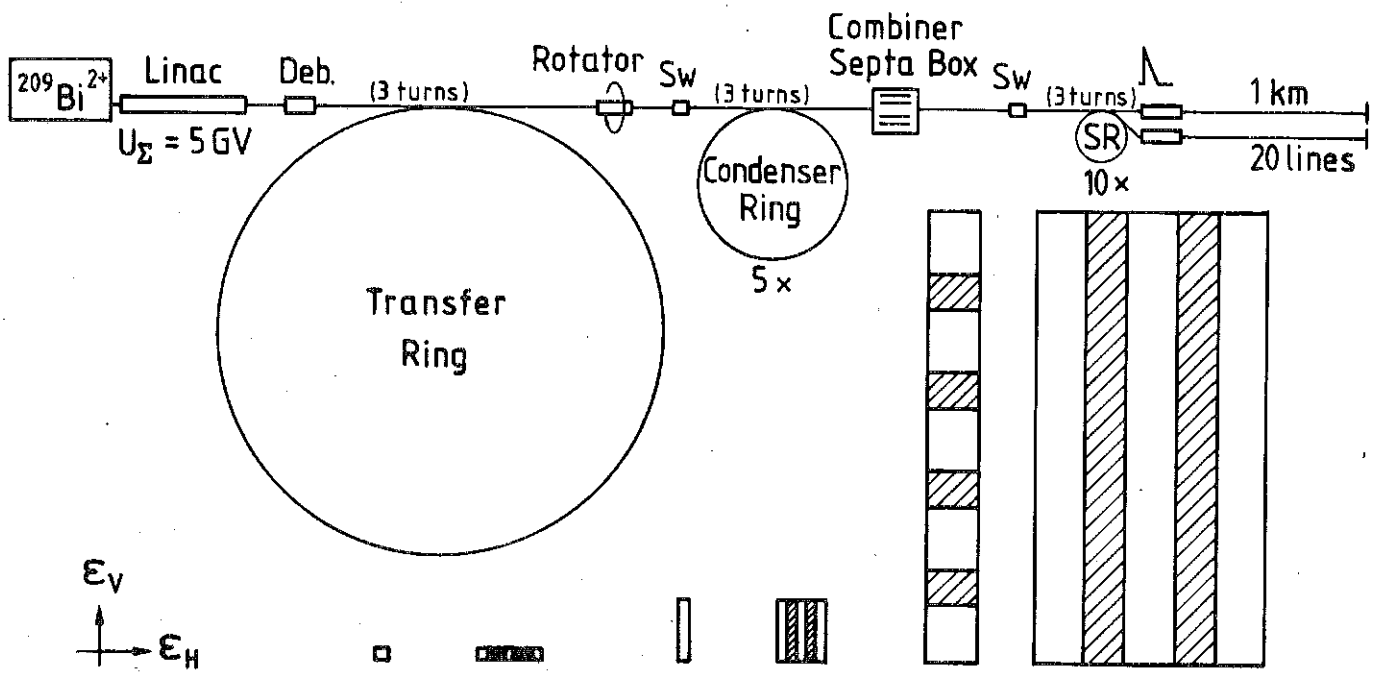

		TR		CR		SR	
Stack. Factor	3		3		5	3	
Dilution Factor	2		1.67		1.5	1.5	
$\varepsilon_H/10^{-6}$ m	2	12	2	10	10	45	
$\varepsilon_V/10^{-6}$ m	2	2	12	12	90	90	
B_F (bunch factor)		0.95		0.95		0.95	0.5 / 0.08
$-\Delta\nu_H$ (hor. tune shift)		0.356		0.287		0.277	0.526 / ≈3.3
$-\Delta\nu_V$ (vert. tune shift)		0.872		0.262		0.196	0.372 / ≈2.3
$C = \overbrace{8\pi^2\varepsilon_0}^{700\ pF/m} \lvert\Delta\nu_1\rvert B_F\varepsilon_1(1+\sqrt{\frac{\varepsilon_i}{\varepsilon_1}})/10^{-15}$ F		4		4		20	
$W = U_\Sigma^2 \cdot C$ / MJ per ring		0.1		0.1		0.5	
$\hat{I}$/Amp	0.16	0.47		1.4		21	40 / 250

Target: 2500 p. channel

$\Delta p/p$: $\pm 5\cdot10^{-4}$ ← $\pm 5\cdot10^{-5}$ → $\pm 8\cdot10^{-5}$ | $\pm 5\cdot10^{-4}$ | $\pm 5\cdot10^{-3}$

τ_{rev}/μsec	45	15	5
Max. residence time/msec	0.25	1.5	20...40

EMITTANCES AND CURRENTS HISTORY, HIBALL POWER STATION SCENARIO, JUNE 1981
5 MJ WITHIN 20 MSEC FROM 20 BEAMS; $^{209}Bi^{2+}$ OF 10 GEV

It is worth noting that the coherent space charge limit is not explicitly dependent on the ring circumference. To obtain pulses as short as possible after (fast) extraction, the rings should be as compact as possible. We anticipate that future developments of superconducting magnet technology will make possible lattices of $\overline{B} \simeq 1.4$ Tesla (with local magnetic fields of 4.5 Tesla), in which Bi^{2+} ions circulate with a revolution time of 5 μsec. With respect to the chromatic aberrations of the final lenses, it turns out that only half of the 5 μsec, namely 2.5 μsec can be processed in one beam channel, and that each ring needs two exits, resulting in 20 beam lines into the target chamber. This number of beam lines is needed for another reason, namely the space-charge transport capacity of individual channels (see Chapter V). On one hand, therefore, it is not necessary to look for denser ring lattices; on the other hand, less dense lattices would require a larger number of exits per ring, or a larger total number of beam lines, or alternatively a narrower $\Delta p/p$ distribution in the rings. It seems as if there is no other reasonable choice for $\overline{B}$, at least for the given set of target parameters.

The assumption of what energy or momentum spread is reasonable in the ring for the forementioned consideration is a result of evaluations of linac particle dynamics, as a trade-off with current-transport considerations. The figure of $\Delta p/p = \pm 5 \times 10^{-5}$ then is the lower limit of what can be achieved with a careful design of the first part of the linac, the RFQ section, and under the assumption of conservation of the longinal emittance.

Two risks are worth mentioning. One is the question of whether debunching a beam in order to arrive at a very good energy definition is possible under the influence of (nonlinear) longitudinal space charge forces. The other is the risk of self-bunching of the beam into erratic bunch modes while coasting in the storage rings. It is known that this self-bunching occurs at

a given level of $\hat{I}/(\Delta p/p)$, and that it is dependent on the number of coasting revolutions. Both questions are the subject of experimental investigations planned on the SNS proton ring at Rutherford Laboratory which will be constructed in the next few years. It is planned to check measures (active feedback) to push $\hat{I}/(\Delta p/p)$ to as high a level as possible.

Next a description of how the beam is put into the storage rings will be given. The part of the linac beam which is to be wrapped into one storage ring has a (virtual) length of 0.675 msec βc = 62.5 km, which is 135 times the circumference of a storage ring. It is, physically and technically, impossible to do a 135-turn radial multiterm injection. Since a combined radial-vertical stacking procedure also seems to be too difficult, (handling a beam power of 800 MW (!)), the next idea is to wrap the beam in a large "transfer" ring radially, say 10 turns, extract it, rotate it by 90°, and wrap it radially again by, say, 15 or 20 turns. Besides the fact that a turn number as high as 10 is still too risky, the additional difficulty is that the coherent tune shift of the beam in the transfer ring is so high that the transverse stacking procedure is disturbed (the same 10^{-4} Coulomb as in the storage ring, with a far smaller transverse beam emittance). So this scheme proves to be impossible.

One solution, a multiplicity of transfer rings all being discharged at one time into one of the storage rings, has been proposed by N.M. King.[2] A still lower risk solution is given here; see Fig. IV.1-1. A transfer ring with a circumference nine times that of a storage ring is filled with three turns. After extraction the beam is rotated by 90° and injected into one of five "condenser" rings, again with three turns. This is repeated five times until all the five condenser rings have been filled. All five rings are discharged simultaneously, their beams are combined in an inverse static beam splitter (as it is in use at UNILAC for 3 beams) and injected into the storage

rings, again with three turns. Now stacking has been done in four steps, with the associated stacking factors of 3,3,5,3, whose product is 135. Though the associated dilution factors also multiply up to the fourth power, the product is small since each of the factors can be kept small when only three turns are stacked.

As proof of physical consistency, the beam emittances, tune shift, currents, etc., are listed in Fig. IV.1-2. The time schedule for the linac pulsing, and the destinations of the individual parts of the linac pulse, are indicated in Fig. IV.1-3.

Up to now, ten energy stores have been filled with all the driving energy needed. If discharged through the 20 extraction channels, the 2.5 μsec long pulses would still be too long. The momentum width in the stored beam of $\Delta p/p = \pm 5 \times 10^{-5}$ allows us to shape the contents into pulses of 20 nsec length and $\pm 5 \times 10^{-3}$ relative momentum half-width, of elliptical phase-space configuration.

Though this is simply possible from Liouville's theorem, the expense for doing this is not trivial. First of all, it requires careful adiabatic bunching in the storage rings, by means of multiplying an RF voltage of exponentially increasing amplitude. Since in the beginning the synchrotron frequency is very low, it requires many milliseconds until a bunching factor of $B_F = 0.5$ is reached. From there on, bunching is faster, but the required RF amplitudes become higher and higher. Therefore, from a suitably chosen point on, bunching should no longer be adiabatic but "fast".

One part of fast bunching is done in the storage rings themselves, by means of the RF cavities (0.4 MHz) whose voltage is raised to a high value suddenly. The second part is done outside the rings in an induction linac

Fig. IV.1-3

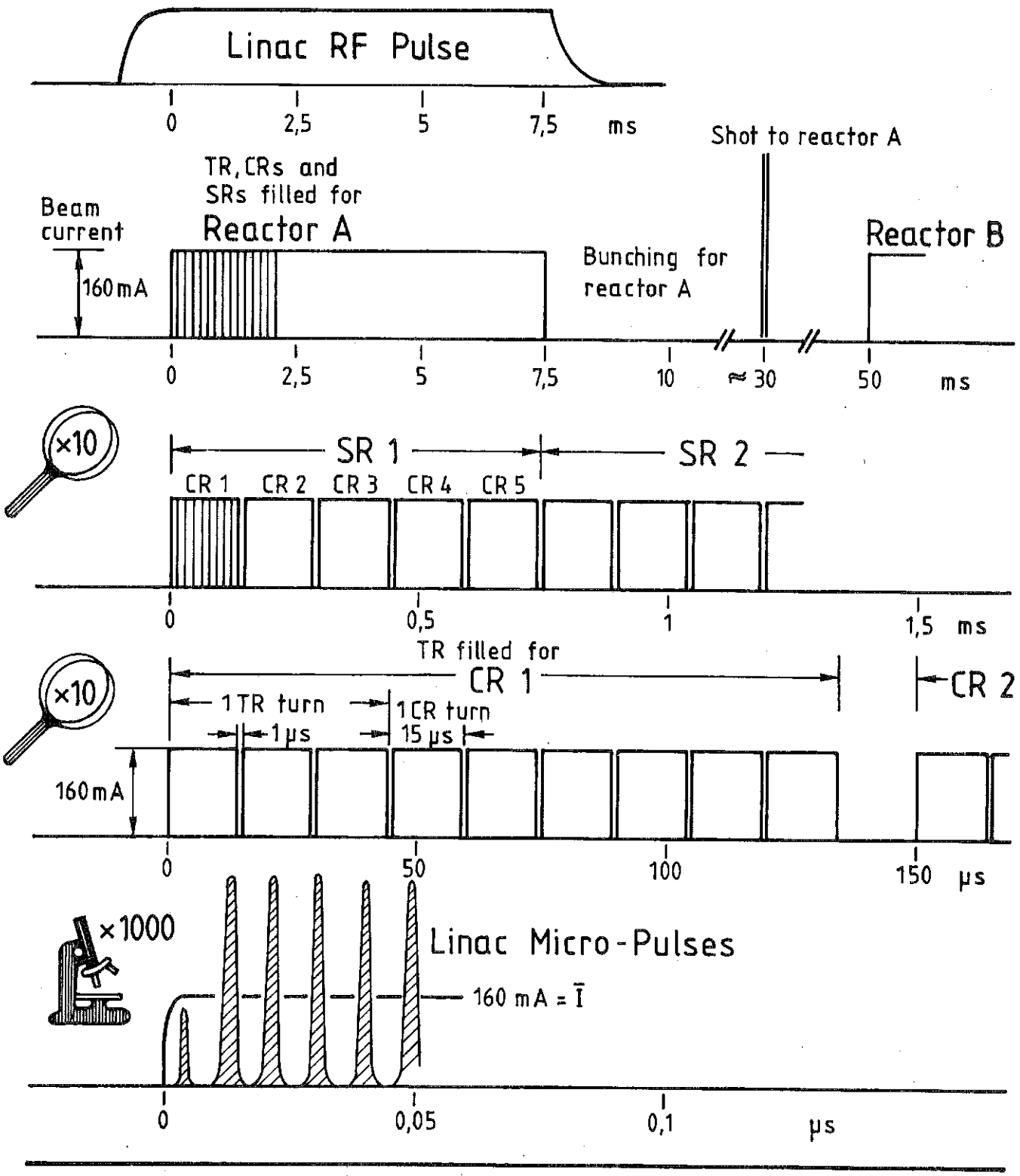

LINAC PULSE TIMING

- HIBALL -
Mar. 81

with sawtooth voltage, and the bunch comes to a time focus after a roughly 1 km long drift. Because of the importance to the investment costs, the details of this procedure are described in a separate section (IV.9).

References for Section IV.1

1. Proceedings of Heavy Ion Fusion Workshops: New York, Oct. 17-21, 1977, BNL-50769; Argonne, Sept. 19-26, 1978, ANL-79-41; Berkeley, Oct. 29-Nov. 9, 1979, LBL-10301/SLAC-PUB-2575.

2. N.M. King, J.R.M. Maidment, "A Storage Ring System for HIF," RL-81-007 (1981).

IV.2 Ion Source

The design goals for the ion source are 50 mA of heavy ions with $A/q \simeq 110$ and a normalized emittance ε_n ($\varepsilon_n = \beta\gamma\varepsilon$, $\varepsilon = F/\pi$, F = area of emittance figure) of $\varepsilon_n < 2 \times 10^{-7}$ m. The desired brightness $B_n = I/(\varepsilon_n^{vert}\ \varepsilon_n^{hor})$, $B_n > 1.25 \times 10^{12}$ A/m^2 implies that the space charge of the extracted ion beam is almost completely compensated. Therefore, the source must provide a homogeneous, stable emitting surface, and the extraction system includes an electron suppressing electrode.

The emitting surface may be either solid (contact ionization sources, limited to very few materials like cesium) or a plasma sheath. As the future knowledge of charge exchange cross sections within the beam may ultimately determine the choice of the ion species a plasma source with its wide range of feeding materials offers great advantages over the former one and was preferred here.

The plasma of our source is generated by a low voltage, heated cathode discharge within a cylindrical anode, and confined radially by a magnetic multipole and axially by two reflector electrodes. This geometry has proved its value with Q (quiet plasma) machines[1] and neutral injection sources.[2]

As a first model, we developed a source for operation with gases, ELSIRE (Einzel-Ladungs-Schwer-Ionen-Reflex-Entladung)[3] which yielded, for example, 26 mA Xe ions with a brightness of $B_n = 1.5 \times 10^{12}$ A/m^2, using a 7-hole extraction system with 0.5 cm^2 total aperture area. An extension of the extraction area up to 1.5 cm^2 is possible and should result in about a 75 mA ion current. Single hole extraction (0.2 cm^2 area) was also tried and gave 4.3 mA with $B_n = 1.37 \times 10^{13}$ A/m^2, but at the extraction voltages involved (20-50 kV) one cannot enlarge this one aperture without severely losing brightness. This limitation may be lost when one extracts directly with a several hundred kV

extraction voltage, using a 4-electrode system. A first step in this direction, designing a 75 kV 4-electrode system, has actually been started.

ELSIRE was extensively tested with helium for high current accelerator experiments,[4] and exhibited good reliability and stable operation without interruption for 50 hours (50 Hz pulses, each one 2 ms long).

For the generation of metal plasmas, the source HORDIS (Hot Reflex Discharge Ion Source)[5] was constructed. It has an electrode configuration identical to that of ELSIRE, but all electrodes are suspended on poorly heat-conducting structures and run hot during source operation. The metal vapor is produced in an oven and conducted through the cathode into the discharge volume. First tests showed that the discharge can be run in a pure metal plasma after the source had been heated up using an auxiliary gas.

The ion species of interest for HIBALL is $^{209}Bi^{2+}$. For a copious production of the second charge state the discharge must be run at quite high power as then both voltage and density of the ionizing electrons are enhanced. High plasma density, on the other hand, means that the extraction apertures must be small, in order not to have the terminating plasma sheath protruding outwards which would cause a badly mismatched beam.

At an oven temperature of 990°C, an 8 mA bismuth beam was extracted from 0.34 cm^2 (7 holes) area at 31 kV. This beam contained 3.2 mA (28% particles) of Bi^{2+}, the brightness for Bi^{2+} then was $B_n > 5 \times 10^{11}$ A/m^2 (calculated from the beam line acceptance; the emittance was not measured). While it seems impossible to further raise the relative abundance of the Bi^{2+} charge state, there is a good chance to increase the total ion beam current by using 13 or even 19 extraction holes.

For still larger extraction areas the source discharge chamber has to be modified. So, presently a wider source, HORDIS II, is in the design state.

One should underline, however, that the calculated lower limit for the brightness is a factor of 3 beneath the design value, and increasing the extraction area can never lead to higher brightness, even with proportionally growing absolute ion current.

Therefore, from the viewpoint on the ion source, ions like In^+ or $^{127}I^+$ are much preferrable as the first charge state can always be extracted with more than 95% abundance. Reduced discharge power, then, would be also beneficial for source life-time and reliability. Once Bi^{2+} is given up, one should also think again of Xe^+ (possibly one enriched isotope) or $^{133}Cs^+$ as candidates.

When employing singly charged, mono-isotopic ions, one can also leave out mass separation before the pre-accelerator and thus eliminate another difficulty, that is, the emittance growth due to loss of space charge compensation and aberrations. This effect had been encountered during the helium experiments.(4) The emittance grew by a factor of 5 when the beam was passed through a magnetic quadrupole triplet. On the test stand this growth could only partially be reduced by once more compensating the space charge, raising the background pressure in the beam line behind the lens. It is doubtful, however, if this technique can be applied to a pre-accelerator beam line. A low voltage beam line as short as possible is therefore strongly indicated by the experiences gained.

References for Section IV.2

1. R. Limpaecher, K.R. McKenzie, Rev. Sci. Instr. 44, 726 (1973).

2. A. Goede, R.S. Green, B. Singh, 8th Europ. Conf. on Controlled Fusion and Plasma Physics, Prague (1977).

3. R. Keller, 3rd Int. Conf. Ion Implantation: Equipment and Technology, Kingston (1980).

4. J. Klabunde, N. Angert, R. Keller, P. Spädtke, J. Struckmeier, H. Trautmann, Particle Accelerator Conf., Washington (1981).

5. R. Keller, F. Nöhmayer, P. Spädtke, to be published.

IV.3 Low-Velocity Accelerator Tree

Several reasons dictate the start of linac acceleration with a low RF frequency, in the specific case, of 13.5 MHz. To have a safe and reliable pre-acceleration technology with quick access to the sources, and to facilitate adiabatic bunching in an RFQ structure, the platform voltage should not be above 0.5 MV. This is our specific choice, based on UNILAC experiences. There are approaches of another group (ANL) with considerably higher static pre-acceleration voltage, losing some of the abovementioned features without arriving at a considerably higher basic frequency.

Always, the velocity βc of the very heavy ions is low, and to arrive at a reasonably long drift tube length, $\beta\lambda/2$, to house the focusing quadrupoles, the only way is to choose the wave length λ high enough or the frequency $f = c/\lambda$ low enough.

A second reason is the space charge transport limit of linear accelerators. For a given transverse acceptance, this limit is proportional to the spatial betatron frequency, σ_0/S, where σ_0 is the phase advance of the betatron oscillation per unit cell length S. In the case of a magnetically, or better, electrostatically focused linac, where the number of quadrupoles of one polarity within one FODO group has no principal limit, the main point of view for the frequency choice is a technical one. For an RFQ accelerator the period length is $\beta\lambda$. Generally, the frequency choice in both cases is not substantially different, but the RFQ accelerator, because of a higher σ_0/S, has the higher beam transport capability. The frequency then should be chosen so that $\sigma_0 \approx 1$ radian, with the electric field strength limited by sparking.

This low frequency, on the other hand, allows one to multiply the beam current in subsequent accelerator sections by injecting into them several (here, two) beams out of a corresponding number of linear accelerators. This

must always be accompanied by a jump of the RF frequency by at least this factor. By this jump of frequency an appropriate number of new RF buckets is created into which the bunches of the injecting linacs are installed, simply by a transversely deflecting RF field of the frequency of the foregoing section. Doing this repeatedly, the low-velocity end of the linac then has the shape of a tree with, e.g., 8 branches of 13.5 MHz confluent into one beam at 108 MHz. This so-called "funneling" scheme is an old idea and is based on several favorable effects:

a) At constant acceleration gradients, and constant equilibrium phase, the bunch width of a beam shrinks like $\beta^{-3/4}$, the well-known phase damping. If the frequency is suddenly doubled, the bucket shape ratio changes with $f^{1/2}$ in such a manner that a matched beam would then have a smaller phase width as $f^{-1/4}$. Generally, at a frequency jump rebunching is necessary to match the beam into the new bucket shape, and it is necessary anyway in order to transport the beam across the funneling deflector (it is also the same reason for which transverse lenses are needed). In total, one can double the frequency after every piece of linac which doubles the particle velocity, provided the acceleration gradient E_{eff} and the equilibrium phase ϕ_s remain unchanged.

In our specific case the adiabatic bunching process is finished at $\beta = 1\%$, or $W = 10$ MeV, a sum voltage of $U_\Sigma = 5$ MV, at a frequency of 13.5 MHz, and at an acceleration gradient of $E_{eff} = 0.6$ MeV/m. At $\beta = 8\%$, $W = 600$ MeV, $U_\Sigma = 300$ MV, or after roughly 200 m length of structure, all eight beams have been combined into one at 108 MHz. Since there $E_{eff} = 2$ MV/m, the phase width is only $60° \cdot (0.6/2)^{1/4} = 44.4°$. For this reason, one might combine the beams even earlier.

b) The transverse space charge "bottleneck" of any linear accelerator is found at its beginning, at low velocities. This is true also at the frequency jumps, as it is seen from analysis of any available formula, or from a simple consideration. Though in a specific structure the geometric length of individual bunches increases slightly as $(\beta\lambda)^{1/4}$, it is compressed again to its original length at a frequency jump with proper longitudinal matching. Also with a constant transverse tune σ_T, the transverse dimensions do not change. Overall, the volume of an individual bunch, and hence the local forces (transverse and longitudinal) seen in the moving frame of the bunch, remain in the same order of magnitude; otherwise the dimensions of the bunch could not remain constant. This consideration is only non-relativistic; with the approach to the velocity of light the space-charge limits are at higher currents.

In the bunch frame, neighboring bunches are shifted away from the observer's bunch; this fact may slightly modify longitudinal space charge forces. But, at a frequency jump, new bunches are inserted, and the observer has the impression of seeing neighboring bunches as close as at the beginning of the foregoing cycle. So, if the space charge limits have been checked for a piece of linac which doubles the particle velocity, one can rely upon the ratio of space-charge forces to external forces being the same again after doubling the frequency and doubling the beam current by inserting new bunches into the new buckets.

After explaining the physical conditions, a technical description of the low-velocity linac tree is to be given. At the beginning, there are eight (alternatively 16) sources, followed by a charge selection and a fast chopping device. For reasons of maintenance, the source should be arranged on separate high voltage platforms, rather than on a common platform. Each platform is on

a positive voltage of 252 kV, powered by a power supply for at least 10 mA, buffered by a capacity of least 75 nF (voltage drop less than 5 kV when 375 μC = 50 mA x 7.5 ms are taken), and housed in an RF-tight cabinet. Static acceleration columns for high current (20 mA ions) are under development; it is sure that they can be made with good optical properties.

Arriving at ground potential, the beam is focused into the transverse acceptance of an RFQ accelerator which will be described in the next section. Here the beam is still a d.c. beam. One or two wide-aperture triplets, and a space-charge correction lens will be needed.

The linac tree begins with 8 parallel RFQ linacs at 13.5 MHz, followed by 4 parallel Widerøe linacs of 27 MHz, 2 parallel Widerøe or Alvarez linacs of 54 MHz, and one Alvarez linac whose first section operates at 108 MHz. In-between, funneling and rebuncher sections combine the beams.

IV.4 RFQ Section

At low particle velocities, focusing by electric quadrupole fields is more effective than by magnetic fields. Feeding the quadrupoles with RF, a higher field strength can be maintained compared with dc voltages, especially since support insulators can be avoided. Though RF power is more expensive to produce than the same amount of dc power, with a careful design one can build the accelerator at a far lower expense per megavolt than a drift tube linac with static focusing devices.

This explains why adiabatic bunching of a dc beam into RF buckets is mostly mentioned in connection with RFQ structures. Adiabatic bunching which in principle is possible with any linac type, demands a certain additional length of linac which normally is regarded to be too expensive for this purpose. An additional reason is that transverse focusing should be very vigorous to avoid excessive long-trans coupling (especially the parametric coupling resonance), and this again would make other structures than the RFQ less effective. Especially, the combination of currents of $^{209}Bi^{2+}$ ions of 20 mA, adiabatic and loss-free bunching out of a particle energy of 0.5 MeV and a frequency of 13.5 MHz is only possible with RFQ techniques.

In an ingenious concept Kapchinskij and Teplyakov[1] have demonstrated how to use RFQ techniques in the most efficient way. Since then, several groups have begun to design or to build RFQ structures, the most successful of which was at Los Alamos. Nearly all of these were for protons or light ions ($A/q < 3$); also the original concept of Kapchinskij and Teplyakov was designed for light ions at fairly high frequencies (> 100 MHz).

Beside an incomplete design of D. Swenson[2] for very heavy ions ($A/q = 100$) the only effort to design an RFQ accelerator for these ions (or even heavier ones) at low frequencies around 10 MHz up to now has been made jointly

by GSI of Darmstadt and the University of Frankfurt. The RF system of this accelerator is quite different from the light ion types.[3] Its features are good power economy in spite of a high capacitive load of the RF cavity (or a good "shunt impedance"), and very good stability of the voltage distribution along the accelerator against disturbing influences (capacitances, geometric errors). A proton model of this design, scaled down 1:4 has been put into operation. Now (1981) a prototype of a full-scale accelerator cavity is built, with a slightly smaller transverse acceptance. As a novelty, so-called radial matching sections are installed at the beginning as well as at the end. By this measure it is tried to keep the transverse emittance blow-up as small as possible. We hope for an emittance blow-up factor as small as 1.5 to 2.0, and this hope is nourished by calculations of the Los Alamos group. A maximum blow-up factor of 3.0 would be tolerable.

A specific problem with adiabatic bunching is the longitudinal emittance of the beam. Without a so-called shaper section, the longitudinal emittance is determined by the fairly large longitudinal acceptance of the so-called "gentle-buncher" into which the beam is filamentated. To decrease the emittance, i.e. to avoid some of the filamentation, a so-called "shaper section" is used before, with no acceleration at all, but with a rising longitudinal field amplitude. Its problem is that it should be very long to be very effective. With a 1 m long shaper, 18 $\beta\lambda$ periods, the longitudinal emittance is 50 degrees x keV/amu, compared with 140 deg x keV/amu without any shaper. The longitudinal emittance should be smaller than 25 deg x keV/amu for the HIBALL accelerator. At the time of writing we try to determine how long the shaper should be. A longer shaper does not improve the capture efficiency substantially, which is now 80 to 90%. Figure IV.4-1 shows a longitudinal section through the RFQ cavity prototype.

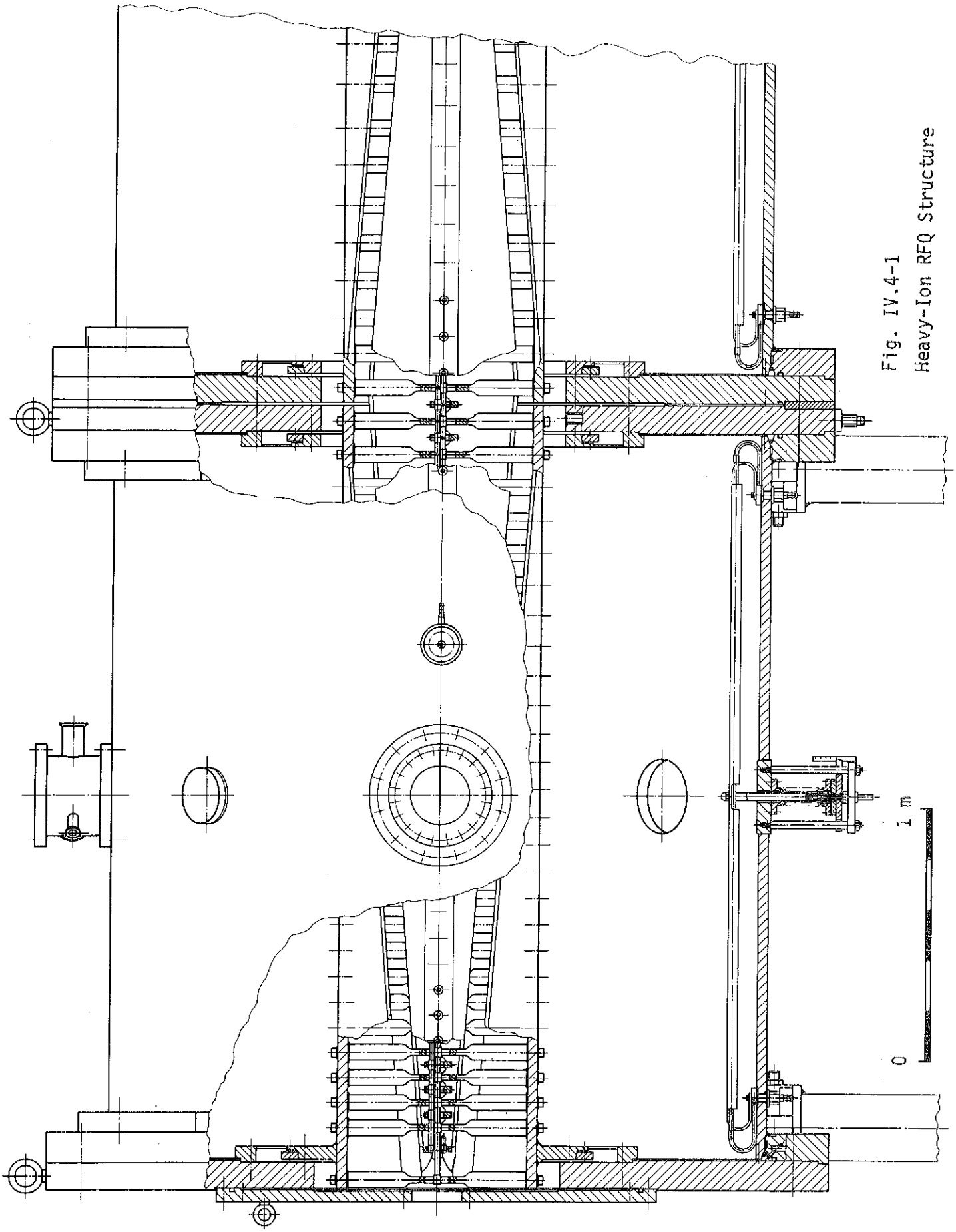

Fig. IV.4-1
Heavy-Ion RFQ Structure

References for Section IV.4

1. I.M. Kapchinskij, V.A. Teplyakov, Pribory i Tekh. Eksp. (1970), 19-22; I.M. Kapchinskij, IHP-INZH 72-29, Serpukhov 1972; translation: GSI-tr-14/76.

2. D.A. Swenson, Proc. HIF Accel. Study, Berkeley, CA (Oct./Nov. 1979).

3. R.W.Müller, Report GSI 79-7 (1979).

IV.5 Wideröe and Alvarez Sections

This is the most conservative and best developed part of the facility. Though it has to be designed for a lower specific ion charge q/A, its technical features may be widely identical with the GSI design of UNILAC cavities, except for the total lengths. Descriptions have to be omitted here, they may be taken from the literature.[1-3] Figure IV.5-1 gives a parameter table of the linac.

While UNILAC is composed of 27.1 and 108.4 MHz structures only, there will be an intermediate 54.2 MHz structure also, probably of the Wideröe design. This structure has not yet been detailed.

Calculations and experiments done recently[4] show that the beam transport capability of the Wideröe structure is sufficient for HIBALL, except the first part of UNILAC cavity W1, the very first one, which in HIBALL will be replaced by an RFQ cavity, see section IV.4.

The last part of the linac, but the largest one as measured in terms of length of structure and installed power, is a 325.2 MHz Alvarez structure. This frequency is preferred over 216.8 MHz because there is no mature power-amplifier technology available between 108 MHz (upper end of FM radio) and the onset of klystron technology for which only recently high-power klystrons of 324 MHz have been developed. This consideration was one of the important reasons of the frequency choice (108 and 324 MHz) for the SNQ Project,[5] a 1.1 GeV proton linac for an intense neutron source. In this project also the type of structure changed in favor of the "disc-and-washer" structure at this frequency jump. We are, however, not able to choose another type of cavity than the Alvarez structure for two reasons: (1) For reasons of space charge transport we have to provide one quadrupole magnet per $\beta\lambda$, i.e. the length of one FODO period should not be more than 1 $\beta\lambda$; so we may not choose a structure

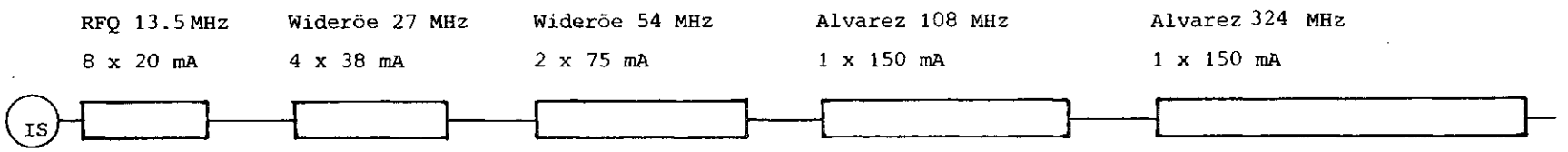

β in %	1,5	3	6	12	32	
W in MeV/u	0,1	0,4	1,7	6,5	50	
ΔU in MV	10	30	130	480	4350	Σ = 5000 MV
Acc. Rate in MV/m	0.5	1	1.25	1.5	1.75	
Length in m	20	30	104	320	2500	Σ = 3000 m
RF Peak Power in MW/m	0.03	0.034	0.05	0.072	0.1	
RF Peak Power per Section	4.8	4.4	10.4	23	250	Σ = 293 MW
RF Duty Factor	0.154	0.154	0.154	0.164	0.155	
Average RF Power	1.22	0.68	1.6	3.8	38.5	Σ = 45.8 MW

Comments: Acc.Rate = $E_o \cdot T \cdot \cos\phi_s$
E_o = Average Axial Field
T = Transittime Factor ∿ 0.86
ϕ_s = Synchron.Phase Angle = - 30°
RF Peak Pwr in MW/m = E_o^2/Z_o
Z_o = Shunt impedance = 50 MΩ/m

Fig. IV.5-1: Preliminary HIBALL Linac Parameters

of "separate functions". (2) The main parameter that determines whether the shunt impedance (which is a figure of merit for optimal power economy) is near its maximum, is the particle velocity. $\beta = 0.32$ is well within the domain of Alvarez, and clearly outside the domain of disc and washer. A little problem seems to arise from the diameter of drift tubes which cannot be scaled down to proportional to λ since the bore diameter does not scale this way. Nevertheless, even if the optimum of drift tube diameter (about 5 to 10% of λ) cannot be matched, the shunt impedance still is higher at 325.2 MHz than at 216.8 MHz. Moreover it is hoped to draw advantage from the newly-developed permanent-quadrupole magnet technology[5] by designing smaller (and energy-conserving) drift tubes.

Probably it will not be necessary to equip the linac with remote handling maintenance devices, in contrast to high-intensity proton and deuteron machines. If ions hit solid materials, elastic and inelastic scattering dominate largely over nuclear reactions. At UNILAC, residual radioactivity in linac components is negligible except in the beam splitter septa which routinely are hit by a large fraction of the beam. However, this device too does not require remote handling. In HIBALL, beam intensities are three or four orders of magnitude higher. Then drift tubes etc. will become slightly radioactive, but only septa in the storage rings will require remote handling.

The RF amplifier systems probably will look a little different from UNILAC techniques. 50% to 75% of the RF power, about 800 MW, will be taken by the beam. Then the 50 Ohm power transmission lines between the amplifiers and the accelerator structures which, though expensive, represent an advantage for status diagnostics under a small beam load, are no longer very reasonable. Instead, we may think of tetrode amplifiers which are coupled directly, on a high impedance level, to the accelerator structures. This may result in

smaller units also, the modularity of these units may improve the reliability. These trends at present do not apply to klystron amplifiers which normally have to operate into a matched waveguide line.

References for Section IV.5

1. K. Kaspar, "The Prestripper Accelerator of the UNILAC," Proton Lin. Acc. Conf., Chalk River (1976).

2. D. Böhne, "The UNILAC, Development and Present Status," Proton Lin. Acc. Conf., Chalk River (1976).

3. T. Niewodniczanski, E. Malwitz, "Mechanical Design Features of the UNILAC," Proton Linear Acc. Conf., Los Alamos (1972).

4. J. Klabunde et al., "High Current Expeiments in a Widerøe Structure," IEEE Trans. NS-28 (1981), 3452-4, Accel. Conf., Washington, D.C. (1981).

5. J.E. Vetter (Ed.), "The Basic Concept of the SNQ Lin. Accelerator," KfK 3180 B (June 1981).

IV.6 Funneling

The purpose of the funneling sections has been described in section IV.1, and is shortly repeated here.

In linacs, the frequency can be doubled each time the velocity of particles has been doubled. At this point, one can combine the beams of two foregoing linacs into the one of higher frequency without any disadvantages concerning space charge containment, since the linac of higher frequency contains double the number of RF buckets. One needs, however, a switch which brings the beams of both foregoing linacs into a common beam axis.

Though in principle one would need a deflector with a step-function behavior (meander or trapez function), in practice a sine function deflecting field will do. The frequency of the deflecting field is that of the foregoing linac, i.e. to combine the beams of two 54.2 MHz linacs into one 108.4 MHz linac, one would use a 54.2 MHz transverse deflector.

Another question is whether the electric field necessarily travels along with the beam pulses, or whether a standing-wave cavity may be used. In the case of sinusoidal field, the field strength which can be generated is high enough to apply a standing wave. The practical problem of a funneling section is that rebunching cavities (for properly matching into the next structure), quadrupole lenses, bending magnets and a septum magnet also have to be arranged in the beam path.

Because of the limited "aperture" of the "time lenses", as rebunchers can be looked at, given by the useful phase width of the sinus curve which has to be sufficiently linear, the space between two rebuncher cavities, or the distance to the objects which have to be matched to, is limited to a few meters. Generally, funneling sections tend to be short and crowded. This problem is looked at by K. Bongardt at KfK. A preliminary design is shown in Fig. IV.6-1,

Fig. IV.6-1

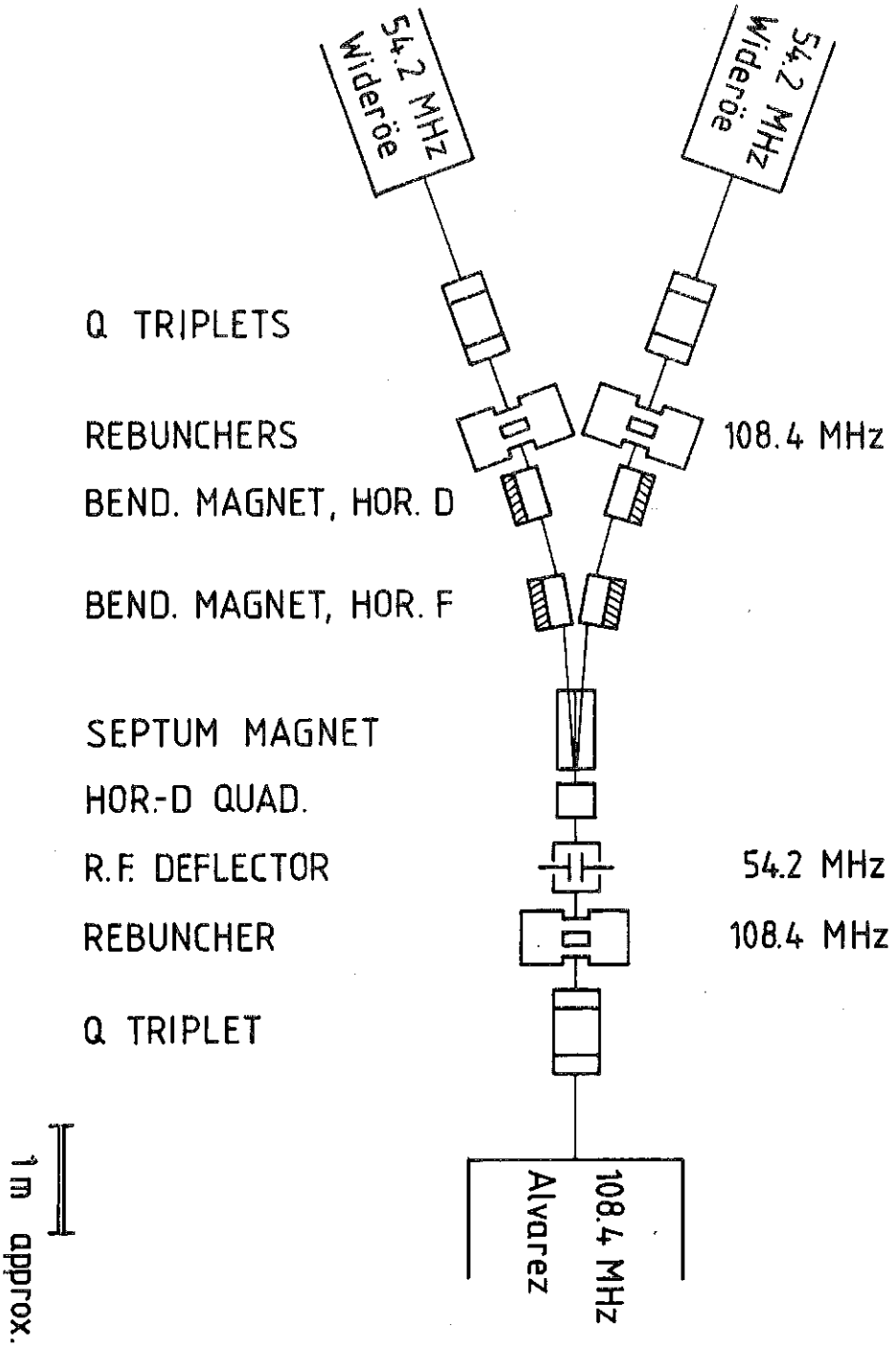

EXAMPLE FOR A FUNNELING SECTION

based on a two-rebuncher-cavity design (which gives enough flexibility for matching).

IV.7 Rings, Lattice, and Magnet Technology

The purpose of the storage ring system, its basic properties and how it fits into the driver concept of HIBALL have been described in Chapter IV.1. Here, additional technical details will be discussed. No significant problems are expected to occur in the transfer ring or in the condenser rings due to their large circumference, the relatively low coasting beam current, and the lower electric charge. Therefore, attention is focused on the small storage rings where part of the necessary bunching procedure takes place. These rings have to be built as compact as possible to minimize the revolution time. On the other hand, that may induce practical problems if the available space in the magnet lattice is too limited for installing beam sensors, RF cavities, correction magnets, and beam manipulating elements.

IV.7.1 Magnet Lattice

The most efficient high-quality lattice for providing alternating gradient transverse focusing is that composed of FODOFODO-cells with bending dipoles placed in space O between quadrupoles F and D. For simultaneous extraction of two bunched beam segments it is convenient that the lattice be made up of 4 identical sectors, the superperiods, each of them consisting of 10 normal periods of 11.58 m length. That puts the betatron tune ν near 10. Besides the two straight sections for extraction purposes, there are two other straights to be used for beam injection and for installing bunching cavities. In each half normal period about 1.6 m are provided to install additional equipment. The preliminary lattice data are summarized in Table IV.7-1.

Table IV.7-1. Magnetic Lattice Data

Lattice Parameters	
Magnetic rigidity of the beam	107.7 Tm
Number of superperiods	4
Number of normal periods	40
Betatron tune	near 10
Circumference of the ring	463.1 m
Length of a superperiod	115.8 m
Length of a normal period	11.6 m
Free space per half normal period	1.6 m
Dipoles	
Total number	144
Number per half normal period	2
Deflection angle	2.5°
Length	1.09 m
Additional free space	0.25 m
Bending radius	25.05 m
Assumed magnetic field strength	4.30 T
Average dipose field	1.43 T
Sagitta	0.06 m
Quadrupoles	
Total number	80
Length	0.63 m
Additional free space	0.20 m
Field gradient	41.9 T/m
(approximate value under assumption of 90° phase advance)	

Schematic layout of half a normal period:

Element:	Quadrupole	Drift Space	2 Dipoles	Drift Space	Quadrupole
Length/m:	0.63	0.45	2.68	2.02	0.63

A more detailed parameter list, including ion optical data, is in preparation.

For additional data see also the complete HIBALL parameter list.

IV.7.2 Magnet Technology

Whereas the transfer ring as well as the condenser rings will be built by using the well established technology of room-temperature iron magnets but probably with superconducting excitation coils, advanced technologies should be applied in the case of storage rings. In the light of the current state of the art in the field in superconducting magnets it will be feasible in the near future to construct the storage rings on the basis of this technology. The problems are less severe than in accelerating synchrotrons because of the fact that no fast pulsing of the magnets is necessary. The biggest advantage is the much lower power consumption of superconducting magnets.

The magnetic inductions of present dipole magnets for accelerators vary between 4 T and about 5 T. This field region can be realized using superconductors of Nb/Ti in a copper matrix, and one can rely on a well proven technology. The present design value for the central induction of 4.3 T is well below the limit of 5 T where difficulties seem to increase rapidly.

A bore size of at least 60 mm is needed. Both solutions -- warm or cold iron -- are realized at present. A decision in that respect could be based on the following points:[1]

- The danger of permanent heat input into the helium by means of RF losses and beam induced currents in the chamber wall is avoided using a warm bore. Especially the high peak currents in HIBALL may create severe problems.
- In the case of beam losses there is no danger of evaporation of frozen impurities from the walls.
- The machine vacuum tube completely at room temperature enables the installation of insertions without interference with the cryogenic system.
- One of the most serious disadvantages of cold iron is the high mass to be cooled down to helium temperature. This means extremely long cooling and

heating times which are very uncomfortable in many cases (tests, replacement in the ring).

- Furthermore it is not easy to avoid difficulties due to the difference in thermal contraction of magnetic steel and the coils.
- In cases where the iron is too close to the coils, saturation effects may cause field distortions which have to be corrected.
- On the other hand, one has the following advantages: coils are easier to align centrally within the iron bore. Magnetic forces can be safely taken at the low temperature of the coil without heat losses. The iron is closer to the coils, which requires less ampere turns for the same field and useful diameter.

The advantages and disadvantages of warm iron are naturally the inverse of those of cold iron.

The final selection should be postponed until extensive experience and information is available from other superconducting systems either already in fabrication or being proposed. Many components and details might still be improved, and completely alternative designs cannot be excluded at the present time. Certainly, the reliability and reproducibility of current superconducting magnets has to be raised considerably.

Assuming about 200 m of magnets per storage ring and a necessary cooling power of about 3 W/m to be delivered at the cold part of the magnet, leads to 600 W of total cooling power per ring. Facilities of up to 3000 W can be built already at present time. Consequently, it would be reasonable to use one cooling facility for a group of 5 storage rings.

References for Section IV.7

1. HERA-Report; ECFA 80/42; 17 March 1980; DESY HERA 80/01.

IV.8 Beam Handling in the Rings (Kickers)

IV.8.1 Injection and Extraction

In the present concept, multiturn injection is used to fill the transfer ring as well as the condenser and storage rings. In any case the principal element is a septum magnet which transports a new turn of beam into the ring and lets pass the previously injected turns of beam on the other (field-free) side of the septum. The septum has to be thin so that the new and the old turns can be stacked next to each other with a minimum of separation between them. The thickness of the septum will be optimized with respect to its cooling properties and the tolerable beam losses. As successive turns are stacked, since it is impossible to move the septum that rapidly, the orbit of the already injected beam is moved by 2 pairs of fast orbit-bump magnets located approximately +90° and -90° betatron phases from the exit of the septum. It will be necessary to shift the bumped orbits in times of the order of 1 μsec. In order not to restrict the acceptance, the bumped orbits are only allowed to appear in the injection straight section. Because of the fact that only 3 turns are injected in the horizontal plane of each ring it should not be a problem to keep the emittance dilution factor well below a value of 2 as required by the present scheme. The filling of the second transverse plane is accomplished by rotating the beam by $\pi/2$ between the transferring and the condenser rings, followed by another stacking procedure in the horizontal plane. Solutions to all these problems are on hand in the frame of the current state-of-the-art of accelerator technology.

Alternatively, a corner septum could be used to stack the beam simultaneously in both transverse planes. That could possibly lead to a simpler configuration with respect to the transfer and condenser rings. But, however, that method has not yet been considered in more detail.

After bunching, two bunches exist in each storage ring and have to be extracted simultaneously by fast kicker magnets. The extraction equipment will be installed in two straight sections on opposite sides of the storage rings.

IV.8.2 Kicker Magnets

The characteristic properties and the technological problems of kickers vary with rise time, flat top time and strength of the kicker field.

The required field strength is determined by the necessary deflection angle ζ, the magnetic rigidity of the beam BR and the allowed length of the kicker magnet itself:

$$\text{kick [Tm]} = \zeta \text{ [rad]} \cdot \text{BR [Tm]} \quad .$$

The corresponding kicker parameters needed for the three types of rings used in the HIBALL concept are given in Table IV.8-1.

A rough estimation of the necessary voltage V, current I and consequently of the required power is possible by using the relations

$$V\ [V] = \frac{w \cdot k}{\tau_R} \quad , \quad I\ [A] = \frac{h \cdot k}{\mu_o \cdot \ell}$$

where ℓ, h, w [m] are the mean length, height, and width of the aperture, τ_R [sec] is the rise time, and k [Tm] the kick needed. The required voltages are in the range from 10 to 100 kV and the corresponding currents vary between 5 and 20 kA.

In principle no problems are expected to occur in the final phase of construction of such kicker magnets from a technological point of view. However, solvable difficulties may arise in connection with the long flat top of type A magnets, and with the limited length of about 3 m allowed in the storage

Table IV.8-1. Kicker Magnet Parameters

	Deflection Angle [mrad]	Rise Time [μsec]	Flat Top [μsec]	Type
Transfer Ring	2.5	≤ 1	45	A
Condenser Rings	2.5	≤ 1	15	A
Storage Rings	6.0	1.5	0.5	B

rings. The characteristic parameters have to be carefully optimized against each other. In any case, prototypes of final size have to be built and tested in advance.

Probably, type B kickers have to be split into several modules driven by discharges of high-voltage L/C-pulse forming networks, which is a proven method for generating kicker pulses of constant current (low ripple and overshoot, etc.). The kicker modules themselves may be designed as asymmetric C-shaped ferrite magnets. Cooling water channels have to be provided in the condenser plates in order to keep the inserted ferrite pieces below their Curie temperature. Alternatively, a design without ferrite may be worthwhile considering. According to the literature,[1] in this case about twice the amount of current and comblike conductors are required for a sufficiently good dipole field.

Methods have also been suggested[2] to recycle at least 50% of the energy stored in such kickers.

References for Section IV.8

1. G. Schaffer; IKOR-Report; Jul-Spez-114; June 1981.
2. G. Schaffer; KfK; April 1981 (unpublished).

IV.9 Bunching

IV.9.1 Bunching in the Storage Rings

Starting from a coasting beam (21 A; 5 μsec revolution time) two bunches (250 A; 200 nsec length) have to be created, with as little loss of particles as possible. The most tedious part is the first one which has to occur carefully and slowly so that substantial dilution of the longitudinal emittance is avoided. A sinusoidal RF voltage of 0.4 MHz is applied, starting with an amplitude of 0.1 kV (per turn) (separatrix half height = 5×10^{-5}; $Q_s = 5 \times 10^{-5}$), and the RF amplitude is increased exponentially with time. It is estimated that it takes at least 10 msec (2000 revolutions) until a bunching factor $B_F = 0.5$, bunch length of 1.9 μsec, has been reached at an RF amplitude (integrated over the circumference) of 0.15 kV per revolution.
The bunching factor is defined as $B_F = \frac{2}{3} \Delta t/\tau$.

Proceeding with adiabatic bunching, the bunch length Δt shrinks as the inverse 1/4th power of the RF voltage:

$$t\Delta \sim B_F \sim U_{RF}^{-1/4} .$$

To arrive at a bunch factor of 1/18 (bunch length of 200 nsec), U_{RF} has to be raised to as much as 1.0 MV. This is probably too high a voltage, in view of the ceramic windows of the cavities.

Instead of this totally adiabatic procedure, one would prefer a mixed procedure: bunching is adiabatic until $B_F = 0.2$ has been reached, at a voltage of about 5.8 kV. Then voltage is raised suddenly, within a few microseconds, to 76 kV. Thereafter the phase space ellipse begins to rotate; when it is in a vertical position, the bunches are extracted. In this non-adiabatic procedure, the shortest bunchwidth is proportional to $U_{RF}^{-1/2}$:

$$\frac{B_{F1}}{B_{Fo}} = \left(\frac{U_{RF\ raised}}{U_{RF\ o}}\right)^{-1/2}$$

that means that $B_F = 1/18$ is achieved with 76 kV.

Since the high RF voltage is applied to a bunch of ±60° phase extent, and the bunch is further compressed by a factor of 3.6 only, it is allowed to be a sine and not sawtooth. We estimate it to be dangerous to have ferrite cavities in the rings, except for the purpose of active feedback for suppression of spurious bunch modes, and with the feedback amplifier being switched on. This is a technique which will be investigated experimentally in the SNS at Rutherford Laboratory. If the feedback amplifier were very powerful one could also apply the bunching voltage directly into this cavity. Some kilovolts would suffice to perform the whole bunching process, with no adiabatic bunching process before. The question whether this technique will be successful is very open, and our description is not based on this (however very advantageous) method.

The storage ring vacuum must be closed from the volume of the RF cavities (with or without ferrites) by a cylindric ceramic window, because the ring vacuum has to be at a pressure of 10^{-12} torr. This limits the RF voltage to < 50 kV (amplitude) per RF cavity, and two or three RF cavities have to be installed per ring.

The RF cavities may be shared by all rings of a ring package (of 5 rings). This sharing does not mean the loss of freedom to bunch the contents of the 20 final beam lines individually in different ways, in order to shape the pulse. Individually bunching is performed by the induction linacs outside the rings (see next subsection), of which there has to be really one per beam line.

IV.9.2 Induction Linac Compressor

IV.9.2.1 Introduction

After the 20 beam pulses are simultaneously extracted from the 10 storage rings, final compression of each beam is initiated with an induction linac compressor. Each compressor, 20 required, applies a ± 150 MV (± 300 MeV) voltage ramp to the beam in 250 kV steps forcing the 200 nsec beam pulse to be ballistically focused to 20 nsec at the target chamber.

A compressor can be viewed as consisting of a beam transport system and induction linac sections which are described below.

IV.9.2.2 Beam Transport System

Each beam will be transported through a compressor with a periodic FODO system which is matched to storage ring extraction. Compressor beam transport parameters are tabulated in Table IV.9-1.

Table IV.9-1. Compressor Beam Transport Parameters

Period	8 m
Occupancy Factor	1/8
Tune Shift	60°-36° (vertical)
	60°-18° (horizontal)
Nominal Current	250 A
Beam Radius	0.052 m
Focusing Strength	53.2 T/m

Allowing 25% beam radius clearance, the following focusing magnet parameters are obtained:

Table IV.9-2. Focusing Magnet Parameters

Bore Tube Radius	0.065 m
Bore Tube Radius Field	3.46 Tesla
Effective magnetic length	0.50 m

Superconducting cosine coil quadrupoles are envisioned for the beam transport system.

IV.9.2.3 Induction Linac Systems

The induction linac sections of the compressor consist each of 12 modules. Each module is fed with a suitably tailored high voltage pulse so that a ramped voltage of 250 kV maximum is applied to the beam pulse. Thus each section applies a 3 MV voltage tilt to a beam pulse and 50 sections (600 modules) provide the required 150 MV.

A conceptual induction linac section is shown in Fig. IV.9-1. A module consists of a ferrite core (nickel-zinc-ferrite), a high voltage supply loop which also functions as the ferrite core support, an insulator and the housing with the feed connection. The housing is filled with oil for high voltage insulation.

The design shown is of simple construction and basically consists of just 2 assemblies. Each ferrite core (fabricated with such shapes as rings, segments or blocks) is captured by a core support and welded to the outer housing; this makes up the core housing assembly. All the insulators are welded together with intermediate short tubes, each containing a captured helical spring contact, which with a pump-out makes up the section insulator assembly. To assemble a section, the insulator assembly is inserted into the core-housing assembly. An oil seal is provided at either end of the core-housing

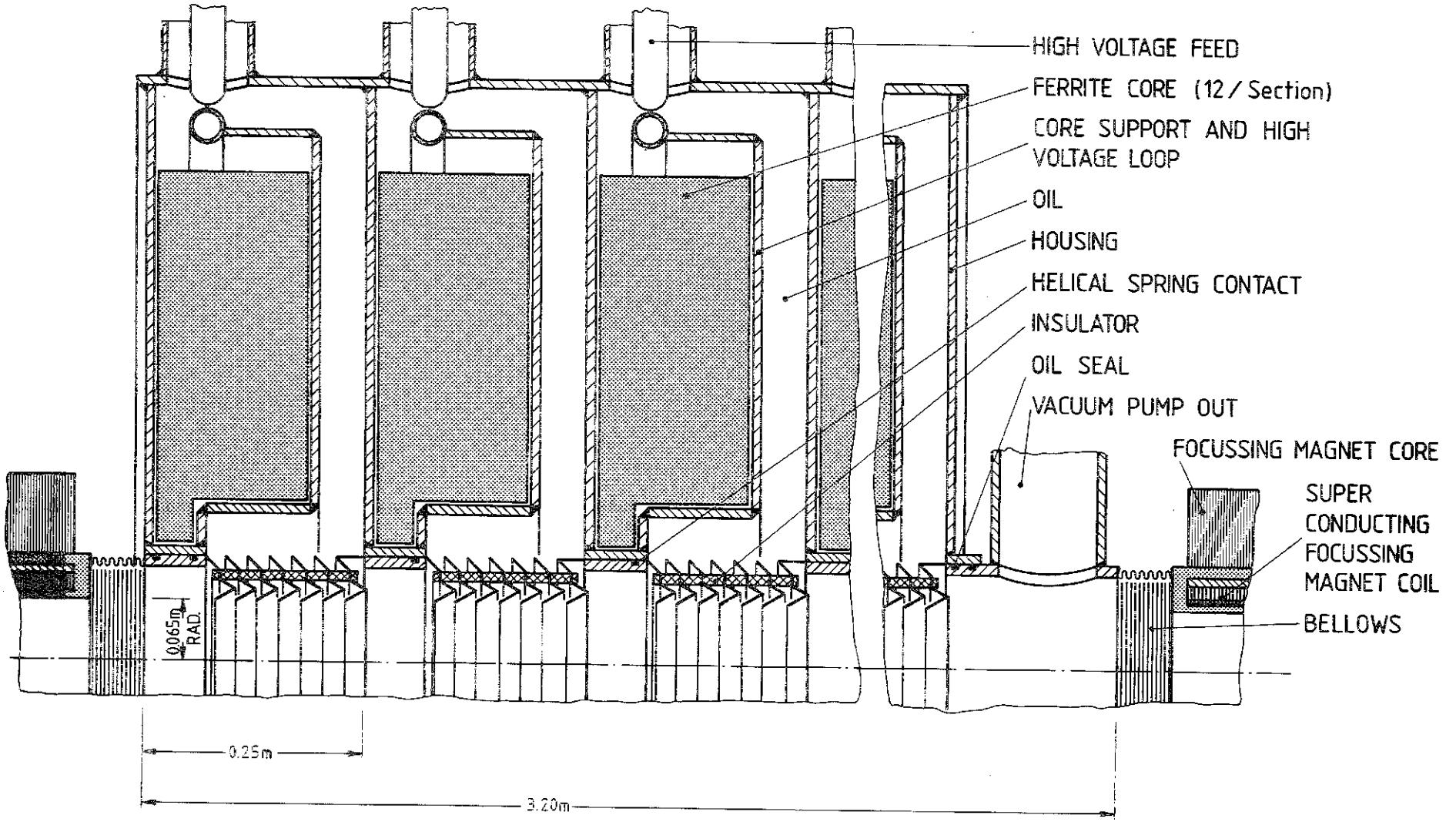

CROSS - SECTIONAL VIEW OF A COMPRESSOR INDUCTION LINAC SECTION

FIGURE IV. 9 -1

SCALE
0 10 20 30 cm

for oil containment. An advantage of this design is that the potentially troublesome components, the insulators and helical springs, can be readily accessed by removing the section insulator from the core-housing.

Compressor length including the beam transport is 200 m with a 0.75 MV/m peak voltage gradient. Relevant module dimension and parameters are tabulated in Table IV.9-3.

Table IV.9-3. Induction Module Dimensions and Parameters

Module Length	0.25 m
Core Length	0.17 m
High Voltage Oil Spacing	0.05 m
Bore Radius	0.065 m
Core Inner Radius	0.135, 0.185 m
Core Outer Radius	0.56 m
Module Outer Radius	0.66 m
Insulator Gradient	17 kV/cm
Ferrite Core Weight	725 kg
Core Loss Energy	24 J
Module Stored Energy	64 J
Module Peak Current	2050 A
Module Power at 20 Hz	1280 kW

The design represents a conservative approach but actual performance must be verified with prototype testing. With module development effort and newer ferrites, it may be possible to operate the compressor at a higher gradient.

Also, the tradeoff between a higher compressor voltage gradient (requiring more ferrite) and a shorter transport line needs to be examined.

The requirements for the 20 compressors are tabulated in Table IV.9-4. The estimated costs (1981), with power supplies, are $33,000 (73,000 DM) per module. The quadrupole magnets are not included; they are cost items of the beam lines.

Table IV.9-4. Requirements for 20 Compressors

No. of Modules	12,000
Total Weight of Ferrite	8,100 tons
Total Stored Energy	0.77 MJ
Total Power	15.3 MW

IV.10 Driver Efficiency

IV.10.1 Introduction

Efficiency is meant to be the particle beam power delivered from the driver divided by the overall power consumption of the driver facility. The fact that a fraction of the beam might miss the target is not included here. The figure below illustrates the simplified power flow diagram of an inertial confinement fusion power plant.

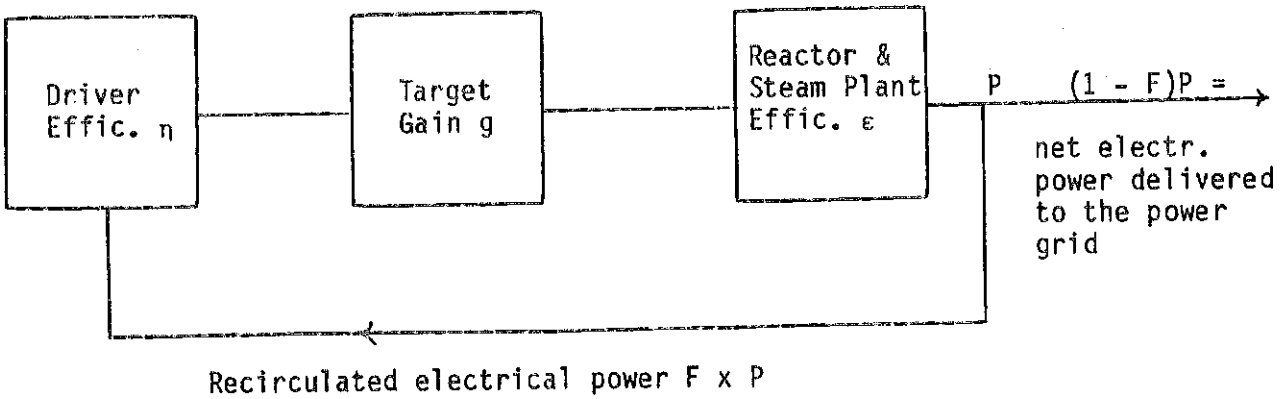

If the fraction of the recirculated power F is chosen to be 1/4 and the thermal efficiency ε of reactor and turbine system is 1/3, then $\eta \cdot g \geq 12$. This immediately demonstrates the implication for the target design: a particle beam driver with an efficiency η of about 1/4 requires a target gain of only ≥ 48, which is regarded to offer many encouraging options in target design. In the case of a laser beam driver the efficiency is presently considered to be less by an order of magnitude and hence the success of an appropriate target design is less certain. While a laser beam efficiency of 2.5% still is a design aim, the corresponding figure of nearly 25% for a particle beam driver will be shown to be realistic. It is neither the purpose of this contribution to calculate this number with the highest possible perfection nor

to make suggestions for further improvements. It is rather the aim to identify accelerator components and subsystems which are most determinative for the overall efficiency and separate them from the others, for which power consumption is not a stringent design parameter.

IV.10.2 The Accelerator

For a beam current equal to 0, the efficiency is also 0. For an extremely high current, the efficiency approaches the conversion efficiency of main power into RF power, typically 0.54. For current values in between both extremes, the efficiency strongly depends on accelerator parameters and hence the machine design must be known, partly in detail. The lay-out of the linac was described in section IV.5 and the numbers given in Fig. IV.5.1.

Most data have been chosen to be similar to the UNILAC. A fourth frequency jump to 324 MHz, which is not correlated to a funneling step, was tentatively included. It was the potential of (a) cutting down the linac cost; (b) increasing the RF efficiency, because it is the lowest frequency, at which a klystron ($\eta \sim 70\%$) seems realistic; (c) the filling time of the cavities being lower by a factor of 3 and hence the RF duty factor being more favorable compared to the beam duty factor; and (d) the possibility of a fourth funneling step, if source currents ultimately fall short or more redundancy is deemed necessary.

An RF power source for 324 MHz will become available soon. However, the RF efficiency figure assumed here is based on the 108 MHz tetrode amplifiers of the UNILAC, hence, the result is overly conservative. The shunt impedance of the linac structure, which is nearly as determinative for the overall efficiency as the RF conversion efficiency, was derived from the UNILAC Alvarez section, 50 MΩ/m. This figure includes losses for end-walls, tuners, etc. This figure might be more favorable for a 324 MHz structure, provided the

drift tube diameter could be decreased from the 20 cm value, used in the UNILAC, to 12-14 cm by using permanent magnet quadrupoles.

The same shunt impedance figure of 50 MΩ/m is assumed for the Wideröe sections too, though this type of structure has a typically higher value. But it is strongly dependent on the particle velocity and frequency and cannot be derived more accurately without a more detailed cavity design. The same is true for the transit time factor: only a final design can yield a more accurate number. Here an average value of the UNILAC Alvarez section is used, T = 0.86. Another number, which determines the linac efficiency, is derived from the UNILAC: the net acceleration rate of 1.75 MV/m. This value is usually selected by a cost optimization of linac length versus RF power installation and usually does not include efficiency considerations. The adapted UNILAC number results in a linac length of 3 km, which actually is the length of the longest linac presently in existence. If the linac length would be doubled the linac efficiency would be 38.5%, rather than 33.3%, as in the proposed design. For the drift tube quadrupoles, permanent magnets are assumed and a DC doublet will be used every 10 m between the cavities for matching purposes. It is not clear from the particle dynamics standpoint whether this limited amount of focusing adjustment is adequate for a beam stability between zero and full beam current. If this idea has to be abandoned the linac efficiency drops from 33.3% to approximately 31%.

Compared to the linac, the transfer ring, the condenser rings, the storage rings, the beam manipulation components and the long beam transport paths are by far less determined at the present stage of the HIBALL scenario. Fortunately, the power consumption of those items, 75 MW, does not dominate the power balance, as the linac with its 300 MW does. Therefore the concern about this final part of the facility is more of a question of feasibility and

cost rather than efficiency. The use of superconducting magnets is almost obligatory. Permanent magnets could be used for beam transport lenses, but hardly for the high fraction of bending dipoles. If room temperature magnets ultimately have to be used, the power requirement of 62 km of beam transport length, including the rings, would go up by a factor of 10 approximately and the overall efficiency would drop from 26% to 17%. In addition, the lay-out of storage rings, beam rotators and final lenses would have to be revised drastically. Among the beam manipulation components, the bunching cavities in the rings and the induction linac, which is included as the final bunch compressor in each of the 20 beam lines, are not yet determined in their electrical parameters and may influence the power balance more significantly.

IV.10.3 The Power Balance

The listing of individual power requirements is based on average values. That means that except for the obvious continuous power consumers, the peak power must be determined and then be multiplied by the individual duty factors, which also must include build-up times and pauses. Therefore the timing scheme of the beam pulse and the excitation pattern of the linac and the beam manipulation elements was determined.

A) Peak Beam Power	150 mA x 5 GV =	750 MW
Average Beam Power	750 x δ_{beam} =	100 MW
B) RF Power Requirement = Beam Pwr + Linac aver. RF Pwr =		145.8 MW
estim. RF Pwr for Rebunchers and Funneling Cavities		2.2 MW
		148 MW

Conversion Eff. Main Pwr/RF Pwr =	0.54
Main Power of RF Installation = 148/0.54 =	275 MW
Conventional Lenses and Steering Magnets 10 kW per 10 m =	3 MW
Vacuum, Controls, Miscel. 1 kW per m	4 MW
Cooling Plant to Remove 150 MW Power Losses: 150 x 0.12 =	18 MW
Total Linac Main Power Consumption	300 MW

$$\text{Linac Efficiency} = \frac{\text{Beam Pwr}}{\text{Total Main Pwr}} = \frac{100}{300} = 33.3\%$$

C) Rings, Beam Transport, Beam Handling, Final Focusing

Length of Beam Path:

First Transfer Ring	3.20 km
5 Condenser Rings	6.94 km
10 Storage Rings	4.63 km
20 Long + 80 Short Transp. L.	48.00 km
	62.77 km

Magnet Filling Factor	~ 0.5
Total Length of Supercond. Magnets	31.40 km
Power Loss at 4°K	2 W/m
Total Refrigerator Capacity at 4°K	62 kW
Conv. Eff. of Refr. Plant Including Utilities	450:1
Cooling Plant Main Power Requirement	28 MW
80 Correction Dipoles at Beam Line Ends	16 MW
Bunching Cavities and Ind. Linac (estim.)	12 MW
20 Slow Switching Magnets (estim.)	4 MW
22 Kicker Magnets	2 MW

22 Septum Magnets	3 MW
Vacuum, Controls, Miscel. 0.2 kW/m	10 MW
	75 MW

$$\text{Total Facility Efficiency} = \frac{\text{Beam Power}}{\text{Linac + Ring + Transp. Pwr Consumpt.}}$$

$$= \frac{100}{300 + 75} = 26.7\% \quad .$$

IV.10.4 Conclusions

1. An overall efficiency of about 25% is realistic for a heavy ion fusion driver, when all beam transport magnets are based on superconducting technology.
2. Reliability and redundancy considerations, potential reserves in beam power and derating of crucial component characteristics have all the tendency to decrease the overall efficiency.
3. The most decisive figure is the conversion efficiency of main power into RF power. If this figure would be 70% (which is expected in the near future), rather than the assumed 54%, the overall efficiency would go up from 26.7% to 32%.
4. The funneling section of the chosen linac contributes only about 1.5% to the total power losses and can therefore be designed freely without degrading the efficiency.

V Beam Transmission and Final Focusing

V.1 General Theory

V.1.1 Introduction

Transport of beams from the accelerator to the target chamber and focusing on a small target are key issues in heavy ion fusion. Their solution determines most of the parameters of the accelerator scenario. The option of transporting beams ballistically as though in vacuum -- without neutralization -- has been recognized as a major advantage of using heavy ions and will be considered here. The alternative use of a plasma channel for final transport of heavy ions -- similar to light ion fusion schemes -- requires considerable additional theoretical and also experimental work before it can be assessed in a reactor design.

The compatibility of nearly vacuum propagation with the cavity design (wall protection, pumping, etc.) will be considered in chapter VI and a proper definition of the vacuum by stripping considerations will be given later in section V.6. A crucial cavity design parameter that determines final transport is the stand-off distance of final focusing magnets from the target (8.5 m). Because of limited space, the number of beam lines (including shielding) is confined to approximately ten on a circumference, hence the use of two rows of beam ports demands a particle current per beam line of the order of 1 kA. It was also felt that elliptic entry ports (with noticeably vertical elongation) rather than circular entry ports of the same area could be advantageous to the design of coolant tubes and possibly be helpful for correcting geometric aberrations of the final magnets.

In addition to these cavity related constraints there are beam dynamics limitations which have to be incorporated into the final transport design. Space charge plays an important role here and is a novel feature compared with

designs of existing high energy beam lines that usually have negligible space charge effects. The current transport limit in the long periodic beam line connecting with the accelerator is not serious as long as low charge states are chosen (q = 1,2). In fact, recent computer simulations have shown (see V.1.2 and Ref. 3) that under certain conditions there is no limit to the transportable current from the physics point of view. Electrostatic repulsion in the final drift can be controlled by increasing the beam divergence, hence the entry port radius. The lens aperture is limited, however, by spherical aberrations and it was felt that a 10-20% increase over the emittance controlled divergence would be reasonable. From the standpoint of aberrations the emittance and momentum spread should be as small as possible. For constant target requirements this is possible only at the expense of the accelerator size. A reasonable compromise has been found in the parameter space around 60 π mm-mrad average horizontal-vertical emittance and 1/2-1% momentum spread.

As to the level of confidence one may have in the transverse transport considerations, we note that computer simulation studies performed at the Naval Research Laboratory and at the Max-Planck-Institut für Plasmaphysik with different codes have led to excellent agreement and also confirm predictions from analytic theory. The situation is different with regard to longitudinal dynamics and longitudinal-transverse coupling under strong space charge conditions during longitudinal compression, which require future work. For the present study a first-order approach has been made by using the longitudinal envelope equation.

During the performance of this study progress has been made also with regard to the development of design programs to treat the final focusing problem. At the University of Giessen, a very flexible computer program GIOS has been

Fig. V.1-1

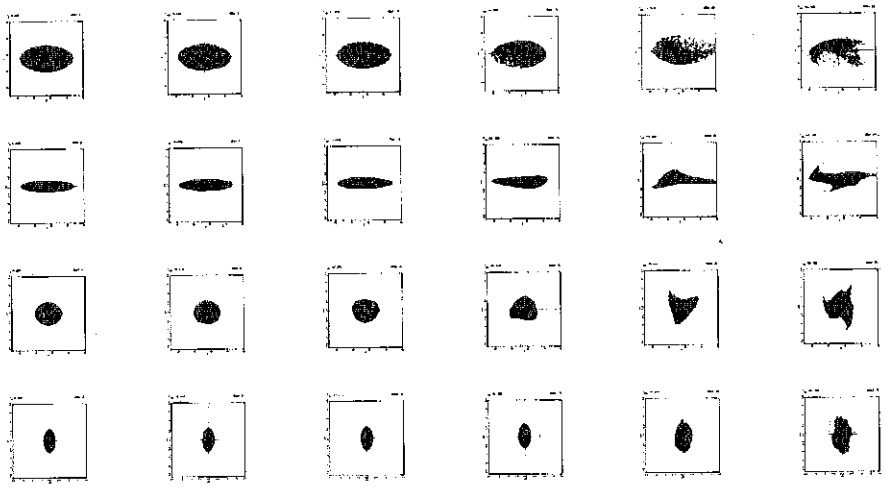

Evolution of initial K-V distribution in periodic FODO focusing with $\sigma_o = 90^o$ and $\sigma = 45^o$ transported over 25 cells ("third order" instability). Projections into the x-y, x-v_x, y-v_y, and v_x-v_y phase planes (from top) are shown.

developed for the design of complex beam guidance systems up to third order. An extension of GIOS to treat beams carrying space charge is under progress. At the Max-Planck-Institut für Plasmaphysik the program SCOP1 has been developed with main emphasis on the treatment of space charge and some design capabilities, including third order effects.

V.1.2 Transverse Stability of Periodic Transport

Beam transfer from the storage rings to the target chamber requires a length of the order of a kilometer to perform longitudinal bunch implosion. It is necessary to ensure transport over a large number of periods of a quadrupole alternating gradient focusing lattice without emittance dilution.

For zero intensity, the requirement for stable trajectories is $\sigma_0 < 180°$, with σ_0 the phase advance per focusing period, to avoid a half-integer resonance with the focusing period. For finite intensity, the defocusing space charge force depresses the tune to a value $0 < \sigma < \sigma_0$ and as a new phenomenon collective modes of oscillation can be in resonance with the focusing period, which may lead to emittance growth unless σ_0 and σ are constrained to stable bands.

Analytic theory[1] and computer simulation[2,3] have suggested that instability of the envelope mode is suppressed if $\sigma_0 \leq 90°$, and instability of the "third order" mode if $\sigma_0 \leq 60°$. This "third order" mode is evolving with three arms in x-p_x or y-p_y phase space and is quite insensitive to the type of distribution function (Fig. V.1-1). The remaining higher order mode instabilities do not spoil the r.m.s. emittance if σ is depressed to small values.[3]

Different emittances in the horizontal and vertical planes may give rise to emittance transfer. The underlying mechanism is a space charge induced coupling instability and requires considerable energy anisotropy and strong tune depression.[3] In most cases the onset of instability is suppressed if

strong tune depression is avoided, for instance $\sigma/\sigma_0 \gtrsim 0.3$ in both planes for $\varepsilon_x/\varepsilon_y = 4$ (see Fig. V.1-2 with linear current ramp to simulate bunch implosion). This limits the current performance compared with equal or almost equal emittances, where no limit has been found so far.

It is convenient to express the current in the channel in terms of the scaled space charge parameter Q' and maximum amplitude u_m (see Ref. 4)

$$I/q = 3.66 \times 10^6 \ (A^{1/3}/q^{4/3}) B_Q^{2/3} (\beta\gamma)^{7/3} \varepsilon^{2/3} Q'/u_m^{2/3} \ [A] \qquad (V.1\text{-}1)$$

where $Q'/u_m^{2/3}$ (Laslett's "figure of merit") is a function of the tune depression σ/σ_0 (see Fig. V.1-3) and the remaining quantities are:

- A atomic weight
- q charge state
- B_Q pole tip field (Tesla)
- β v/c
- ε unnormalized emittance [m-rad] (for unequal emittances the larger one)

V.1.3 Longitudinal Bunch Compression

Longitudinal drift bunching is described by an envelope equation[4]

$$z_m'' = \frac{\varepsilon^2}{\gamma^4 z_m^3} + \frac{3}{2}\frac{q^2}{A}\frac{g}{\beta^2\gamma^5}\frac{Nr_p}{z_m^2} \qquad (V.1\text{-}2)$$

with: z_m = envelope in z

ε = 1/π x emittance in (z, Δp/p)

N = total number of ions

r_p = classical proton radius (= 1.52×10^{-18} m)

Equation (V.1-2) assumes a linear space charge force, i.e. parabolic line charge density. This assumption is consistent with a particular distribution

Fig. V.1-2

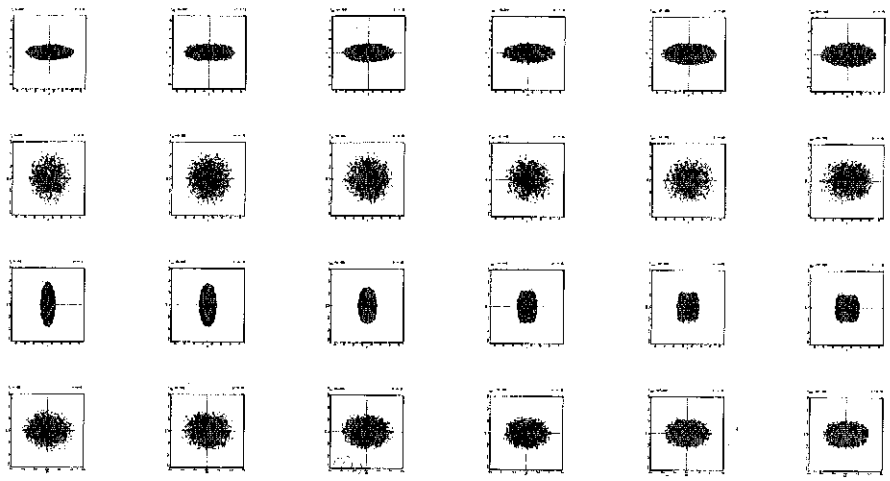

Evolution of initial waterbag distribution in FODO with $\sigma_o = 60^o$ and current ramp depressing tunes from 55^o to 36^o in x and 50^o to 18^o in y over 80 cells. Nearly adiabatic behavior.

Fig. V.1-3

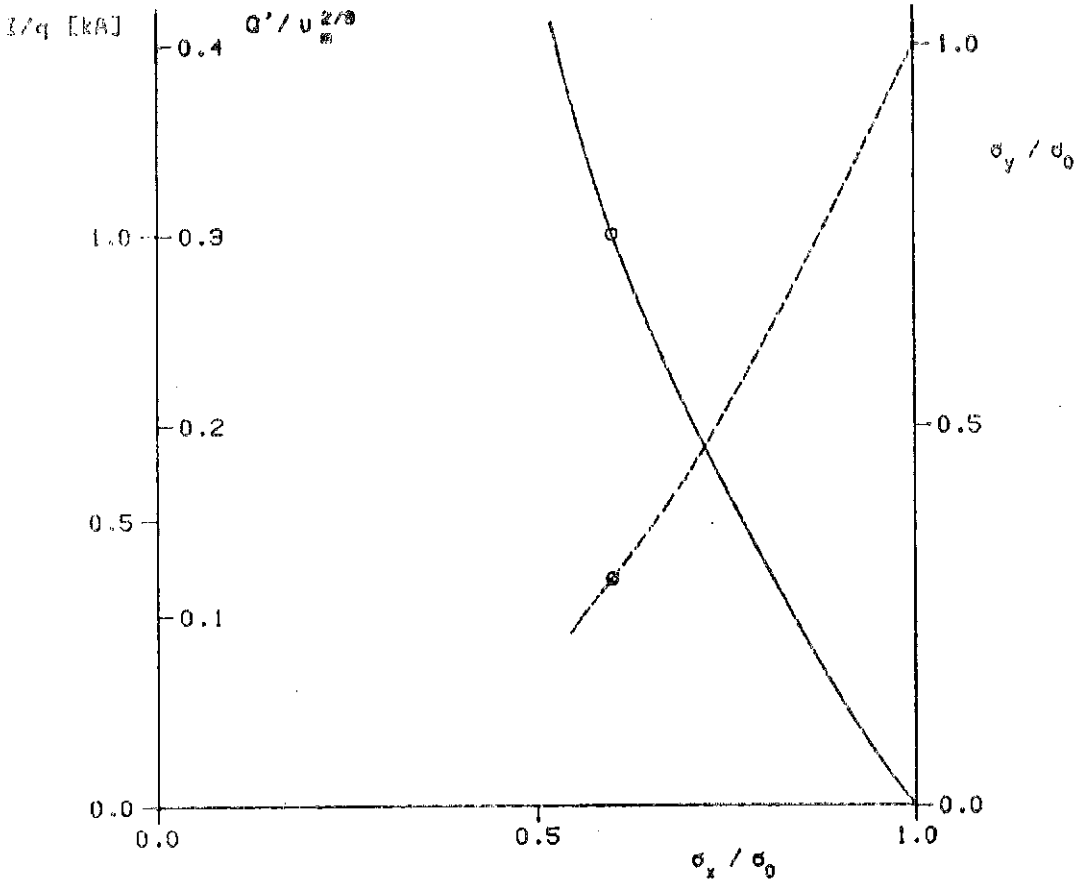

Fig. V.1-3. Intensity coefficient vs. tune depression in x for a $\sigma_o = 60^o$ symmetric FODO lattice and $\varepsilon_x/\varepsilon_y = 4$. I/q as example for HIBALL parameters. The dashed line gives the corresponding tune depression in y and the circles indicate stability limits beyond which emittance transfer is possible.

function (see Ref. 5), whereas in practice deviations from the linear force compression must be expected due to the presumably Gaussian shaped distribution function. In addition, the geometry factor g depends on the transverse position. For a uniform density beam of radius, a, in a pipe with radius, b,

$$g = 1 + 2 \ln (b/a) - (r/a)^2 \qquad \text{(V.1-3)}$$

Hence it varies between 1 + 2 ln (b/a) and 2 ln (b/a) from the center to the edge of the beam. A quantitative evaluation of this non-ideal compression scheme and the associated longitudinal emittance dilution requires a simulation program employing r-z or x-y-z geometry. A simulation code solving Poisson's equation in r-z geometry in a long circular cross section pipe is presently being tested at the Max-Planck-Institut für Plasmaphysik.

In spite of these limitations Eq. (V.1-2) is a useful starting point to describe the longitudinal bunching process. The initial tilt of the phase space ellipse is provided by the ramped voltage of an induction linac section of several hundred meters length. The phase space rotation is completed in a long drift space (see Fig. V.1-4).

Assuming constant longitudinal emittance during bunching, the coherent initial momentum spread $(\Delta p/p)_i$ necessary to achieve the desired final pulse length can be easily derived from Eq. (V.1-2) by carrying out an integration (see Ref. 4). For large compression ratio we have,

$$(\Delta p/p)_i^2 = (\Delta p/p)_t^2 + 3 \frac{q^2}{A} \frac{g}{\beta^2 \gamma} \frac{N r_p}{z_t} \quad . \qquad \text{(V.1-4)}$$

Note that the incoherent momentum spread at target $(\Delta p/p)_t$ is reduced below $(\Delta p/p)_i$ because of the space charge repulsion which becomes effective close to

Fig. V.1-4

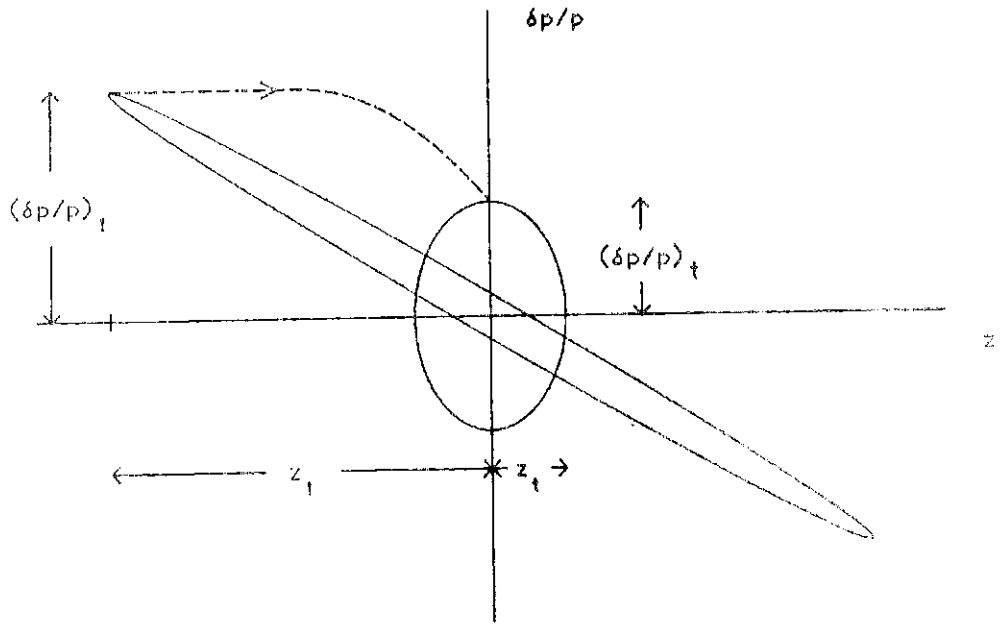

Fig.V.1-4. Ellipse rotation in longitudinal phase space for longitudinal bunch implosion under space charge conditions

the end of the bunching process, when the line charge density has almost come to its final high value.

The necessary drift length is approximately given by

$$L \sim \gamma^2 z_i/(\Delta p/p)_i \quad .$$

$(\Delta p/p)_t$ is limited by chromatic aberrations of the final focusing system. The final momentum transmission of a long beam line with bending sections will set a limit to $(\Delta p/p)_i$, but it is assumed here that the final focusing constraint on $\Delta p/p$ is more stringent and thus determines the momentum width in the storage rings.

V.1.4 Final Focusing Constraints

A final quadrupole doublet or triplet is adequate to perform focusing onto the small target. The large beam size required in the final lens is matched to the periodic transport line with several quadrupoles. There is not a unique way of defining an appropriate final focusing system and some thought is necessary to keep both chromatic and geometric aberrations at as low a level as desirable with regard to the constraints imposed by storage ring considerations. Second order chromatic aberrations (dependence of focal length on momentum) are given by (Ref. 6):

$$\Delta x \sim \frac{\Delta p}{p} \frac{1}{x_t'} \int_0^{s_t} (x')^2 \, ds \qquad \text{(V.1-5)}$$

with $x_t' \equiv dx/ds$ at target, and similar for y. A simple estimate results in

$$\Delta x \sim \alpha \frac{\varepsilon L}{r_o} \frac{\Delta p}{p} \qquad \text{(V.1-6)}$$

with: r_o = target radius

L = distance F.F.M.-target

ε = transverse emittance.

The coefficient α exceeds unity for a focusing system with quadrupoles only. Its actual value depends on the first order design and can be minimized according to Eq. (V.1-5) by an appropriate setting of sufficiently many matching quadrupoles so as to avoid unnecessary fluttering of envelope.

Sextupole correction of chromatic aberrations has not been attempted here, but we have tried to keep $\Delta p/p$ at the level of ± 0.005 where correction is unnecessary. Due to the variation of space charge defocusing within the bunch and with distance from the target there is concern that sextupoles might do more harm than good if they are used according to concepts developed for high energy beam lines without space charge (Ref. 7). Further study is required to clarify sextupole correction in the presence of varying space charge.

According to Ref. 8 third order geometric aberrations are tolerable if

$$\varepsilon \lesssim 0.15\, r_o^{5/4}\, \rho^{-1/4} \quad . \tag{V.1-7}$$

Here ρ is the radius of curvature related to the pole-tip field, and the coefficient 0.15 is about the minimum value that can be achieved by a large class of focusing systems. A brief examination shows that for HIBALL parameters with $\rho \gtrsim 25$ m ($B\rho$ = 106 T-m) the spot size will be spoiled by aberration if ε exceeds in both planes the value 30 mm-mrad. We note that the aberration properties of the Reference Design are very well described by Eq. (V.1-7) as detailed calculation will show.

References for Section V.1

1. L. Smith et al., LBL, unpublished (1977).

2. I. Haber, IEEE Trans. Nucl. Sci. NS-26, 3090 (1979).

3. I. Hofmann, IEEE Trans. Nucl. Sci. NS-28, 2399 (1981).

4. G. Lambertson et al., IEEE Trans. Nucl. Sci. NS-24, 993 (1977).

5. D. Neuffer, IEEE Trans. Nucl. Sci. NS-26, 3031 (1979).

6. K.G. Steffen, High Energy Beam Optics, Interscience Publishers, New York, 1965.

7. K.L. Brown and J.M. Peterson, Proc. of the Heavy Ion Fusion Workshop, Berkeley, Oct. 29 - Nov. 9, 1979, SLAC-PUB-2575 (1980).

8. D. Neuffer, Proc. of the Heavy Ion Fusion Workshop, Argonne, Sept. 19-26, 1978, ANL-79-41 (1979).

V.2 Final Transport and Focusing for HIBALL

V.2.1 Periodic Transport Lattice for Imploding Bunch

The goal is to transport and simultaneously bunch individual beamlets (20 per cavity) from the accelerator to the target with the following specifications at target:

particle current/beam (averaged over pulse)		1.2 kA
unnormalized emittance:	vertical	120 π mm-mrad
	horizontal	30 π mm-mrad
momentum spread $\Delta p/p$		± 0.005
pulse length		20 nsec

The requirements to achieve this by ten-fold drift bunching are (see Fig. V.2-1)

initial momentum spread $\Delta p/p$ (coherent + incoherent)	± 0.017
induction linac voltage	± 150 MV
length of induction linac	> 150 m
drift distance (induction linac-target)	655 m

There are several options to determine the periodic lattice of these beam lines. The maximum particle current at the end of the periodic lattice is 1.0 kA, assuming a flat pulse shape (note that the final current of 1.2 kA is achieved after drifting through 60 m of large diameter final focusing lenses where space charge is less important). While it is clear from Eq. (V.1-1) that quadrupoles at the 1 kA particle current level have to be superconducting (4 T), it appears attractive to divide the lattice at lower currents into

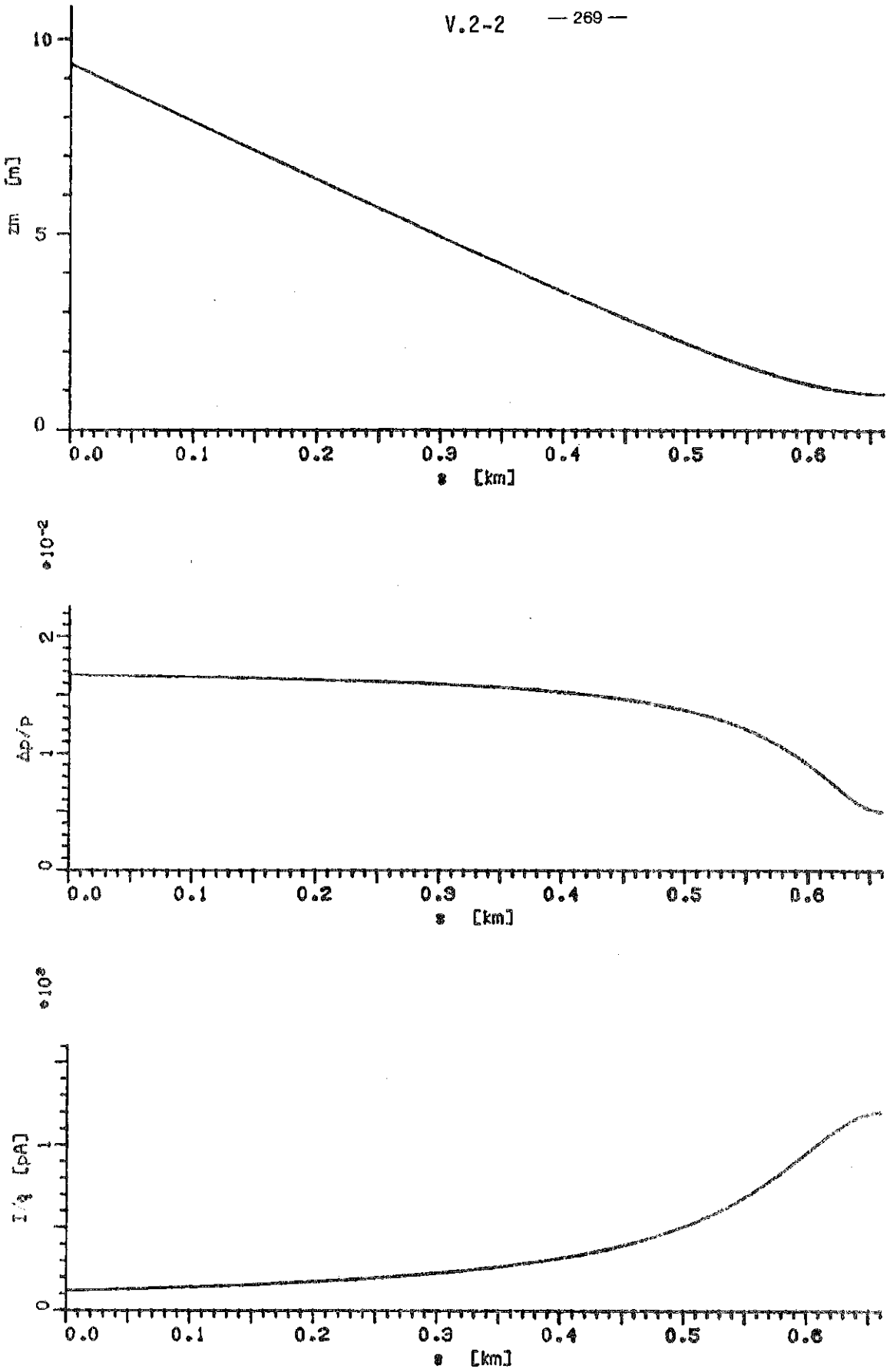

Fig.V.2-1. Longitudinal bunch compression by ten-fold drift bunching between induction linac and target. Longitudinal envelope z_m[m], momentum spread $\Delta p/p$ and particle current I/q [kA] according to envelope equation (with g = 2) as function of distance s from induction linac.

sections with normal conducting (< 2 T) and permanent (< 1 T) magnets. The split is performed according to

$$\frac{I}{q} \lesssim 410 \times B_Q^{2/3} \text{ [A]} \qquad \text{(V.2-1)}$$

with an upper limit of 0.3 for $Q'/u_m^{2/3}$ equivalent to a tune of $\sigma_{vert} = 36°$, $\sigma_{hor} = 18°$ at the end of each lattice section (see stability discussion in section V.1.1). Within a section the lattice is exactly periodic except for the first few magnets that are assumed to perform matching into the changed lattice structure. Details of this lattice are given in Table V.2-1.

Table V.2-1. Periodic Transport Lattice for Rising Beam Current (The Beam Tube Diameter is Assumed 25% larger than the Actual Beam Diameter)

lattice	FODO (symmetric)
occupancy factor	$\eta = 1/2$
zero intensity tune	$\sigma_o = 60°$
tune at max. current in each section	$\sigma_{vert} = 36°$
	$\sigma_{hor} = 18°$
length	595 m
bending radius	150/220 m
average dipole field	0.707/0.482 T

Cell	Part. Current [A]	Pole-Tip B_Q [T]	Max. Beam Diam. [m]	Gradient B_Q/a[T/m]	Length of Cell [m]
1-51 (0-415 m)	120-350	1	0.102	15.7	8.142
52-69 (415-508 m)	350-560	2	0.082	39.0	5.162
70-100 (508-595 m)	560-1000	4	0.060	133.3	2.790

V.2.2 Final Focusing - Reference Design

A reference design for the final focusing has been determined along the following lines:

1. In order to keep the beam size and thus second order chromatic and also third order geometric aberrations as small as possible (without correction) the maximum obtainable focusing power is put into the first two quadrupoles, which calls for superconducting magnets. It is assumed that the field at the conductors is limited to 10 Tesla, with a 50 cm thick shield included in the aperture.
2. Matching of the large beam size in the final magnets to the small beam size in the periodic transport is performed as smoothly as possible, searching for a minimum of the integral in Eq. (V.1-5), which determines the size of chromatic aberrations.

The design has been performed using the computer program SCOP1 (space charge optics program 1) developed at the Max-Planck-Institut für Plasmaphysik. The program has two options:

A. Integration of the Kapchinskij-Vladimirskij envelope equations for first-order design.
B. Raytracing of a random set of trajectories with initial K-V distribution in transverse phase space and square distribution in momentum space. It assumes a linear space charge force derived from the r.m.s. beam envelopes calculated at each time-step. Second order chromatic and third order geometric aberrations can be turned on as well as multipole fields for correction.

Both options use fitting routines for matching (A) and correction (B). Results can be checked with the particle-in-cell code SCOP2 for arbitrary initial distribution with self-consistent space charge force calculation.

First Order Design

The results of a design with hard-edge quadrupoles are shown in Table V.2-2 and Fig. V.2-2. Note that the first order spot diameter is taken 5 mm to account somewhat for a nonideal beam profile. The plotted beam size has been assumed everywhere 25% larger than the r.m.s. size (K-V envelope) for the same reason.

Higher Order Effects and Beam Characteristics on Target

A distribution of momenta and deviations from paraxial focusing result in an increased spot size. A momentum width of ±0.005 can be accomodated in the 3 mm radius spot. The situation is different with regard to third order geometric aberrations. Without correction only 40% of the intensity hit the target and it takes a 10 mm radius target to contain 80% of particles, the actual spot being elliptic rather than circular.

Applying fields with octupole symmetry in Q_3, Q_7 and Q_8 has brought some improvement to the degree that a fairly circular spot is obtained with 80% of the particles contained in a radius of 5 mm. This modest improvement might be due to the first order design which does not allow effective (i.e. sufficiently independent) coupling of octupoles to the various aberration terms. In a previous design it has been possible to almost entirely correct aberrations with three octupoles,[1] but this design had a larger momentum sensivitity. No attempt has been made to optimize the design for reduced geometric and chromatic aberrations, which will be desirable for future work.

Nonparaxial effects due to a nonuniform space charge have been found in previous work[2] to be comparatively small under similar conditions (similar electric current and beam size, which led to a 20% intensity reduction within the first order spot size).

Table V.2-2. Reference Design Specifications With Hard-Edge Quadrupoles

Unnormalized emittance (r.m.s.) (no dilution in periodic transport)	
vertical	120 π mm-mrad
horizontal	30 π mm-mrad
Particle current/beam	1.2 kA
First order spot diameter	5 mm
Distance F.F.M.-target	8.5 m
Total length of final focusing	60.374 m
Length of quadrupoles	2.683 m
Drift sections between magnets	1.789 m
Drift section after period. transp.	17.890 m
beam size (1.25 x r.m.s. diameter)	
at exit of periodic transp.	7 x 3 cm
inside front magnet (Q_8)	120 x 60 cm

Gradients [Telsa/m]

Q_1	Q_2	Q_3	Q_4	Q_5	Q_6	Q_7	Q_8
0.711	4.762	6.561	4.722	1.611	2.868	8.221	7.922
F	D	F	D	F	F	D	F in vertical direction

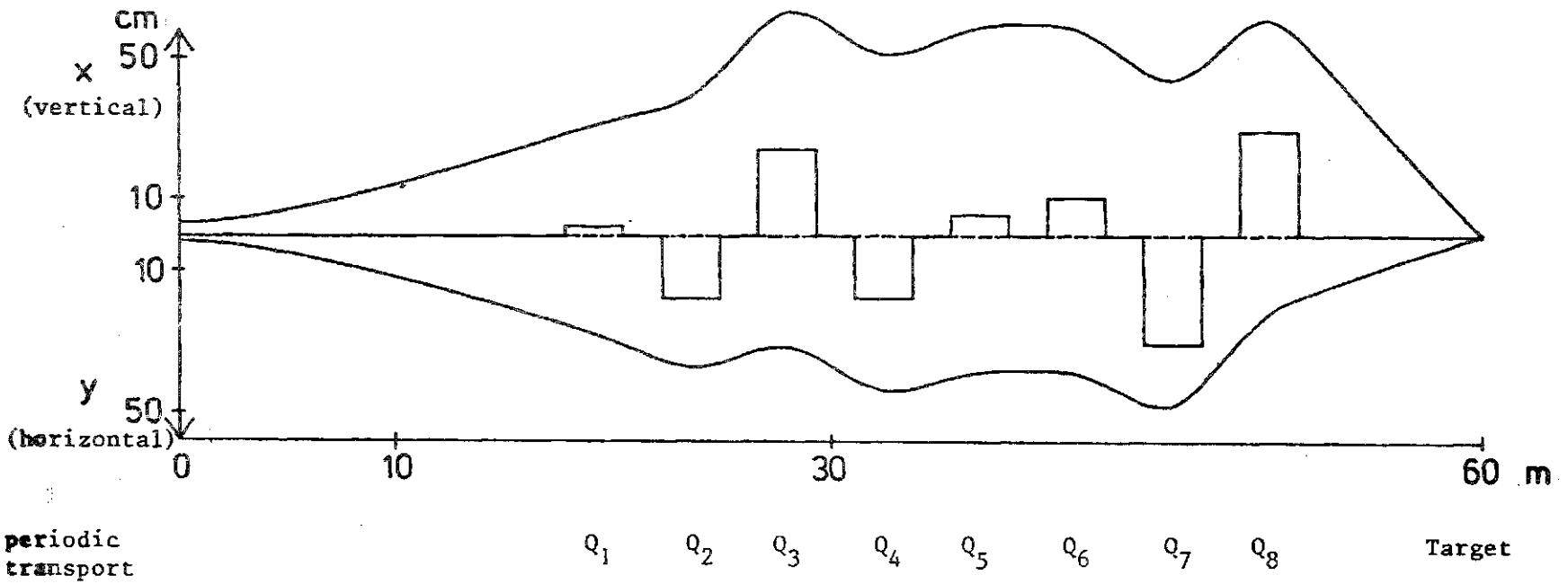

Fig.V. 2-2 . Reference design for final focusing employing 8 quadrupole magnets for beam transfer from the periodic lattice to the target. The square line represents the focusing strength (gradient) in vertical direction.

Summarizing, the present reference design delivers about 50% (or 40% without octupoles) of the beam intensity on a target with 3 mm radius. The remaining intensity is spread out because of aberrations. Third order geometric aberrations are the dominant constituent; octupoles have been shown to give an improvement at least in principle. The size of the uncorrected aberrations is not discouraging, and it is conceivable that the desired spot can be achieved with improved design.

V.2.3 Study of the Overall Beam Line Arrangement

When designing the final focusing system one must pay attention not only to the geometry and field distribution of the last quadrupole lens multiplet but also to the preceding last section of the beam guidance system. Though many different arrangements are feasible it seems inevitable that the final focusing quadrupole lenses will be arranged along lines inclined relative to a horizontal plane of symmetry. The beam guidance system which must feed these inclined beam lines must deviate even more from this horizontal plane of symmetry. An example of a possible overall arrangement is shown in Fig. V.2-3. Though here quadrupoles of maximal flux densities of 5 T are assumed, the bending magnets are postulated to have only 3.2 T. Attention should here be paid to the fact that the apexes of the vertically curved beam guidance systems are more than 20 m above and below the horizontal plane of symmetry. Since altogether 20 beam lines are planned, 10 arrangements as in Fig. V.2-3 must be foreseen, the planes of which are inclined by 36° relative to each other with the axis of rotational symmetry of the reactor vessel being common to all. Thus there is a true three-dimensional structure to be built having a radius of about 200 m and a height of about ±20 m. Most probably, such a structure is best built underground. In any case the costs for the complex civil engineering should be considered.

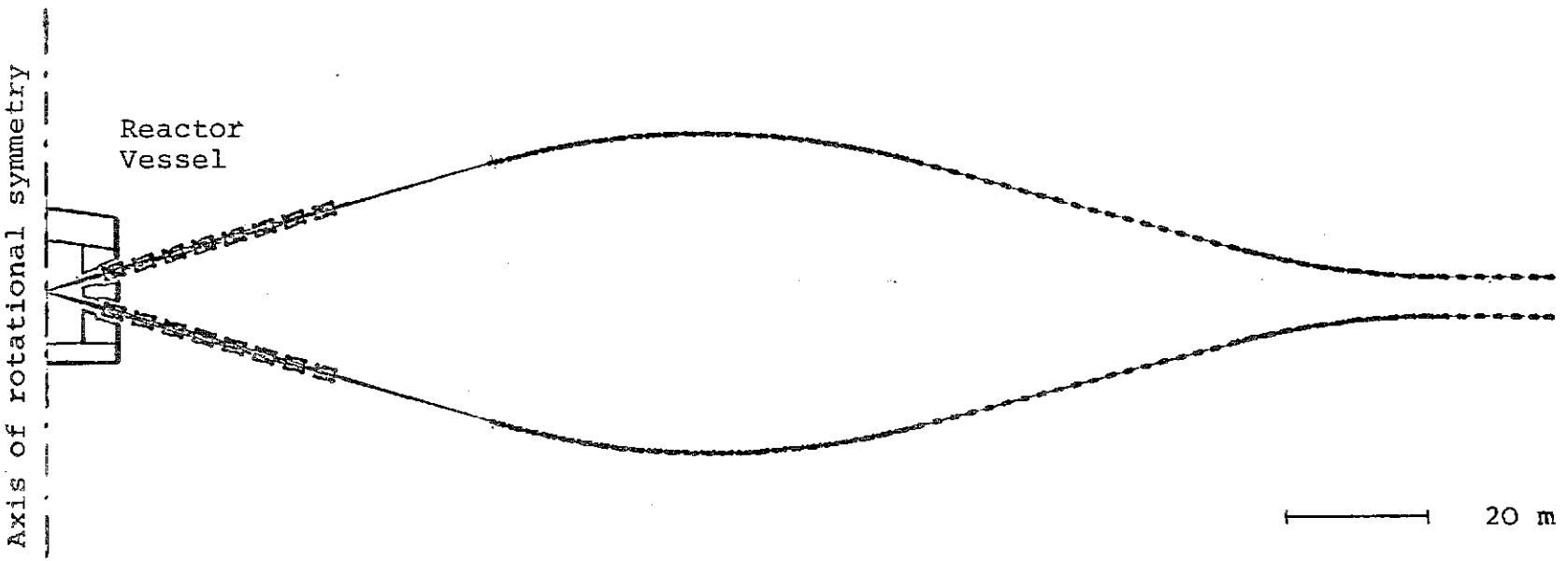

Fig. V.2-3 The possible overall arrangement of a radial section of the final focusing quadrupole and the final portions of two beam lines. For each of these beam lines three unit cells are shown which altogether feed final focusing lenses which are inclined by $\pm 16^{\circ}$ to a horizontal plane of symmetry.
Note that 10 such beam line arrangements are necessary for the final system and that the planes of these arrangements are inclined relative to each other by 36° with the axis of rotation of the reaction chamber being common to all.

References for Section V.2

1. I. Hofmann, unpublished (January 1981)

2. I. Bozsik and I. Hofmann, Proc. of the Conference on Charged Particle Optics, Giessen, 1980, to be published in Nucl. Instr. and Meth.

V.3 Final Focusing Quadrupole Design

Within the set of final focusing quadrupoles in each beam line, the most severe constraints for design and operation must be met by Q_7 and Q_8. They are subjected to fusion neutrons more strongly than the other quadrupoles, and they have to provide a magnetic gradient of g = 8 T/m to a beam of diameter 2a = 1.2 m. The product g·a of gradient and minimum aperture radius is almost 5 T, excluding the efficient utilization of ferromagnetic poles.

The quadrupole field must therefore be generated by an appropriate current distribution (Fig. V.3-1) which is standard practice in the layout of superconducting quadrupole magnets.(1)

For the HIBALL quadrupoles, the current carrying conductors may be normal conducting or superconducting. Normal conducting coils, e.g., of copper and inorganic insulation, may be subjected to 10^{12} rad before their performance degrades. For a reasonable lifetime of the coils, the radiation shielding must be at least 0.2 m thick, yielding a minimum inner coil radius of 0.2 m + a = 0.8 m. Each quadrupole of this type would consume 20 to 50 MW of electric power depending on the trade-off between current density and radial thickness (weight, materials cost). With a lifetime of about 1 year, these coils would require frequent maintenance. Power balance and frequent remote repair excludes the use of normal conducting coils in HIBALL final focusing systems.

For superconducting coils, the shielding requirements are dictated by the operating temeprature of 4.2 K or below much more strongly than by radiation damage considerations. The heat load into the coils may be sufficiently reduced by a neutron- and γ-shield of 0.6 m which, together with cryostat and supports, gives an inner coil radius of 1.3 m. It can be assumed that with these parameters, a superconducting coil will operate for about 30 years of

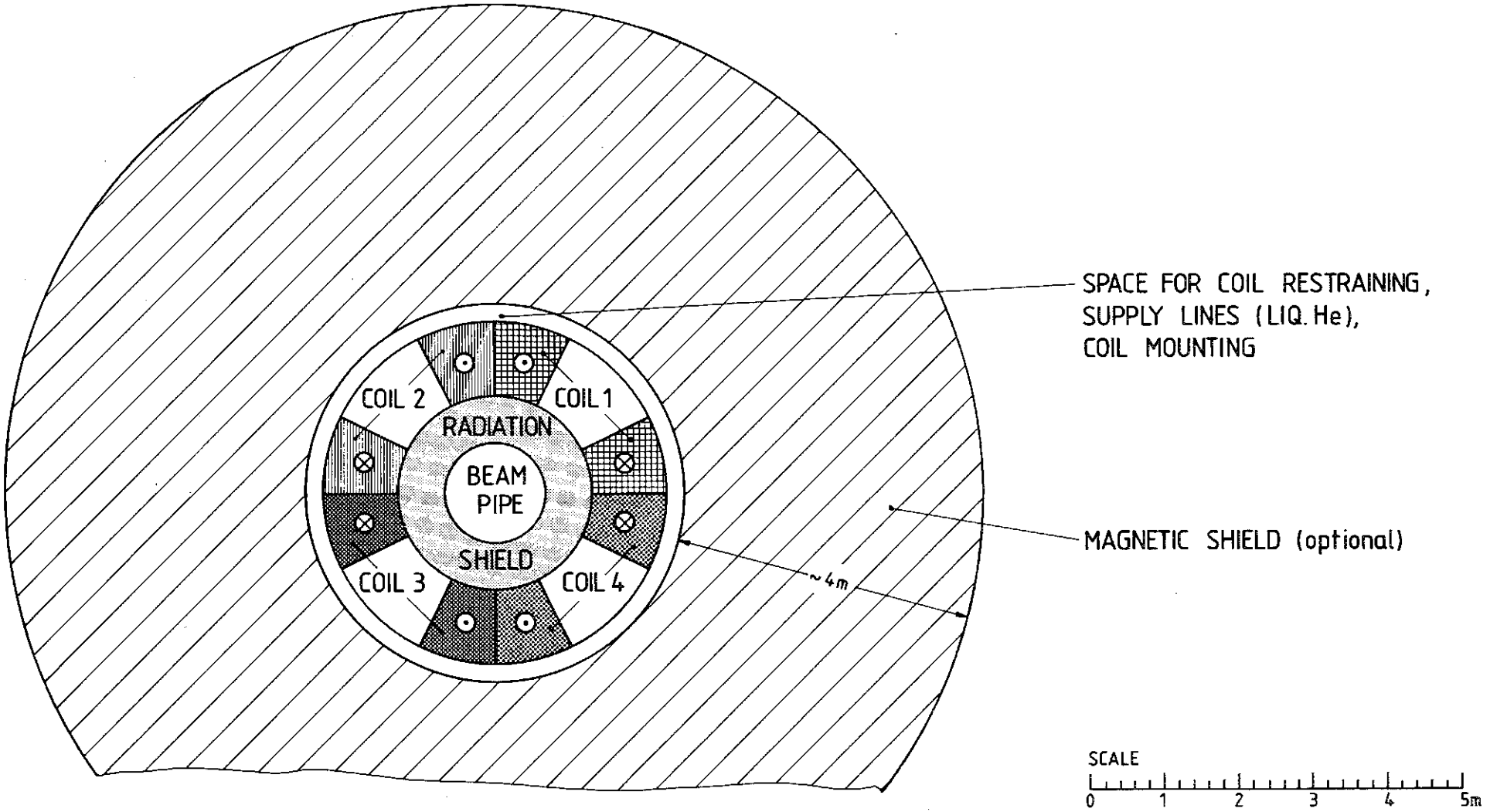

SCHEMATIC CROSS SECTION OF SUPER CONDUCTING END FOCUSSING QUADRUPOLE

FIGURE V.3-1

lifetime before radiation damage of the insulation becomes an issue. The Nb-Ti superconductor itself is relatively insensitive to radiation.

The main parameters of a conceptual quadrupole are given in Table V.3-1, its cross section is shown in Fig. V.3-1 (see Fig. II.1-8 for a visualization).

Table V.3-1. Parameters of Final Focusing Quadrupole

Inner coil radius	1.3 m
Outer coil radius	2.3 m
Radiation shield thickness	0.6 m
Field gradient in coil midplane	8 T/m
Average current density in coil	2 kA/cm^2
Peak induction in coil	12 T
Superconductor	- Nb_3Sn - NbTi in low field regions
Length of coil straight section to achieve a focusing strength of 20 T/m·m	~ 2.5 m
Overall coil length	4-6 m
Iron shield thickness (optional)	$\gtrsim$ 4 m

These parameters represent the limits of presently conceivable superconductor technology. In particular, the average current density cannot be increased:

- Large magnets ($\gtrsim 10^8$ J) require a fully stabilized superconductor, i.e. a sufficient amount of good normal conducting material must be provided in parallel with the conductor.

The Lorentz forces which have a particularly complicated pattern in multipole magnets must be accommodated without conductor degradation. A large fraction of the coil cross section must therefore be taken by steel or similar materials.

The current density and peak field attained correspond to parameters which are presently discussed for large superconducting magnets in tokamaks and mirrors.

Two aspects of the magnet design require special attention as they relate to the overall layout of HIBALL:

a) If the stray field must be shielded, iron of about 4 m radial thickness is needed (about 3000 tons per quadrupole). If this shielding is not considered, the mutual distortion of fields in neighboring beam lines and the stray field in the reactor chamber must be taken into account.

b) The overall axial length of the quadrupoles is determined by the coil and type, i.e. the spatial pattern in which the direction of current carrying conductors is reversed. At least 6 m of total length result if the coil end is provided in the same radial region in which the coil itself is situated (see Fig. (V.3-1). If the coil end is bent radially outward, the total length comes down to about 3.5 m but the radial dimensions and thus the magnetic shielding requirements are aggravated.

Reference for Section V.3

1. H. Brechna, Superconducting Magnet Systems. Berlin, Heidelberg, New York: Springer 1973, Techn. Physik in Einzeldarstellungen Bd. 18.

V.4 Shielding of Final Focussing Magnets

V.4.1 Introduction

Fusion reactors are required to accommodate a variety of penetrations. The purpose and size of these penetrations vary depending on the reactor type.[1-3] However, in all cases proper shielding is required to protect the vital components in the penetration from excessive radiation damage caused by radiation streaming. The major penetration in a heavy ion beam fusion reactor is the ion beam line. Such a penetration is characterized by a large area (~ 1 m^2). Furthermore, a large number of these penetrations (~ 20) is required to provide uniform illumination of the target.

The HIBALL reactor utilizes twenty 10 GeV Bi^{++} ion beams to bring the target to ignition. Each beam port is rectangular in shape with a height of 102.8 cm and a width of 34.3 cm at the reactor cavity wall of radius 7 m. There will be 8.14×10^{16} neutrons streaming through each beam line penetration per shot for a DT yield of 400 MJ. A number of superconducting magnets are arranged along the beam line to focus the ion beam to a spot 6 mm in diameter at the target. Adequate penetration shielding is required to protect these beam focussing magnets from excessive radiation damage.

Various beam line penetration shield shapes have been considered to assess their effectiveness in reducing the radiation effects in the HIBALL beam focussing magnets. A three-dimensional neutronics and photonics analysis must be performed to account for the geometrical complexity of the penetration. The design criteria used to determine the shielding requirements for the magnets are:

1) A 50% radiation induced resistivity increase in the copper stabilizer which corresponds to 1.4×10^{-4} dpa (displacements per atom).

2) A radiation dose of 5×10^{9} Rad in the epoxy electrical insulation.

3) A peak nuclear heating of 10^{-4} W/cm^3 in the magnet.

V.4.2 Calculational Model

The blanket region in HIBALL is 2 m thick and consists of SiC tubes through which $Li_{17}Pb_{83}$ liquid metal eutectic flows. The tubes occupy 33% of the blanket region. A cylindrical vacuum wall having a radius of 7 m is used. The first wall is made of ferritic steel (HT-9) and is 1 cm thick. A 0.4 m thick reflector composed of 90 v/o ferritic steel structure and 10 v/o $Li_{17}Pb_{83}$ coolant is used. The reactor utilizes a 3.5 m thick concrete biological shield. A more detailed discussion is given later in section VI.3. Because of its small thickness and negligible effect on radiation damage in the penetration, the first wall is neglected in the present analysis. The results presented here are based on a DT yield of 400 MJ and a repetition rate of 5 Hz yielding 7.1 x 10^{20} fusion neutrons per second. Neutron multiplication, spectrum softening and gamma production in the target have been taken into account by performing one-dimensional neutronics and photonics calculations[4] in the spherical target using the discrete ordinates code ANISN[5] as described in section III.1.

The final focussing system in HIBALL which focuses the beam from the periodic beam line onto the target, consists of eight quadrupole magnets. The total length of the system is 60.4 m. Each quadrupole has a length of 2.7 m with the drift sections between the quadrupoles being 1.8 m long. Figure V.4-1 shows the vertical and horizontal envelopes for the beam as it is transported from the periodic line to the target. The positions of the eight quadrupoles used for focussing the beam are also shown. The inner dimensions of the magnet shield have been chosen to be at least 2 cm larger than the beam size, as determined from the envelopes in Fig. V.4-1, at all places along the penetration.

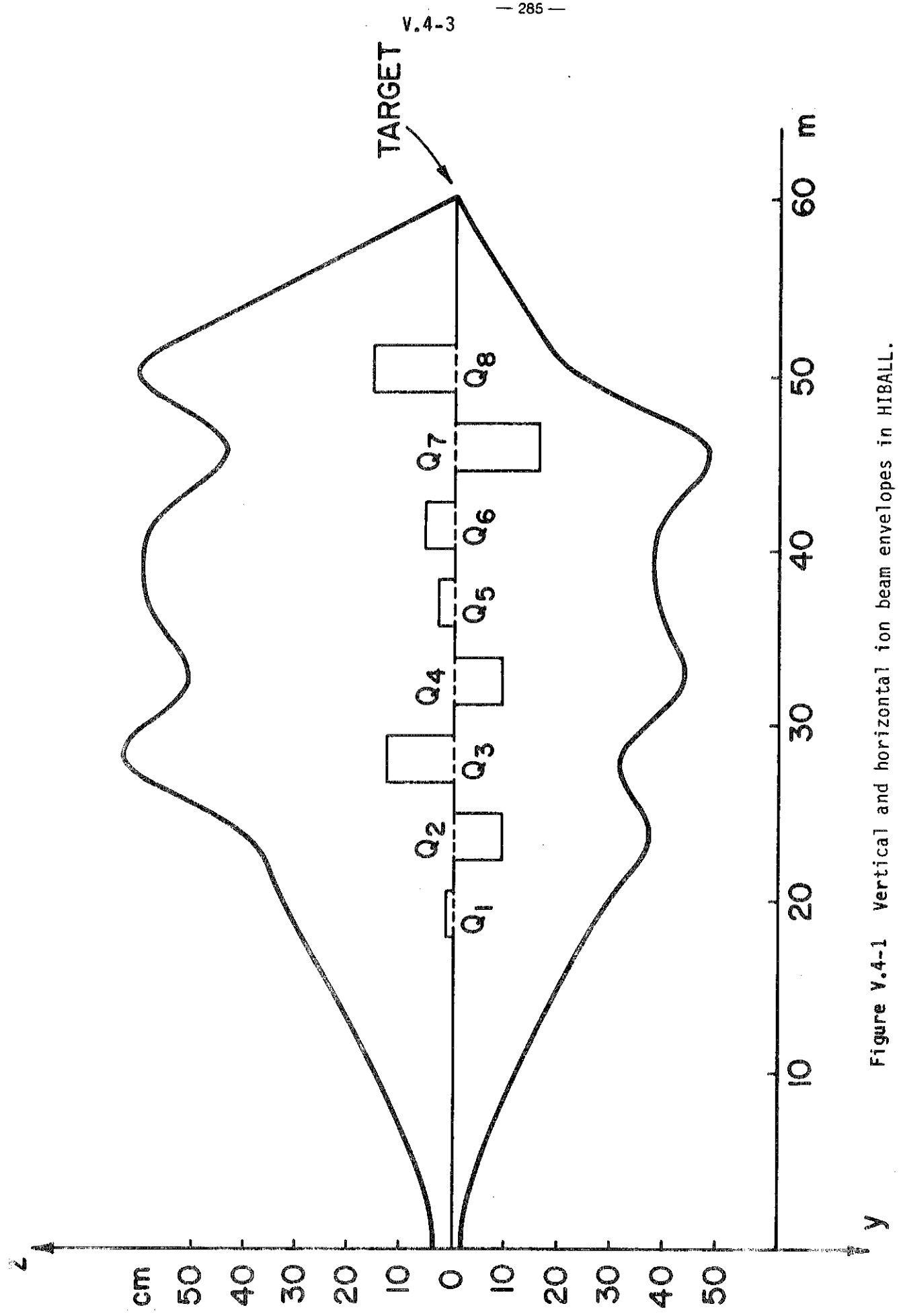

Figure V.4-1 Vertical and horizontal ion beam envelopes in HIBALL.

The 20 beam ports are arranged in two rows which are symmetric about the reactor midplane (z=0). The beam ports are 4 m apart vertically at the reactor vacuum wall. Because of symmetry only half a penetration is modelled in the present analysis with reflecting albedo boundaries used at the planes of symmetry. Consequently, only 1/40 of the reactor is modelled. This corresponds to a "pie slice" of the upper half of the reactor with an azimuthal angle of 18°. The angle between the centerline of the beam line penetration and the reactor midplane is 16°. The axes are rotated by 16° around the y axis for the penetration centerline to coincide with the x axis of the calculational model. This simplifies the description of the penetration geometry. Figure V.4-2 gives the vertical cross section for the focussing magnets and shield. Figure V.4-3 gives the cross section at the plane z'=0. Each quadrupole has a length of 2.7 m and a thickness of 1 m. Each magnet coil is modelled to have 7.52 v/o NbTi superconductor coils, 67.48 v/o copper stabilizer, 15 v/o liquid helium coolant, and 10 v/o insulation. The magnet shield is taken to be made of 60 v/o 316 SS, 15 v/o Pb, 15 v/o B_4C and 5 v/o H_2O coolant. The shield has a minimum thickness of 0.5 m in the quadrupole sections. The inner surface of the shield in the quadrupole section is tapered such that it does not see direct line of sight 14.1 MeV source neutrons. This will be shown to be more advantageous than using a shield with flat inner surface.

The neutronics and photonics calculations were performed using the three-dimensional Monte Carlo code MORSE.[6] A coupled 25 neutron - 21 gamma group cross section library was used. The library consists of the RSIC DLC-41B/VITAMIN-C data library[7] and the DLC-60/MACKLIB-IV response data library.[8] Since only 1/40 of the reactor is considered, we start with 1.775×10^{19} 14.1 MeV fusion neutrons per second and perform target calculations to determine

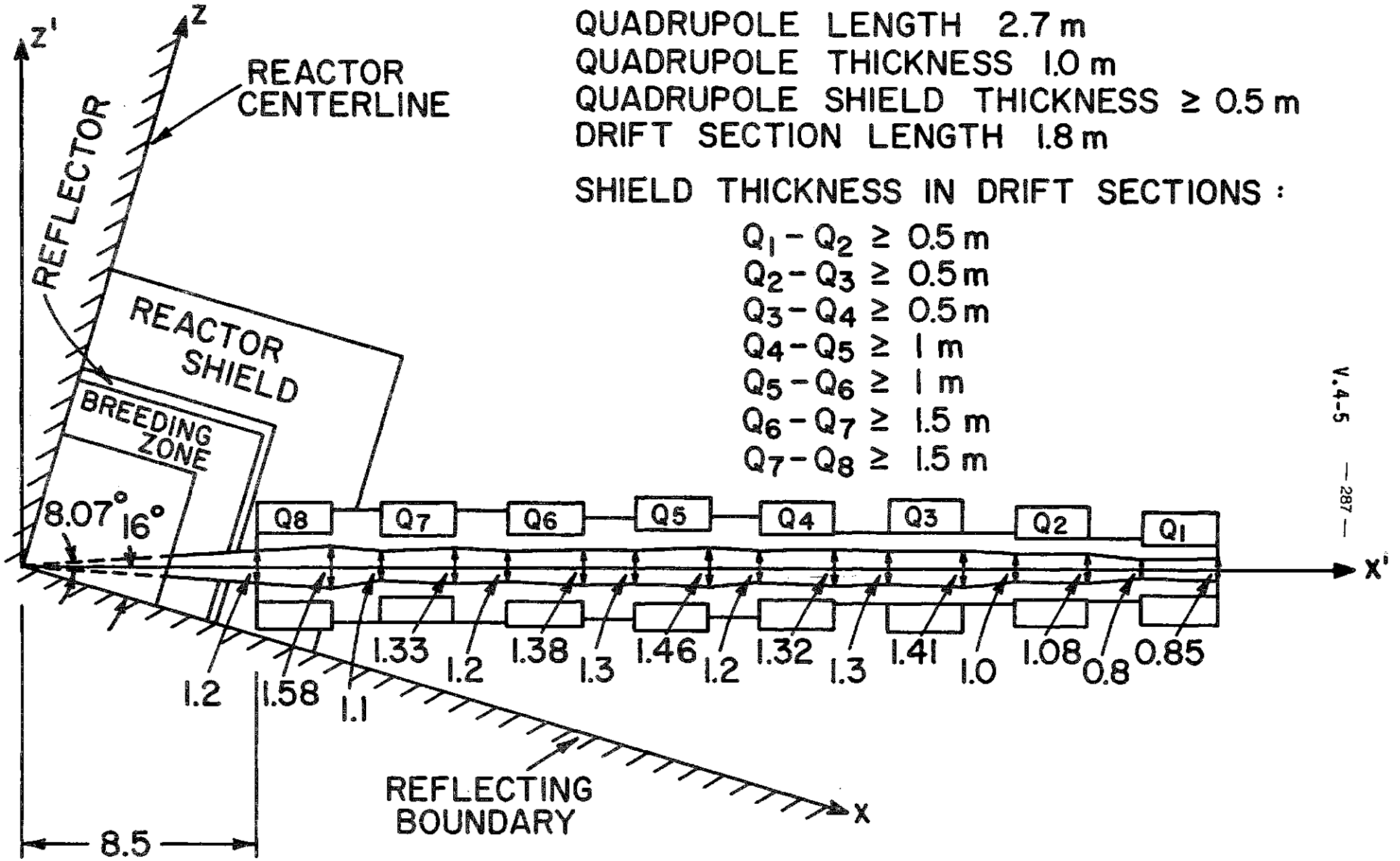

Figure V.4-2 Vertical cross section for focussing magnets and shield.

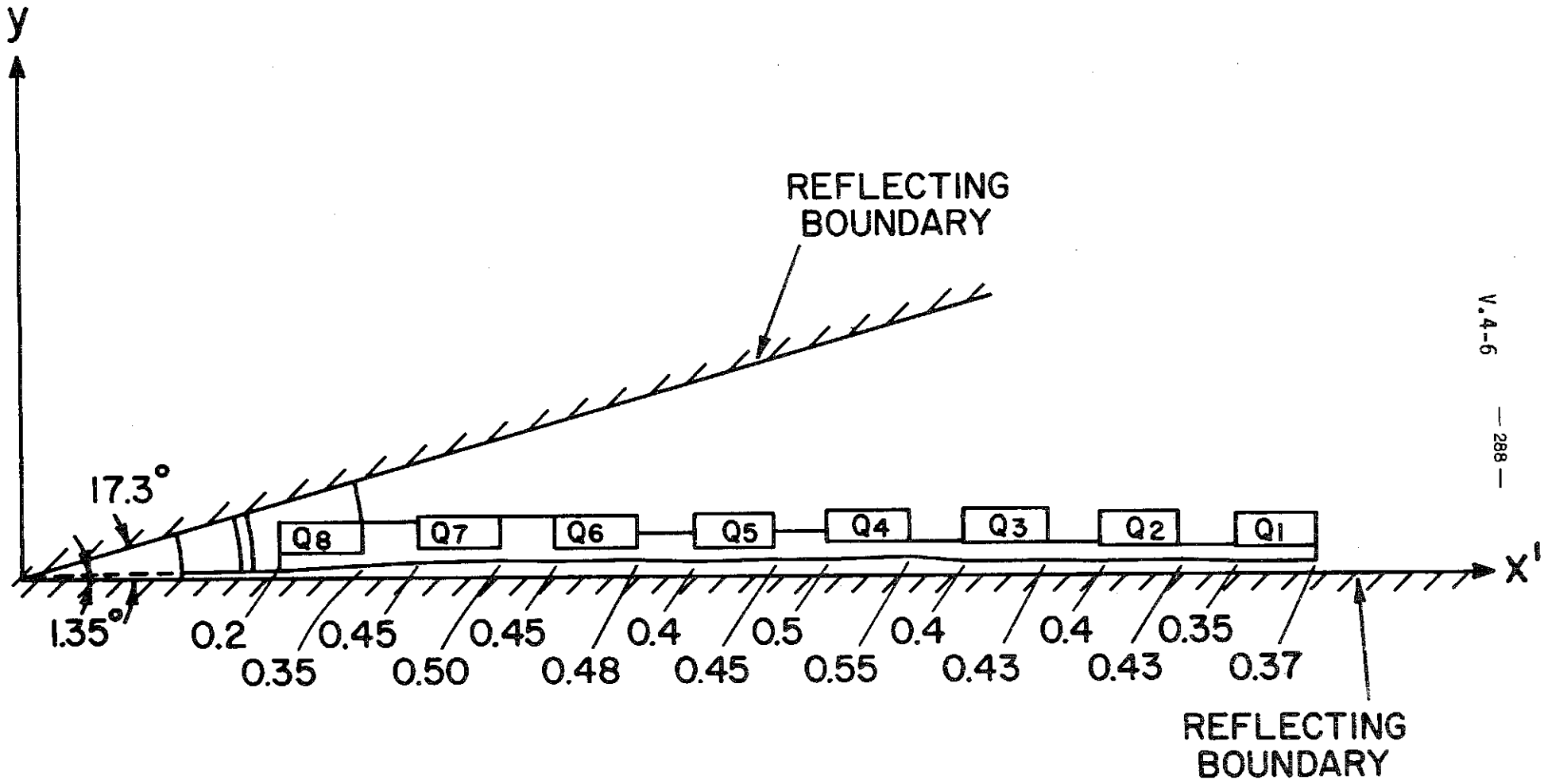

Figure V.4-3 Cross section at plane z'=0 for focussing magnets and shield.

the source intensity and spectrum for neutrons and gammas emitted from the target. These source neutrons and gammas are considered to be emitted isotropically at the origin.

In order to get statistically adequate estimates for the flux in the focussing magnets with a reasonable number of histories, an angular source biasing is used. The biasing technique is similar to that used previously for the analysis of the end plug of a tandem mirror fusion reactor.[3] However, in this case, the distribution is biased in both polar and azimuthal angles.

The distribution function from which the polar and azimuthal angles are picked is

$$P(\underline{\Omega})\ d\underline{\Omega} = P(\mu)\ P(\phi)\ d\mu\ d\phi\ . \qquad (V.4\text{-}1)$$

For the unbiased isotropic distribution we have

$$P(\mu) = 1\ ,\ (0 \leq \mu \leq 1)$$

and

$$P(\phi) = 10/\pi\ ,\ (0 \leq \phi \leq \frac{\pi}{10})$$

where $\mu=\cos\theta$, and θ and ϕ are the polar and azimuthal angles with respect to the frame xyz. If the biased distribution function is given by

$$P'(\underline{\Omega})d\underline{\Omega} = P'(\mu)\ P'(\phi)\ d\mu\ d\phi\ , \qquad (V.4\text{-}2)$$

the statistical weight of the source should be modified by the ratio of the

unbiased to the biased distribution functions at any particular solid angle (θ,ϕ) for the final estimates to be unbiased. Therefore, the weight for the biased case, w', is related to the weight for the unbiased case, w, by

$$w' = w \frac{P(\mu)P(\phi)}{P'(\mu)P'(\phi)} . \qquad (V.4\text{-}3)$$

In this work, μ is picked from a biased distribution which forces 90% of the source neutrons to have $\theta_p - \frac{\Delta\theta_p}{2} < \theta < \theta_p + \frac{\Delta\theta_p}{2}$, where $\theta_p = 74^0$ is the angle between the axes x' and z, and $\Delta\theta_p = 8.07^0$ as shown in Fig. V.4-2. A schematic of the biased and unbiased distributions for μ is given in Fig. V.4-4(a). The azimuthal angle, ϕ, is picked from a biased distribution that forces 90% of the source neutrons to have $0 < \phi < \Delta\phi_p$, where $\Delta\phi_p = 1.4^0$ is the azimuthal angle in the plane z=0 subtended by the penetration. A schematic of the biased and unbiased distributions for ϕ is given in Fig. V.4-4(b). After picking μ and ϕ, the direction cosines of the source particle with respect to the frame xyz are calculated. An orthogonal transformation is performed to determine the corresponding direction cosines with respect to the frame x'yz' used in the calculations.

Because of the $1/R^2$ geometrical attenuation, the largest radiation effects occur in the magnets closer to the source. For this reason and to reduce the computing time, only the last two quadrupoles Q_7 and Q_8 are modelled. The geometry for the computational model used is given in Fig. V.4-5. Each quadrupole is divided into three zones and each quadrupole shield is divided into two zones. Zone 12 represents the biological shield. Zones 13 and 14 represent the reflector and blanket, respectively. The inner vacuum region (zone 15) is extended to the region outside the biological shield and the focussing magnets. This allows the neutrons leaking out of the biological

V.4-9

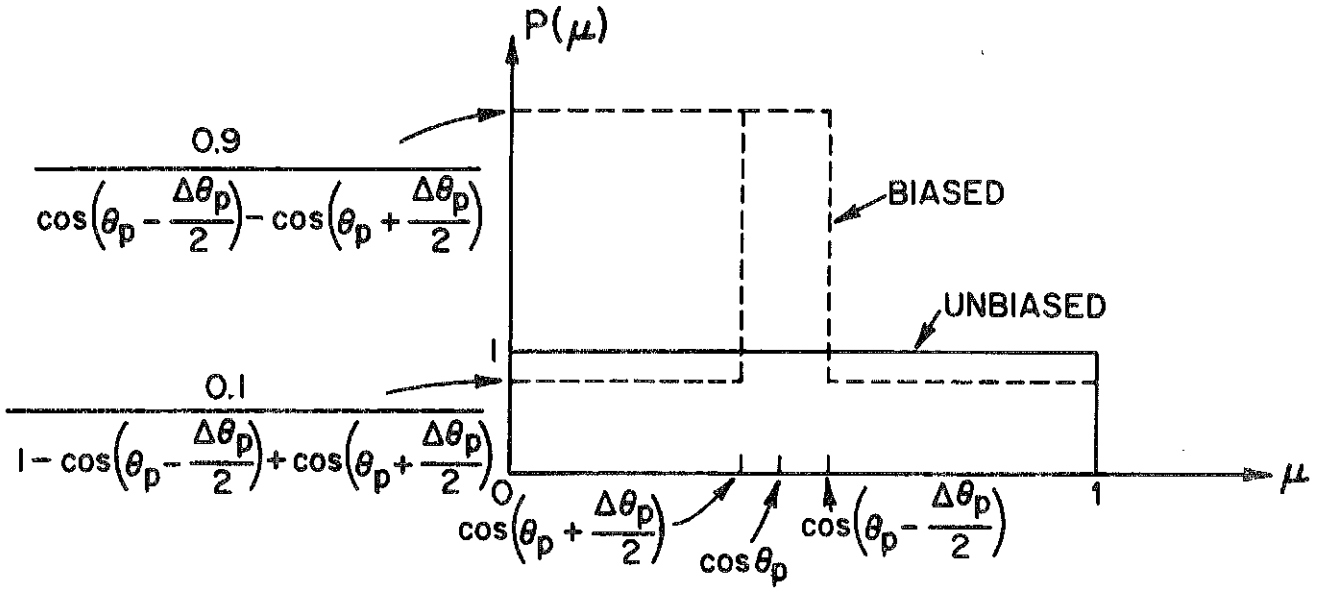

(a) ANGULAR BIASING FOR POLAR ANGLE

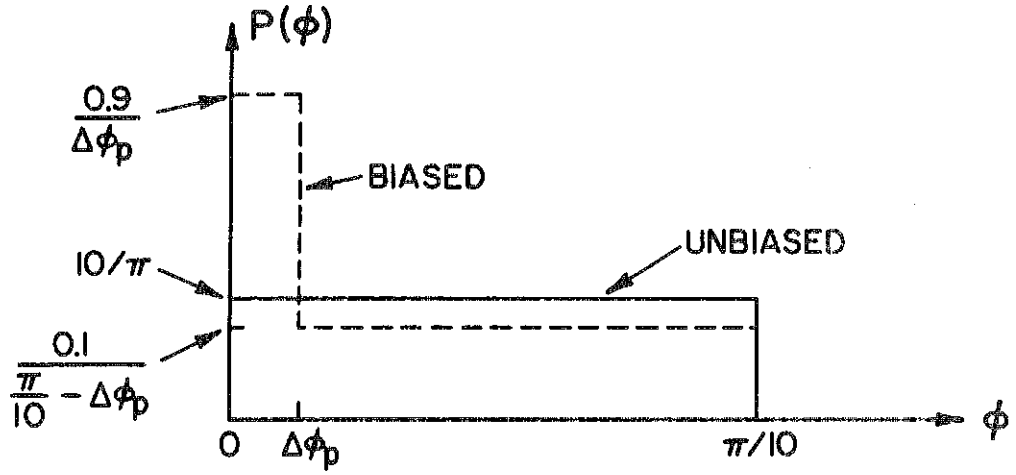

(b) ANGULAR BIASING FOR AZIMUTHAL ANGLE

Figure V.4-4 Angular source biasing scheme.

V.4-10

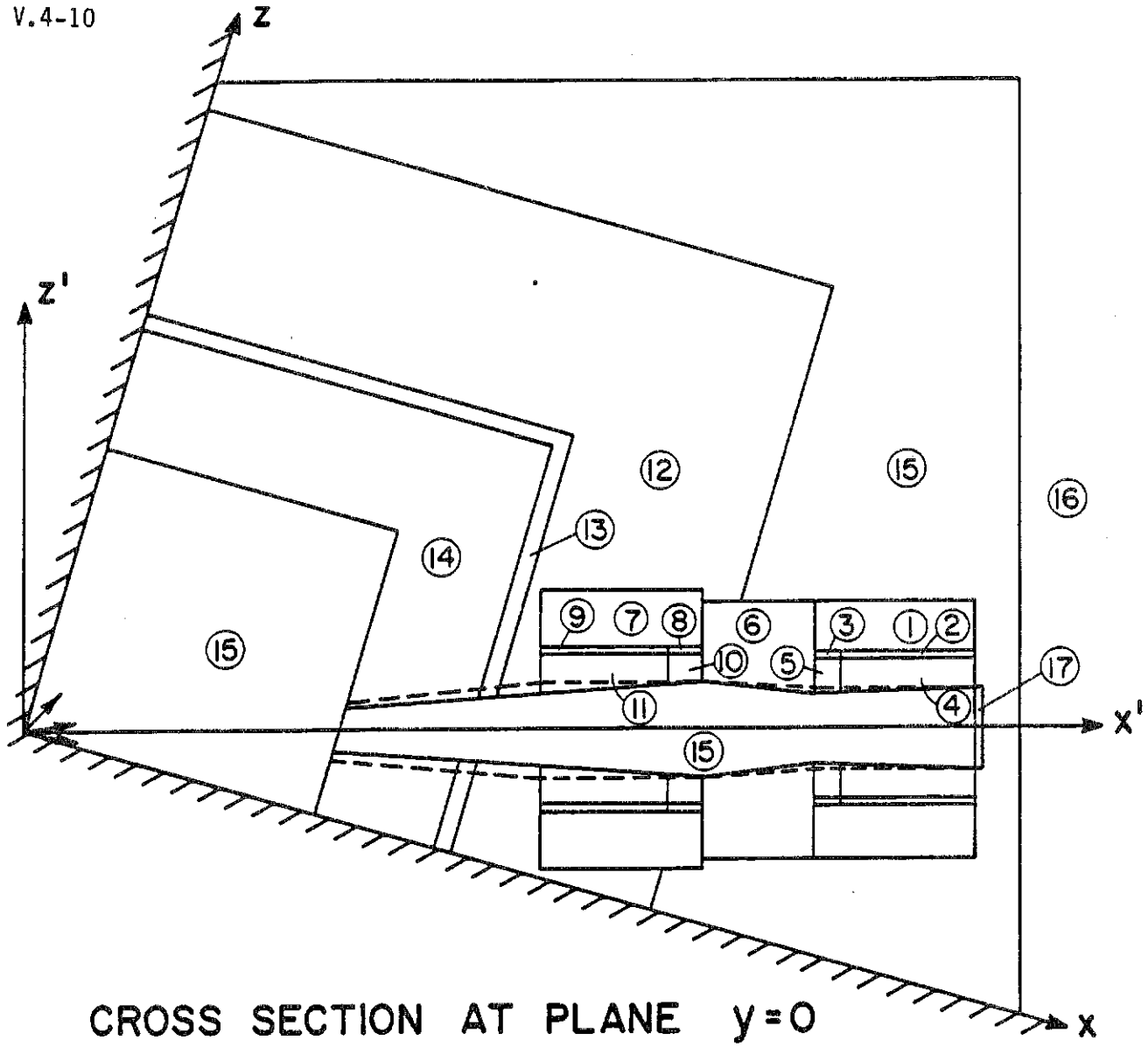

CROSS SECTION AT PLANE y=0

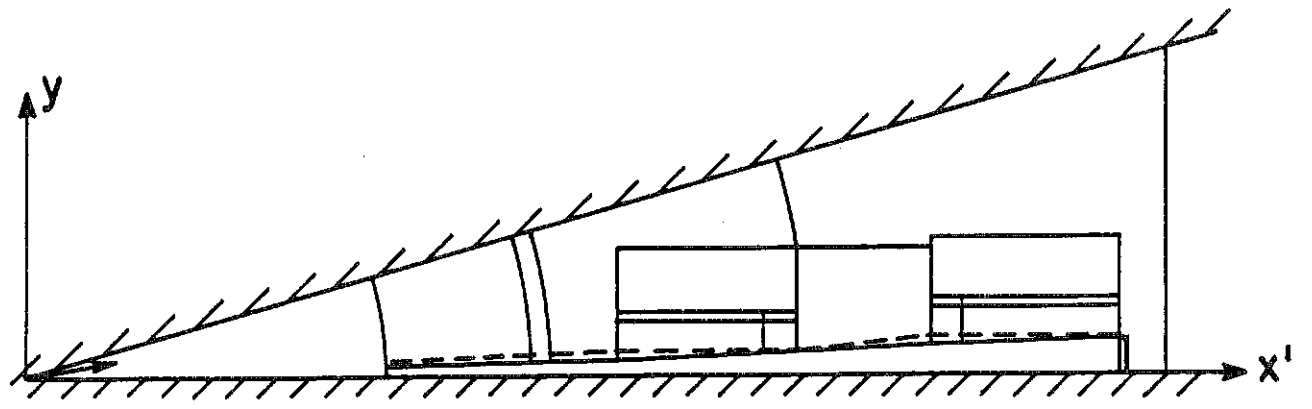

CROSS SECTION AT PLANE z'=0

Figure V.4-5 Geometry of computational model for final two focussing magnets.

shield to have additional collisions in the focussing magnets instead of being discarded as they would be if an outer vacuum region is used. To quantify leakage from the penetration a 1 cm thick penetration plug is designated as zone 17. The dotted lines in Fig. V.4-5 represent the geometry for a flat shield in the quadrupole sections. The solid lines represent the case with the shield being tapered in the quadrupole sections. Table V.4-1 gives the dimensions and material composition used in the different zones. The results presented here are obtained using 20,000 histories in the Monte Carlo problem.

V.4.3 Results and Discussion

The effect of tapering the shield in the quadrupole sections on the flux in the magnets was investigated. The geometrical models used for the flat and tapered shield cases are shown in Fig. V.4-5. In the tapered shield case, the shield is tapered along the direct line of sight of source neutrons. In this case, no direct 14.1 MeV source neutrons impinge on the part of the shield in the quadrupole sections. All source neutrons impinge on the inner surface of the shield in the drift section. Table V.4-2 shows the effect of tapering the shield on the neutron scalar flux in the different penetration zones.

It is clear from the results in Table V.4-2 that tapering the shield in the quadrupole sections reduces the neutron flux in the magnets. The peak neutron flux in quadrupole 7 occurring in zone 3 is reduced by a factor of 1.8 when the shield is tapered. On the other hand, the peak neutron flux in quadrupole 8 occurring in zone 8 is reduced by an order of magnitude. The effect of shield tapering on the flux in quadrupole 8 is more pronounced than that in quadrupole 7 because scattering of 14.1 MeV neutrons is highly forward peaked. It is clear also that the flux in the shield for quadrupole 8 is reduced significantly by tapering. The reason is that in the tapered case no direct line of sight source neutrons reach zones 10 and 11 and neutrons reach

Table V.4-1 Zones Used to Model the Final Two Focussing Quadrupoles and Their Shields

Region	Zone Number	Length (m)	Thickness (m) Tapered Shield	Flat Shield	Material Composition
Quadrupole 7	1	2.7	.9	.9	7.52 v/o NbTi + 67.48 v/o Cu
	2	2.2	.1	.1	+ 15 v/o Liq. He + 10 v/o
	3	.5	.1	.1	Insulation
Shield for Q_7	4	2.2	.5-.55	.5	60 v/o 316 SS + 15 v/o Pb
	5	.5	.54-.56	.5	+ 15 v/o B_4C + 5 v/o H_2O
Drift Section Shield	6	1.8	1.37-1.56	1.35-1.50	
Quadrupole 8	7	2.7	.9	.9	7.52 v/o NbTi + 67.48 v/o Cu
	8	.5	.1	.1	+ 15 v/o Liq. He + 10 v/o
	9	2.2	.1	.1	Insulation
Shield for Q_8	10	.5	.5-.54	.5	60 v/o 316 SS + 15 v/o Pb
	11	2.2	.53-.69	.5	+ 15 v/o B_4C + 5 v/o H_2O
Biological Shield	12	-	3.5	3.5	95 v/o Concrete + 5 v/o H_2O
Reflector	13	-	.4	.4	90 v/o ferritic steel + 10 v/o $Li_{17}Pb_{83}$
Blanket	14	-	2.0	2.0	98 v/o $Li_{17}Pb_{83}$ + 2 v/o SiC (.33 d.f.)
Inner Vacuum	15	-	-	-	Void
Outer Vacuum	16	-	-	-	Void
Penetration Plug	17	-	.01	.01	316 SS

Table V.4-2 Effect of Tapering the Shield on the Flux Estimates in Penetration Zones

Region	Zone Number	Neutron Scalar Flux (n/cm^2 s) Flat Shield	Tapered Shield
Quadrupole 7	1	2.767×10^8 (0.60)*	1.631×10^8 (0.77)
	2	4.504×10^9 (0.40)	3.441×10^9 (0.52)
	3	2.156×10^{10} (0.38)	1.217×10^{10} (0.48)
Shield for Q_7	4	1.552×10^{12} (0.13)	7.728×10^{11} (0.14)
	5	3.606×10^{12} (0.17)	2.224×10^{12} (0.15)
Drift Section Shield	6	1.299×10^{12} (0.09)	9.765×10^{11} (0.08)
Quadrupole 8	7	7.388×10^9 (0.75)	9.720×10^6 (0.77)
	8	9.854×10^{10} (0.76)	9.758×10^9 (0.69)
	9	1.780×10^{11} (0.50)	NS**
Shield for Q_8	10	6.624×10^{12} (0.14)	8.108×10^{11} (0.18)
	11	8.181×10^{12} (0.11)	1.980×10^{11} (0.30)
Penetration Plug	17	5.936×10^{13} (0.13)	5.368×10^{13} (0.10)

* Numbers in parentheses are fractional standard deviations.

** No score in this zone for the 20,000 histories used.

these zones only after having collisions in the drift section shield (zone 6). On the other hand, the neutron flux in the shield for quadrupole 7 decreases only slightly because the 14.1 MeV source neutrons have a larger chance to go in the forward direction into zones 4 and 5 than to go in the backward direction into zones 10 and 11 after colliding in the drift section (zone 6). The neutron flux at the first surface of the HIBALL blanket at the reactor midplane is 2.364×10^{14} n/cm^2 s. This implies that the peak flux in the

focussing magnets is more than four orders of magnitude lower than the flux at the first surface of the blanket.

The neutron leakage flux at the penetration plug is 5.368×10^{13} n/cm^2 s for the tapered shield case. The direct line of sight 14.1 MeV neutron flux leaking from the penetration is 2.398×10^{13} n/cm^2 s which amounts to 45% of the neutron leakage flux. It is clear from the results in Table V.4-2 that the neutron flux in the penetration plug decreases by tapering the shield. The reason is that the amount of neutrons leaking after colliding along the penetration decreases when no direct line of sight source neutrons are incident on the shield for quadrupole 7. Even though an appreciable amount of neutrons are leaking through the penetration modelled here, this does not pose a serious problem because only the last two quadrupoles are modelled here. The other six quadrupoles are shielded in the same manner as shown in Figs. V.4-2 and V.4-3. Considering $1/R^2$ attenuation, the neutron leakage flux at quadrupole 1 is estimated to be 7.257×10^{12} n/cm^2 s.

Further modification in the shape of the shield in the drift section is considered to improve the effectiveness of the penetration shield. The inner surface of the shield in the drift section is tapered at both ends such that it coincides with the direct line of sight from the source as shown in Fig. V.4-6. In this case, all source neutrons impinge on a vertical neutron dump in the shield. This increases the minimum distance between the magnet and the point on the surface of the shield where the source neutron has its first collision and is expected to reduce the radiation damage in the magnets. Two positions are considered for the neutron dump as shown in Fig. V.4-6.

Table V.4-3 gives the atomic displacements per full power year (FPY) in the Cu stabilizer in the different magnet zones for the cases of flat shield and tapered shield with the different options for the drift section shield

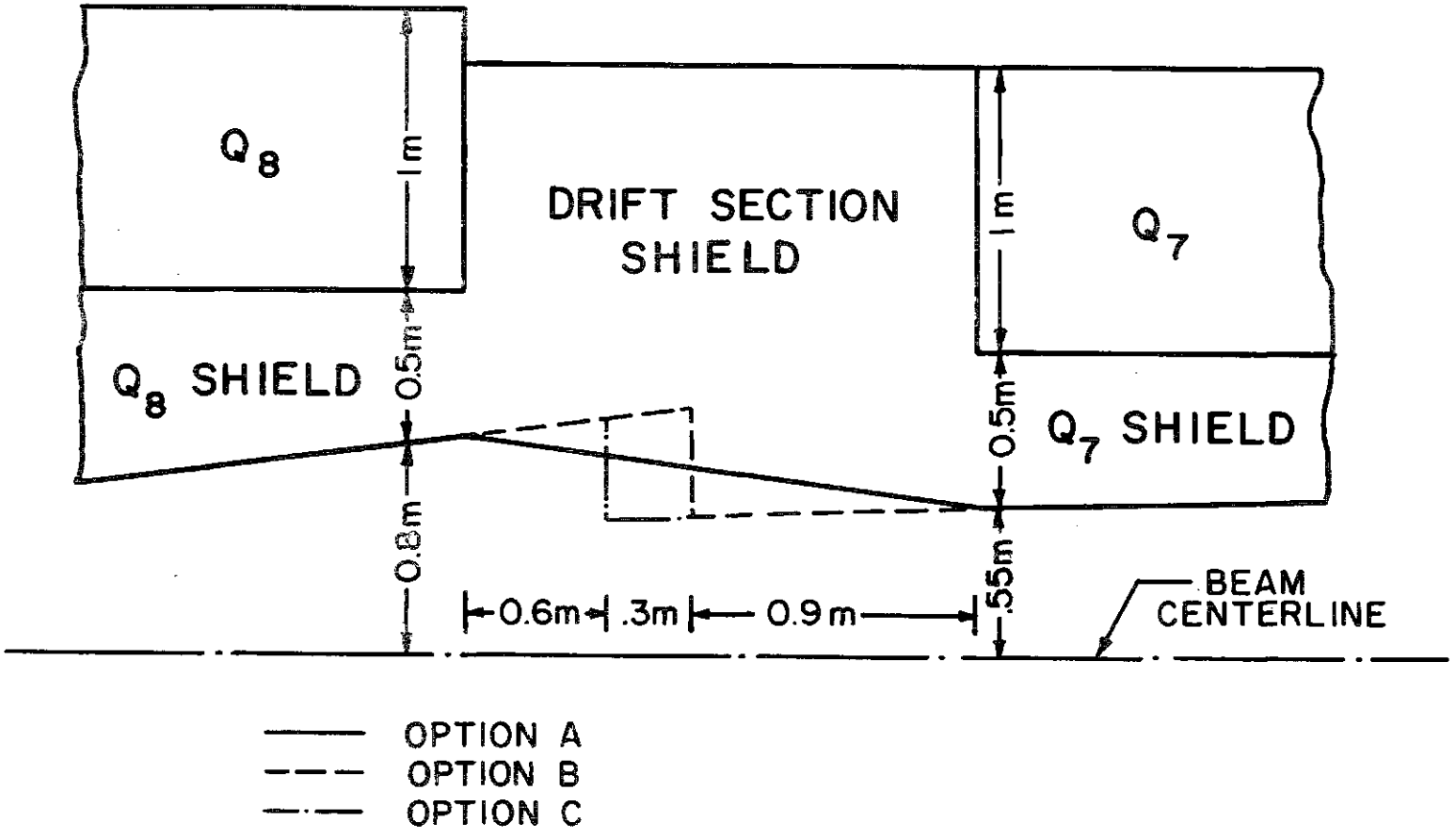

Figure V.4-6 Options for tapering drift section shield.

Table V.4-3 Effect of Penetration Shield Shape on DPA Rate in the Copper Stabilizer

Region	Zone Number	DPA Rate (dpa/FPY) Flat Shield	Tapered Shield in Quadrupole Section Option A	Option B	Option C
Quadrupole 7	1	2.167×10^{-6}	1.142×10^{-6}	1.023×10^{-7}	NS
	2	3.129×10^{-5}	3.686×10^{-5}	1.256×10^{-5}	NS
	3	9.115×10^{-5}	9.702×10^{-5}	1.600×10^{-5}	2.710×10^{-6}
Quadrupole 8	7	1.690×10^{-5}	1.742×10^{-7}	NS	1.749×10^{-8}
	8	6.182×10^{-4}	1.151×10^{-4}	NS	4.483×10^{-6}
	9	1.056×10^{-3}	NS	NS	7.580×10^{-7}

shown in Fig. V.4-6. Notice that even though the scalar flux in zones 2 and 3 of quadrupole 7 decrease when the shield is tapered with option A (Table V.4-2), the dpa rate slightly increases. The reason is that when the shield is tapered, all 14.1 MeV source neutrons fall on the drift section shield (zone 6) instead of falling on zones 4 and 5 as well. Since elastic scattering of high energy neutrons is highly forward peaked, this results in a slight increase in the high energy flux in zones 2 and 3 of quadrupole 7 yielding higher dpa values. As the neutrons slow down in the shield the scattering becomes more isotropic with the low energy flux decreasing in zones 2 and 3. The net effect is to decrease the total neutron scalar flux as shown in Table V.4-2. On the other hand, tapering the shield with option A results in significant reduction in the dpa rate in quadrupole 8.

If shielding option B is used, it is found that the peak dpa rate in quadrupole 7 is decreased by a factor of ~ 6 as compared to option A in

addition to decreasing the peak dpa rate in quadrupole 8 significantly. In the run of 20,000 histories, no contribution was obtained in quadrupole 8. Because scattering is forward peaked at high neutron energies, locating the source neutron dump halfway between Q_7 and Q_8 results in considerable reduction in damage in Q_8 and a smaller reduction in Q_7. Using option A the peak damage occurs in Q_8 while it occurs in Q_7 when option B is used. In option C, the source neutron dump is moved closer to Q_8. This is found to decrease the peak dpa rate in Q_7 considerably and increase the peak damage rate in Q_8 only slightly. The peak in Q_8 when option C is used is a factor of ~ 25 lower than that when option A is used.

Table V.4-4 gives the radiation dose rate in the epoxy electrical insulation in the different magnet zones for the different geometrical options considered. Again, it is clear that significant reduction in the radiation dose is obtained when the suggested shield geometrical modifications are adopted. The results given in Table V.4-4 include the contribution from both neutron and gamma energy deposition. Table V.4-5 gives the peak dpa rate, the peak radiation dose, and the peak power density in the focussing magnets for the different geometrical options considered. It is clear that the tapered shield with option C is the most effective shield design. Using option C for the drift section shield is found to result in a peak dpa rate in the Cu stabilizer of only 4.483×10^{-6} dpa/FPY. The neutron leakage flux at the penetration plug is found also to decrease to a value of 4.615×10^{13} n/cm^2 s with option B and 3.361×10^{13} n/cm^2 s for option C. This results from increasing the attenuation distance in the shield for neutrons impinging on the source neutron dump.

Radiation damage to the stabilizing material in the superconducting magnets results in increasing the electrical resistivity. The radiation induced

Table V.4-4 Effect of Penetration Shield Shape on Radiation Dose Rate in the Epoxy Insulation

Region	Zone Number	Radiation Dose Rate (Rad/FPY) Flat Shield	Tapered Shield in Quadrupole Section Option A	Option B	Option C
Quadrupole 7	1	5.220×10^{6}	2.149×10^{6}	7.966×10^{5}	1.625×10^{2}
	2	5.914×10^{7}	7.637×10^{7}	1.978×10^{7}	7.390×10^{3}
	3	1.831×10^{8}	2.195×10^{8}	2.526×10^{7}	4.174×10^{6}
Quadrupole 8	7	4.961×10^{7}	3.350×10^{5}	NS	1.031×10^{5}
	8	1.616×10^{9}	2.552×10^{8}	NS	7.188×10^{6}
	9	3.467×10^{9}	NS	NS	1.250×10^{6}

Table V.4-5 Effect of Penetration Shield Shape on Peak Values of DPA, Radiation Dose, and Nuclear Heating in the Focussing Magnets

	Flat Shield	Tapered Shield in Quadrupole Section Option A	Option B	Option C
Peak dpa/FPY in Cu Stabilizer	1.056×10^{-3}	1.151×10^{-4}	1.600×10^{-5}	4.480×10^{-6}
Peak Radiation Dose in Insulation	3.467×10^{9}	2.552×10^{8}	2.526×10^{7}	7.20×10^{6}
Peak Power Density (W/cm^3)	4.380×10^{-3}	2.44×10^{-4}	3.554×10^{-6}	5.350×10^{-7}

resistivity is related to the number of displacements per atom in the stabilizer. A 50% radiation induced resistivity increase in the copper stabilizer is considered as a design criterion. A resistivity of this amount is produced by a damage level of 1.4×10^{-4} dpa. This value is obtained using the relation between the induced resistivity in Cu, ρ_i and the total displacements per atom, d, given by the following equation:[9]

$$\rho_i = 3 \times 10^{-7} \left(1 - e^{-563d}\right) \Omega \cdot \text{cm} . \qquad \text{(V.4-4)}$$

However, recovery is possible by annealing. Increasing the time span between required anneals is desirable for reducing the maintenance cost. Decreasing the number of anneals required during the reactor lifetime also minimizes any possible undesirable consequences of cyclic irradiation. Using the shield design with option C, the maximum period of operation without annealing is ~ 31 full power years. This is compared to 8.5 FPY when option B is used and ~ 1 FPY when option A is used. If a flat shield design is used, one needs to anneal every ~ 45 days. This implies that when the shield design with option C is used, no annealing is needed for an estimated reactor lifetime of 20 full power years.

The radiation effects on the insulator are not reversible and it is essential that it lasts the whole reactor lifetime. The design limit used for the radiation dose in the epoxy electrical insulator is 5×10^9 rad. The results show that for an estimated reactor lifetime of 20 full power years, the designs with options B and C result in an accumulated radiation dose well below the design limit, while the designs with a flat shield and with option A do not satisfy the design criterion. The design limit on the peak power density is set to be 10^{-4} W/cm^3. It is clear from the results of Table V.4-5

that the tapered shield design with options B and C satisfy this design criterion while the designs with a flat shield and option A do not fulfill this requirement. It is concluded from the results presented here that a magnet shield which is tapered in the quadrupole sections with option C for the drift section shield shape satisfies the design criteria on the radiation dose in the insulator and the nuclear heating in the magnet with the possibility of eliminating the need for magnet annealing during the whole reactor lifetime.

Our calculations show that the edges of quadrupole 8 close to the reflector are exposed to relatively high levels of radiation because of the poor shielding effectiveness of concrete. To meet the design criteria, the dpa rate, radiation dose and power density at the corner of Q_8 close to the reflector need to be reduced by factors of 5, 10, and 40, respectively. This can be achieved by surrounding the magnet at these spots by more effective shielding. Tungsten can be used to attenuate neutrons and hence reduce the dpa and neutron heating. Lead can also be used to attenuate the high gamma flux which is the main source for nuclear heating in these parts of the magnet.

V.4.4 Summary

Tapering the shield in the quadrupole sections in such a way that all direct line of sight 14.1 MeV source neutrons fall on the inner surface of the drift section shield was found to reduce the radiation damage in the magnets. Several options for the shape of the shield in the drift sections were analyzed. The smallest radiation effects in the magnet were obtained when the inner surface of the shield in the drift sections was also tapered resulting in a vertical neutron dump between the magnets. Better shielding was obtained when the neutron dump between the last two quadrupoles was placed closer to the last quadrupole. With this design, the period between required magnet

anneals was increased to ~ 31 full power years compared to 45 days for the flat shield design. This implies that using the recommended shield design, the need for annealing during the reactor lifetime can be eliminated completely. The recommended shield design reduces the peak radiation dose in the insulator allowing it to last for the whole reactor lifetime. The peak power density in the magnet is also reduced significantly. We conclude that with proper shield design the final focusing magnets for HIBALL can be protected sufficiently so that radiation damage will not limit their lifetime and that the nuclear heating loads are not serious.

References for Section V.4

1. J. Jung and M.A. Abdou, Nuclear Technology, 41, 71 (1978).

2. M. Ragheb, A. Klein, and C.W. Maynard, Nuclear Technology/Fusion, 1, 99 (1981).

3. M. Ragheb and C.W. Maynard, UWFDM-398, University of Wisconsin (1981).

4. M. Sawan, W. Vogelsang, and G. Moses, UWFDM-395, University of Wisconsin (1980).

5. RSIC Code Package CCC-254, "ANISN-ORNL", Radiation Shielding Information Center, ORNL.

6. RSIC Code Package CCC-203, "MORSE-CG", Radiation Shielding Information Center, ORNL.

7. RSIC Data Library Collection, "VITAMIN-C, 171 Neutron, 36 Gamma-Ray Group Cross Sections Library in AMPX Interface Format for Fusion Neutronics Studies", DLC-41, ORNL.

8. RSIC Data Library Collection, "MACKLIB-IV, 171 Neutron, 36 Gamma-Ray Group Kerma Factor Library", DLC-60, ORNL.

9. M. Abdou and R. Roussin, ORNL/TM-3706, Oak Ridge National Laboratory (1976).

V.5 Considerations for Future Design

To focus several intense ion beams on a spot of 3 mm radius it is advantageous to choose ion beams with differently large phase space areas in the horizontal and the vertical planes. One main reason for this is that the INPORT tube protection of the reactor vessel is easier to fabricate by requiring vertically long and horizontally narrow beam apertures instead of round openings of equal area. Another main reason is that the choice of unequal phase space areas simplifies the correction of image aberrations of the final focusing lens system. Some problems in this case arise in the design of the beam guidance systems which mainly result in larger beam apertures and thus larger magnet elements. To accommodate the required phase space area of about 30 x 120 $\pi^2 mm^2$ $mrad^2$ for 20 beam lines a horizontal phase space area of 30 π mm-mrad and a vertical phase space area of 120 π mm-mrad, each was chosen as basis of all geometric designs in this section, resulting in beam apertures of ±110 and ±340 mm in the middle of the 3 m thick wall of the reactor vessel.

In order to achieve a homogeneous bombardment of the target and at the same time allow a Pb-Li flow which is as little disturbed as possible the 20 beam lines were arranged in 10 pairs inclined by ±16°. An even more homogeneous bombardment of the target would be feasible by choosing not only two but three or possibly four rows of beam lines each of which transmits a smaller phase space. This may be understood as a smaller lateral phase space for a beam pulse of equal length or, which may be of high importance, a shorter ion pulse for beams of constant lateral phase space.

Since all focusing lenses must be placed outside of the reactor vessel their diameters must be larger than the openings in the reactor wall resulting in quite bulky magnets of high flux densities. To keep these lens diameters

within limits it seems reasonable to use as short lenses as possible. Thus superconducting quadrupole lenses with high magnetic flux densities are attractive. Unfortunately cooled superconductors are rather sensitive to ionizing radiation so that rather well-designed shielding against neutrons is necessary. However, such radiation shields increase the lens apertures considerably. For lens coils which have a direct view to the target this increase in diameter is about ±500 mm so that the cross section within any lens is mainly filled by shielding material and only to a minor percentage by the ion beam. For lens coils which have no direct view to the target this increase in diameter is around ±300 mm.

In the design of such final focusing lenses attention must be paid to the existing space charge of the ion beams. Since ion beams of comparable intensities are not yet available experimentally it is difficult to predict to what extent the positive charge of ions is compensated by slow electrons or slow negative ions within the beam. The predictions of achievable space charge compensations vary from 0% to 100% since it seems possible to modify the experimental conditions to favor either one of these limits.

As long as no experimental information on such ion beams is available it seems most useful to either look for solutions which are relatively insensitive to varying space charge by avoiding narrow beam cross overs and long drift distances[1] (most probably, however, the required focusing precision cannot be preserved over a wide range of space charge values). We could also look for solutions in which the effects of varying space charge can be compensated by varying the magnet flux densities in some or all lenses of the final focusing section. Since both types of solutions can be expected to work only for narrow regions of space charge compensation, any design for an arbitrarily chosen fixed percentage can only be an example.

To provide a summary about possible solutions for the final focusing lens systems and at the same time pay some attention to the mentioned problems we shall below discuss three principle solutions:

1. The first type of lens system consists of 6 or 8 quadrupoles to which the rather narrow ion bundle from a beam transport line is matched by normally 3 additional quadrupoles.[2] Though such solutions seem quite reasonable at first and second sight, they all have the draw-back that the lens coils have a direct view to the fusion target and thus require heavy shielding. While the final focusing lenses of the reference design (see section V.2) require maximal magnetic flux densities in excess of 4 T at the beam envelope, resulting in more than 8 T at the quadrupole coils outside of the heavy shielding, it is also possible to find solutions for which the maximal flux densities stay below 2 T at the beam envelope. Thus good magnet iron could be used to concentrate the magnetic flux without saturation effects in the pole tips. This would result in considerably less costly systems for which the shielding problem is much simpler. Such solutions, however, must be expected to have increased image aberrations so that possibly the acceptable phase space for each ion beam must be reduced slightly in order that the major portion of the ions in a beam can be delivered to the target.
2. The second type of lens system consists not only of quadrupole lenses but also includes magnetic sector fields in the lens arrangement outside of the reactor vessel so that only the first sector field (see Fig. V.5-1a) has a direct view to the fusion target. Consequently, the radiation shielding for all following quadrupole lenses must only increase the corresponding lens diameters by about 0.3 m. However, it should not be overlooked that the first one of these lenses is no longer 10 m away from

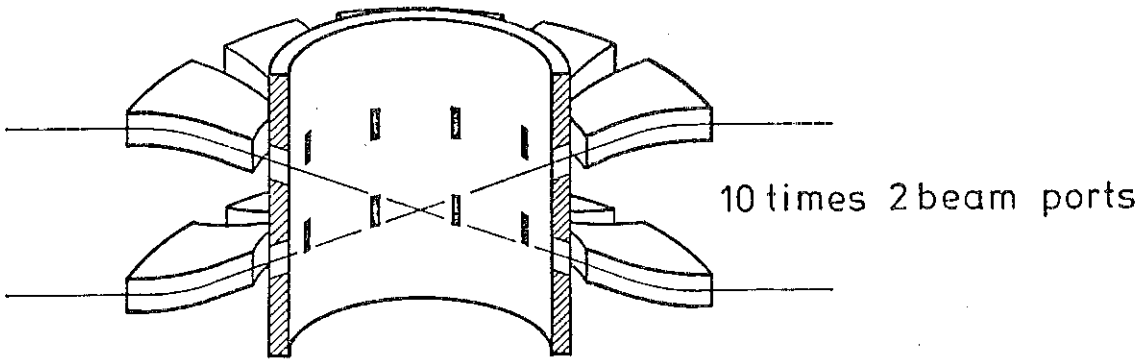

(a)

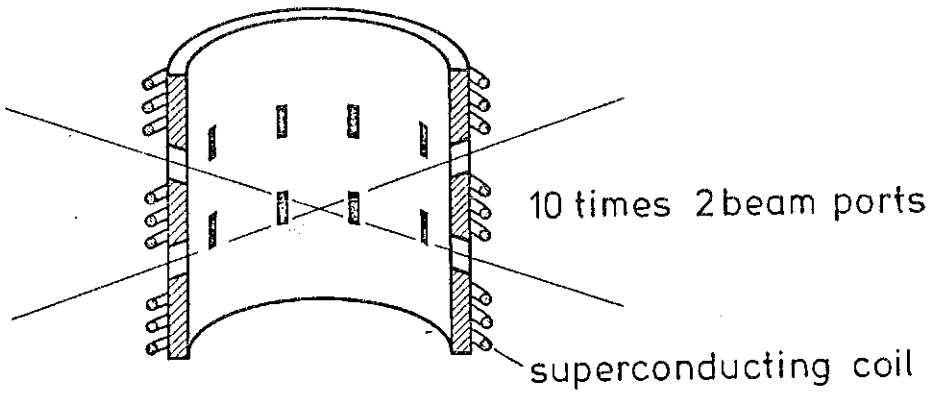

(b)

Fig. V.5-1 Two possible arrangements of a last sector field in the final focusing system are shown which both reduce the radiation level for the final focusing quadrupoles. One first solution (a) postulates vertically deflecting dipole fields immediately outside of the reactor vessel. Note here the race track design of the sector fields which allows tolerable fringing fields and limited amounts of iron. A second solution (b) assumes a large magnetic coil to form a magnet flux parallel to the vessel axis. In this case the optical elements outside of the reactor vessel must focus the ion beam not onto the fusion pellet but to a point about 1 m away from it so that the magnetic field in the reactor vessel can bring it onto the pellet.

the fusion target, that is, the radius of the reactor chamber, but almost 20 m. Thus the lens diameters must be rather large at least in the vertical direction because of the aperture angles of ±40 mrad which are only slightly modified by the first sector field (see Fig. V.5-2). Because of the high rigidity of the ion beams under consideration, the angle of deflection of this first sector field cannot be very large. One should postulate, however, that it must completely separate the ions from the neutron beam at the boundary of the reactor vessel. Choosing a sector magnet of 2 T (or 4 T) one thus finds from simple geometry a deflection angle $\phi_0 \simeq 15°$ (or $\simeq 19°$) and a magnet length of $\rho_0\phi_0 \simeq 8.2$ (or $\simeq 5.8$) meters. In spite of these rather small differences, it seems advantageous to use a sector magnet of 2 T so that good magnet iron can be used to concentrate the magnetic flux and to avoid any problems arising from a high radiation dose. The corresponding magnet is preferably constructed in the race track design as indicated in Fig. V.5-1a.

3. A third type of lens system requires a large preferably superconducting coil to be wound around the reactor vessel (see Fig. V.5-1b) so that a magnetic flux parallel to the axis of this vessel is created. For an optical system outside of the reactor vessel then the ions seem to be focused to a point almost one meter away from the target. Forming a channel of shielding material which is directed towards the virtual target position the neutron and γ-radiation from the target can be shielded effectively. The shielding material can be partially the Pb-Li cooling liquid and partially explicit shielding material placed in and a little outside of the reactor wall. Depending on the design of the Pb-Li sheet probably only a minor amount of shielding material must be added to the reactor wall so that one can employ quadrupole lenses similarly as in case 1.

The conclusions of the previous analysis can be stated as follows:

1. The magnitude of the space charge to be taken into account is unknown for all three focusing schemes. Corresponding experimental investigations of the magnitude of space charge compensation seem indispensable. This includes investigations in the presence of strong magnetic fields.
2. A system as shown in Fig. V.5-2 deflects the ion beam vertically by two magnets. In this design the highest and the lowest points of the two ion beams stacked on top of each other vertically are only about 5 m above and 5 m below the plane of symmetry of Fig. V.5-1a. Systems as shown in Figs. V.5-2 and V.5-3 include much longer straight sections so that vertical deflections can occur only in the beam guidance lines. The highest and lowest points of the two ion beams in these two cases thus are more than 20 m above and below the plane of symmetry as outlined in section V.2.3.
3. Detailed calculations of image aberrations of the final focusing lenses should be performed as soon as the questions of point 1 are better known or reasonable assumptions can be made and as soon as one has fixed a first order design. In such calculations, the effects of the complex beam guidance systems must be included since their influence is not negligible.

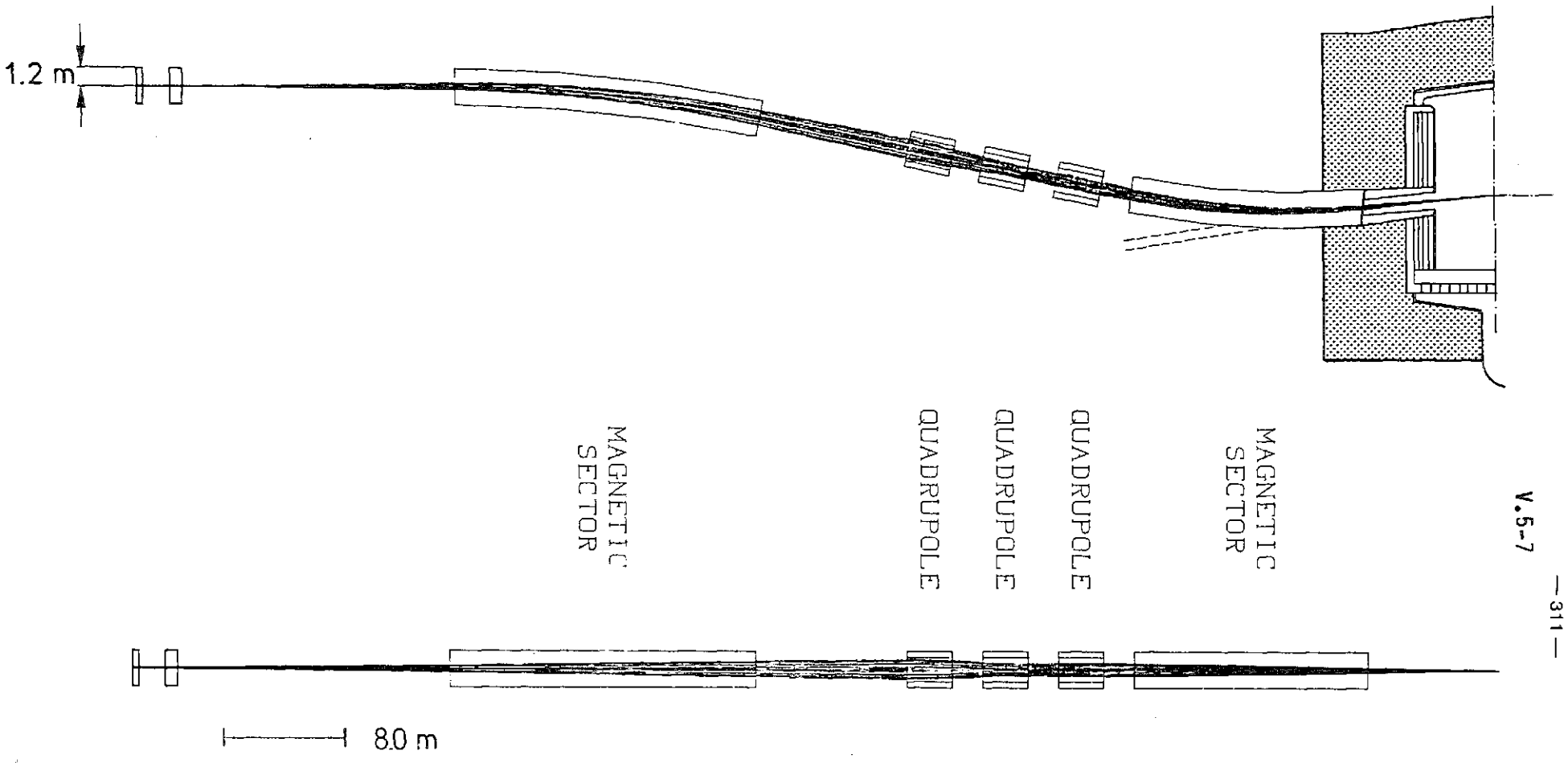

Fig. V. 5-2: Final focusing lens system which uses a magnetic sector field as its last element is shown in a vertical (upper part) and horizontal (lower part) projection. This sector magnet deflects the ion beam so that all quadrupole lenses upstream are out of sight of the fusion pellet and thus subject to a considerably reduced neutron flux only. The neutron and γ-radiation beam is indicated by dashed lines. The draw-back of this design is that the length of the first 2T sector field is 8.2 m so that the first quadrupole lens is about 17m away from the fusion pellet. Because of the large phase space area of $30 \times 120\ \pi^2\ \text{mrad}^2$ the beam radii of these quadrupole lenses then are almost 2 m with flux densities of about 6 T.

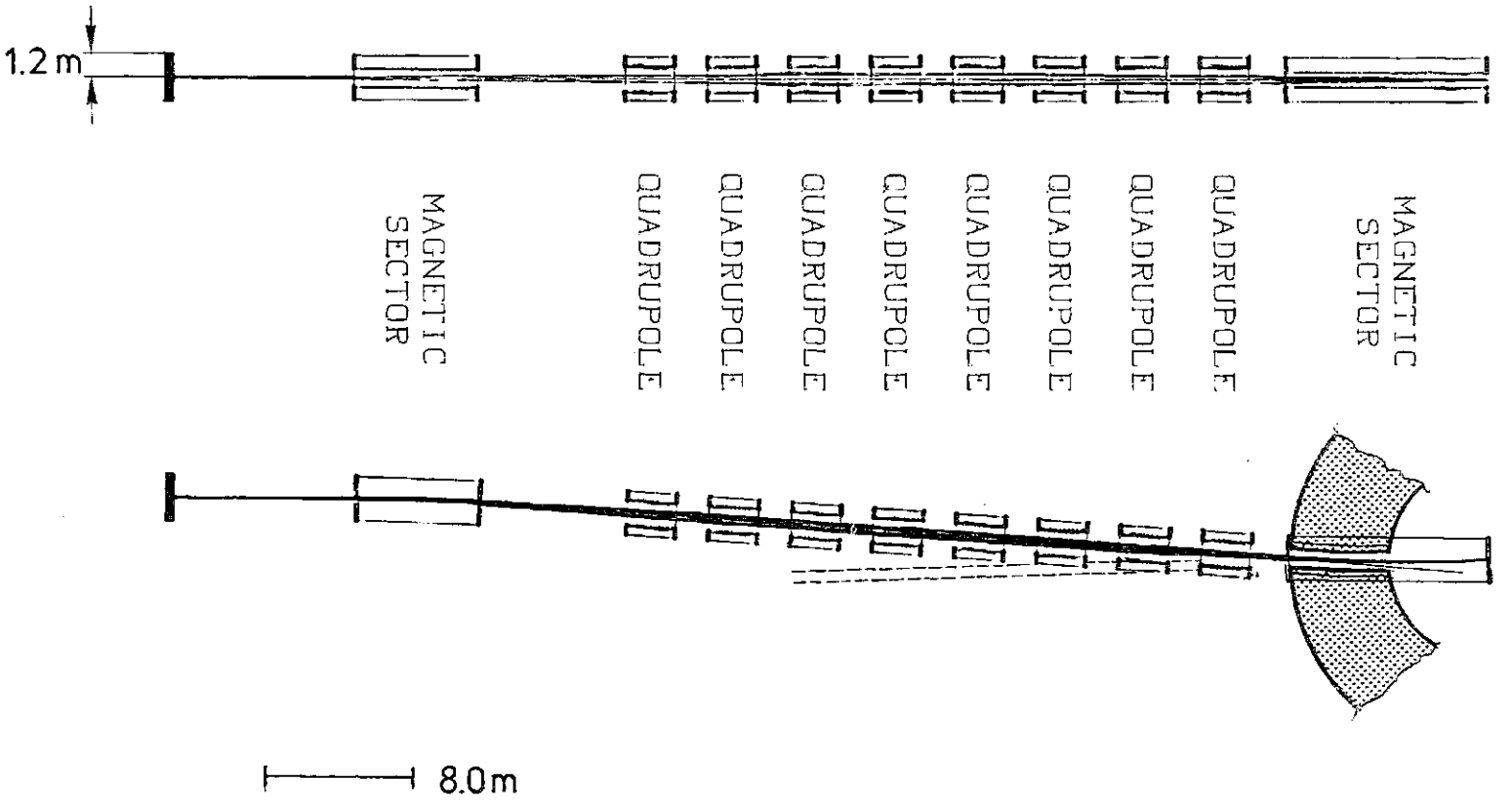

Fig. V. 5-3: A quadrupole lens octett preceded by a sector field and followed by a dipole field of 1T formed by the large coil of fig. V. 5-1b is shown in a vertical (upper part) and horizontal (lower part) projection. Because of the magnetic beam deflection in the reactor vessel the neutron and γ-radiation is already considerably reduced at the reactor wall so that only limited shielding is necessary in the quadrupole lenses and the beam line. Note the neutron and γ radiation indicated by dashed lines.

References for Section V.5

1. G. Krafft, Univ. of California, private communication, October 1980.

2. I. Hofmann, MPP-München, private communication, January 1981.

V.6 Beam Stripping Theory

V.6.1 Stripping Cross Section

The total inelastic scattering cross section for Bi^{+2} on Pb has been calculated in Born approximation by Y. K. Kim.[1] Following the method described in Ref. 2, he has calculated the parameters given in Table V.6-1, which are to be inserted in formulas (1)-(4) of Ref. 2. Table V.6-2 gives the atomic properties needed in the calculation. Kim finds

$$\sigma_{in} = 2.2 \times 10^{-16} \text{ cm}^2/\beta^2 \quad .$$

The first order correction to this formula is estimated to be given by the factor[1]

$$1 - 0.002/\beta^2 \quad ,$$

so that the Born approximation should be very good at $\beta^2 = 0.1$. If we assume that the stripping cross section is 1/3 of this, then

$$\sigma_{st} \doteq 0.7 \times 10^{-16} \text{ cm}^2/\beta^2 \quad .$$

For $\beta^2 = 0.1$, this is

$$\sigma_{st} \doteq 7 \times 10^{-16} \text{ cm}^2 \quad .$$

The best estimate of Pb density in the target cavity when the beam enters is 4×10^{10} atoms/cm^3. This is below the equilibrium density at 470°C which is 8×10^{10} atoms/cm^3. If we take the latter figure as more conservative, we

Table V.6-1 Bethe Cross Sections for the Excitation of Bi^{2+} by Pb (see Ref. 2)

Quantity	Value
$I_{in,el}$	5634.1
$I_{in,in}$	161.83
$\gamma_{in,el}$	-68080.5
$\gamma_{in,in}$	$\sim$ -172150*

*In Eq. (17) of Reference 2, $-2E_{total}$(a.u.) was used instead of S(1). This leads to a value of $|\gamma|$ larger than the correct one.

Table V.6-2 Atomic Properties of Bi^{2+} and Pb

Property*	Bi^{2+}	Pb
Z_N	83	82
Z_e	81	82
$-E_{total}$(a.u.)	21539.4	20889.3
$\langle r^2 \rangle_{6p}(a_0^2)$	6.914	11.423
I.P.$_{6p}$ (eV)	25.08	6.91
S(-1) (Ryd^{-1})	9.433	14.482

*Based on Dirac-Fock wave functions.

get for the mean free path

$$\ell_{st} \sim 150 \text{ m} \quad .$$

The fraction of beam stripped is

$$1 - \exp(-7\text{m}/150\text{m}) \sim 5\% \quad .$$

V.6.2 Beam Loss on Target Due to Stripping

Stripping of a beam ion from $q = 2 \rightarrow 3$ results in a larger deflecting force due to the beam space charge. The displacement at target depends on the distance of the projectile from the target as well as from the beam axis at the moment of stripping.

In order to determine what fraction of stripped ions actually miss the target we introduce a loss factor λ in the rate equation

$$dn(s) = -\sigma_{st}\rho n(s)\lambda(s)\, ds \qquad \text{(V.6-1)}$$

with ρ the background gas density, n the beam density (atoms/cm^3) and s the distance from target. We have calculated λ for different values of s by tracing trajectories of a randomly distributed set of 100 ions (initial K-V distribution) stripped at distance s and moving under the influence of the space charge force of the focused beam, which results from the zero order envelope motion (see Fig. V.6-1). This is valid if only a small fraction of the beam is stripped. By integrating $\lambda(s)$ from 7 m up to the target one finds that the actual loss is only 1/2 the fraction of beam stripped.

Fig. V.6-1

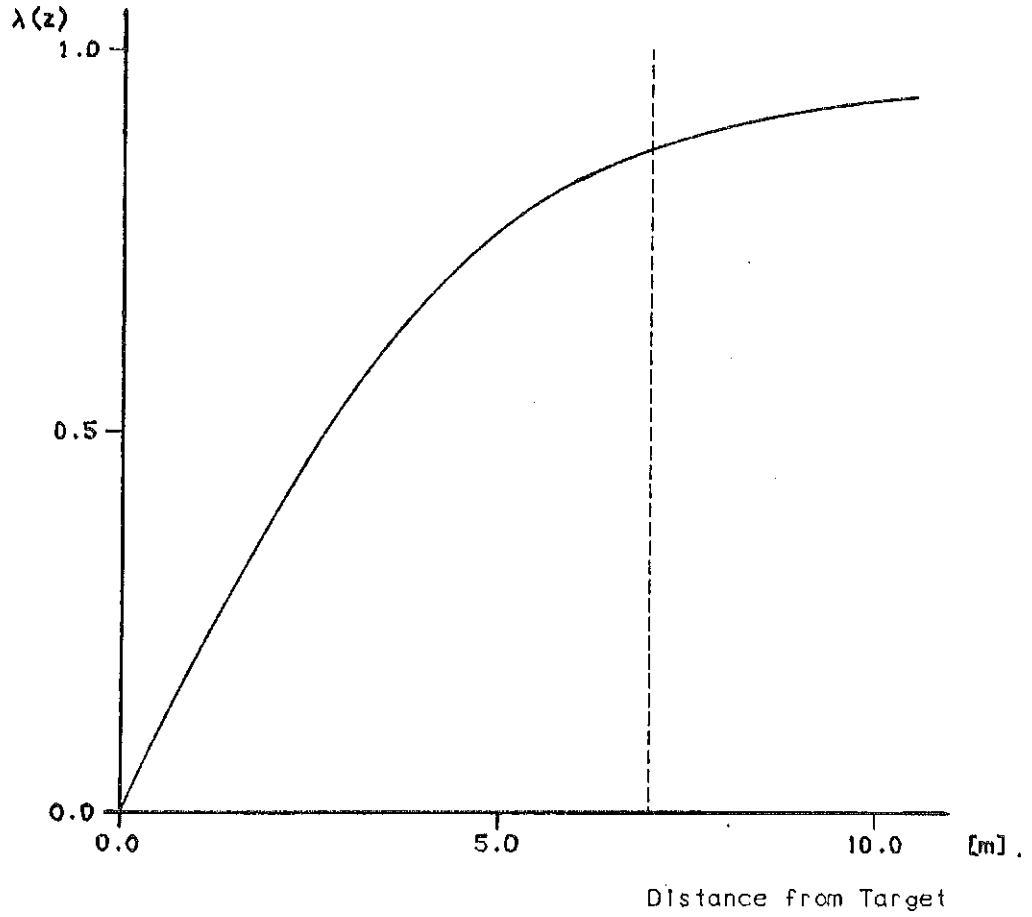

Fig.V.6-1. Loss factor λ(s) (lost ions/stripped ions) as function of distance from target for HIBALL beam and an assumed K-V transverse distribution.

V.6.3 Discussion

For the equilibrium density of Pb at 470°C, i.e. 8×10^{10} atoms/cm^3 the predicted stripping is 5% and the loss on target 2.5%. These rates might be up to a factor of two larger if the ratio $\sigma_{st}/\sigma_{in} = 1/3$ is too optimistic. A more accurate calculation of σ_{st} could be carried out by subtracting from σ_{in} the dominant discrete excitations of Bi^{++} by Pb; this would involve several months of computational effort. On the other hand very crude estimates of non-Born corrections suggest a reduction of the cross sections of 20-30% at the energy considered.(3)

All this amounts to the conclusion that the assumed stripping cross section, 7×10^{-16} cm^2, is probably conservative and leads to less than 5% loss for the assumed background gas density.

We note that beam neutralization due to background gas ionization is negligible here, contrary to a lithium cavity fill gas, where the relevant ionization cross section is an order of magnitude larger than the beam stripping cross section.(4)

References for Section V.6

1. A.K. Kim, Argonne National Laboratory, Argonne, IL, private communication. We are grateful to Dr. Kim for supplying us with the results of these calculations.

2. G.H. Gillespie, Y.K. Kim, and K.T. Cheng, Phys. Rev. A 17, 1284 (April 1978).

3. G.H. Gillespie, private communication (1981).

4. G.H. Gillespie, Heavy Ion Fusion Beam Transport Workshop, LASL, Los Alamos, NM, Aug. 26-27, 1980.